Japan - ASEAN
Science, Technology and
Innovation Platform

Annual Activity Report
on
Japan-ASEAN Science, Technology and Innovation Platform (JASTIP),
Work Package 2 (WP2) –Energy and Environment

2021 Sep. – 2022 Aug.

Index

Surface Modifications of Catalysts in Nanoscale for Improvement of Selectivity and Durability of Photoconversion of Environmental Pollutant and Biomass

Researchers

1. Prof. Dr. Takashi Sagawa	Graduate School of Energy Science, Kyoto University
2. Dr. Verawat Champreda	National Center for Genetic Engineering and Biotechnology (BIOTEC), NSTDA
3. Assoc. Prof. Dr. Surawut Chuangchote	Department of Tool and Materials Engineering, King Mongkut's University of Technology Thonburi (KMUTT)
4. Prof. Dr. Navadol Laosiripojana	Joint Graduate School of Energy and Environment (JGSEE), King Mongkut's University of Technology Thonburi (KMUTT)
5. Miss Nattida Srisasiwimon	Joint Graduate School of Energy and Environment (JGSEE), King Mongkut's University of Technology Thonburi (KMUTT)
6. Dr. Nopparat Suriyachai	University of Phayao

Abstract

Photocatalytic processes for purifications of wastewater to environmentally friendly materials and conversion of sugars to energy and valuable chemicals are considered as new renewable energy technologies and innovations in terms of energy transitions. This work focused on the modification of photocatalysts for the purification of wastewater and conversion of sugars to high-value chemicals. The photocatalysts were designed by optimization of preparation conditions or surface modifications. In terms of purification of wastewater, the photocatalysts were modified using the molecular imprinting technique to create the specific binding cavity for dye molecules on the surface of TiO_2. This technique can increase the selectivity of the photocatalysts. While, the application of conversion of sugars focused on the optimization of preparation TiO_2 coating on supporters (ceramic ball, glass ball, and alumina ball) to apply in a flow reactor. The developments of those photocatalytic systems provide strong platforms for photo-purification of environmental pollutants and photoconversions of sugars to value-added chemicals.

Keyword: Photocatalysts; Wastewater purification; Sugar conversion to high-value chemicals

Introduction

Photocatalysis is considered as a favorable technology for the purification of wastewater and/or conversion of sugars to valuable chemicals due to its environmentally friendly method and low cost [1]. TiO_2 photocatalyst has received the most research attention because of its affordability, nontoxicity, high photoactivity, and high chemical stability [2]. The challenges for the photocatalytic reaction are the fabrication of photocatalysts, recycling of photocatalysts after use, and improving the selectivity of the photocatalysts. In this work, we described the fabrication and modifications of photocatalysts for purification of wastewater and conversion of sugars to high-value chemicals (*e.g.* functional sugar derivatives) through the improvement of catalyst specificity by optimization of preparation conditions or surface modifications and design and assembly of a prototype flow reactor. The modifications of photocatalyst and development of the photocatalytic system can enhance a strong efficiency in photo-purification of environmental pollutants and photoconversion of sugars to value-added chemicals [3-4].

Research Summary

(1) Photodegradation of an environmental pollutant (methyl red) by molecular imprinted TiO_2:

Effective and selective photodegradation of an environmental pollutant (methyl red, MR) was investigated by using molecular imprinted TiO_2 hollow nanofibers (MIHNF-TiO_2). MIHNF-TiO_2 was prepared from the mixture of methyl red, $Ti(OiPr)_3Cl$, acetylacetone, polyvinylpyrrolidone (PVP), and $Ti(OBu)_4$ in EtOH through electrospinning biased under 15 kV at the distance of 15 cm and a feeding rate of 3.0 mL h^{-1}. After the dryness under the atmospheric conditions followed by dipping into 1% NH_3 aq, the obtained fibers were calcined at 600 ˚C for 3 h. SEM images and specific surface areas of electrospun TiO_2 nanofibers were indicated in Figure 1.

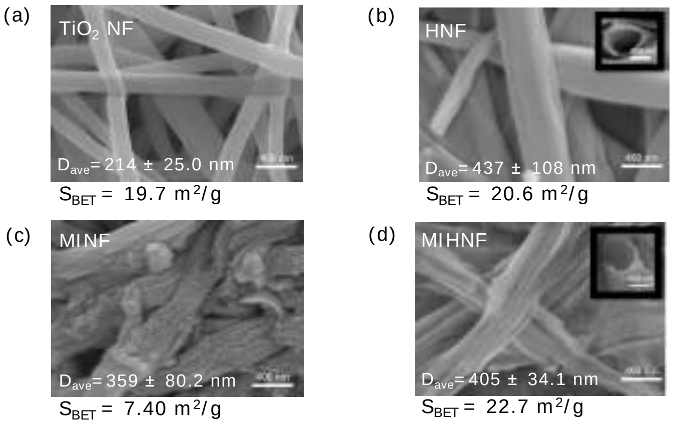

Figure 1. SEM images and specific surface areas of electrospun TiO_2 nanofibers (a), hollow nanofibers (b), molecular imprinted nanofibers (c), and molecular imprinted hollow nanofibers (d).

Photodegradation of MR (6.25, 12.5, 25, and 50 ppm) by MIHNF-TiO_2 in water (pH 7.0) under the irradiation of a 500 W Xe lamp at room temperature was performed and the decrease of the absorbance of MR was monitored.

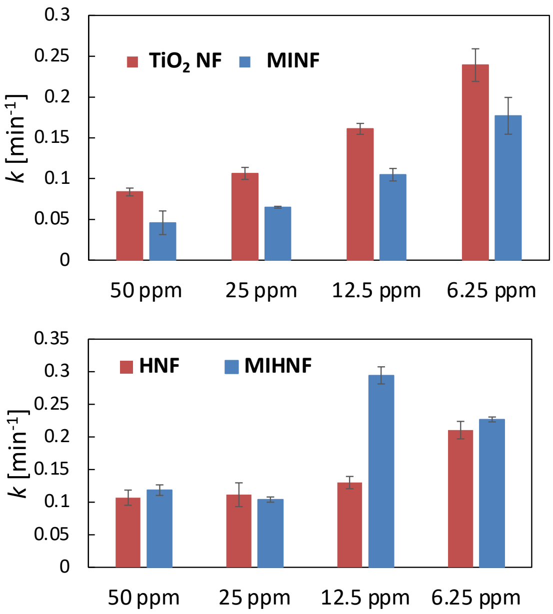

Figure 2. Pseudo 1st order rate constants (k) for MR photodegradation with TiO_2.

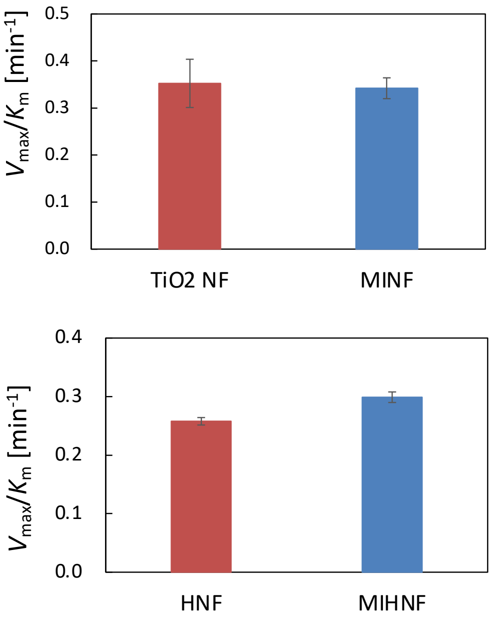

Figure 3. Michaelis-Menten parameters (V_{max}/K_m) for MR photodegradation with TiO_2.

The time-course changes in the concentration of MR obeyed the pseudo-first-order kinetics (Figure 2) with good linearity and the estimated rate constants were replotted as a Lineweaver Bulk plot. Michaelis constant (K_m) and apparent maximal rate constant (V_{max}/K_m) after the formation of MR-TiO_2 complex were estimated (Figure 3). It was found that i) TiO_2 NF has larger k because of larger S_{BET} than MINF, ii) MIHNF shows remarkable large k at lower concentration of MR, iii) MINF has 2.09 times higher affinity ($1/K_m$) for MR than TiO_2 NF, and iv) MIHNF has 1.16 times larger V_{max}/K_m value than non-imprinted HNF. The affinity (*viz.* comparison of $1/K_m$ value) of the molecular imprinted TiO_2 for methyl red is 4 times higher than that of the non-imprinted one. Larger V_{max}/K_m of molecular imprinted TiO_2 than that of non-imprinted one was reflected by the predominant formation of MR-TiO_2 complex through molecular imprinting, which might be able to create the specific binding cavity for MR on the surface of TiO_2. It can conclude that the improvement of selectivity of molecular imprinted TiO_2 photocatalysts for purification of wastewater could be increased.

(2) Photoconversion of sugar by photocatalytic flow reactor:

We developed a flow reactor using Ag/N-TiO_2 as a photocatalyst coated on several supports (ceramic balls, glass beads, and alumina balls) to solve the problem of catalyst separation and recovery. After coating with Ag-N/TiO_2, the surface morphology of ceramic balls and glass beads were covered with Ag-N/TiO_2 in the form of nanoparticles. It could be seen that the catalyst-coated ceramic balls achieved particles with very fine size and well dispersion compared with those in cases of glass beads and alumina balls as shown in Figure 4A-4C. Among the several coating techniques tested, the impregnation process resulted in the highest efficiency for photocatalytic conversion of sugar. Moreover, we found that the rate of glucose conversion was increased with an increase in the flow rate because more glucose molecules can contact catalyst surfaces per unit of time. The flow rate of 100 mL min^{-1} showed the highest glucose conversion of 50% for 6 h with a high yield of gluconic acid, arabinose, xylitol, and formic acid (Figure 4 D-E) as same as a previous report [5]. The durability of the catalysts was studied and 99% catalyst recovery could be achieved.

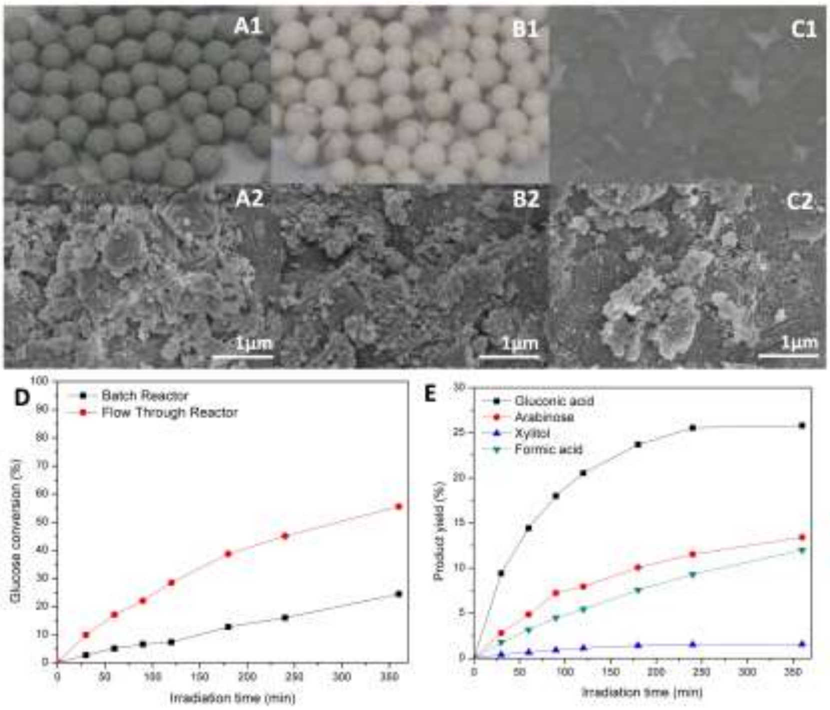

Figure 4. Photograph and SEM images of three different supporting materials (A1) ceramic ball, (B1) alumina ball, and (C1) glass bead. Numbers 2 refer to Ag-N/TiO_2 coated on supporting material at image magnifications of 30k (scale bar = 1 µm) and (D) Photoconversion of glucose over Ag-N/TiO_2 on ceramic ball carried out in photo-bio flow reactor (E) product yields of photocatalytic glucose conversion over Ag/N-TiO_2 nanoparticles.

Conclusion

This collaborative work between BIOTEC/KMUTT and Kyoto University under the JASTIP program was focused on continual research on fabrication and modification of photocatalysts for photoconversion of environmental pollutant and biomass. According to the results, the surface modification by using the molecular imprinting technique to create the specific binding cavity for dye molecules on the surface of TiO_2. This technique can increase the selectivity of the photocatalysts.While, the photocatalytic glucose conversion could convert to a mixture of value added chemicals by using continuous flow reactor under UV-light. Ag-N/TiO_2 coated on ceramic balls using impregnation technique showed the highest photocatalytic performance with high efficiency and stability on photocatalytic glucose conversion. This technique can solve problem on catalyst separation and recovery.

Reference

1. Rafiq, A.; Ikram, M.; Ali, S.; Niaz, F.; Khan, M.; Khan, Q.; Maqbool, M. 2021, *J. Industrial Eng. Chem.*, **2021**, *97*, 111-128.
2. Das, A.; Adak, M.K.; Mahata, N.; Biswas, B. *J. Mol. Liq.*, **2021**, *338*, 116479.
3. Roongraung, K.; Chuangchote, S.; Laosiripojana, N. *Catalysts*, **2020**,*10*, 423.
4. Suriyachai, N.; Chuangchote, S.; Laosiripojana, N.; Champreda, V.; Sagawa, T. *ACS Omega*, **2020**, *5*, 20373-20381.
5. Roongraung, K.; Chuangchote, S.; Laosiripojana, N.; Sagawa, T. *ACS Omega*, **2020**, *5*, 5862-5872.

Publications and Presentations

Roongraung, K.; Chuangchote, S.; Suriyachai, N.; Champreda, V.; Laosiripojana, N.; Maeda, T.; Kimura, T.; Okazaki, Y.; Qu, C.; Sagawa, T. “Surface Modifications of Catalysts in Nanoscale for Improvement of Selectivity and Durability of Photoconversion of Environmental Pollutant and Biomass,” ASEAN International Conference on Energy and Environment in Phnom Penh, Cambodia (Hybrid Conference), 14-15 Sep 2022.

Group Workshops, meetings, and researcher exchange

Supaporn Klabklaydee of KMUTT stayed at Kyoto University from 9 Jun to 31 Jul 2022, supported by the Amgen Scholars Program.

Other outcomes

N.A

Development of Bio-based Carbon Materials for Energy Storage Applications

Researchers

1. Prof. Dr. Takeshi Abe	Kyoto University
2. Dr. Sumittra Charojrochkul	National Energy Technology Center (ENTEC), NSTDA
3. Dr. Pimpa Limthongkul	National Energy Technology Center (ENTEC), NSTDA
4. Dr. Vituruch Goodwin	National Energy Technology Center (ENTEC), NSTDA
5. Asst.Prof. Dr. Yuto Miyahara	Kyoto University
6. Mr. Thanathon Sesuk	National Energy Technology Center (ENTEC), NSTDA

Abstract

The Development of bio-based carbon materials is a part a Bio Circular Green Economy (BCG) model promotion according to current Thai government policy. Oil palm agricultural waste, including palm empty fruit bunch (PEFB) and palm shell (PS) was studied as raw materials to product activated carbon for supercapacitor applications. This study aims to investigate the synthesis condition and nitrogen doping on activated carbon from oil palm biomass for high-performance supercapacitors. A unique combination between chemical and surface modification processes have been carried out using hydrothermal and nitrogen doping with various nitrogen sources to achieve high surface area activated carbon with designed pore and surface properties. This research is an extension of the previous success work in producing activated carbon from palm empty fruit bunch (PEFB) and palm shell (PS) which exhibit a capacitance higher than that of commercially available activated carbon in an aqueous electrolyte. (JASTIP, phase I)

The different nitrogen sources are doped on activated carbon from PEFB and PS to enhance the ion conductivity of electrode and electrolyte in supercapacitor. The effect of nitrogen addition on pore generation both micropore and mesopore is investigated. In addition, It was reported from previous research that nitrogen functional groups formed on the surface of activated carbon could promote the surface ion transportation in supercapacitors. Thus, nitrogen doping when combined with chemical activation process could enhance the electrochemical properties of activated carbon when used as an electrode in either aqueous or organic electrolyte supercapacitors.

The activated carbon from PEFB and PS biomass has shown good properties in terms of high surface area and porosity. To improve the electrical conductivity of the activated carbon, the modification by nitrogen doping with ammonium chloride, urea and melamine was studied. The effect of different nitrogen sources on electrochemical performance were reported. The modified mesopore carbon was tested in a symmetrical swagelok supercapacitor cell to evaluate the specific capacitance and efficiency using galvanostatic charge-discharge method. The nitrogen doped PEFB activated carbon with urea doped exhibits the highest specific capacitance of 130 F g^{-1} at current loading of 0.1 A g^{-1} in an aqueous 1M H_2SO_4 electrolyte. The nitrogen doped PEFB activated carbon with urea doped has lower internal resistance due to nitrogen from urea enhance the electronic conductivity of the electrodes and thus increase the supercapacitor performance.

Research Summary

1. Study the effect of nitrogen doping on the electrochemical performance of activated carbon from oil palm biomass using different nitrogen sources

The effect of different nitrogen sources doping onto the activated carbon produced from oil palm biomass was studied. All experiments used empty palm bunches (PEFB) as the starting biomass. PEFB hydrochar from hydrothermal carbonization (HTC) of palm empty fruit bunches was mixed with $ZnCl_2$ and three different nitrogen sources, which are ammonium chloride, urea and melamine. Then the mixture was activated at 800°C under CO_2 atmosphere. The nitrogen-doped activated carbon was used as electrode materials in a swagelok cell for GCD test using aqueous 1 M H_2SO_4 electrolyte. Figure 1 shows a schematic of the overall nitrogen-doped activated carbon production process.

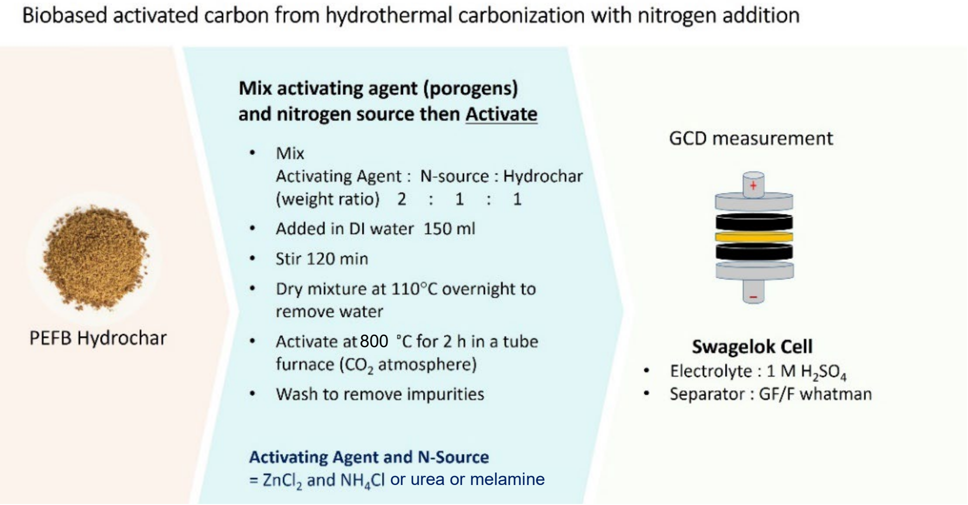
Biobased activated carbon from hydrothermal carbonization with nitrogen addition

Mix activating agent (porogens) and nitrogen source then Activate

- Mix
  Activating Agent : N-source : Hydrochar
  (weight ratio) 2 : 1 : 1
- Added in DI water 150 ml
- Stir 120 min
- Dry mixture at 110°C overnight to remove water
- Activate at 800 °C for 2 h in a tube furnace (CO_2 atmosphere)
- Wash to remove impurities

Activating Agent and N-Source
= $ZnCl_2$ and NH_4Cl or urea or melamine

Swagelok Cell
- Electrolyte : 1 M H_2SO_4
- Separator : GF/F whatman

Figure 1 The schematic of a production process of nitrogen doped PEFB activated carbon.

The preliminary capacitance value of nitrogen doped PEFB activated carbon was tested using two-electrode swaglok assembly as shown in Figure 2. The nitrogen-doped activated carbon and conductive carbon was dried at 80°C for at least 3 hours in a vacuum oven. Then the activated carbon sample and conductive carbon were mixed in mortar with the ratio of 80:10 by weight. Then transfer the carbon mixture into the mixing container and add 12% by weight PVDF in NMP binder to the carbon powder mixture. The mixture was mixed in Planetary centrifugal mixer at 1200 rpm for 10 min or until the slurry was homogenous. The carbon slurry was spread on the stainless-steel foil which is a current collector. The slurry was casted using doctor blade which was set at 80 micron height. The stainless-steel foil coated with activated carbon is dried in a vacuum oven at 80°C for at least 12 hours. The prepared activated carbon electrode sheet was cut with an electrode puncher to a diameter of 11 mm. After that, the electrode sheet was dried for at least 3 hours at 80°C in a vacuum oven. Then let cool to room temperature in a dehumidifier.

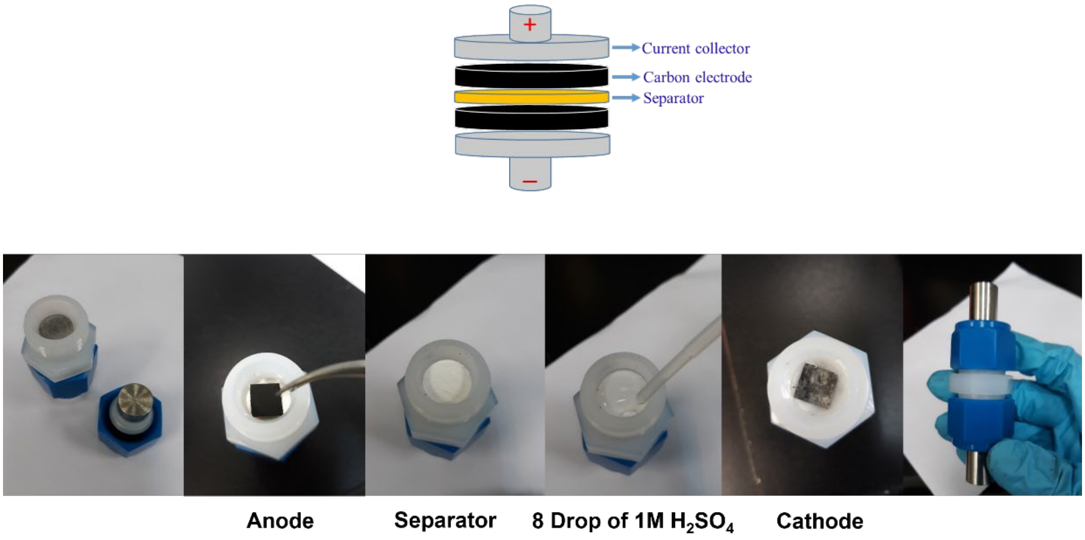

Figure 2 Swagelok cell assembly for GCD electrochemical performance test of nitrogen doped PEFB activated carbon.

Galvanostatic Charge-Discharge test (GCD) is a constant current charge-discharge perform on energy storage cell. The charge-discharge test for rate test performance was performed using Maccor machine, where the charge and discharge rates were set at the current densities of 0.1, 0.2, 0.5, 1 and 2 A/g, 5 cycles at each rate. The voltage range is set at 0 – 0.6 V to measure the capacitance of the carbon electrode. All the supercapacitor tests were in aqueous electrolyte, 1 M sulfuric acid.

The capacitance value of nitrogen doped PEFB activated carbon is shown in Figure 3. The capacitance of nitrogen-doped activated carbons with different nitrogen sources added on hydrochar and activated with $ZnCl_2$ at activation temperature of 800°C were compared. The ACs doped with nitrogen from Ammonium chloride (NH_4Cl), urea (Urea) exhibits higher specific capacitance value from GCD test than the commercial carbon, YP-50F. This promising preliminary result of the nitrogen-doped PEFB activated carbon shows that it has high opportunity to improve the bio-based PEFB activated carbon supercapacitor performance via nitrogen doping method.

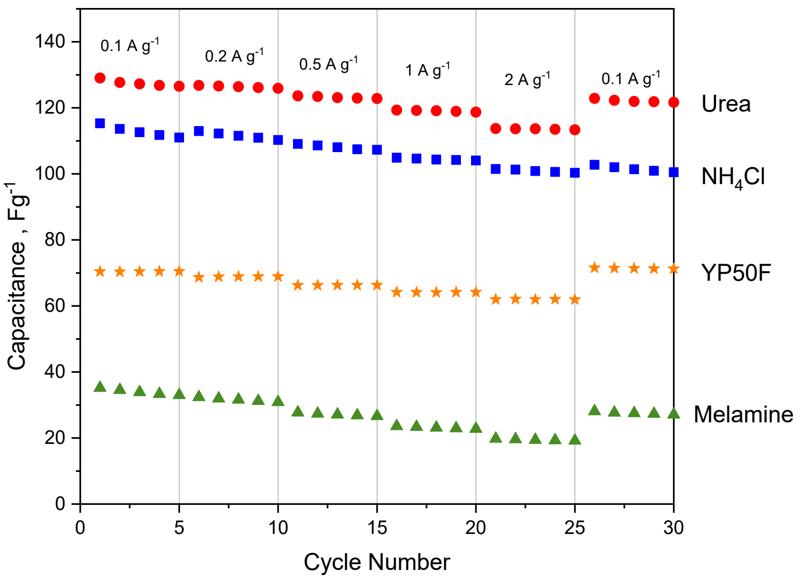

Figure 3 Specific capacitance from GCD test of nitrogen doped PEFB activated carbon, using NH_4Cl, urea and melamine as nitrogen sources and YP50F commercial activated carbon as a benchmark.

2. Study the effect activated temperature on the electrochemical performance of nitrogen doped activated carbon from oil palm biomass

Biochar from hydrothermal carbonization (HTC) of palm empty fruit bunches (PEFB) is mixed with Zinc chloride ($ZnCl_2$) and nitrogen-source with Char:$ZnCl_2$:nitrogen source weight ratios of 2:1:1. Then the char mixture was activated in a furnace at 700 and 800°C under CO_2 atmosphere at a flow rate of 60 ml/min for 2 h. The activated carbon was washed to remove any residue impurities. The final nitrogen doped activated carbon samples were made into an electrode with 11 mm diameter. A Swagelok cell with 1 M H_2SO_4 electrolyte was assembled and employed on the electrochemical test, galvanostatic charge-discharge (GCD), to evaluate the supercapacitor performance. The galvanostatic charge-discharge test was performed by charging and discharging between 0 – 0.6 V using constant current levels of 0.1, 0.2, 0.5, 1 and 2 A g^{-1} of activated carbon.

2.1 The specific capacitance of nitrogen doped PEFB Activated Carbon

The results of capacitance determined from the charge-discharge test using GCD technique showed that activated carbon doped with nitrogen using urea and ammonium have higher specific capacity than the benchmark activated carbon, YP-50F (Figure 4). It was found that the activated carbon with the highest capacitance at a current density of 0.1 A/g was Urea-700. But when increasing the current density, Urea-700 activated carbon has consistently decreased in capacitance (low rate capability). On the other hand, the Urea-800 activated carbon samples show only a small decrease in their capacitance (Good or High rate capability), when the current density rate is increased from 0.1 to 2 A/g. This could be resulting from Urea-800 samples has pore structure with higher mesopore volume than the sample activated at 700°C. Mesopore was reported to help the ion transportation which contributed to the better retention of capacitance at high discharge rate. The same behavior was observed with ammonium chloride doped activated carbon.

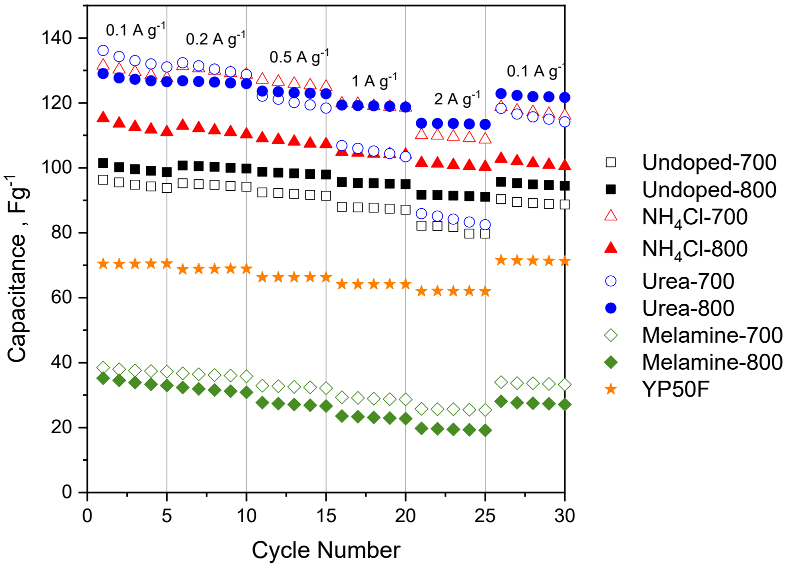

Figure 4 Capacitance from GCD test of N-doped PEFB activated carbon, undoped PEFB activated carbon activated at 700 and 800°C and YP50F commercial activated carbon as a benchmark.

2.2 The specific surface area and pore properties of nitrogen doped PEFB Activated Carbon

The pore distribution plot of nitrogen doped activated PEFB activated carbons are shown in Figure 5. All nitrogen doped activated carbons have high surface area which contained mostly micropore (<2 nm). It was found that when the activating temperature was increased, the mesoporous volume of activated carbon was also increased. The results of specific surface area (BET) and pore volume shown in Table 1.

Table 1. BET surface area and pore volume of nitrogen doped PEFB activated carbons and YP-50F.

Activated Carbon	BET Total Surface Area (m^2/g)	Mesopore (%)	Total pore volume (cm^3/g)	Micropore volume (cm^3/g)	Mesopore Volume (cm^3/g)
Undoped-700	1579	57.95	1.28	0.54	0.74
Undoped-800	1599	57.78	1.24	0.52	0.72
NH$_4$Cl-700	1793	24.72	0.89	0.67	0.22
NH$_4$Cl-800	1608	32.61	0.92	0.62	0.30
Urea-700	1497	12.20	0.72	0.63	0.09
Urea-800	1496	17.61	0.69	0.57	0.12
Melamine-700	371	7.49	0.15	0.14	0.01
Melamine-800	310	8.05	0.15	0.13	0.02
YP50F	1654	8.00	0.71	0.65	0.06

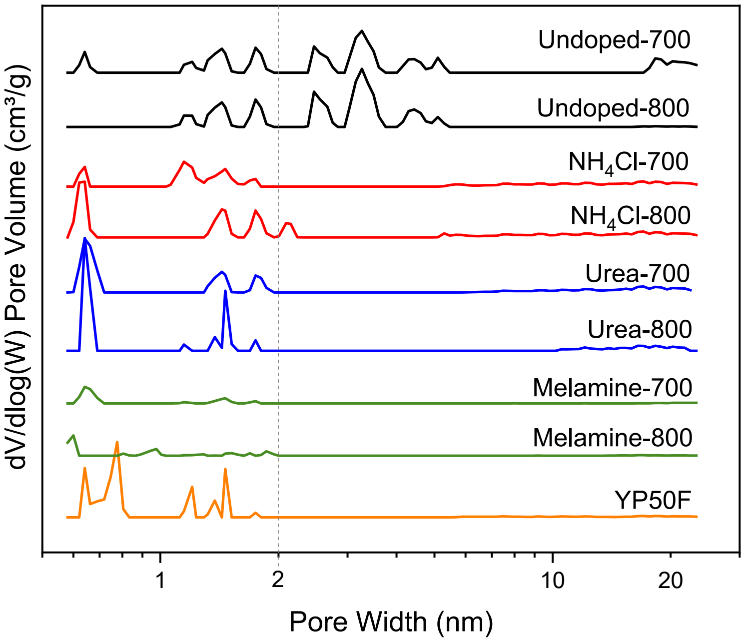

Figure 5 Pore size distribution plot of commercial activated carbon, YP-50F compared to undoped and nitrogen doped activated carbons from different nitrogen sources.

From Table 1, the ammonium chloride and urea doped activated carbon produced using ahas the largest amount of micropore volume between 0.57 to 0.67 cm^3/g. From Figure 5, most of the nitrogen doped activated carbons has pore size ~ 0.6 - 0.7 nm which is able to accommodate the ion in aqueous electrolyte system. This results showed combination of micro and mesopore in the nitrogen doped PEFB activated carbon enhances the electrical capacitance when nitrogen doped carbon is utilized as an electrode in supercapacitors.

Conclusion

Nitrogen doping effect during activation process was investigated using palm empty fruit bunches (PEFB) as starting biomass. It was found that nitrogen doping in the activated carbon activation process did not significantly affect the surface area. However, the effect of the activation temperature directly affects the surface area and mesopore volume. The activated carbons obtained via the activation temperature of 800°C exhibit higher mesopore volume. The electrical capacitance of undoped activated carbon in this process was slightly lower than that of nitrogen doped activated carbon. The ammonium chloride and ura doped and activated at 800°C could retained high capacitance value with increasing current density ratio, indicating the nitrogen doped EFB activated carbon produced at ENTEC has good rate capability. In conclusion, the best process for nitrogen doping for activated carbon is using ammonium chloride or urea as nitrogen source and activating at 800°C. Both nitrogen doped activated carbons yielded high specific capacitance at 130 and 115 F/g at 0.1 A/g which are higher than YP-50F at 75 F/g.

3. Production of nitrogen doped palm shell (PS) activated carbon

In this part of the activated carbon production and electrochemical performance experiments, the testing conditions and steps for the preparation of activated carbon from empty palm fruit bunches (PEFB) in previous section were used as described earlier. However, in this section the nitrogen doped activated carbons were prepare from palm shell biomass as raw materials. Three samples of PS activated carbon were prepared as follows:

PS-HWZ 800 prepared without nitrogen doping. 30 g of palm shell were used and $ZnCl^2$ was used as the activator with $ZnCl_2$:hydrochar weight ratio of 2:1 and the activated was done at 800°C.

PS-HWZA 800 was prepared using nitrogen doping with ammonium chloride in the activation step. 15 g of hydrochar from palm shell, $ZnCl_2$ was used as the activator at the $ZnCl_2$:hydrochar weight ratio of 2:1 and 15 g of ammonium chloride was mixed and then activated at temperature of 800°C.

PS-HWZU 800 was prepared using urea as nitrogen source. 15 g of urea was added in the activation step to 15 g of hydrochar from palm shell. The activating agent, $ZnCl_2$ was used with the $ZnCl_2$:hydrochar ratio of 2:1 and activated at 800°C.

The specific surface area and pore properties of nitrogen doped PS Activated Carbon

The results of the specific surface area and porosity are shown in Table 2. When considering the specific surface area, it was found that the specific surface area of undoped PS activated carbon is lower at 1487 m^2/g than the ammonium chloride doped PS activated carbon which has surface area of 1641 m^2/g. For PS activated carbon doped with ammonia chloride and activated at 800 °C and PS activated carbon doped with urea and activated at 800 °C, the mesopore content of activated carbon from palm shell doped with ammonium chloride have more mesopore than PS activated carbon doping with urea. As a result, the larger molecular size of urea has effect on the mesopore generation. The pore size distribution of the nitrogen doped PS activated carbons are shown in Figure 6.

Table 2. BET surface area and pore volume of nitrogen doped PS activated carbons and YP-50F.

Activated Carbon	BET Total Surface Area (m^2/g)	Mesopore (%)	Micropore volume (cm^3/g)	Mesopore Volume (cm^3/g)
PS-HWZ-800	1487	45.0	0.56	0.45
PS-HWZA-800	1641	19.2	0.66	0.16
PS-HWZU-800	1404	1.63	0.60	0.01
YP50F	1654	8.0	0.65	0.06

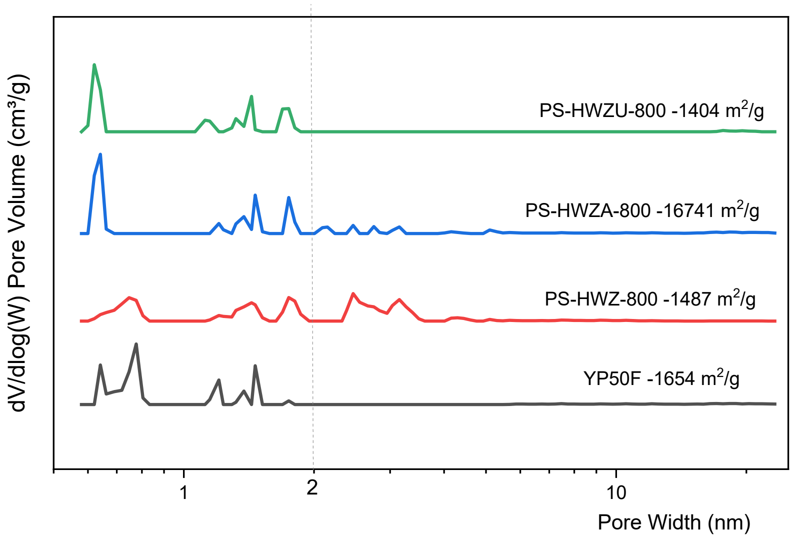

Figure 6 Pore size distribution plot of commercial activated carbon, YP-50F compared to nitrogen doped PS activated carbons.

Electrochemical test, GCD result of nitrogen doped PS Activated Carbon

The GCD results test of PS activated carbons are shown in Figure 7. It can be seen that the nitrogen doped PS activated carbons (PS-HWZA and PS-HWZU) have higher specific capacitance than the undoped activated carbon (PS-HWZ). When compared to the commercial carbon, YP-50F, It was found that PS-HWZU-800 had higher capacitance at a current density of 0.1 A/g than YP-50F. The effect of urea doping is prominent in this case. However, PS-HWZU-800 activated carbon has a continuous decrease in capacitance when discharge at high current density (2 A/g). This could be resulting from low mesoporous structure of the samples. Whereas with commercial carbon, YP50F showed a small decrease in capacitance with increasing current density, indicated that commercial carbon has a structure with a higher mesopore volume. This results in a good rate capability of carbon electrode (Good rate capability), which is the same behavior found in undoped PS activated carbon.

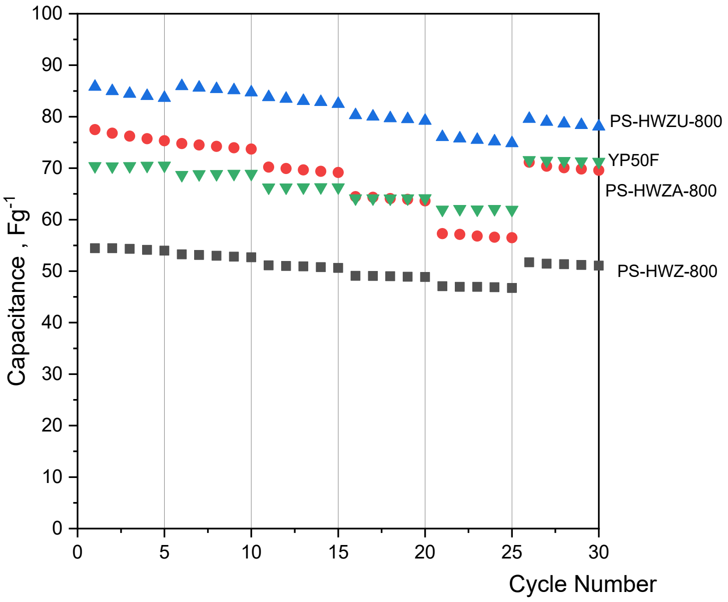

Figure 7 Capacitance results from GCD test of PS activated carbon compare with YP-50F.

Conclusion

The production of activated carbon from palm shell biomass and nitrogen doping by ammonium chloride and urea was achieved. Activated carbon from palm shell has high surface area and porosity. When testing the electrical discharge with GCD technique, the urea doped PS activated carbon gives the highest specific capacitance. The low rate capability of nitrogen doped PS activated carbon could be improve with higher activation temperature to increase mesopore volume. The optimization of nitrogen doping and activation conditions to produce activated carbons with both micro and mesopore structures is necessary to enhance the capacitance of PS activated carbon to perform better as an electrode for aqueous electrolyte supercapacitors.

4. Study the electrochemical performance of nitrogen-doped oil palm bio-based activated carbon in non-aqueous electrolyte (KU)

Specific capacitances of nitrogen-doped EFB-based ACs were evaluated in organic electrolyte. EFB-HMZA-800N and EFB-HMZU-800N were used for the test and commercial AC was used for comparison. The ACs, acetylene black, and polyvinylidene difluoride (PVdF) with weight ratio of 7 : 1 : 2 were homogeneously dispersed in N-methylpyrrolidone by mixing and deaerating the slurry, followed by coating the slurry on Al current collector to fabricate thin-film layer of the AC composite electrode. Two pieces of the vacuum-dried electrode sheet with diameter of 15.95 mm, separator (Celgard #2400), 1 M $(C_2H_5)_4NBF_4$/propylene carbonate was used for coin cell assembly as shown in Figure 8.

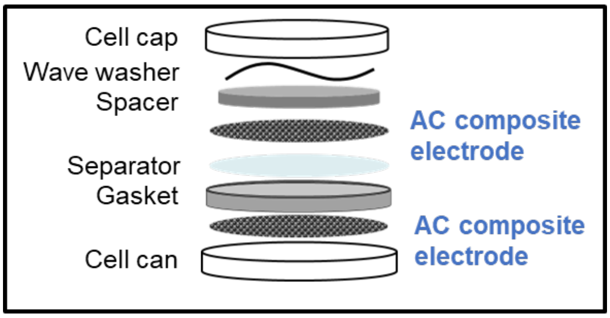

Figure 8 Schematic illustration of the coin cell

Comparison of specific capacitance at various current densities was shown in Figure 9. As shown in Table 2, additionally, their capacitances at 0.05 A/g and 0.1 A/g were normalized with the ones at 0.02 A/g. Although the EFB-based ACs showed relatively smaller capacitances than YP-50F, they exhibited similar rate capabilities to YP-50F, implying that the synthesized ACs would have suitable structure to facilitate both electronic conduction and ionic transport. Moreover, since the normalized capacitances in this work was better than that in previous study employing simple dry mixing of AC, acetylene black, and polytetrafluoroethylene to fabricate self-standing electrodes, present thin-film configuration would be a preferable method to exhibit better rate capability.

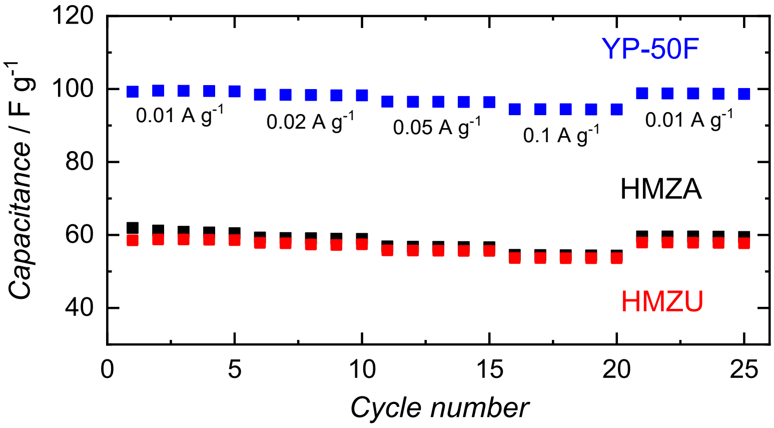

Figure 9 Specific capacitances of ACs as a function of cycle number at various current densities. (HMZA and HMZU is the nitrogen-doped EFB-ACs and YP-50F is commercial carbon)

Table 2 Normalized specific capacitance of the ACs at 0.05 and 0.1 A/g.

Electrode	Carbon	Normalized capacitance	
		@0.05 A/g	@0.1 A/g
This work (Thin film)	YP-50F	98 %	96 %
	EFB-HMZU	97 %	93 %
Previous (self-standing)	EFB-21900	89 %	75 %

Publications and Presentations

1. Parinya Jitreewas, Thanathon Sesuk, Vituruch Goodwin, Arintarached Sirinantawittaya, Pimpa Limthongkul and Sumittra Charojrochkul, "One-pot hydrothermal synthesis and nitrogen-doped activated carbons from palm empty fruit bunches for supercapacitor electrode material", Pure and Applied Chemistry International Conference 2022 (PACCON2022), 30th June – 1st July 2022, Bangkok, Thailand.
2. Vituruch Goodwin, Parinya Jitreewas, Thanathon Sesuk, Pimpa Limthongkul and Sumittra Charojrochkul, "Development of Modified Mesoporous Carbon from Palm oil Biomass for Energy Storage Supercapacitor Application", 2nd ASEAN International Conference on Energy and Environment (AICEE) 14th – 15th September 2022, Phnom Penh, Cambodia (online).
3. Vituruch Goodwin, Parinya Jitreewas, Thanathon Sesuk, Pimpa Limthongkul Sumittra Charojrochkul, "Development of Modified Mesoporous Carbon from Palm oil Biomass for Energy Storage Supercapacitor Application", *Journal of Physics: Conference* (submitted).

Nanocarbon Materials for Sustainable Production and Storage of Green Fuels and Platform Chemicals

1. Research team

Prof.Dr. Noriaki Sano, Kyoto University (PI, Japan side)
Dr. Kajornsak Faungnawakij, NANOTEC, NSTDA (PI, Thailand side)
Dr. Pongkarn Chakthranont, NANOTEC, NSTDA
Dr. Pongtanawat Khemthong, NANOTEC, NSTDA
Dr. Sirapassorn Kiatphuengporn, NANOTEC, NSTDA
Dr. Bunyarat Rungtaweevoranit, NANOTEC, NSTDA
Dr. Jeeranan Nonkumwong, NANOTEC, NSTDA
Dr. Anchalee Jankaew, NANOTEC, NSTDA
Dr. Pussana Hirunsit, NANOTEC, NSTDA
Dr. Tanasan Intana, NANOTEC, NSTDA
Miss. Sutarat Thongratkaew, NANOTEC, NSTDA
Dr. Supawadee Namuangruk, NANOTEC, NSTDA
Dr. Sareeya Bureekaew, VISTEC
Prof. Dr. Metta Chareonpanich, Kasetsart University
Prof. Dr. Thongthai Witoon, Kasetsart University
Assoc. Prof. Anusorn Seubsai, Kasetsart University
Asst. Prof. Dr. Waleeporn Donphai, Kasetsart University
Dr. Narong Chanlek, Synchrotron Light Research Institute (Thailand)

2. Purpose of Collaborative Research

The effects of climate change caused by anthropogenic CO_2 emission have increased the average global temperature by 1 °C above the pre-industrial level. If this current trend is continued, the average global temperature is expected to inevitably elevate by 4-5 °C by 2100. To slow down this global crisis, greenhouse gas emissions must be drastically reduced towards zero emissions within this century. This need has led to the blossom of green technological concepts including biorefinery and bio-energy devices where renewable resources replace the need for fossil fuel in the future. The catalytic productions of carbon-based materials, biofuels, and biochemicals are at the heart of the biorefinery industry. The collaborative researches carried out by the groups in NANOTEC/NSTDA (Faungnawakij's team) and Kyoto University (Sano's team) aim to develop new and innovative knowledge on biomass conversion to useful materials and the development of bio-energy devices.

This year, 3 major research activities have been done as follows.

- Microwave-induced plasma with KOH (MiWP-KOH) activation for preparation of high-surface-area activated carbon: Controllability of pore structures by KOH-to-carbon ratio in feed and activating time

- Optimization of H_2O_2 Electrogeneration from Tea-Leaf-Derived N-Doped Carbon Catalyst and Demonstration of H_2O_2-Assisted Electrocatalytic 5-Hydroxymethylfurfural Oxidation
- Development of Spinel Catalysts for the Selective Hydrogenation of Furfural to Furfuryl alcohol

3. Research Outcome

1.1 Microwave-induced plasma with KOH (MiWP-KOH) activation for preparation of high-surface-area activated carbon: Controllability of pore structures by KOH-to-carbon ratio in feed and activating time

Purichaya Kuptajit, Noriaki Sano, Kyuya Nakagawa, Tetsuo Suzuki*
Department of Chemical Engineering, Graduate School of Engineering, Kyoto University,
Nishikyo-ku, Kyoto 615-8510, Japan

ABSTRACT

Recently, it was found that the activation by microwave-induced plasma (MiWP-KOH) can be used to prepare high-surface-area activated carbon (AC) within a few minutes. In the present study, microwave-activation time and KOH concentration in the feed mixture are focused as key factors governing the pore formation. In addition to BET surface area, micropores and mesopores volumes were used to estimate structures of resulted AC prepared by MiWP-KOH activation. The experimental results show that activated carbon with specific surface area of 1,251 and 2,718 m^2g^{-1} can be obtained within 80 and 270 s. When the activation time and KOH concentration are increases, micro and mesopore volumes are also increase. However, excessively long activation time was not useful to increase these volumes. It was observed that the concentration of KOH should be high enough to stabilize the pore structures. It was suggested that the hierarchical pore structure can be controlled as function of the KOH concentration, so that the microporosity can be increased by increasing KOH concentration. In addition, mass yield percentage of the AC is 12.3 wt-% in the conditions to achieve the stabilized values of micropore volume and specific surface area, which seems higher than the mass yield percentage of the AC prepared by a conventional activation using electric furnace.

Introduction

A high surface activated carbon (AC) is a porous carbon material, which has specific surface area of 1,000-3,000 $m^2\ g^{-1}$. It has been used widely owing to its high surface reactivity, hierarchical pore structure, and high surface area provided more adsorption-site (Sayğılı et al., 2015). It can be used in purification and separation processes. For example, H_2 purification (He et al., 2020), glycerol purification (Habaki et al., 2019), and syngas purification (Pena et al., 2020). Moreover, it was used as a catalysts or catalyst supports for syngas production (Su et al., 2020), phosgene formation (Rossi et al., 2020), and phenols production (Huo et al., 2020). AC can be used as electrode materials for supercapacitors (Inal et al., 2020, Jiang et al., 2020, Cossutta et al., 2020). Owing to those varieties of application, the demand for AC has been increasing worldwide.

AC has a hierarchical pore structure consisting of micropores, which their pore diameter is smaller than 2 nm, mesopores, which have pore diameter in the range of 2-50 nm, and macropores, which their pore diameter is larger than 50 nm (Lozano-Castello et al., 2002, Aroua et al., 2008, Ahmed et al., 2016a, Ahmed et al., 2016b, Rashidi et al., 2017). Although AC with microporous structure has high adsorption efficiency for small molecules (acetone, dichloromethane, ethyl formate), it is not so effective for large molecules or ions. On the contrary, AC with mesoporous structure is suitable to adsorb macromolecules such as dyes, proteins, antibiotics, and polycyclic aromatic compounds (Benhouria et al., 2015). The large molecule can diffuse into mesopores and be adsorbed onto the surface of the pores.

Various activating agents can be used to produce the AC with mesoporous structure. For example, steam (Lam et al., 2019, Yek et al., 2019), CO_2 (Xin-hui et al., 2011), $ZnCl_2$ (Nasrullah et al., 2019), H_3PO_4 (Liu et al., 2010, Koyuncu et al., 2018), NaOH (Zhang et al., 2019, Boujibar et al., 2019, Yu et al., 2019), K2CO3 (Deng et al., 2010, Foo and Hameed, 2012) and KOH (Li et al., 2019, Erdoğan et al., 2017). To prepare high surface area AC with mesoporous structure, activating agents is mixed with carbon precursors. Then, the mixture must be heated at elevated temperature for some period (Selvaraju and Bakar, 2018, Loya-González et al., 2019, Zabaniotou et al., 2004, Zhang et al., 2019). Among activation methods mentioned above, KOH activation is a well-established method that can be used to prepare high-surface-area AC in industrial scale (Liang et al., 2018). Previous study reported that the high-surface-area AC with micro and mesoporous structures can be prepared by mixing KOH with the carbon precursor using KOH/carbon mass ratio of 6 (Njoku et al., 2014).

In a conventional process, the feed material (activating agents and carbon precursors) was heated at 700-850 °C for 0.5-2.5 h to get the AC with specific surface area in the range of 647-2,413 m^2 g^{-1} (Li et al., 2019, Nasrullah et al., 2019, and Sulaiman et al., 2018). Nowadays, preparation process of AC is limited to batch system due to the long activation time. The batch system cannot efficiently produce AC in large scale. If the preparation time becomes shorter (several minutes), the AC preparation process can be operated in continuous system.

Many researchers have been seeking for a new method to reduce activation time by applying microwave irradiation to the KOH activation. For example, previous study (Deng et al., 2010) reported that AC can be synthesized using KOH activation with microwave irradiation, suggesting that AC with specific surface area of 729 m^2 g^{-1} can be prepared within 10 min. In another study, AC was prepared by microwave-KOH activation (Foo and Hameed, 2011), suggesting that the mixture of carbon precursors and KOH was heated by microwave irradiation for 7 min to obtain AC with specific surface area of 752 m^2 g^{-1}. Furthermore, AC with specific surface areas of 972 m^2 g^{-1} and 1229 m^2 g^{-1} can be prepared within 12 min (Njoku et al., 2014) and within 3 min (Liang et al., 2018), respectively, using microwave-KOH activation. In these studies, the preparation methods required at least 3 min to get high-surface-area AC, and none of them report the synthesis of AC of which specific surface area is above 2,000 m^2 g^{-1}. And, none of them report the generation of the plasma in the reaction zone, but only electromagnetic heating on the surface of the feed.

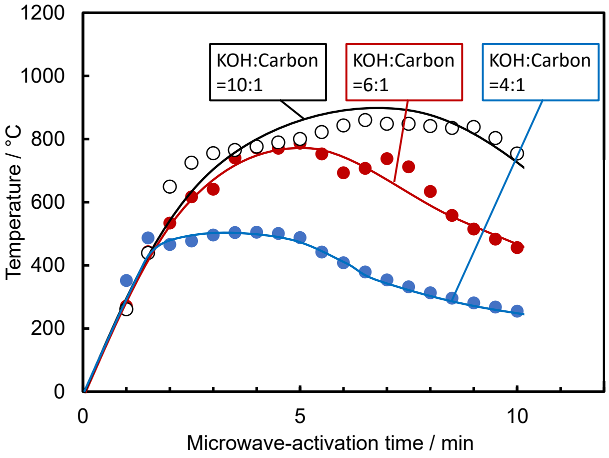

Figure 1 Temperature-change of CCG-KOH mixture in the MiWP-KOH activation with varied KOH:Carbon ratio.

Recently, we found that the activation by microwave-induced plasma with KOH (MiWP-KOH activation) can prepare high surface area AC (1,007 and 2,084 m^2 g^{-1}) using microwave-activation time of 80 and 330 s (Kuptajit and Sano, 2019). Economically, the consumed energy and the cost for the preparation of AC should depend on the activation time. The preparation of AC with high-surface-area and micro and mesoporous structures in a short-time is considered to be very important from an energy point of view.

Previous studies suggested that activation time and concentration of the activating agents in the feed mixture play an important role in pore formation of AC prepared by a standard method (Zhu et al., 2017, Üner and Bayrak, 2018, Huber and Hauser, 2019). Therefore, this work aims to go into the influence of the concentration of the activating agents, KOH, to use MiWP-KOH activation for the preparation of AC with high specific surface area (higher than 2,000 m^2 g^{-1}) and its hierarchical pore structures with micropores and mesopores. Also the effect of the microwave-activation time was investigated on the pore structures, with relating the effect of the KOH concentration.

4. Experimental

1.1 AC Preparation

In this study, a carbon precursor is a synthetic carbon gel. According to Mukai et al. (2005), the carbon gel can be prepared by putting phenol (0.5 mol L^{-1}), formaldehyde (1.0 mol L^{-1}), and catalyst together. Here, sodium carbonate is used as catalyst. The ratio of phenol to sodium carbonate is at 1.5. The mixture was heated at 95 °C for 72 h before being kept at room temperature for 72 h to terminate the polymerization. Then, a purple gel, so called synthetic carbon gel, was obtained. This gel was dried at 110 °C for 1 h. Then, it was carbonized at 700 °C for 1 h under N_2 atmosphere to get carbonized carbon gel (CCG).

CCG was activated by MiWP-KOH activation (Kuptajit and Sano, 2019) under various conditions by adjusting the microwave-activation time (80, 180, and 270 s) as well as KOH concentration (9-91 wt-%) in the feed mixture, which is CCG-KOH mixture. The MiWP-KOH activation was carried out in a modified household microwave oven (Sanyo Electric EM-LA1(HL)) in nitrogen flow with a flowrate of 300 cm^3 min^{-1} in a quartz tube. The microwave oven was operated at 500 W and 2.45 GHz. The resulting mixture was washed with distilled water after being cooled in nitrogen flow at room temperature until the filtrate became neutral. The AC was dried at 50 °C for 12 h before being collected and measured its weight to evaluate mass yield percentage using Eq. (1).

$$\text{Mass yield percentage of AC} = \frac{\text{AC Mass}}{\text{CCG Mass}} \times 100\% \qquad (1)$$

2.2 Investigation of activation temperature

Microwave-induced plasma can be clearly observed as a uniquely bright plasma above the CCG-KON mixture bed. The previous report indicated that the temperature of this plasma was estimated to be above 5000 K from the analysis of the emission spectra (Kuptajit and Sano, 2019). The contact of this hot plasma with the CCG-KOH mixture bed should enhance the fast increase of its temperature.

It was observed that thermocouples were corroded heavily by KOH at high temperature, suggesting that commonly-used thermocouples protected by metallic sheath cannot be used to measure the temperature of the CCG-KOH mixture in the MiWP-KOH activation. Therefore, the temperature-change of the CCG-KOH mixture was observed using a radiation thermometer (Japan Sensor, FTHX-0200S V-1563).

2.3 Characterization of AC via N_2 adsorption

Pore structures of the AC was studied via obtaining N_2 adsorption-desorption isotherms using an automated physisorption surface area analyzer (MicrotracBEL, BELSORP-miniII-S). The samples were outgassed at 200 °C in vacuum for 4 h before the measurements. The isotherms was used to evaluate pore properties of the AC.

The total pore volume was assessed, corresponding to volume of N_2 adsorbed at relative pressure (P/P_0) of 0.90. Micropore volume was calculated by applying *V*-*t* plot method (Lippens et al., 1965) to N_2 adsorption data. Mesopore volume was calculated from the difference between total pore volume and micropore volume.

Specific surface area was calculated by Brunauer–Emmett–Teller (BET) equation using N_2 adsorption isotherms of 0.01-0.03P/P_0 (Brunauer et al., 1938). The calculation considered the molecular cross-sectional area of N_2 at 77 K to be 0.162 nm^2.

Microporosity was calculated by Eq. (2) to indicate the degree of micropore-domination in AC structure.

$$\text{Microporosity} = \frac{\text{micropore volume}}{\text{total pore volume}} \times 100 \qquad (2)$$

5. Results ad Discussion

2.1 Activating temperature

Temperature-change of the feed mixture was recorded as illustrated in **Figure 1**. It is shown that the temperature rises along with microwave irradiation time to about 450 ^{o}C by 80-90 s with almost same temperature-elevating rate in all KOH-concentration cases, and the difference can be seen in the temperature elevation rate after this time range. The result suggested that the maximum activation-temperature was 505, 787, and 860 °C when KOH to CCG ratio is 4:1, 6:1,

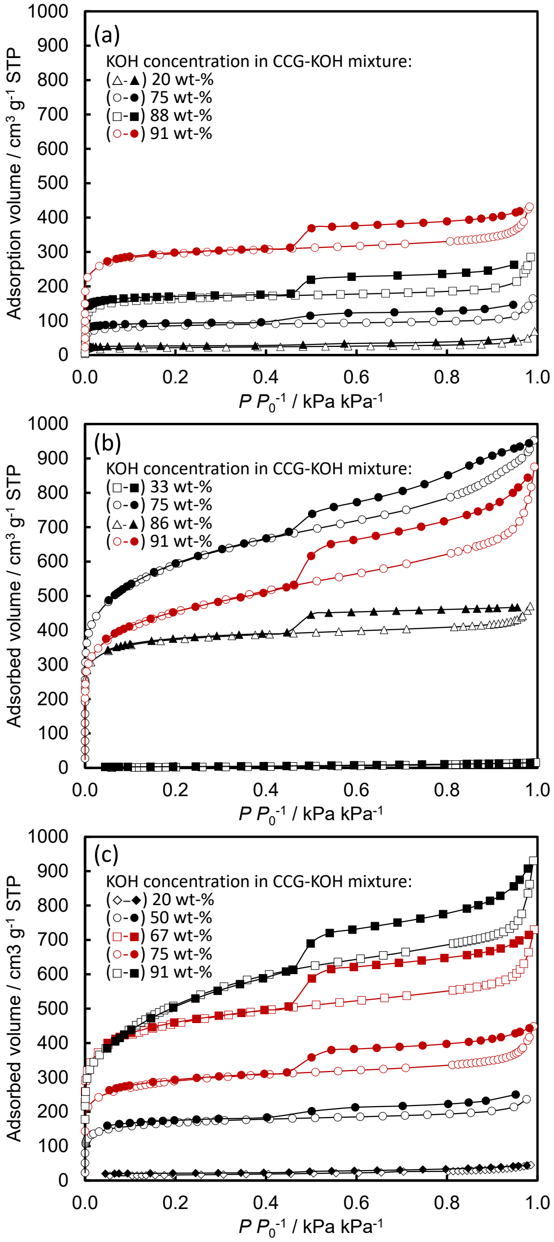

Figure 2 N_2 adsorption-desorption isotherms of AC prepared by MiWP-KOH activation with microwave-activation time of (a) 80, (b) 180, (c) 270 s.

and 10:1, respectively. It indicates that the activation-temperature increases along with the increasing of KOH concentration in feed material.

2.2 Pore formation of AC

Figure 2 presents N_2 adsorption-desorption isotherms of the AC prepared using various KOH concentration in the feed mixture. **Figures 2 (a)**, **(b)**, and **(c)** show the isotherms of the AC prepared using microwave-activation time of 80, 180, and 270 s, respectively. The adsorption isotherms show adsorption of N_2 at low relative pressure ($P/P_0 < 0.01$), indicating microporous structure in AC (Schneider, 1995, Sing, 1982). The results suggested that the adsorbed volume of N_2 at low P/P_0 tends to increase with an increase of the KOH concentration, leading to an increase of micropore volume. In addition, each isotherm shows a hysteresis loop, indicating mesoporous structure (Sing, 1982, Schneider, 1995, Thommes, 2010, Cychosz and Thommes, 2018). The size of hysteresis loops seem to be wider as the KOH concentration increases. It can imply that the volume of mesopores increases with the increase of the KOH concentration.

Figure 3 presents the specific surface area of AC prepared using different KOH concentration in the feed mixture and the activation time. **Figures 3 (a)**, **(b)**, and **(c)** show specific surface area of the AC prepared using microwave-activation time of 80, 180, and 270 s, respectively. It can be shown that the maximum specific surface area are 1,266, 2,189, and 2,332 $m^2\ g^{-1}$ in AC obtained by microwave-activation time of 80, 180, and 270 s, respectively. The results illustrate that specific surface area tends to increase as the KOH concentration increases.

Here, “stable zone” is defined as the operating conditions used to produce AC with pore properties that have narrow fluctuation-range. The stable zone can be observed in the results of AC prepared by microwave-activation time of 180 and 270 s. However, no stable zone can be seen in the results of AC prepared by microwave-activation time of 80 s. This tendency suggests that it takes time more than 80 s to realize uniformity of heating. It should be noted that the electrical conductivity of carbon increases with temperature (Morgan, 1971), and the electrical conductivity of CCG may become high enough to cause the uniform plasma at higher than 450 °C of CCG temperature, when the microwave irradiation time exceed 80 s. It seemed in the experiments that when the average CCG temperature is not high enough, the plasma above the GGC-KOH mixture becomes narrowly localized, so that the CCG can be activated just in non-uniform manner.

One should be reminded that, unless the KOH concentration is substantially high, the stable zone can not be seen even if the average temperature of CCG-KOH is high enough. It seems that KOH is vaporized during the microwave-activation process. Thus, if the amount of KOH in GGC-KOH mixture is not large enough, the uniformly-occurred reaction between carbon and KOH can not be preserved during the microwave-activation process.

Similarly to a previous study (Kuptajit and Sano, 2019), it can be shown here that the specific surface area of AC significantly increases as microwave-activation time increases until microwave-activation time becomes 120 s. When microwave-activation time is longer than 120 s, the specific surface area of the AC seem to increase very slowly with an increase of microwave-activation time. This tendency might be due to the loss of KOH from CCG-KOH mixture by the vaporization of KOH.

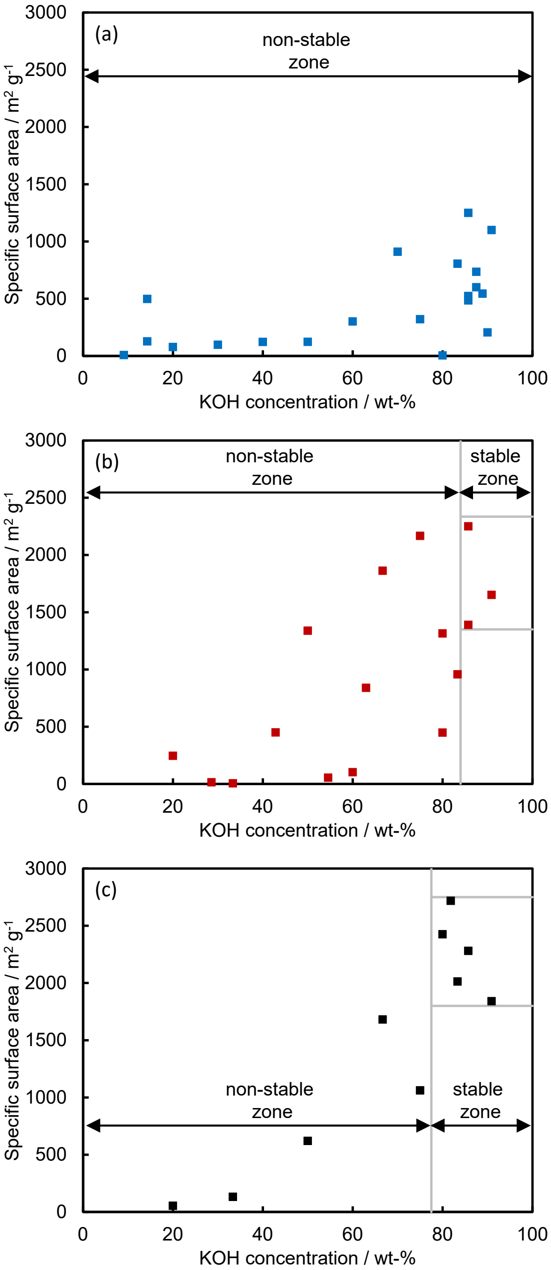

Figure 3 Effect of KOH concentration on specific surface area of AC prepared by MiWP-KOH activation using different KOH concentration and microwave-activation time of (a) 80, (b) 180, (c) 270 s.

The analytical results of micropore volume show the similar tendency with those of the specific surface area. **Figure 4** shows the micropore volume of AC prepared using different KOH concentration and the microwave activation time. **Figures 4 (a)**, **(b)**, and **(c)** show the micropore volume of the AC prepared using microwave-activation time of 80, 180, and 270 s, respectively. The results show that micropore volume tends to increase as the KOH concentration increases.

Moreover, the stable zone can be observed in the results of the AC prepared by microwave-activation time of 180 and 270 s at the high KOH concentration range. However, no stable zone is shown in the results of AC obtained from microwave-activation time of 80 s. The results indicate that in the suitably high ranges of KOH concentration and microwave-activation time, the stable zone can be secured for specific surface area and micropore volume.

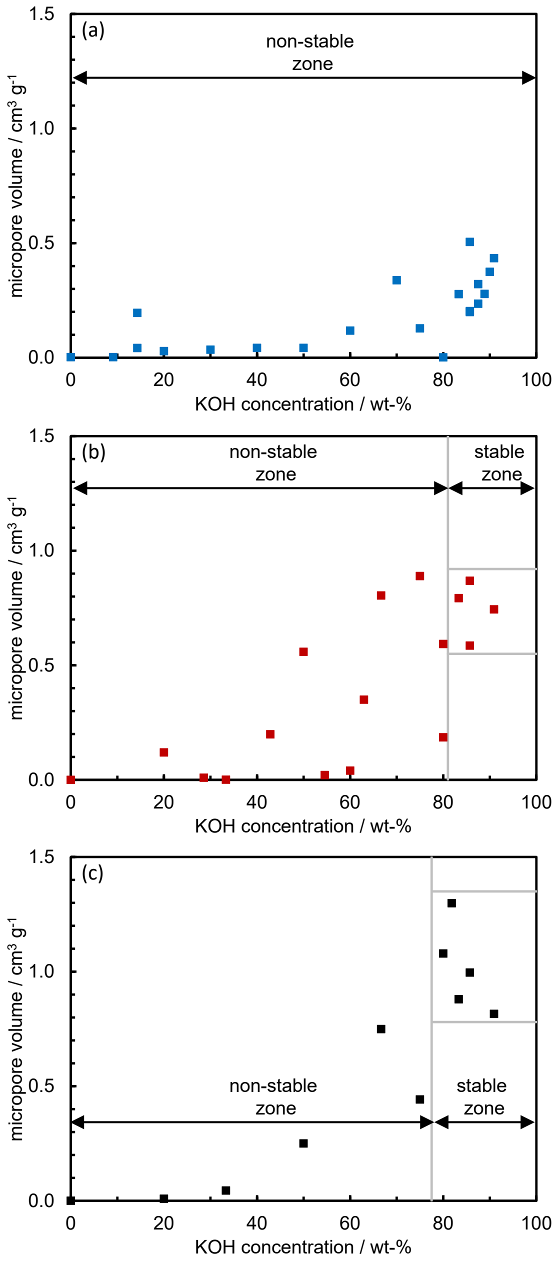

Figure 4 Effect of KOH concentration in feed mixture on micropore volume AC prepared by MiWP-KOH activation using different KOH concentration and microwave-activation time of (a) 80, (b) 180, (c) 270 s.

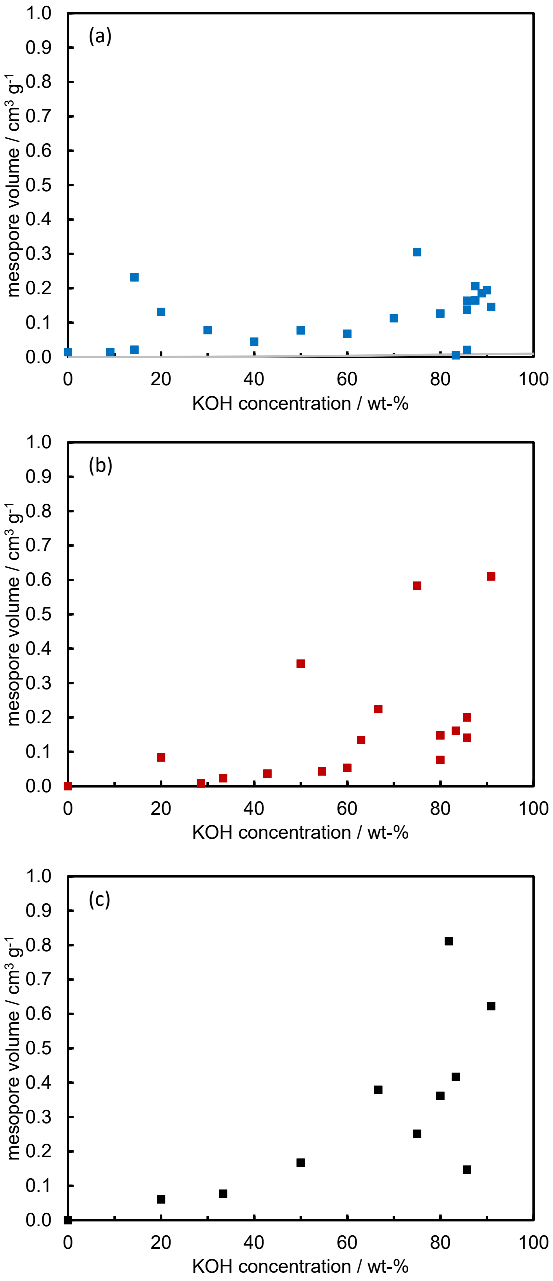

Figure 5 Effect of KOH concentration in the feed mixture on mesopore volume of AC prepared by MiWP-KOH activation using different KOH concentration and microwave-activation time of (a) 80, (b) 180, (c) 270 s.

Figure 5 presents mesopore volume of the AC prepared using different concentration of KOH and microwave activation time. **Figures 5 (a)**, **(b)**, and **(c)** show mesopore volume of the AC prepared using microwave-activation time of 80, 180, and 270 s, respectively. The results show that mesopore volume increases with an increase of the KOH concentration. Also, the mesopore volume increases with the time of the microwave activation time. The influence of the time of the microwave activation time seems similar to the cases of the specific surface area and the micropore volume. However, differently from the cases of the specific surface area and the micropore volume, the mesopore volume does not exhibit the stable values in the high KOH concentration range, which corresponds to the stable zone to the specific surface area and the micropore volume.

Figure 6 shows the N_2 adsorption-desorption isotherms of AC synthesized at 82 and 86 wt-% of KOH concentration with 270 s of the microwave activation time. These conditions are categorized into the stable zone to obtain the stable values of high specific surface area and the micropore volume. One can notice that the shapes of in these isotherms are different in the relatively high pressure range, where the one synthesized at 82 wt-% of KOH concentration is expected to contain well-grown mesopres and the other should not contain significant volume of the mesopores. The reason why mesopore volume is difficult to control can be explained as follows.

In the MiWP-KOH activation, the growth of micropores can be proceeded since activation time is short, but mesopores grow much slower at the high temperature while the CCG-KOH is heated by the plasma (Kuptajit et al., 2021). In fact, the timing to start stable plasma that can heat CCG-KOH mixture uniformly is not well repeatable. Therefore, if the timing to obtain such stable plasma is late, the duration of such plasma until the activation is terminated is not long enough to obtain well-grown mesopores, but this duration can be long enough to form well-grown micorpores. If the timing to start such stable plasma is early, the both of micro and mesopores can be grown well. To improve the stability of mesopore volume, further study to investigate the reaction conditions to stabilize the timing to obtain such stable plasma will be necessary.

2.3 Mass yield percentage in MiWP-KOH activation

Figure 7 illustrates the mass yield percentage of AC prepared using microwave-activation time of 180 and 270 s. The mass yield percentage was calculated using Eq. (1). The average value of the mass yield percentage for the condition when high-surface-area AC with surface area larger than 1500 $m^2\ g^{-1}$ was synthesized in the stabilized zone is 12.3 %. It is similar to the mass yield percentage of the activated carbon prepared by conventional conduction heating, which is 9.3 wt% in average.

2.4 Comparison with past studies

A comparison of the present study with past studies about the use of microwave to produce AC is summarized in **Table 1**. Here, the values of the maximum specific surface area of AC obtained by each of the past studies are shown. This table also shows the information of some reports of the conventional activation. By looking the comparison in this table, it could be said that the present study exhibits the best microwave performance. Koyuncu et al. (2018) reported

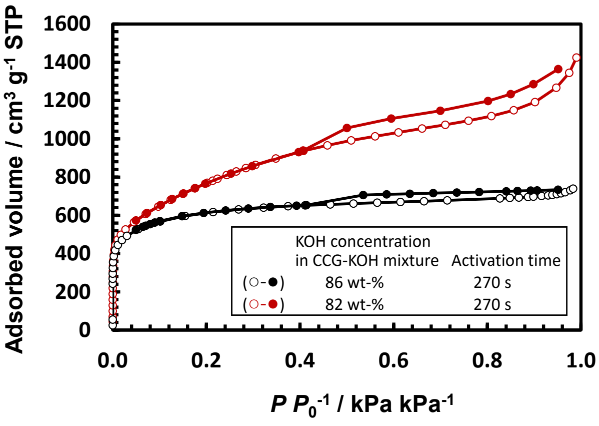

Figure 6 N_2 adsorption-desorption isotherms of AC prepared by MiWP-KOH activation with two KOH concentrations, 86 and 82 wt-% and microwave-activation time of 270 s.

that AC with specific surface area of 1021 $m^2\ g^{-1}$ was obtained within 40 s, but the power to generate microwave used by them was 900 W. On the other hand, the power used by the present MiWP-KOH activation to produce the AC with similar surface area was only 500 W. Liu et al., (2010) used the even lower power, 350 W, to obtain AC with specific surface area of 1410 $m^2\ g^{-1}$, but a long microwave-activation time such as 20 min was required there. Other works used longer time and higher power to make the microwave activation. And importantly, none of the microwave activation methods except MiWP-KOH activation realized the synthesis of AC of which specific surface area was above 2000 $m^2\ g^{-1}$.

One can see in this table that the conventional methods can be used to prepare AC with high specific surface area, but they need 60-90 min to finish the activation (Lv et al., 2012, Erdoğan et al., 2017, Boujibar et al., 2019). One may imagine that such time-consuming activation of MiWP-KOH may result in high energy consumption. As a feature of the pore structure of AC prepared by MiWP-KOH activation, the microporosity seems to be relatively high. The characteristics of the MiWP-KOH activation which need relatively short activation time and less power to generate microwave may indicate the potential to realize the energy saving process to produce high-surface-area AC.

2.5 Controllability of microporosity

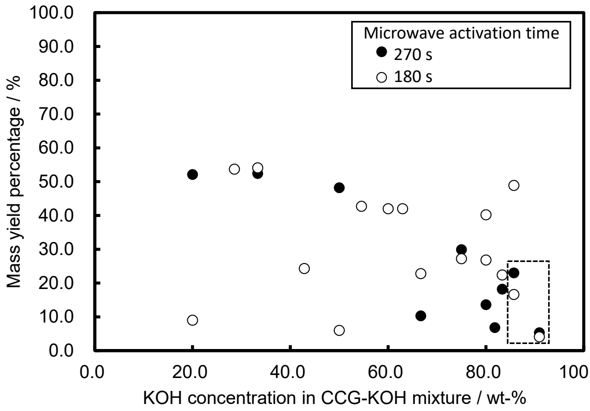

Figure 7 Effect of KOH concentration on mass yield percentage of AC prepared by MiWP-KOH activation using microwave-activation time of 180 and 270 s.
The plots marked by square are the one obtained when high-surface-area AC with surface area larger than 1500 $m^2\ g^{-1}$ was synthesized in the stabilized zone.

Figure 8 shows the microporosity calculated by Eq. (2) for the results obtained with all of the KOH concentration and microwave activation time adopted in this study. The results suggest that the microporosity trends to increase as KOH concentration increases. On the other hand, the influence of the microwave-activation time is not clearly seen.

The relation between the microporosity and KOH concentration within the observed KOH concentration range seem to be described by a linear equation, although relatively large variations from this correlation line can be seen. This correlation line can be written as (Microporosity) = (0.529)(KOH concentration [wt-%]) + 22.65, where coefficient of determination R^2 is 0.414.

The mesoporosity defined here is considered to be a kind of criteria to know how much the micropores dominate the porous structures. When one needs to use AC to adsorb relatively large molecules, or wants quick adsorption with high diffusivity of adsorbate molecules in AC, the activation condition with high KOH concentration can be recommended. The result here can be used to synthesize AC by MiWP-KOH activation to answer such demands for the pore structures of AC.

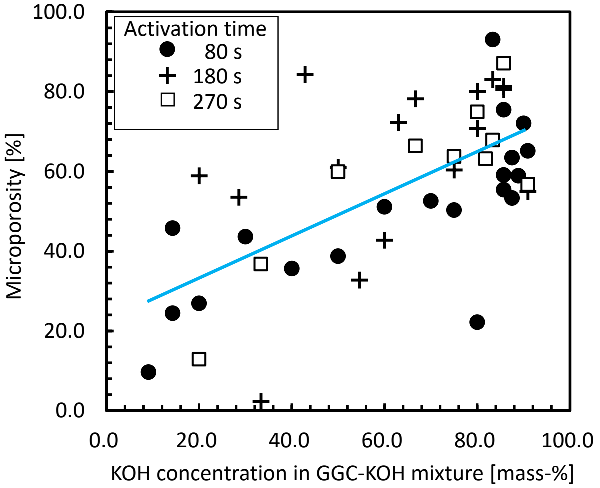

Figure 8 Microporosity of AC prepared by MiWP-KOH activation defined by eq. 2 related with microwave-activation time and KOH concentration in feed-material.

Conclusions

MiWP-KOH activation can be used to prepare a high surface area AC with specific surface area of 1251, 2250, and 2718 $m^2 g^{-1}$ within 80, 180, and 270 s. The MiWP-KOH activation can be done rapidly because the high-temperature plasma may support the quick heating of the feed material. It was suggested that the increases of the activation time and KOH concentration resulted in the increase of micro and mesopore volumes, but excessively long activation time was not useful to increase these volumes. It was observed that the concentration of KOH should be high enough to stabilize the high values of the micropore volume and the specific surface area of resulted AC. This condition is referred to as “stable zone” in this study. The stable zone can not be observed for mesopore volume at this stage. The mass yield percentage of the AC prepared by MiWP-KOH activation was 12.3 wt-% in average in the stable condition. This mass yield percentage is higher than the mass yield percentage of the AC prepared by the conventional activation. The result about microporosity indicates that the microporous structure become more dominant

Table 1 Comparison of pore properties of various AC prepare from microwave and conventional activation.

Carbon precursor	Activation method	Activating Agent	Activation time / min	Activation temperature / °C	Microwave power / W	Surface Area / $m^2 g^{-1}$	Microporosity / percent	Reference
CCG	Microwave (Present study)	KOH	1:20		500	1266	90.76	
			3:00		500	2189	80.58	
			4:30		500	2238	74.89	
Mandarin shells	Microwave	H_3PO_4	0:40		900	1021	3.12	Koyuncu et al., 2018
Orange peel	Microwave	K_2CO_3	6:00		600	1104	40.16	Foo et al., 2012
Rice husks	Microwave	K_2CO_3	7:00		600	1165	42.31	Foo et al., 2011
Rice husks	Microwave	KOH	7:00		600	752	40.63	Foo et al., 2011
Cotton stalk	Microwave	K_2CO_3	8:00		660	621	28.95	Deng et al., 2010
Banana peel	Microwave	KOH + NaOH	10:00		700	1038	38.36	Liew et al., 2018
Cotton stalk	Microwave	KOH	10:00		680	729	68.42	Deng et al., 2010
Rambutan	Microwave	KOH	12:00		600	972	25.23	Njoku et al., 2014
Bamboo	Microwave	H_3PO_4	20:00		350	1432	72.27	Liu et al., 2010
Palm kernel shells	Microwave	Steam	30:00		700	419	76.06	Lam et al., 2019
Coal	Conventional	KOH	60:00	800		1001	74.58	Erdoğan et al., 2017
Anthracite	Conventional	NaOH	60:00	850		1200	94.00	Boujibar et al., 2019
Phenol/formaldehyde resol	Conventional	KOH	90:00	700		1410	52.05	Lv et al., 2012

when KOH concentration become higher. The results obtained here may be useful to control the pore structures of AC with high specific surface area for various demands for adsorption applications.

Acknowledgment

P. Kuptajit would like to thank the scholarship by Asahi Glass Foundation (AF) on this theme, and all authors acknowledge the support by the Japan ASEAN Science, Technology and Innovation Platform (JASTIP) under the Japan Science and Technology Agency (JST).

Literature Cited

Ahmed, M. B., Zhou, J. L., Ngo, H. H., and Guo, W; "Insight into biochar properties and its cost analysis," *Biomass Bioenergy*, 84, 76-86 (2016a)

Ahmed, M. B., Zhou, J. L., Ngo, H. H., Guo, W., and Chen, M.; "Progress in the preparation and application of modified biochar for improved contaminant removal from water and wastewater," *Bioresour. Technol*, 214, 836-851 (2016b)

Aroua, M. K., Daud, W. M. A. W., Yin, C. Y., and Adinata, D.; "Adsorption capacities of carbon dioxide, oxygen, nitrogen and methane on carbon molecular basket derived from polyethyleneimine impregnation on microporous palm shell activated carbon," *Sep. Purif. Technol*, 62, 609-613 (2008)

Benhouria, A., Islam, M. A., Zaghouane-Boudiaf, H., Boutahala, M., and Hameed, B. H.; "Calcium alginate–bentonite–activated carbon composite beads as highly effective adsorbent for methylene blue," *Chem. Eng*, 270, 621-630 (2015)

Boujibar, O., Ghamouss, F., Ghosh, A., Achak, O., and Chafik, T.; "Activated carbon with exceptionally high surface area and tailored nanoporosity obtained from natural anthracite and its use in supercapacitors," *J. Power Sources*, 436, 226882 (2019)

Cossutta, M., Vretenar, V., Centeno, T. A., Kotrusz, P., McKechnie, J., and Pickering, S. J.; "A comparative life cycle assessment of graphene and activated carbon in a supercapacitor application," *J. Clean. Prod*, 242, 118468 (2020)

Deng, H., Li, G., Yang, H., Tang, J., and Tang, J.; "Preparation of activated carbons from cotton stalk by microwave assisted KOH and K_2CO_3 activation," *Chem. Eng.*, 163(3), 373-381 (2010)

Erdoğan, S., Akmil Başar, C., and Önal, Y.; "Particle size effect of raw material on the pore structure of carbon support and its adsorption capability," *Particul. Sci. Technol*, 35(3), 330-337 (2017)

Foo, K. Y., and Hameed, B. H.; "Utilization of rice husks as a feedstock for preparation of activated carbon by microwave induced KOH and K_2CO_3 activation," *Bioresour. Technol.*, 102(20), 9814-9817 (2011)

Foo, K. Y., and Hameed, B. H.; "Microwave-assisted regeneration of activated carbon," *Bioresour. Technol.*, 119, 234-240 (2012)

He, B., Liu, J., Zhang, Y., Zhang, S., Wang, P., and Xu, H.; "Comparison of Structured Activated Carbon and Traditional Adsorbents for Purification of H_2," *Sep. Purif.*, 116529 (2020)

Huber, L., Hauser, S.B., Brendlé, E., Ruch, P., Ammann, J., Hauert, R., Widmer, R.N., Ubert, C.J., Matam, S.K., Yoon, S., Zhang, Y.; "The effect of activation time on water sorption behavior of nitrogen-doped, physically activated, monolithic carbon for adsorption cooling," *Microporous Mesoporous Mater*, 276, 239-250 (2019)

Huo, E., Duan, D., Lei, H., Liu, C., Zhang, Y., Wu, J., Zhao, Y., Huang, Z., Qian, M., Zhang, Q., and Lin, X.; "Phenols production form Douglas fir catalytic pyrolysis with MgO and biomass-derived activated carbon catalysts," *Energy*, 117459 (2020)

Inal, I. I. G., and Aktas, Z.; "Enhancing the performance of activated carbon based scalable supercapacitors by heat treatment," *Appl. Surf*., 145895 (2020)

Jiang, C., Yakaboylu, G. A., Yumak, T., Zondlo, J. W., Sabolsky, E. M., and Wang, J.; "Activated carbons prepared by indirect and direct CO_2 activation of lignocellulosic biomass for supercapacitor electrodes," *Renew. Energy*, 155, 38-52 (2020)

Koyuncu, F., Güzel, F., and Sayğılı, H.; "Role of optimization parameters in the production of nanoporous carbon from mandarin shells by microwave-assisted chemical activation and utilization as dye adsorbent," *Adv. Powder Technol*., 29(9), 2108-2118 (2018)

Kuptajit, P., and Sano, N.; "Application of microwave-induced plasma for extremely fast synthesis of large surface-area activated carbon," *Appl. Phys. Express*., 12, 086001 (2019)

Kuptajit, P., Nakagawa, K., Suzuki, T., and Sano, N.; "Pseudo continuous reactor with microwave-plasma for preparation of high surface area activated carbon," *J. Jpn. Inst. Energy*, 100(8), 110-115 (2021)

Lam, S.S., Su, M.H., Nam, W.L., Thoo, D.S., Ng, C.M., Liew, R.K., Yuh Yek, P.N., Ma, N.L., and Nguyen Vo, D.V.; "Microwave pyrolysis with steam activation in producing activated carbon for removal of herbicides in agricultural surface water," *Ind. Eng. Chem*., 58(2), 695-703 (2018)

Li, K., Zhou, M., Liang, L., Jiang, L., and Wang, W.; "Ultrahigh-surface-area activated carbon aerogels derived from glucose for high-performance organic pollutants adsorption," *J. Colloid Interf. Sci*., 546, 333-343 (2019)

Liang, J., Qu, T., Kun, X., Zhang, Y., Chen, S., Cao, Y.C., Xie, M. and Guo, X.; "Microwave assisted synthesis of camellia oleifera shell-derived porous carbon with rich oxygen functionalities and superior supercapacitor performance," *Appl. Surf*., 436, 934-940 (2018)

Lippens, B., and de Boer, J.; "Studies on Pore Systems in Catalysts V. The t Method," *J. Catal*. 4, 319-323 (1965)

Liu, Q. S., Zheng, T., Wang, P., and Guo, L.; "Preparation and characterization of activated carbon from bamboo by microwave-induced phosphoric acid activation," *Ind. Crops Prod*., 31(2), 233-238 (2010)

Loya-González, D., Loredo-Cancino, M., Soto-Regalado, E., Rivas-García, P., de Jesús Cerino-Córdova,F., García-Reyes, R.B., Bustos-Martínez, D., and Estrada-Baltazar, A.; "Optimal activated carbon production from corn pericarp: A life cycle assessment approach," *J. Clean. Prod*., 219, 316-325 (2019)

Lozano-Castello, D., Alcaniz-Monge, J., De la Casa-Lillo, M. A., Cazorla-Amoros, D., and Linares-Solano, A.; "Advances in the study of methane storage in porous carbonaceous materials," *Fuel*, 81, 1777-1803 (2002)

Lv, Y., Zhang, F., Dou, Y., Zhai, Y., Wang, J., Liu, H., Xia, Y., Tu, B., and Zhao, D.; "A comprehensive study on KOH activation of ordered mesoporous carbons and their supercapacitor application," *J. Mater. Chem*., 22, 93–99 (2012)

Mukai, S. R., Tamitsuji, C., Nishihara, H., and Tamon, H.; “Preparation of mesoporous carbon gels from an inexpensive combination of phenol and formaldehyde,” *Carbon*, 12, 2628-2630 (2005)

Njoku, V. O., Foo, K. Y., Asif, M., and Hameed, B. H.; “Preparation of activated carbons from rambutan (Nephelium lappaceum) peel by microwave-induced KOH activation for acid yellow 17 dye adsorption,” *Chem. Eng*., 250, 198-204 (2014)

Morgan, M.; “Electrical conduction in amorphous carbon films,” *Thin Solid Films*, 7, 313-323 (1971)

Nasrullah, A., Saad, B., Bhat, A. H., Khan, A. S., Danish, M., Isa, M. H., and Naeem, A.; “Mangosteen peel waste as a sustainable precursor for high surface area mesoporous activated carbon: Characterization and application for methylene blue removal,” *J. Clean. Prod*., 211, 1190-1200 (2019)

Pena, J., Villot, A., and Gerente, C.; “Pyrolysis chars and physically activated carbons prepared from buckwheat husks for catalytic purification of syngas,” *Biomass Bioenergy*, 132, 105435 (2020)

Rashidi, N. A., and Yusup, S.; “Potential of palm kernel shell as activated carbon precursors through single stage activation technique for carbon dioxide adsorption,” *J. Clean. Prod*., 168, 474-486 (2017)

Rossi, G. E., Winfield, J. M., Mitchell, C. J., van der Borden, W., van der Velde, K., Carr, R. H., and Lennon, D.; “Phosgene formation via carbon monoxide and dichlorine reaction over an activated carbon catalyst: Reaction testing arrangements,” *Appl. Catal A-Gen*. 594, 117467 (2020)

Sayğili, H., Güzel, F., and Önal, Y.; “Conversion of grape industrial processing waste to activated carbon sorbent and its performance in cationic and anionic dyes adsorption,” *J. Clean. Prod*., 93, 84-93 (2015)

Selvaraju, G., and Bakar, N. K. A.; “Process conditions for the manufacture of highly micro-mesoporous eco-friendly activated carbon from artocarpus integer bio-waste by steam activation,” *J. Taiwan Inst. Chem. Eng*., 93, 414-426 (2018)

Su, Y., Liu, L., Xu, D., Du, H., Xie, Y., Xiong, Y., and Zhang, S.; “Syngas production at low temperature via the combination of hydrothermal pretreatment and activated carbon catalyst along with value-added utilization of tar and bio-char,” *Energy Convers. Manag*., 205, 112382 (2020)

Sulaiman, N. S., Hashim, R., Amini, M. H. M., Danish, M., and Sulaiman, O.; “Optimization of activated carbon preparation from cassava stem using response surface methodology on surface area and yield,” *J. Clean. Prod*., 198, 1422-1430 (2018)

Üner, O., and Bayrak, Y.; “The effect of carbonization temperature, carbonization time and impregnation ratio on the properties of activated carbon produced from *Arundo donax*,” *Microporous Mesoporous Mater*., 268, 225-234 (2018)

Xin-Hui, D., Srinivasakannan, C., Jin-Hui, P., Li-Bo, Z., and Zheng-Yong, Z.; “Comparison of activated carbon prepared from Jatropha hull by conventional heating and microwave heating,” *Biomass Bioenergy*, 35(9), 3920-3926 (2011)

Yek, P. N. Y., Liew, R. K., Osman, M. S., Lee, C. L., Chuah, J. H., Park, Y. K., and Lam, S. S.; "Microwave steam activation, an innovative pyrolysis approach to convert waste palm shell into highly microporous activated carbon," *J. Environ*., 236, 245-253 (2019)

Yu, Y., Qiao, N., Wang, D., Zhu, Q., Fu, F., Cao, R., Wang, R., Liu, W., and Xu, B.; "Fluffy honeycomb-like activated carbon from popcorn with high surface area and well-developed porosity for ultra-high efficiency adsorption of organic dyes," *Bioresour. Technol*., 285, 121340 (2019)

Zabaniotou, A., Madau, P., Oudenne, P. D., Jung, C. G., Delplancke, M. P., and Fontana, A.; "Active carbon production from used tire in two-stage procedure: industrial pyrolysis and bench scale activation with H_2O–CO_2 mixture," *J. Anal. Appl. Pyrolysis*, 72, 289-297 (2004)

Zhang, Y., Song, X., Xu, Y., Shen, H., Kong, X., and Xu, H.,; "Utilization of wheat bran for producing activated carbon with high specific surface area via NaOH activation using industrial furnace," *J. Clean. Prod*., 210, 366-375 (2019)

Zhu, X., Gao, Y., Yue, Q., Kan, Y., Kong, W., and Gao, B.; "Preparation of green alga-based activated carbon with lower impregnation ratio and less activation time by potassium tartrate for adsorption of chloramphenicol," *Ecotoxicol. Environ*., 145, 289-294 (2017)

1.2 Optimization of H_2O_2 Electrogeneration from Tea-Leaf-Derived N-Doped Carbon Catalyst and Demonstration of H_2O_2-Assisted Electrocatalytic 5-Hydroxymethylfurfural Oxidation

Naphat Ormsapsin[1], Warith Powichien[1], Patcharapol Intrasorn[1], khanin nueangnoraj[1], Pongkarn Chakthranont[2]**

[1]School of Bio-chemical Engineering and Technology, Sirindhorn International Institute of Technology, Thammasat University, Pathum Thani, 12120, Thailand

[2]National Nanotechnology Center (NANOTEC), National Science and Technology Development Agency (NSTDA), Pathum Thani, 12120, Thailand

1. ABSTRACT

Hydrogen peroxide (H_2O_2) is a strong oxidizing agent used in varieties of applications. Due to the energy intensity, waste generation, and explosivity of the conventional anthraquinone process, the two-electron electrochemical oxygen reduction reaction (ORR) is then proposed for H_2O_2 production using a nitrogen-doped catalyst derived from tea leaves. Then, the gas diffusion electrode is fabricated from the carbon catalyst derived from tea leaves carbonized at 800 °C. The current density and the catalyst ink thickness are optimized to maximize H_2O_2 production. At the optimal H_2O_2 production condition (30 mA/cm^2 and 100 µm), the highest H_2O_2 concentration was found to be 2.42 mM. The gas diffusion electrode is then employed as a cathode in an electrosynthesis device which converts 5-hydroxymethylfurfural (HMF) to furandicarboxylic acid (FDCA) with Ni foam as an anode. When compared to a controlled device where N_2 is fed to the

cathode, the HMF oxidation in combination with ORR at the cathode leads to an increase in FDCA yield from 76.78% to 90.94%, an increase in HMF conversion from 92.10% to 98.01%, increased faradaic efficiency for FDCA production from 18.97% to 25.99%, and a reduction in the overall cell voltage. Our work demonstrates that the electrochemical H_2O_2 production via the ORR route can be used in a practical application such as in an electrosynthesis device.

2. INTRODUCTION

Hydrogen peroxide (H_2O_2) is a chemical with many applications ranging from a chemical precursor, bleaching agent, disinfectant, and cleaning chemical (Zhang et al., 2020; Wang et al., 2021; Shi et al., 2021; Chakthranont et al., 2021). The environmental regulations drive the H_2O_2 market growth as a result of zero-emission production and the ecological friendliness properties of H_2O_2 (Zhang et al., 2020). When using H_2O_2 as an oxidizing agent, the byproducts of the reaction are only non-hazardous compounds like water and oxygen (Zhang et al., 2020). Generally, the conventional H_2O_2 production process is called the anthraquinone process, which can provide high H_2O_2 concentrations (Zhang et al., 2020; Shi et al., 2021; Chakthranont et al., 2021). The process requires subsequent steps including hydrogenation using a precious metal catalyst, oxidation of the products, and a separation step to obtain high purity of H_2O_2 (Nishimi et al., 2011). However, the anthraquinone process is energy-intensive, waste-generating, and explosive due to high H_2O_2 concentrations (Zhang et al., 2020; Shi et al., 2021; Chakthranont et al., 2021). Alternatively, the two-electron electrochemical oxygen reduction reaction (ORR) is then proposed for H_2O_2 production. In comparison to the conventional anthraquinone process, the electrochemical method has the advantages of environmental friendliness due to the absence of fossil fuel and organic waste, mild conditions with ambient temperature and pressure, and low possibility of explosion (Zhang et al., 2020; Shi et al., 2021).

One of the attractive classes of catalysts for H_2O_2 production via the two-electron ORR is noble metals and their alloys such as Pt-Hg and Au-Pd. While these reported catalysts favor a two-electron pathway with small overpotential and high H_2O_2 selectivity, the scarcity results in the catalysts' high cost and low feasibility on large-scale applications. A more practical electrocatalyst for H_2O_2 production is nitrogen-doped carbon, which is low-cost, abundant, and has high electrochemical stability under reaction conditions (Li et al., 2020). Moreover, biomass can offer hierarchical pore structures that assist the mass transfer and possess high surface area (Li et al., 2020). Besides, the biomass may already have a nitrogen element inside its component, and this could allow self-doping that eliminates the complexity of the synthesis process and the hazardous properties of the precursors. In this project, tea leaves are selected as the source of carbon material, as they are widely cultivated all over the world. Because tea leaves contain caffeine content, it is suspected that caffeine could serve as a source of the nitrogen element and act as the active site for H_2O_2 production via the two-electron ORR pathway. Moreover, the tea leaves used in this project may also act as both a gas diffusion layer and catalyst layer and may facilitate the gas diffusion electrode that was used in this project.

Nevertheless, regardless of the nitrogen-doped carbon catalyst activity that promotes H_2O_2 production, H_2O_2 is still concerned for its decomposition under alkaline conditions, limiting the practical used of electro-generated H_2O_2 (Zhang et al., 2020; Shi et al., 2021). Because of the oxidizing property of H_2O_2, several researchers utilized H_2O_2 in the oxidation reaction such as the oxidation of alcohol, phenol hydroxylation, sulfide oxidation, and cyclohexane oxidation (Chen et al., 2017). On the other hand, the control of reaction selectivity and the decomposition of H_2O_2 is still under development for the use of H_2O_2. Therefore, it is challenging to use H_2O_2 in general oxidation reactions solely. Herein, the ORR system is then coupled with the oxidation of 5-hydroxymethylfurfural (HMF) to 2,5-furandicarboxylic acid (FDCA) to demonstrate the system and to utilize the H_2O_2 produced within the electrochemical cell.

The FDCA has the potential to be a precursor for various renewable and biodegradable materials in the packaging, textile, and coating fields (Pila et al., 2021). For instance, the unsustainable polyethylene terephthalate (PET) made from the petroleum industry can be substituted by the bio-based polymer polyethylene furanoate (PEF) that can significantly reduce greenhouse gas emissions and non-renewable energy use (Pila et al., 2021). Also, the PEF possesses a higher gas barrier for oxygen, carbon dioxide, and water vapor than PET (Yang et al., 2020). In general, the FDCA is produced from the conversion of HMF by aerobic oxidation reaction using Pd-based catalysts through oxygen gas as an oxidizing agent, which prefers high pressure making the process explosive (Pila et al., 2021). Normally, the HMF is obtained from lignocellulosic biomass conversion or dehydration of reducing sugars from the heating of sugar-containing food (Chen et al., 2017). Compared to the general conversion process of HMF, the electrochemical oxidation of HMF has advantages including ambient conditions, single-phase reactions with H_2O_2 as the oxidizing agent, absence of toxic components, and the non-precious metal catalysts such as Ni and Co that are cheaper than Pd (Pila et al., 2021).

It is claimed that the HMF conversion to FDCA can be facilitated by alkaline conditions (Pila et al., 2021; Chen et al., 2017; Sun et al., 2021; Vuyyuru & Strasser, 2012; Kang et al., 2019). Henceforth, in this project, the electrochemical ORR system was optimized to find the optimal condition with maximized H_2O_2 production yield. Subsequently, the previously discussed ORR system was then brought and combined with the oxidation of HMF in the flow cell electrolyzer system to study the production of FDCA assisted by the presence of H_2O_2. The project will allow exploiting the current produced from the ORR reaction for the HMF conversion to FDCA.

3. EXPERIMENTAL METHOD

3.1 Synthesis of TL-800 and Electrode Fabrication

The carbon material was derived from dried tea leaves with potassium carbonate (K_2CO_3) as an activating agent in a mass ratio of 1:1.5, and the composite material was mixed with reverse osmosis (RO) water to produce a slurry. The mixture was stirred using a hot plate magnetic stirrer for 8 to 10 hours, then dried in an oven at 120°C for 12 hours and ground to a fine powder. The composite powders then were put into a porcelain combustion boat and carried to the tubular furnace being fed with nitrogen gas at a flow rate of 200 mL min^{-1} and a pressure of 1 bar. The composite powder was heated at a rate of 5 °C min^{-1} up to 800°C and then held at this temperature for 1 hour. To remove contaminants and produce a neutral pH, the activated carbon was crushed into powder and cleansed using RO water. Lastly, the carbon catalyst was dried in a 120°C oven for 24 hours.

The carbon catalyst ink is produced from a mixture of carbon catalyst, PVDF (Alfa Aesar), and carbon black. The catalyst ink mass ratio was 8:1:1. The mixture and grinding balls were put into the glass vial. After mixing for a minute, the N-Methyl-2-Pyrrolidone (NMP) solvent (99%, Alfa Aesar) was added to the composites at the NMP: slurry ratio of 16:1 by weight. After that, the mixture was mixed for a minute until it became homogeneous using a vortex mixer at 1500-2000 rpm. The mixture was sonicated for 10 minutes before being stirred using a magnetic stirrer for an hour. Finally, the ink was sonicated again for 10 minutes.

For the electrode preparation, the Toray carbon fiber composite carbon paper (3.5×3.5 cm^2, TGP-H-120) was cut and put on the glass, and fixed with the Kapton tape (Figure 1). The carbon paper used here only acts as the catalyst backing layer with hydrophobicity, so that the porosity of the synthesized carbon catalyst can be studied. Then, the slurry was poured on top of the carbon paper to fill the desired width, and the doctor's blade was swept to produce the electrode film. After that, the electrode film was put into the vacuum oven at 60 °C for 6 hours to dry the electrode film. Then, the Kapton tape was removed and the electrode can be obtained. The electrode was characterized for its true thickness using a contact profilometer. Also, the electrode was cut cross-sectionally and observed using an optical microscope. The finished electrodes' weight was measured after the drying process to compare with the carbon paper weight to determine the carbon loading.

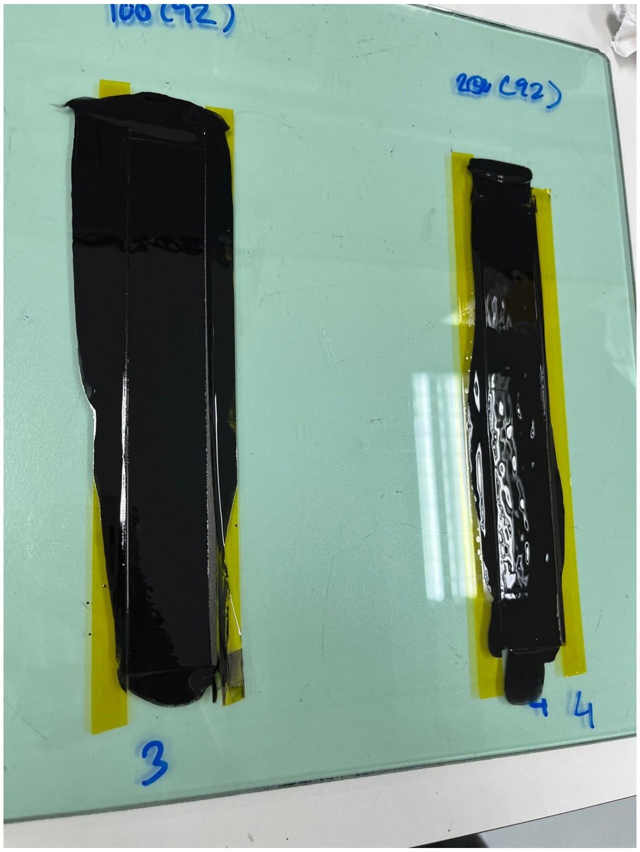

Figure 1. The electrode coated with a thickness of 100 μm and 250 μm

3.2 Electrochemical Measurements

All electrochemical experiments were operated at ambient temperature and pressure, and the measurements were conducted using a Metrohm Multi Autolab M204. Firstly, in the H_2O_2 production system, the three-electrodes system was used in the electrochemical device setup (Figure 2). The conventional flow cell device is a 3-compartment Teflon compression cell including an O_2 gas compartment, a cathode compartment, and an anode compartment. Also, the cell was constructed and tested with different factors that are going to be varied. A miniature leakless

Ag/AgCl electrode (eDAQ) was used as the reference electrode. The anode of the system (counter electrode) was the Ni foam (0.5 mm, pore density 110 PPI, Hunan Tad New Materials Co., Ltd) for the water oxidation on the anodic side of the system. Before the compartment setup, Ni foam is cleaned using acetone and sonicated for 30 minutes. Then 30% HCl (QRëC™) is used to remove any oxide of Ni that is rinsed with DI water after the sonication. The cleaned Ni foam was further rinsed with DI water. At the cathodic side, the fabricated TL800 electrode was used as the working electrode for the electrochemical ORR to occur. The O_2 flow was continuously supplied to the gas chamber contacting the gas diffusion layer of the cathode. The electrolyte used in this system was 0.33 M KOH (99.99%, Sigma-Aldrich) continuously circulating through the flow cell using the peristaltic pumps on both cathodic and anodic sides. And the electrolyte was separated by the anion exchange selective membrane (Selemion AMVN, AGC Engineering Co. Ltd.). The total electrolyte volume was 30 mL. The active area of the working electrode was 3.14 cm^2. Before any measurements, the electrochemically active surface area of the TL800 electrode was compared by averaging the anodic and cathodic current at the middle potential of -0.05 V with the applied potential range of -0.2 to 0.1 V and the scan rate of 0.05, 0.0375, 0.025, 0.01, and 0.005 V/s. Also, impedance spectroscopy (EIS) was performed at the open circuit potential to correct the ohmic loss for every setup change.

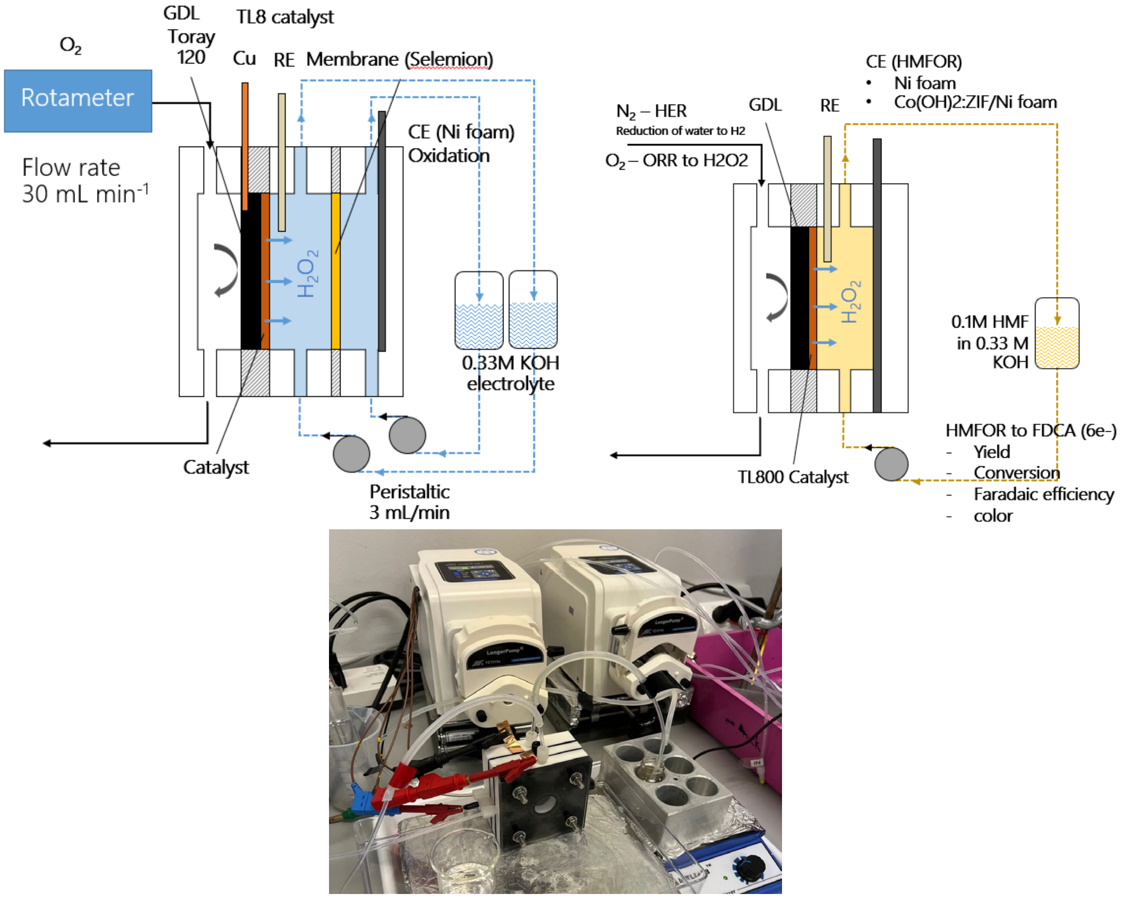

Figure 2. Schematic diagrams of (a) ORR GDE system, (b) HMF conversion, and (c) real setup.

First, the cyclic voltammetry (CV) with 30 mL min^{-1} of N_2 flowing was performed to sweep the potential and stabilize the system until a consistent voltammogram is observed. Then, the CV with 30 mL min^{-1} of O_2 flowing was performed again to observe the electrochemical activity for each potential. After that, the electrochemical of the ORR was conducted using a chronopotentiometry (CP) method at a fixed current density. The chronopotentiogram was observed for 30 min. For each CP analysis, the catholyte was sampled at 10 and 30 minutes and analyzed by the Ce^{4+} titration method.

The thickness of the catalyst layer was varied having 100 and 250 μm with the applied current density of 10, 30, and 50 mA cm^{-2} for each, the KOH flow rate of 3 mL min^{-1} , and the O_2 flow rate of 30 mL min^{-1}.

After the amount of H_2O_2 is determined, the electrochemical measurement results were further used to determine the faradaic efficiency (FE%) for H_2O_2 production in the flow cell by the equation below. The H_2O_2 production performance from the TL800 electrode was compared with the electrode made from the commercial Sigracet 39BB carbon paper (Ion power) for its possibility to use in the gas diffusion electrode system as a substitute.

$$FE\%_{H_2O_2} = \frac{mole\ of\ generated\ H_2O_2 \times 2 \times 96485}{total\ consumed\ charge\ (C)} \times 100\%$$

Next, in the FDCA production system, the same setup is applied, except that the membrane between the catholyte and the anolyte was removed to study the effect of HMF conversion in the presence of H_2O_2. The Ni foam electrode (1.6 mm, pore density 110 PPI, Hunan Tad New Materials Co., Ltd) was used as the anode to facilitate the HMF oxidation reaction. The electrolyte was 30 mL of 10 mM HMF solution in 0.33 M KOH (99.99%, Sigma-Aldrich). The mixture was circulated using a peristaltic pump with 3 mL min^{-1} flow. To perform the reaction, CP is run for 2 hours and the solution is sampled every 30 minutes for 0.1 mL while the HMF solution is continuously stirred by a magnetic stirrer. The samples were further diluted to 1 mL using DI water and stored in the refrigerator to avoid degradation before they are analyzed using high-performance liquid chromatography (HPLC). The faradaic efficiency for the FDCA generation was determined by the equation below.

$$FE\%_{FDCA} = \frac{mole\ of\ generated\ FDCA \times 6 \times 96485}{total\ consumed\ charge\ (C)} \times 100\%$$

Lastly, the CP system with 10 mA cm^{-2} current density applied under flowing O_2 and N_2 at 30 mL min^{-1} for 6 hours with the cell potential measured using a multimeter was performed to observe the cell potential and compare the faradaic efficiency and the anodic half-cell potential between the systems with and without O_2 using Ni foam as the anodic catalyst.

3.3 Product Quantification

Ce^{4+} titration was used to measure the produced H_2O_2 based on the reaction as follows:

$$2Ce^{4+} + H_2O_2 \rightarrow 2Ce^{3+} + 2H^+ + O_2$$

The H_2O_2 yield is measured by the mole that Ce^{4+} consumed which was determined by UV-vis spectroscopy at the detector wavelength of 317 nm. Because the Ce^{4+} solution has a yellow color and the Ce^{3+} is colorless. The stock standard solution of Ce^{4+} is prepared by dissolving $Ce(SO_4)_2$ (97%, Sigma-Aldrich) in 0.1 M of H_2SO_4 (96%, Sigma-Aldrich) to obtain 0.5 mM of $Ce(SO_4)_2$ solution, the sample was mixed with the Ce^{4+} solution by the volume ratio of 1:300. A calibration curve was plotted for concentrations of 0.05, 0.1, 0.25, and 0.5, mM of Ce^{4+}.

For the HMF conversion system, the anode product was determined by the use of HPLC. 5 mM sulfuric acid aqueous solution was used as mobile phases with an injection volume of 5 μL. The column applied is Aminex® HPX-87H column 300 x 7.8 mm. The conversion rate of HMF and FDCA yield was calculated by the equations below using the values obtained from the quantification using HPLC.

$$\%Conversion_{HMF} = \frac{mole\ of\ consumed\ HMF}{mole\ of\ initial\ HMF} \times 100\%$$

$$\%Yield_{FDCA} = \frac{mole\ of\ produced\ FDCA}{mole\ of\ initial\ HMF} \times 100\%$$

4. RESULTS AND DISCUSSION

4.1 Electrode Characterization

Doctor blades with a thickness of 100 and 250 µm were used to coat the electrodes. With the results from the optical microscope, the layer between the Toray carbon paper and the TL800 carbon ink can be seen. The carbon paper was found to display a reflective and spiky structure, while the carbon ink presented an opaque and black layer coating on the carbon paper structure. According to the image scale in Figure 3, the thickness of the TL800 carbon ink layer using 100 µm a doctor blade is approximately 50 µm.

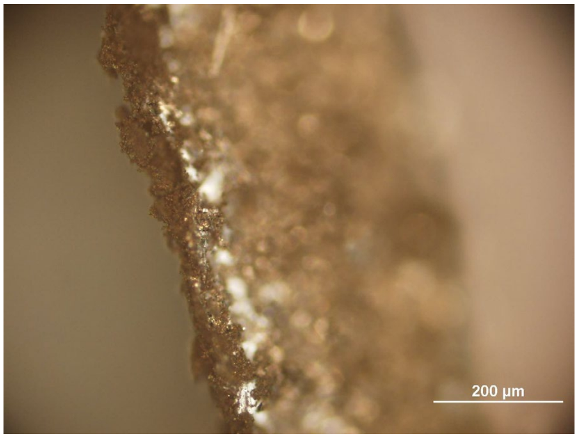

Figure 3. Optical microscope image of TL800 electrode with a thickness of 100 μm

Due to the inconvenience of the optical microscopic method to determine the thickness and to further confirm the results from the optical microscope, the characterization using the profilometer was performed instead. The results revealed that the thickness of 100 µm has a real thickness with an average of 36.67 µm, and the thickness of 250 µm has a real thickness with an average of 49.56 µm. With this, it can be interpreted that the thickness loss was caused by the NMP solution component in the carbon ink that was evaporated when the electrode was baked in the oven at 60 °C prior to the characterization.

In addition to the results from the profilometer and the optical microscope, the ECSA value increased in the same manner as the thickness increased as shown in Figure 4 indicating the increase of electrochemically active surface area with the increased thickness. Moreover, in terms of carbon loading (Table 1), the difference between the two thicknesses was significant as the loading of active carbon catalyst increases with larger thickness due to more ink coated on the carbon paper.

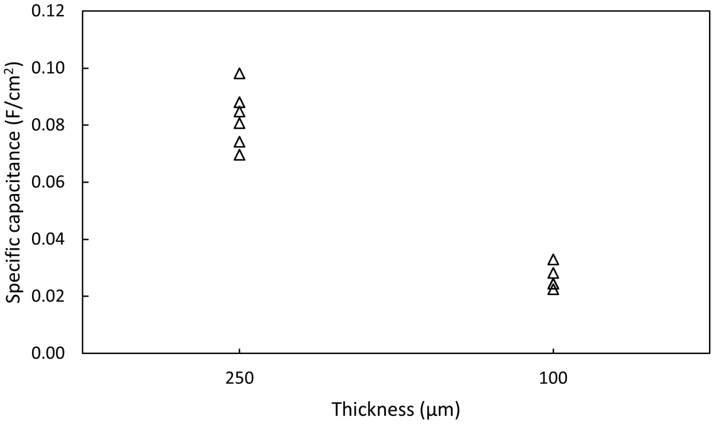

Figure 4. ECSA results for TL800 electrodes

Table 1. The carbon loading data for TL800 electrodes

Thickness from doctor blade (µm)	**Carbon loading (µg/cm²)**
100	415
250	962

4.2 Electrochemical H_2O_2 production optimization

The optimization of the H_2O_2 production was done to find the optimum condition for the maximum H_2O_2 production. Firstly, the CV was performed to observe the current occurring across applied potentials (Figure 5). With the applied potential window of -1.45 to 0.1 V vs. Ag/AgCl, for TL800 coated on Toray paper, the O_2 system clearly provides significantly higher current due to ORR activity. Also, the increased thickness slightly increased the resulting current. Outstandingly, commercial Sigracet paper gives the highest cathodic current at very low potential. To optimize the H_2O_2 production condition, CP runs (Figure 6) were performed on each electrode and their faradaic efficiency for H_2O_2 production and H_2O_2 concentration are compared in Figure 7-8.

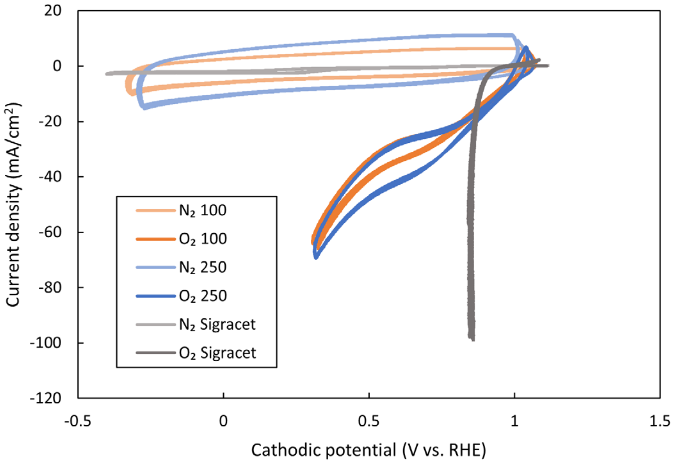

Figure 5. CV of TL800 electrodes with 100 and 250 μm and Sigracet paper under O_2 and N_2

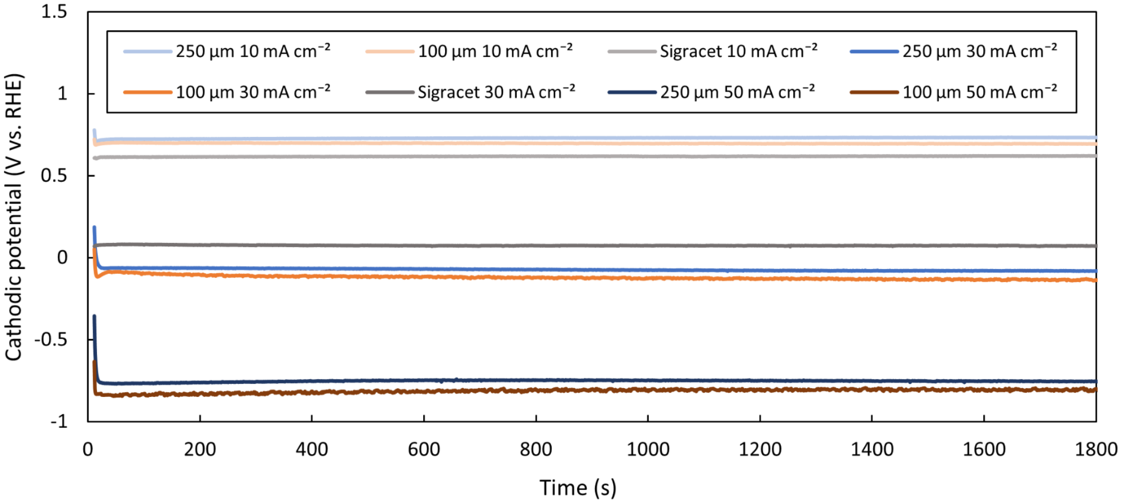

Figure 6. CP of TL800 electrodes with 100 and 250 μm and sigracet paper under O_2 and N_2

The trend was observed that the lower current density can provide higher faradaic efficiency. This indicates the reduced selectivity of the catalyst towards the H_2O_2 production. The anticipated outcome with higher current density may be the selectivity towards water production. Also, the faradaic efficiency observed from the thickness of 250 μm tends to reduce after time has passed. Meanwhile, time had a negligible effect on the faradaic efficiency from the thickness of 100.

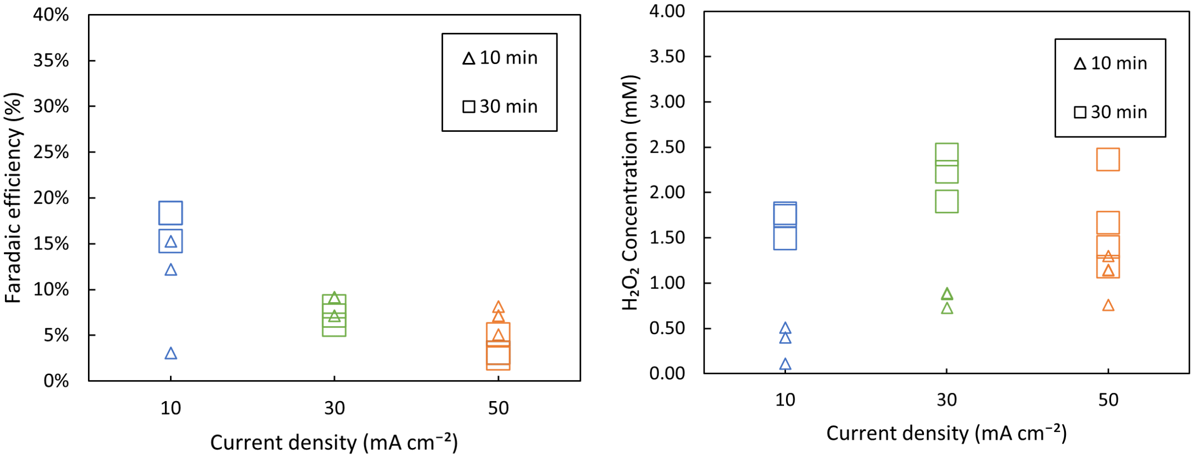

Figure 7. Faradaic efficiency and of H_2O_2 concentration of Toray 100 μm

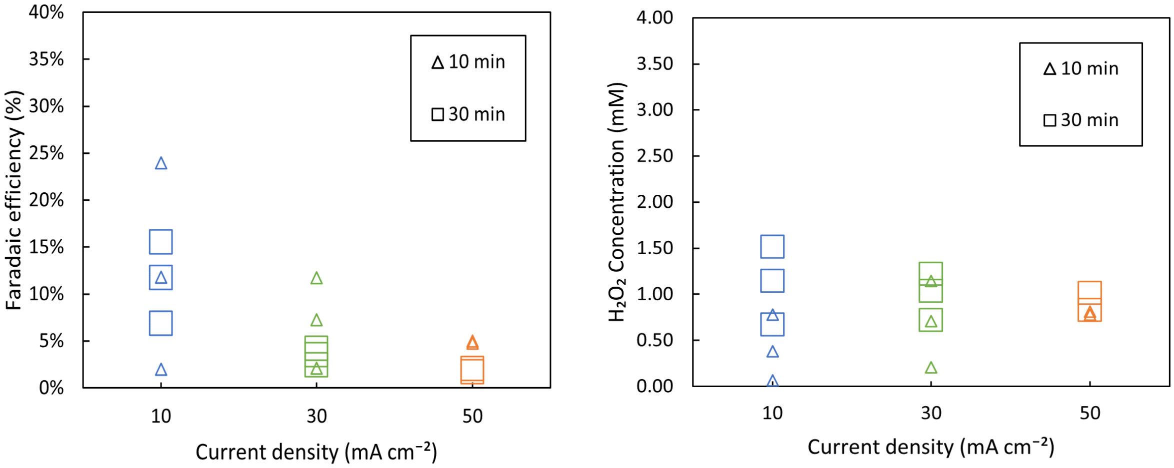

Figure 8. Faradaic efficiency and of H_2O_2 concentration of Toray 250 μm

Between the two thicknesses, the H_2O_2 production performances had a slight difference. This might be because the actual thicknesses of 100 and 250 μm as characterized by a profilometer were not significantly different. The TL800 electrode performance can be compared with the setup using the commercial sigracet paper as the cathode has a similar current density applied as shown in Figures 7 and 8. Overall, the system using the commercial Sigracet paper (Figure 9) performed better than the fabricated TL800 electrodes. The sigracet paper can supply up to 34% of faradaic efficiency at 10 minutes with 10 mA cm^{-2}, and the H_2O_2 production was about 7 mM at maximum. This suggests that there is room for improvement for the TL800 electrode.

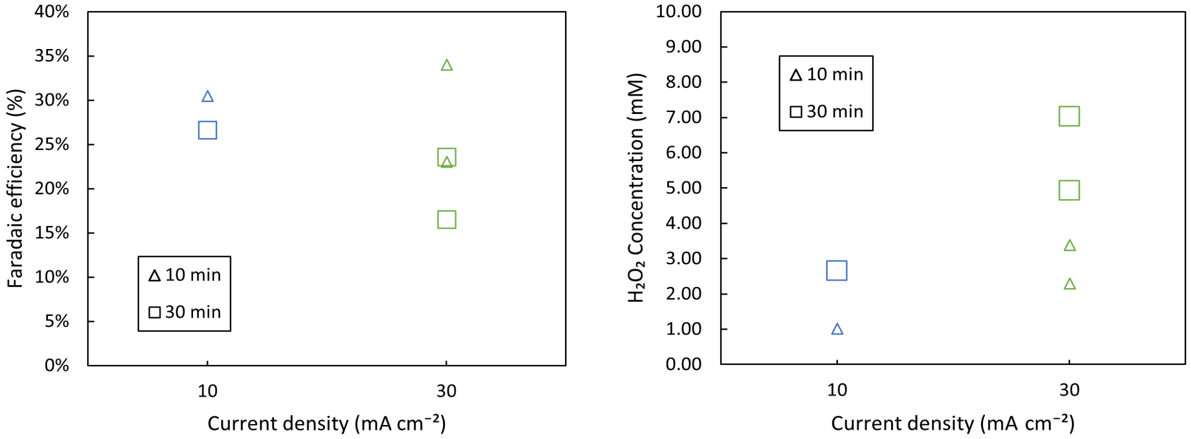

Figure 9. Faradaic efficiency and of H_2O_2 concentration of Sigracet paper

The highest concentration (2.417 mM) was observed from the use of 100 µm thickness at 30 mA cm^{-2} for 30 minutes. Hence, this condition was then selected for the next experimental section, which is the electrochemical FDCA production from HMF.

4.3 Electrochemical FDCA production from HMF

Using the optimum condition for H_2O_2 production, the HMF oxidation to FDCA was performed under two conditions where O_2 or N_2 were fed to the cathode gas chamber. N_2 gas was used as a control to observe the effects of H_2O_2 production on the electrosynthesis of FDCA. Figure 10 shows the yields of DFF, HMFCA, FFCA, and FDCA from the HMF conversion. Table 2 shows the results with a significant difference in FDCA yield (77 % with N_2 and 91% with O_2) and conversion (92% with N_2 and 98% with O_2) at 2 hours of reaction, indicating that the presence of O_2 in the cathode chamber is beneficial to the HMF oxidation reaction. Moreover, the faradaic efficiency was calculated to be 26% with O_2 and 19% with N_2. As time passed, it can be seen that the amount of HMF reduced continuously in contrast to the amount of FDCA. Apart from the main reactant and the main product, intermediates such as HMFCA, FFCA, and DFF were observed with low amounts overall. In addition, there are more yields of FDCA and other intermediates with O_2 than with N_2 indicating more oxidative activity in the presence of O_2 than N_2. As the reaction proceeded in both systems, the intermediates continued to disappear indicating the further transformation of the intermediates to FDCA as the amount of FDCA increased over time. It was found that there were more HMFCA than DFF suggesting that the oxidation pathway through HMFCA might be preferable, which agrees with previous work (Pila et al., 2021). The difference between the total yield of FDCA, HMFCA, DFF, and FFCA and the HMF conversion is smaller in the O_2 system than that in the N_2 system. This suggests a lower loss of HMF to humin formation in the O_2 system. Figure 11 shows the image of the product solutions from each CP run. The clear solution of the system with O_2 indicates the conversion of HMF to FDCA, which is colorless. On the other hand, the system with N_2 has yellow color from the remaining HMF and humin.

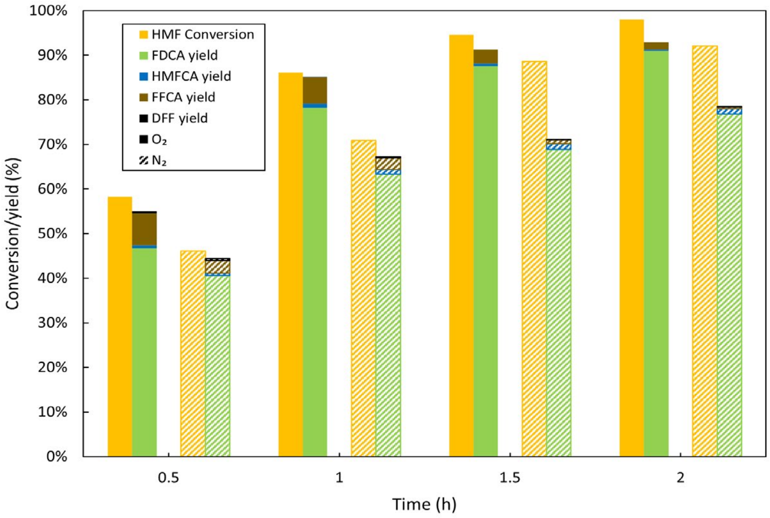

Figure 10. Performance results including HMF conversion and yield of FDCA, HMFCA, FFCA, and DFF between O_2 and N_2 systems

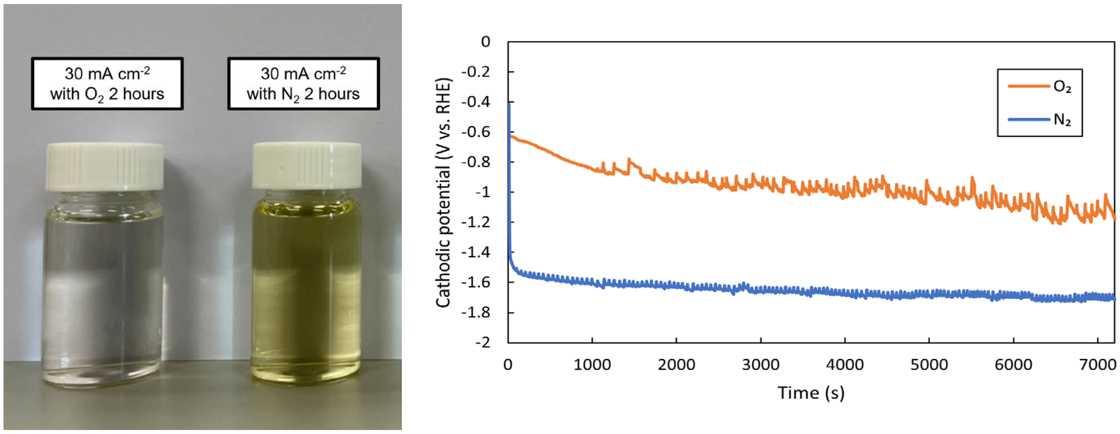

Figure 11. (left) Image showing the color of converted HMF solution from each CP run and (right) CP of HMF conversion with 30 mA cm^{-2} applied

Table 2. Faradaic efficiency for FDCA production, conversion, and yield for the system with O_2 and N_2

	With O_2	**With N_2**
FE%	25.99%	18.97%
Conversion%	98.01%	92.10%
Yield%	90.94%	76.78%

Figure 12 shows the CP curves of the flow cell system with O_2 and N_2. The increase in cathodic potential can be credited to the presence of ORR under O_2 and the hydrogen evolution reaction (HER) under N_2 (-0.961 V with O_2 and -1.654 V with N_2 vs. RHE). Therefore, the presence of ORR activity largely reduces the voltage required for the studied electrolytic cell. In addition, the faradaic efficiency also increased (50% at 1 hour for 10 mA cm^{-2} and 45% at 1 hour for 30 mA cm^{-2}) with lower current density. As the reaction proceeded, the faradaic efficiency under 10 mA cm^{-2} dropped but with a lower degree compared to the reaction under 30 mA cm^{-2} current density (FE% became 26.61% after 6 hours of reaction with 10 mA cm^{-2}, while 25.99% was obtained after 2 hours of reaction with 30 mA cm^{-2}).

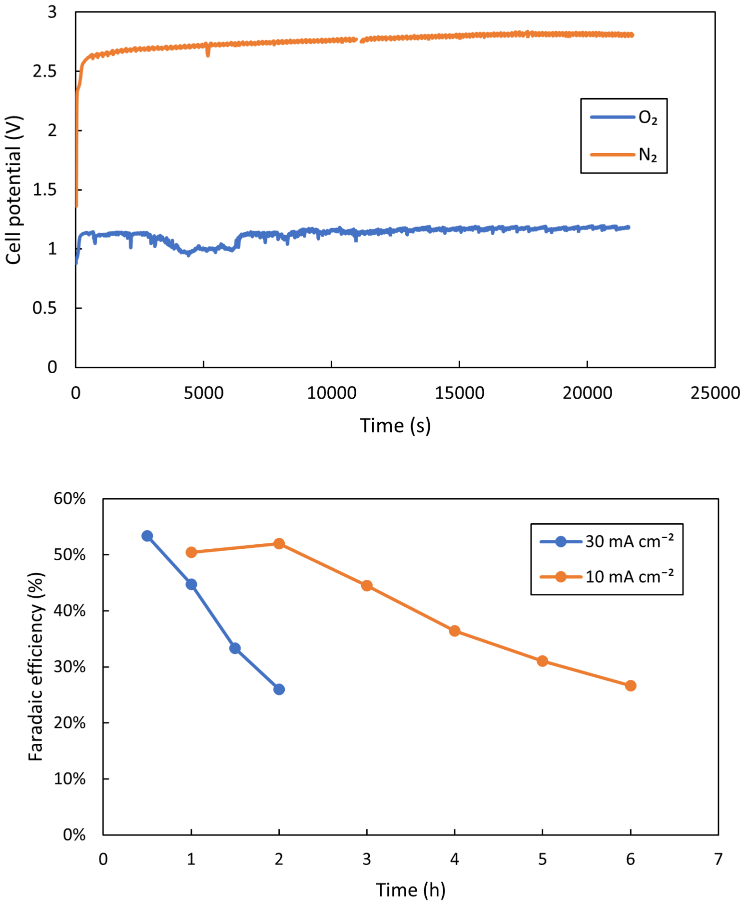

Figure 12. (Top) Cell voltage under 10 mA cm^{-2} applied and (bottom) Faradaic efficiency of HMF conversion reaction under O_2 between 30 mA cm^{-2} for 2 hours and 10 mA cm^{-2} for 6 hours

Table 3. The potential of cell, cathode, and anode for the system with O_2 and N_2

	Cell potential (V)	**Cathode potential (V vs. Ag/AgCl)**	**Anode potential (V vs. Ag/AgCl)**	**Anode potential (V vs. RHE)**
With O_2	1.130	-0.289	0.841	1.749
With N_2	2.753	-1.826	0.927	1.839

The electro-conversion of HMF to FDCA using Ni foam as the anode and TL800 electrode as the cathode under the presence of O_2 fed to the gas diffusion electrode was successfully demonstrated. Our results show that simultaneous H_2O_2 production and HMF oxidation result in higher FDCA yield and HMF conversion, improved faradaic efficiency, and reduced electrolytic cell potential. This device suggests a practical use of electrochemical H_2O_2 production as a cathode in the electrolytic conversion of HMF to produce FDCA.

5. CONCLUSION

The tea leaves carbonized at 800 °C (TL800) was used to prepare the nitrogen-doped carbon catalyst for electrochemical H_2O_2 production via ORR. Catalyst coatings onto carbon paper with two different thicknesses: 100 and 250 µm were investigated as gas diffusion electrodes in an electrochemical flow cell. It was discovered that the 100 and 250 µm thicknesses offered similar H_2O_2 faradaic efficiency for each current density applied (10, 30, and 50 mA cm^{-2}). The trends suggest lower H_2O_2 faradaic efficiency with higher current density and longer reaction time. From the results, the highest H_2O_2 produced concentration was found for the coating thickness of 100 µm. Thus, the system with the optimized condition was further used in an electrolytic device for HMF oxidation to FDCA. Under 2 hours of reaction time, the system with O_2 input offered significantly higher yield and conversion (91% yield and 98% conversion) compared to the system with N_2 (77% yield and 92% conversion). Additionally, the presence of O_2 in the system reduced the cell voltage and improved the faradaic efficiency (26% with O_2 and 19% with N_2 under 2 hours at 30 mA cm^{-2}). At 10 mA cm^{-2} with O_2, the faradaic efficiency can increase up to more than 50% at 2 hours. Finally, the electrochemical system with O_2 was proven to provide higher FDCA yield and HMF conversion, better faradaic efficiency, and reduced cell voltage.

6. REFERENCES

Al Ghatta, A.; Zhou, X.; Casarano, G.; Wilton-Ely, J. D.; Hallett, J. P. Characterization and Valorization of Humins Produced by HMF Degradation in Ionic Liquids: A Valuable Carbonaceous Material for Antimony Removal. *ACS Sustainable Chemistry & Engineering* **2021**, *9* (5), 2212–2223.

Al-Bayati, F. A.; Mohammed, M. J. Isolation, Identification and Purification of Caffeine Fromcoffea Arabical. Andcamellia Sinensisl.: A Combination Antibacterial Study. *International Journal of Green Pharmacy* **2009**, *3* (1), 52.

Berni, A.; Mennig, M.; Schmidt, H. Doctor Blade. *Sol-Gel Technologies for Glass Producers and Users* **2004**, 89–92.

Bontempelli, G.; Dossi, N.; Toniolo, R. Linear Sweep and Cyclic☆. *Reference Module in Chemistry, Molecular Sciences and Chemical Engineering* **2016**.

Campos-Martin, J. M.; Blanco-Brieva, G.; Fierro, J. L. Hydrogen Peroxide Synthesis: An Outlook beyond the Anthraquinone Process. *Angewandte Chemie International Edition* **2006**, *45* (42), 6962–6984.

Capuano, E.; Fogliano, V. Acrylamide and 5-Hydroxymethylfurfural (HMF): A Review on Metabolism, Toxicity, Occurrence in Food and Mitigation Strategies. *LWT - Food Science and Technology* **2011**, *44* (4), 793–810.

Cardiel, A. C.; Taitt, B. J.; Choi, K.-S. Stabilities, Regeneration Pathways, and Electrocatalytic Properties of Nitroxyl Radicals for the Electrochemical Oxidation of 5-Hydroxymethylfurfural. *ACS Sustainable Chemistry & Engineering* **2019**, *7* (13), 11138–11149.

Chakthranont, P.; Nitrathorn, S.; Thongratkaew, S.; Khemthong, P.; Nakajima, H.; Supruangnet, R.; Butburee, T.; Sano, N.; Faungnawakij, K. Rational Design of Metal-Free Doped Carbon Nanohorn Catalysts for Efficient Electrosynthesis of H2O2 from O2 Reduction. *ACS Applied Energy Materials* **2021**.

Chen, C.-T.; Nguyen, C. V.; Wang, Z.-Y.; Bando, Y.; Yamauchi, Y.; Bazziz, M. T.; Fatehmulla, A.; Farooq, W. A.; Yoshikawa, T.; Masuda, T.; Wu, K. C.-W. Hydrogen Peroxide Assisted Selective Oxidation of 5-Hydroxymethylfurfural in Water under Mild Conditions. *ChemCatChem* **2017**, *10* (2), 361–365.

Chen, G.; Wu, L.; Fan, H.; Li, B.-geng. Highly Efficient Two-Step Synthesis of 2,5-Furandicarboxylic Acid from Fructose without 5-Hydroxymethylfurfural (HMF) Separation: In Situ Oxidation of HMF in Alkaline Aqueous H2O/DMSO Mixed Solvent under Mild Conditions. *Industrial & Engineering Chemistry Research* **2018**, *57* (48), 16172–16181.

Chen, W.; Xu, M.-L.; Li, M.-F.; Wei, Z.; Cai, J.; Chen, Y.-X. Quantifying Intrinsic Kinetics of Electrochemical Reaction Controlled by Mass Transfer of Multiple Species under Rotating Disk Electrode Configuration. *Journal of Electroanalytical Chemistry* **2020**, *872*, 114042.

Climent, V.; Feliu, J. M. Cyclic Voltammetry. *Encyclopedia of Interfacial Chemistry* **2018**, 48–74.

Dai, L.; Xue, Y.; Qu, L.; Choi, H.-J.; Baek, J.-B. Metal-Free Catalysts for Oxygen Reduction Reaction. *Chemical Reviews* **2015**, *115* (11), 4823–4892.

Du, C.; Tan, Q.; Yin, G.; Zhang, J. Rotating Disk Electrode Method. *Rotating Electrode Methods and Oxygen Reduction Electrocatalysts* **2014**, 171–198.

Fallahzadeh, R. A.; Ehrampoush, M. H.; Mahvi, A. H.; Ghaneian, M. T.; Dalvand, A.; Salmani, M. H.; Fallahzadeh, H.; Nabi Meybodi, M. Designing and Modeling of a Novel Electrolysis Reactor Using Porous Cathode to Produce H2O2 as an Oxidant. *MethodsX* **2019**, *6*, 1305–1312.

Forster, R. J.; Walsh, D.; Adamson, K.; Spain, E. Voltammetry Overview. *Reference Module in Chemistry, Molecular Sciences and Chemical Engineering* **2018**.

Guo, Z.; Xiao, Z.; Ren, G.; Xiao, G.; Zhu, Y.; Dai, L.; Jiang, L. Natural Tea-Leaf-Derived, Ternary-Doped 3D Porous Carbon as a High-Performance Electrocatalyst for the Oxygen Reduction Reaction. *Nano Research* **2016**, *9* (5), 1244–1255.

Hauke, P.; Klingenhof, M.; Wang, X.; de Araújo, J. F.; Strasser, P. Efficient Electrolysis of 5-Hydroxymethylfurfural to the Biopolymer-Precursor Furandicarboxylic Acid in a Zero-Gap Mea-Type Electrolyzer. *Cell Reports Physical Science* **2021**, 100650.

Hou, J.; Xu, Z.; Ji, J.; Zhao, Y.; Gao, M.; Jin, C. Enhanced in-Situ Electro-Generation of H2O2 Using PTFE and NH4HCO3 Modified C/PTFE Electrode for Treatment of Landfill Leachate. *Journal of Environmental Management* **2021**, *295*, 112933.

Hwang, D. S.; Park, C. H.; Yi, S. C.; Lee, Y. M. Optimal Catalyst Layer Structure of Polymer Electrolyte Membrane Fuel Cell. *International Journal of Hydrogen Energy* **2011**, *36* (16), 9876–9885.

Jia, Z.; Yin, G.; Zhang, J. Rotating Ring-Disk Electrode Method. *Rotating Electrode Methods and Oxygen Reduction Electrocatalysts* **2014**, 199–229.

Kang, M. J.; Park, H.; Jegal, J.; Hwang, S. Y.; Kang, Y. S.; Cha, H. G. Electrocatalysis of 5-Hydroxymethylfurfural at Cobalt Based Spinel Catalysts with Filamentous Nanoarchitecture in Alkaline Media. *Applied Catalysis B: Environmental* **2019**, *242*, 85–91.

Khataee, A. R.; Safarpour, M.; Zarei, M.; Aber, S. Electrochemical Generation of H2O2 Using Immobilized Carbon Nanotubes on Graphite Electrode Fed with Air: Investigation of Operational Parameters. *Journal of Electroanalytical Chemistry* **2011**, *659* (1), 63–68.

Kim, D.-wook; Li, O. L.; Saito, N. Enhancement of Orr Catalytic Activity by Multiple Heteroatom-Doped Carbon Materials. *Physical Chemistry Chemical Physics* **2015**, *17* (1), 407–413.

Li, L.; Tang, C.; Zheng, Y.; Xia, B.; Zhou, X.; Xu, H.; Qiao, S. Z. Tailoring Selectivity of Electrochemical Hydrogen Peroxide Generation by Tunable Pyrrolic-Nitrogen-Carbon. *Advanced Energy Materials* **2020**, *10* (21), 2000789.

Liu, W.-J.; Dang, L.; Xu, Z.; Yu, H.-Q.; Jin, S.; Huber, G. W. Electrochemical Oxidation of 5-Hydroxymethylfurfural with Nife Layered Double Hydroxide (LDH) Nanosheet Catalysts. *ACS Catalysis* **2018**, *8* (6), 5533–5541.

Moraes, A.; Assumpção, M. H. M. T.; Papai, R.; Gaubeur, I.; Rocha, R. S.; Reis, R. M.; Calegaro, M. L.; Lanza, M. R. V.; Santos, M. C. Use of a Vanadium Nanostructured Material for Hydrogen Peroxide Electrogeneration. *Journal of Electroanalytical Chemistry* **2014**, *719*, 127–132.

Nishimi, T.; Kamachi, T.; Kato, K.; Kato, T.; Yoshizawa, K. Mechanistic Study on the Production of Hydrogen Peroxide in the Anthraquinone Process. *European Journal of Organic Chemistry* **2011**, *2011* (22), 4113–4120.

Pila, T.; Nueangnoraj, K.; Ketrat, S.; Somjit, V.; Kongpatpanich, K. Electrochemical Production of 2,5-Furandicarboxylic from 5-Hydroxymethylfurfural Using Ultrathin Co(Oh)2 on Zif-67. *ACS Applied Energy Materials* **2021**.

Qi, C.; Khalkhali, M.; Grundy, J. S.; Liu, B.; Wang, A.; Liu, Q. Unraveling H2O2-Stimulated Surface Oxidation of Non-Magnetic Pyrrhotite and Pentlandite by Underlying Electronic Structures. *Minerals Engineering* **2021**, *170*, 106964.

Qiang, Z.; Chang, J.-H.; Huang, C.-P. Electrochemical Generation of Hydrogen Peroxide from Dissolved Oxygen in Acidic Solutions. *Water Research* **2002**, *36* (1), 85–94.

Reis, R. M.; Beati, A. A.; Rocha, R. S.; Assumpção, M. H.; Santos, M. C.; Bertazzoli, R.; Lanza, M. R. Use of Gas Diffusion Electrode for the in Situ Generation of Hydrogen Peroxide in an Electrochemical Flow-by Reactor. *Industrial & Engineering Chemistry Research* **2011**, *51* (2), 649–654.

Salmerón, I.; Plakas, K. V.; Sirés, I.; Oller, I.; Maldonado, M. I.; Karabelas, A. J.; Malato, S. Optimization of Electrocatalytic H2O2 Production at Pilot Plant Scale for Solar-Assisted Water Treatment. *Applied Catalysis B: Environmental* **2019**, *242*, 327–336.

Shi, X.; Back, S.; Gill, T. M.; Siahrostami, S.; Zheng, X. Electrochemical Synthesis of H2O2 by Two-Electron Water Oxidation Reaction. *Chem* **2021**, *7* (1), 38–63.

Shrotri, A.; Kobayashi, H.; Fukuoka, A. Catalytic Conversion of Structural Carbohydrates and Lignin to Chemicals. *Advances in Catalysis* **2017**, 59–123.

Sun, M.; Wang, Y.; Sun, C.; Qi, Y.; Cheng, J.; Song, Y.; Zhang, L. Nitrogen-Doped Co3O4 Nanowires Enable High-Efficiency Electrochemical Oxidation of 5-Hydroxymethylfurfural. *Chinese Chemical Letters* **2021**.

Sun, Y.; Li, S.; Jovanov, Z. P.; Bernsmeier, D.; Wang, H.; Paul, B.; Wang, X.; Kühl, S.; Strasser, P. Structure, Activity, and Faradaic Efficiency of Nitrogen-Doped Porous Carbon Catalysts for Direct Electrochemical Hydrogen Peroxide Production. *ChemSusChem* **2018**, *11* (19), 3388–3395.

Tan, T.; Tao, P.; Li, X.; Imhanria, S.; Deng, J.; Wang, W. Nitrogen-Modified Metal-Organic Framework-Based Carbon: An Effective Non-Precious Electrocatalyst for Oxygen Reduction Reaction. *Catalysis Communications* **2020**, *146*, 106135.

Vesztergom, S. Rotating Disk and Ring–Disk Electrodes. *Encyclopedia of Interfacial Chemistry* **2018**, 421–444.

Vuyyuru, K. R.; Strasser, P. Oxidation of Biomass Derived 5-Hydroxymethylfurfural Using Heterogeneous and Electrochemical Catalysis. *Catalysis Today* **2012**, *195* (1), 144–154.

Wang, J.; Li, C.; Rauf, M.; Luo, H.; Sun, X.; Jiang, Y. Gas Diffusion Electrodes for H2O2 Production and Their Applications for Electrochemical Degradation of Organic Pollutants in Water: A Review. *Science of The Total Environment* **2021**, *759*, 143459.

Wang, Y.; Ding, Y.; Li, L.; Hu, P. Nitrogen-Doped Carbon Nanotubes Decorated Poly (L-Cysteine) as a Novel, Ultrasensitive Electrochemical Sensor for Simultaneous Determination of Theophylline and Caffeine. *Talanta* **2018**, *178*, 449–457.

Xiao, L.-P.; Song, G.-Y.; Sun, R.-C. Effect of Hydrothermal Processing on Hemicellulose Structure. *Hydrothermal Processing in Biorefineries* **2017**, 45–94.

Yang, C.; Li, X.; Zhang, Z.; Lv, B.; Li, J.; Liu, Z.; Zhu, W.; Tao, F.; Lv, G.; Yang, Y. High Efficient Catalytic Oxidation of 5-Hydroxymethylfurfural into 2,5-Furandicarboxylic Acid under Benign Conditions with Nitrogen-Doped Graphene Encapsulated Cu Nanoparticles. *Journal of Energy Chemistry* **2020**, *50*, 96–105.

Yeganeh Ghotbi, M.; Feli, B.; Azadfalah, M.; Javaheri, M. Ultra High Performance n-Doped Carbon Catalysts for the ORR Derived from the Reaction between Organic-Nitrate Anions inside a Layered Nanoreactor. *RSC Advances* **2015**, *5* (112), 92577–92584.

Zhang, J.; Song, C. Electrocatalytic Oxygen Reduction Reaction. *PEM Fuel Cell Electrocatalysts and Catalyst Layers* **2008**, 89–134.

Zhang, J.; Zhang, H.; Wu, J.; Zhang, J. Techniques for PEM Fuel Cell Testing and Diagnosis. *Pem Fuel Cell Testing and Diagnosis* **2013**, 81–119.

Zhang, Q.; Zhou, M.; Ren, G.; Li, Y.; Li, Y.; Du, X. Highly Efficient Electrosynthesis of Hydrogen Peroxide on a Superhydrophobic Three-Phase Interface by Natural Air Diffusion. *Nature Communications* **2020**, *11* (1).

Zhang, X.; Xia, Y.; Xia, C.; Wang, H. Insights into Practical-Scale Electrochemical H2O2 Synthesis. *Trends in Chemistry* **2020**, *2* (10), 942–953.

1.3 Cu-Al Spinel-Oxide Catalysts for Selective Hydrogenation of Furfural to Furfuryl Alcohol

Sutarat Thongratkaew, Chuleeporn Luadthong, Sirapassorn Kiatphuengporn, Pongtanawat Khemthong, Pussana Hirunsit, and Kajornsak Faungnawakij*

National Nanotechnology Center (NANOTEC), National Science and Technology Development Agency (NSTDA), 111 Thailand Science Park, Paholyothin Rd., Klong Laung, Pathumthani 12120, Thailand

ABSTRACT: Furfuryl alcohol, one of the important platform chemicals for polymer, food, and pharmaceutical industries, was produced by the liquid-phase hydrogenation of furfural. The Cu-Al spinel-oxide catalyst ($CuAl_2O_4$) was developed for the furfural hydrogenation to furfuryl alcohol. The spinel $CuAl_2O_4$ showed excellent activity as compared to the impregnated Cu/Al_2O_3 and reported non-noble metal catalysts. The influence of reaction parameters including temperature, time, and H_2 initial pressure were systematically investigated. The furfural conversion and the yield of furfuryl alcohol were achieved on $CuAl_2O_4$ catalyst at >99 % and >95 %, respectively. The excellent activity could be attributed to the spinel structure providing the high H_2 adsorption and desorption ability. DFT calculations suggested that the spinel structure would have the stronger interaction with furfural and the higher amounts of active sites for H_2 dissociation, resulting in the lower reaction free energy and energy barriers for the hydrogenation. Furthermore, it was observed that the $CuAl_2O_4$ showed a positive effect on the tolerance against water impurity in the liquid-phase hydrogenation of furfural.

Introduction

Recently, bio-based products derived from renewable biomass have gained increasing attention to replace petroleum-based products. The lignocellulosic biomass is mainly composed of three compounds: cellulose, hemicellulose, and lignin with variation in composition of each component depending on type of plants (Yan *et al.*, 2014), while these compounds can be utilized as raw materials of a variety of biochemicals and biofuels. Furfural is a key chemical intermediate in the conversion pathway of hemicellulose to high value-added products such as furfuryl alcohol, methyl furan and various resins (Vargas-Hernández *et al.*).

Due to the attractive economic value and wide range of application, furfuryl alcohol is an important derivative of furfural produced via hydrogenation process which can be used as solvent, pharmaceutical made to vitamin C, lubricant, lysine, plasticizer, dispersing agent, adhesive and thermostatic resins (Jacek Kije´Nski A and Andrzej Lewicki B, 2002; Nagaraja *et al.*, 2003). On the industrial scale of furfuryl alcohol production from furfural, the traditional catalyst is Cu-Cr providing 98 % yield of furfuryl alcohol. However, the chromium species can contaminate the target products and impede their further use (Nagaraja *et al.*, 2003). Therefore, heterogeneous Cr free catalysts have been developed to overcome these limitations (Mongkolchanok Pramottana, 2002).

Noble metal catalysts including Pt, Pd, and Ru have been investigated for the liquid- and gas-phase hydrogenation of furfural. It turned out that they can replace the Cr-containing systems, even though their use increases the cost of the process (Qin *et al.*, 2017). Concerning all catalysts studied to date, Cu-based catalysts have been considered as the most promising choice for the selective hydrogenation of furfural as they are highly active and cost effective (Nagaraja *et al.*, 2007; Vargas-Hernández *et al.*, 2014; Yan *et al.*, 2014). Nagaraja et al. (Nagaraja *et al.*) reported that Cu-MgO catalyst prepared by co-precipitation method showed the excellent activity in hydrogenation of furfural to furfuryl alcohol with 98 % conversion and > 98 % selectivity. Sitthisa et al. (Nagaraja *et al.*; Sitthisa and Resasco, 2011) compared the activity of Cu, Pd and Ni catalysts and found that Cu/SiO_2 was highly selective to furfuryl alcohol with small amount of 2-methyl furan while Pd/SiO_2 and Ni/SiO_2 catalysts produced mainly furan by decarbonylation and ring opening products (butanal, butanol and butane), respectively. Moreover, most of the researchers reported that the metal oxides, e.g., Ca, Co, Al, Mg, Mo, Fe have been used as a support to improve the activity and product selectivity of Cu-based catalysts by reducing the surface carbonization and the agglomeration of active particles (Huang *et al.*, 2007; Nagaraja *et al.*, 2007; Sitthisa and Resasco, 2011; Sitthisa *et al.*, 2011; Vargas-Hernández *et al.*, 2014). Regarding a choice of support, it could be expected that Cu-Al catalysts are the most promising choice as they are cheap, active and selective to desired products. Moreover, Cu species was highly dispersed on alumina support along with an increase in distributed acidic and basic sites (Hajduk *et al.*). Nonetheless, the performance of the copper catalysts can be varied depending on the microstructure of the copper and the additives, while the synthesis condition needed to be controlled precisely.

In the present work, Cu-Al spinel oxide catalysts have been proposed for the liquid-phase hydrogenation of furfural. The spinel catalyst has been prepared by sol-gel combustion technique and compared to the state-of-the-art Cu/Al_2O_3 prepared by conventional impregnation technique in terms of catalytic performances and physicochemical properties. Cu based spinel structured catalysts have been considered as the key features to provide excellent catalytic performance in hydrogenation of furfural since hydrogen can occlude in their structure, providing a high performance in hydrogenation reaction. (Kwak *et al.*). The influences of the reaction temperature, time, H_2 initial pressure, and water content on furfural hydrogenation were fully investigated over Cu-Al spinel catalysts. DFT calculation also suggested that the active copper species and copper-aluminate spinel have strong interaction that help expedite the hydrogenation reaction. Furthermore, Cu-Al spinel showed high tolerance against water that would come together with furfural feedstock which is normally produced by dehydration of xylose in water media. Therefore, the present catalytic system has good potential to reduce the cost of furfural-water azeotrope separation.

Experimental

- *Catalyst Preparation*

The $CuAl_2O_4$ was synthesized by sol-gel combustion and the CuO/Al_2O_3 was synthesized by conventional impregnation. The former was prepared by dissolving copper nitrate hemi(pentahydrate) ($Cu(NO_3)_2.2.5H_2O$) and aluminum nitrate nonahydrate ($Al(NO_3)_3.9H_2O$) with a molar ratio of 1:2 in deionized water. The mixture was continuously stirred at 60 °C for 2 h. Then, excess amount of citric acid was added into the obtained solution. After continuous stirring for 1 h, the solution was heated up to 100 °C to evaporate water. The temperature of dried precipitate was then raised up to 200 °C until black fine powder was obtained. The solid product was calcined in air at 900 °C for 4 h.

For the latter, copper (35 wt. %) was loaded on γ-Al_2O_3 (specific surface area of 216.3 m^2/g). Certain amount of $Cu(NO_3)_2 \cdot 2.5H_2O$ was dissolved in deionized water and then the copper solution was slowly dropped into γ-Al_2O_3 support under stirring. The mixture was dried at 120 °C for 12 h and calcined in air at 450 °C for 4 h.

- *Catalyst Characterization*

The crystalline phases of catalysts were investigated by wide angle X-ray diffraction (XRD: Bruker D8 ADVANCE) using Cu Kα radiation. The measurement was operated under an electric tension of 40 kV and a current of 40 mA in the 2θ range of 20−80° with a step size of 0.02°/s. The textural properties of Cu-based catalysts were analyzed by nitrogen adsorption-desorption technique (Quantachrome Instruments, Nova 2000e). Prior to the measurement, the sample was degassed at 300 °C for 3 h. The specific surface area of the catalysts was examined using the Brunauer-Emmett-Teller (BET) analysis in a relative pressure (p/p_0) range between 0.05 and 0.95, where the specific pore volume was measured at a relative pressure of 0.995. Pore diameters and volumes were calculated using Barrett-Joyner-Halenda (BJH) method. The morphology of catalysts was investigated by transmission electron microscope (TEM: JEOL JEM-2100) with the acceleration voltage of 200 kV. The samples were prepared by suspending in ethanol and then dispersing on holey carbon-coated grids. The reducibility of catalysts was analyzed using temperature programmed reduction (TPR: CHEMBET-Pulsar Quantachrome Instruments). In each TPR experiment, catalyst was heated in a flow of gas mixture of hydrogen (H_2) and argon (Ar). The experiment was carried out in the temperature range of 45−800 °C with a heating rate of 5 °C/min. The H_2 uptake of catalysts was investigated by a hydrogen temperature programmed desorption (H_2-TPD) using ChemStar™ Quantachrome Instruments equipped with a thermal conductivity detector (TCD). Pior to each measurement, the catalyst was placed in a quartz tube and then reduced with 10 % H_2 in Ar at 300 °C 3 h. After that, the sample was cooled down to room temperature and saturated with H_2 for 1 h. Next, a stream of He (30 ml/min) was fed to remove physically adsorbed H_2. Subsequently, the measurements were conducted under a He flow in the temperature range of 30−900 °C with a heating rate of 10 °C/min. N_2O pulse chemisorption was carried out in the flow system to measure the active sites of Cu (Quantachrome, CHEMBET-3000 with mass spectroscopy). Prior to the test, the catalyst was placed in the quartz tube and reduced at 300 °C for 3 h in 10 % H_2/Ar. Then, the sample was cooled down to room temperature under a He flow, and 25 % N_2O/He were subsequently introduced into a calibrated injection volume of 61 µL using He as a carrier gas. The formation of N_2 and consumption of N_2O in the effluent were monitored by a thermal conductivity detector (TCD) and mass spectroscopy. The number of Cu surface atoms was obtained by a stoichiometry between N_2O and Cu of 1:2 according to the following equation.

$$2Cu + N_2O \rightarrow Cu_2O + N_2 \qquad (1)$$

The X-ray photoelectron spectroscopy (XPS) was performed *ex-situ* and *in-situ* using a PHI5000 Versa Probe II Scanning XPS Microprobe (ULVAC-PHI) with primary radiation source micro-focused scanning X-ray (Al Kα 1486.6 eV). For *in-situ* XPS, the sample was reduced in the internal pre-treatment chamber at 300 °C for 3 h under 10% H_2/N_2 with a flow rate of 40 ml/min. The local geometry changes of Cu species in catalysts after reduction process with hydrogen gas at 300 ^oC for 3 h were investigated by in-situ x-ray absorption spectroscopy (XAS) at Cu K-edges in Transmission mode. Prior to the in situ XAS study, the sample was pelletized with diameter of 1.5 mm (edge jump of 1.4) and placed into the testing cell. XAS spectra were analyzed by the Athena programs included in the IFEFFIT package. A principal component analysis (PCA) followed by LCF analysis was applied on the normalized XANES spectra in the -20 eV < E0 < 60 eV range. The Cu_2O, CuO and $CuAl_2O_4$ were selected as the reference compounds for Cu K-edge.

- *Performance of Cu-based catalysts on furfural hydrogenation reaction*

The Cu-based catalysts were tested for furfural hydrogenation reaction in a stainless-steel autoclave with magnetic stirrer. Prior to each experiment, the catalyst was activated by reduction with 10% H_2 in N_2 at 300 ^oC for 3 h. After the catalyst activation, 1.5 M of furfural (Sigma-Aldrich, 99%) in 2-propanol (Fisher Scientific, 99.98%) and 0.5 g of a pre-reduced catalyst were mixed together. The reaction was carried out at initial H_2 pressure of 20−40 bar and temperature of 150−190 ^oC. After the reaction, the autoclave was cooled down to the ambient temperature with an ice-water bath. Liquid phase product was collected and then centrifuged to remove the solid catalyst. Then the liquid samples were analyzed by gas chromatography (GC-2010, Shimadzu) with a flame ionization detector using capillary column (DB-WAX, Agilent technologies).

The furfural conversion, furfuryl alcohol yield and turn over frequency (TOF) are calculated using the following equations:

$$\text{Conversion } (\%) = \left(\frac{\text{moles of furfural consumed}}{\text{moles of furfural initially charged}}\right) \times 100 \qquad (2)$$

$$\text{Yield } (\%) = \left(\frac{\text{moles of furfuryl alcohol produced}}{\text{theoretical moles of furfuryl alcohol}}\right) \times 100 \qquad (3)$$

$$\text{TOF } (s^{-1}) = \left(\frac{\text{moles of furfural consumed}}{\text{active sites of catalyst x reaction time}}\right) \times 1 \qquad (4)$$

- *Computational method*

The catalyst models were constructed as Cu_{13} cluster supported on $CuAl_2O_4$ and γ-Al_2O_3. The support $CuAl_2O_4$ (311) facet was selected based on the XRD results (see Fig. 4c) that the (311) showed the highest intensity of the XRD diffraction peak. The γ-Al_2O_3 (110) facet which was reported to dominate in γ-Al_2O_3 nanocrystallites (~70-83% of total area) was applied (Nortier *et al.*, 1990; Digne *et al.*, 2004). The possible M_{13} nanoparticle structures; icosahedral (ICO), face centered cubic (FCC), hexagonal close packed (HCP), capped cubic (CC), buckled biplanar (BBP), triangular biplanar (TBP), and cage-like (CAG), which were reported in previous studies (Chou *et al.*, 2009; Piotrowski *et al.*, 2010) were initially investigated. The high-symmetry Cu_{13} cluster structure of ICO was found to be the most stable one. Then, the ICO-Cu_{13} cluster were initially deposited on $CuAl_2O_4$ (311) and γ-Al_2O_3 (110) surfaces at various possible positions and orientations. Here, we report the details of the most stable surface model structures in **Fig. S1** and the structures of $Cu_{13}/CuAl_2O_4$ (311) and Cu_{13}/γ-Al_2O_3 (110) surfaces are shown in **Fig. S2** in supplementary information. The structures were applied to study hydrogenation of furfural to furfuryl alcohol. The M_{13} cluster model can represent small particle approximate 1 nm. It should be noted that catalytic reactivity is also affected by the copper particle size and shape which may be ascribed to the variation of the number of low coordinated defect sites. In this work, we focus on the effect of the supports and to determine active sites for furfural hydrogenation. The surface models can adequately represent those. Furthermore, the M_{13} cluster and supported M_{13} cluster on support such as γ-Al_2O_3 were broadly applied to study catalytic reaction and catalysts properties for example NO oxidation, CO oxidation, H_2 dissociation, ammonia dissociation and stability of clusters on support (Hu *et al.*, 2010; Hirunsit *et al.*, 2014; Gao, 2016; Zeng *et al.*, 2016; Chen *et al.*, 2017; Dessal *et al.*, 2019; Li, T. T. *et al.*, 2019).

(a) side view and top view of bare $CuAl_2O_4$(311) surface

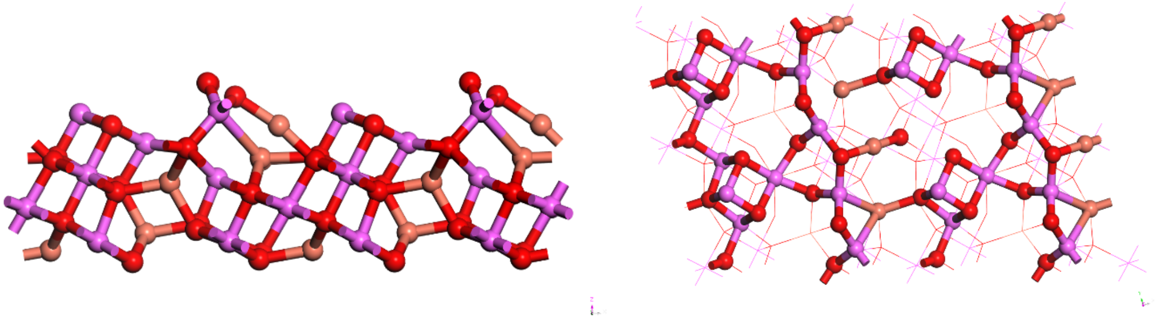

(b) side view and top view of bare γ-Al_2O_3(110) surface

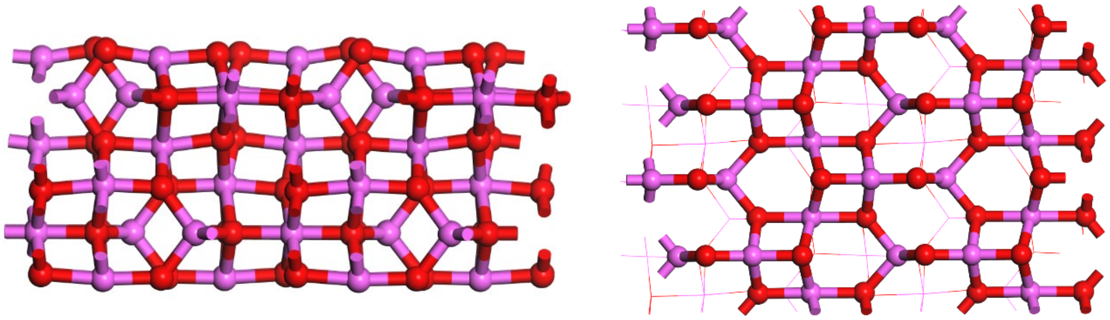

Fig. S1. Bare surfaces model structures of (a) $CuAl_2O_4$(311) and (b) γ-Al_2O_3(110)

(a) Isolated icosahedral (ICO) Cu_{13} cluster

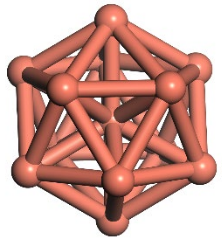

(b) $Cu_{13}/CuAl_2O_4(311)$ (c) $Cu_{13}/\gamma\text{-}Al_2O_3(110)$

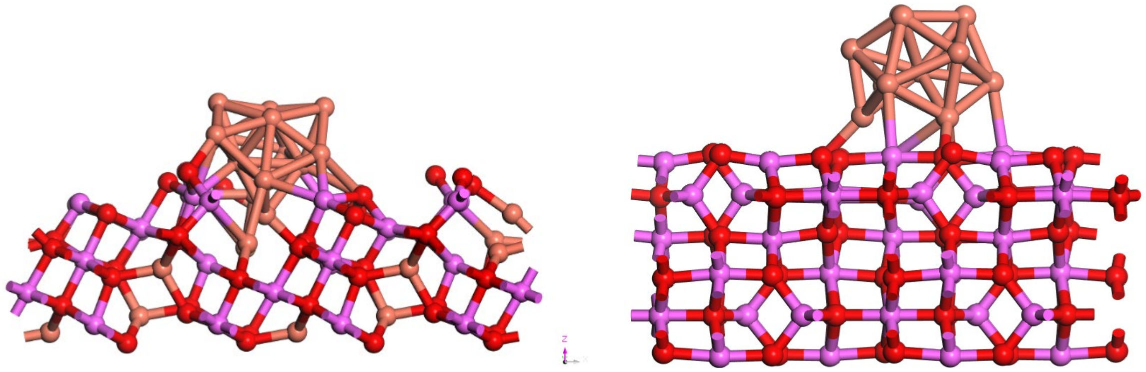

Fig. S2. The model structures of (a) isolated icosahedral Cu_{13} cluster, and surfaces of (b) $Cu_{13}/CuAl_2O_4(311)$ and (c) $Cu_{13}/\gamma\text{-}Al_2O_3(110)$.

The fully periodic plane-wave density functional theory (DFT) calculations were carried out using the Vienna *ab initio* Simulation Program (VASP) (Kresse and Furthmüller, 1996a; b). Spin-polarized DFT calculations were performed with the exchange-correlation functional Perdew-Burke-Ernzerhof (Perdew *et al.*, 1996) described within the generalized gradient approximation implemented with the projector augmented wavefunction (PAW) method (Blöchl, 1994; Kresse and Joubert, 1999) for representing the non-valence core electrons. For the inclusion of long-range dispersion, the semi-empirical dispersion potential correction method described by Grimme and coworkers (DFT-D3) (Grimme, 2006; Grimme *et al.*, 2010) was applied. The calculations employed 2 × 2 × 1 k-points Monkhorst-Pack mesh sampling (Monkhorst and Pack, 1976) in the surface Brillouin zone. The plane-wave cutoff energy was optimized at 500 eV. The results were checked for convergence with respect to the applied energy cutoff and number of k-points. The Gaussian broadening (Fu and Ho, 1983) with a value of smearing parameter σ of 0.05 eV was applied. The convergence criteria for electronic self-consistent iteration were set to 1.0×10^{-6} eV and the ionic relaxation loop was limited for all forces smaller than 0.02 eV/Å for free atoms. The dipole corrections in all three spatial directions were included only in z direction for surface calculations. The free energy calculations included zero-point energy, enthalpic and entropic corrections at T = 170 ^{o}C which the highest yield of furfuryl alcohol was experimentally observed. The transition states were located using Nudged Elastic Band (NEB) (Sheppard *et al.*, 2008; Sheppard and Henkelman, 2011; Sheppard *et al.*, 2012) and Dimer (Henkelman and Jónsson, 1999; Heyden *et al.*, 2005; Kästner and Sherwood, 2008; Xiao *et al.*, 2014) methods which are implemented in VTST tool. The transition state structures were characterized by a normal mode analysis to ensure the presence of one imaginary frequency. Bader charge analysis (Henkelman *et al.*, 2006; Sanville *et al.*, 2007; Tang *et al.*, 2009a; Yu and Trinkle, 2011) was also performed using the method implemented in VTST tool.

Results and discussion

- *Characterization of Cu-based catalysts*

The specific surface area, average pore diameter and total pore volume of $CuAl_2O_4$ and CuO/Al_2O_3 catalysts are listed in **Table 1**. CuO/Al_2O_3 catalyst synthesized by impregnation method exhibited the surface area of 123.4 m^2/g, average pore diameter of 7.5 nm, and total pore volume of 0.306 cm^3/g. It was found that the surface area and total pore volume of CuO/Al_2O_3 catalyst decreased approximately 1.7 times compared to those of bare Al_2O_3 support (216 m^2/g and 0.610 cm^3/g, respectively). The decrease in surface area and pore volume after copper loading might occur from Cu particles blocking and/or entering into the pore of Al_2O_3 during the impregnation process (Pantaleo *et al.*, 2009). However, $CuAl_2O_4$ catalyst displayed extremely low surface area (1.8 m^2/g) and pore volume (0.020 cm^3/g), suggesting its less-porous nature after the high temperature calcination. From the above results, the Cu-based catalysts synthesized by different methods exhibited different physical properties, especially specific surface area. Thus, TEM micrograph was used to confirm the structure of the catalysts as shown in **Fig. 1**. It can be seen that $CuAl_2O_4$ (in **Fig. 1a)** showed the primary particle size of 10−25 nm, while they tended to form secondary particles that sintered to a larger size of 200–400 nm. The CuO/Al_2O_3 sample (in **Fig. 1b)** showed a rod-like structure which should be mainly alumina particles with length of 10−30 nm, while they tended to agglomerate to a larger cluster. Note that copper particles were not clearly distinguished in this TEM image.

Table 1 Specific surface area, average pore size, total pore volume and H_2 sorption capacity of Al_2O_3 support and Cu-based catalysts.

Catalyst	Specific surface area (m^2/g)	Average pore size (nm)	Total pore volume (cm^3/g)	H_2 sorption capacity[a] ($\mu mol\ H_2/g$)
$CuAl_2O_4$	1.8	11.4	0.020	266.9
Cu/Al_2O_3	123.4	7.5	0.306	434.5
Al_2O_3	216.0	7.8	0.610	-

[a] Calculated using the area under the H_2-TPD profiles.

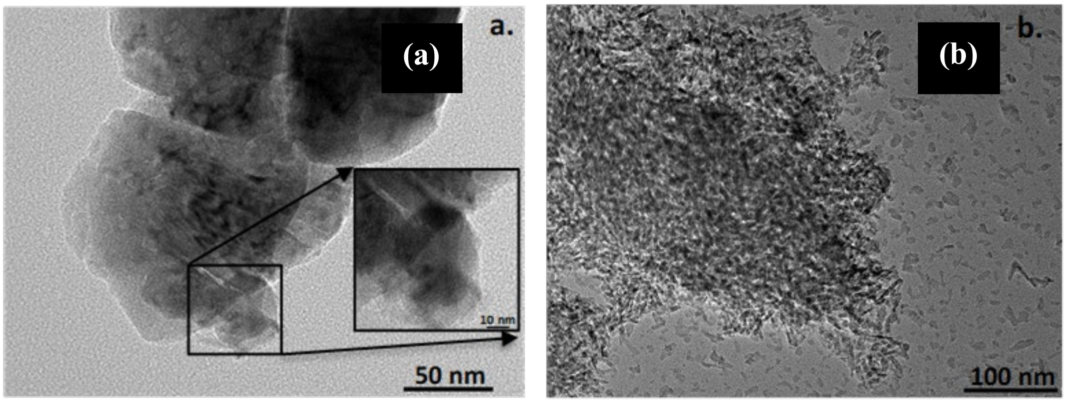

Fig. 1 TEM images of (a) $CuAl_2O_4$ and (b) CuO/Al_2O_3 catalysts.

The reduction behavior of catalysts was investigated as the corresponding H_2-TPR profiles are shown in **Fig. 2.** It was observed the two-step reduction mechanism on both catalysts. The low reduction peak at 260-270 ^oC was attributed to highly dispersed CuO particles or isolated Cu ions on the catalyst surface, whereas the peak at high temperature was attributed to the reduction of bulk CuO or composite metal oxides (Vargas-Hernández *et al.*). Accordingly, CuO/Al_2O_3 catalyst was reduced at lower temperatures (maximum at 400 ^oC) compared to $CuAl_2O_4$ catalyst (at 520 ^oC), owing to the low interaction between Cu oxides and Al_2O_3 support These results were in good agreement with the stepwise reductions of copper oxide species to Cu^0 reported by S. M. Pudi (Pudi *et al.*, 2015). Note that XRD could not clearly detect the CuO phase since its content is too small (see **Fig.4c**). Although the higher temperature would bring about more complete reduction process to form metallic copper, it was observed that the reduction temperature higher than 300 ^oC would decrease the activity of catalysts (both $CuAl_2O_4$ and CuO/Al_2O_3), probably due to the sintering effect of copper particles (results not shown). Therefore, the reduction temperature of 300 ^oC was used for the catalyst activation.

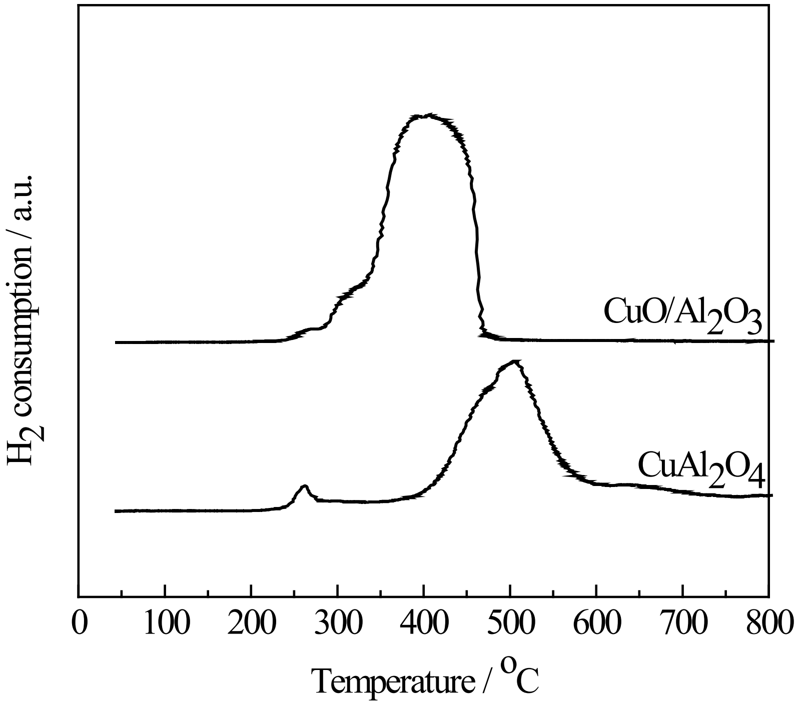

Fig. 2 H_2-TPR profiles of $CuAl_2O_4$ and CuO/Al_2O_3 catalysts.

The H_2-TPD was performed to investigate the adsorption capacity and interaction of hydrogen on the Cu-based catalysts (**Fig. 3)**. The H_2 uptake data would be useful information since the hydrogenation reaction needs the interaction between H_2 molecules and catalyst surface to proceed. As a result, CuO/Al_2O_3 showed a broad peak in the range of 150−600 °C, suggesting the low H_2 sorption ability. On the other hand, $CuAl_2O_4$ clearly showed two major desorption peaks in the range of 90−120 °C and 250−650 °C, suggesting to the desorption of atomic hydrogen on Cu sites and the desorption of strongly-adsorbed hydrogen on the bulk Cu particles or metal oxide, respectively (Chunjie Huang). The H_2 uptake of CuO/Al_2O_3 and $CuAl_2O_4$ catalysts were determined as 266.9 and 434.5 µmol/g, respectively (in **Table 1)**. The spinel $CuAl_2O_4$ catalyst showed the higher amount of H_2 uptake compared to CuO/Al_2O_3 catalyst, indicating that atomic hydrogen species could be inserted into the spinel structure.

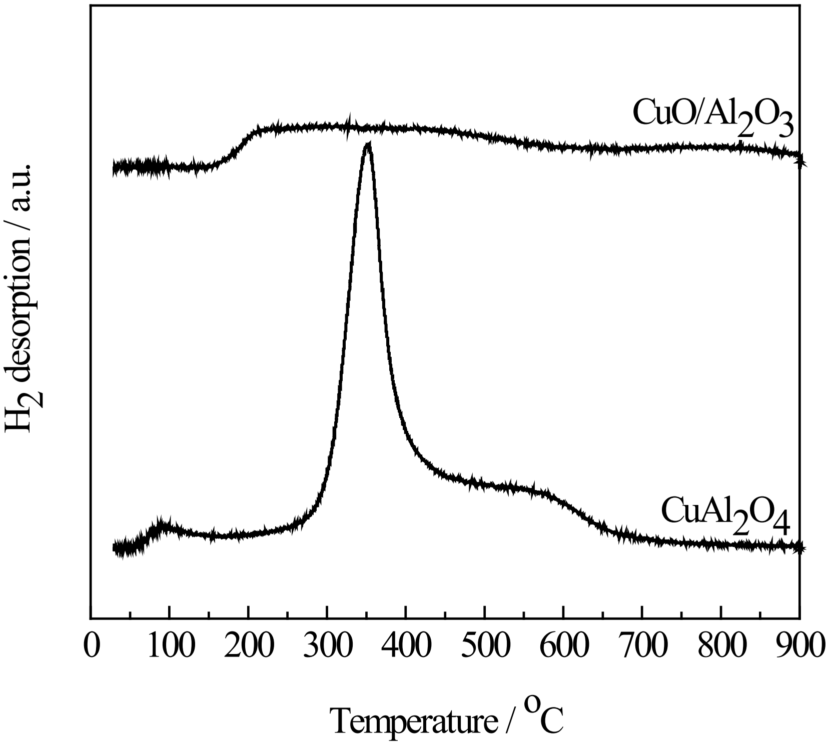

Fig. 3 H_2-TPD profiles of $CuAl_2O_4$ and CuO/Al_2O_3 catalysts.

The crystalline phases of the Cu-based catalysts were investigated using wide angle XRD technique as shown in **Fig. 4.** The spinel catalyst prepared with sol-gel combustion displayed the diffraction patterns at 2θ of 31.3°, 36.9°, 44.8°, 55.7°, 59.4°, and 65.3°, corresponding to reflection planes of cubic spinel $CuAl_2O_4$ including (220), (311), (400), (422), (511), and (440) (PDF 01-075-4256) (Salavati-Niasari *et al.*, 2009). For CuO/Al_2O_3 catalyst, the diffraction patterns exhibited two phases of γ-Al_2O_3 at 2θ of 46.5 ° (PDF 00–010-0425) and monoclinic CuO at 2θ of 32.5°, 35.5°, 38.7°, 48.7°, 53.5°, 58.2°, 61.5°, 66.2°, and 68.1°, corresponding to the reflection of (110), (11-1), (111), (20-2), (020), (202), (11-3), (31-1), and (220) (PDF 00-048-1548) (Luo *et al.*, 2005).

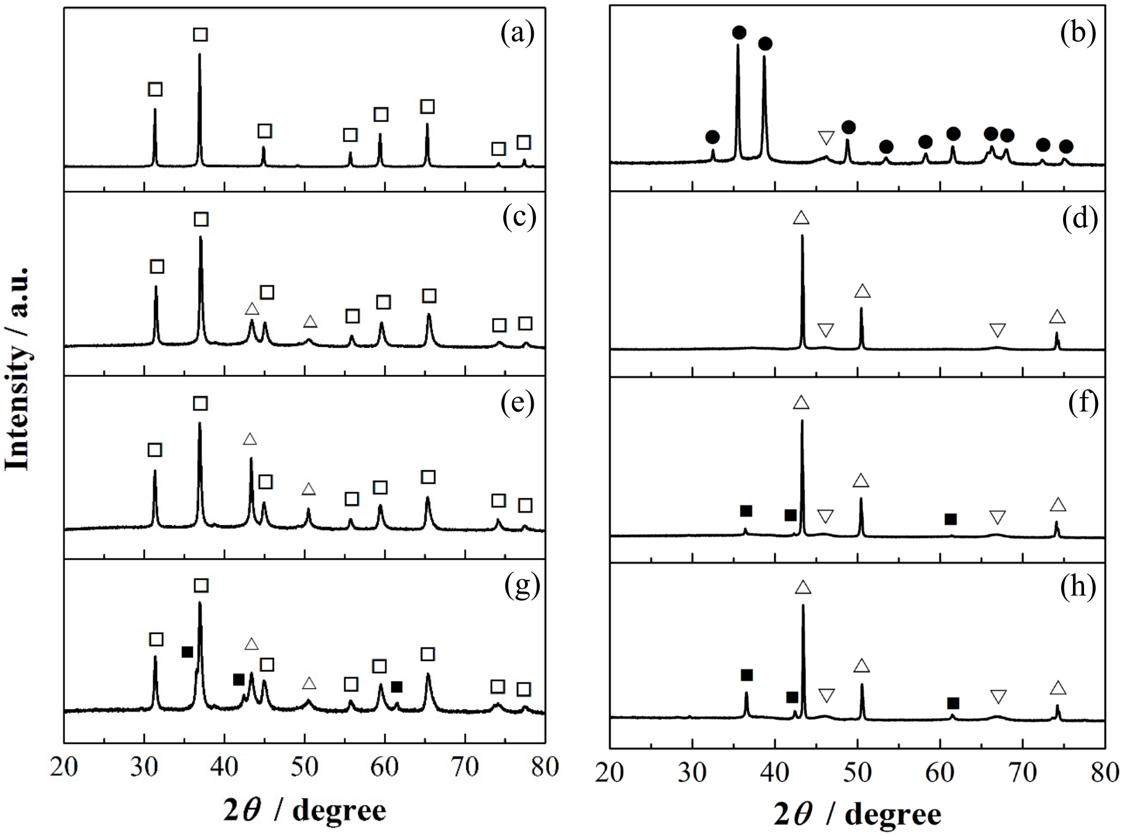

Fig. 4 XRD patterns of $CuAl_2O_4$ (left) and CuO/Al_2O_3 (right) catalysts: (a) as-synthesized $CuAl_2O_4$, (b) as-synthesized CuO/Al_2O_3, (c) reduced $CuAl_2O_4$, (d) reduced CuO/Al_2O_3, (e) spent $CuAl_2O_4$ in isopropanol system, (f) spent CuO/Al_2O_3 in isopropanol system, (g) spent $CuAl_2O_4$ in isopropanol/water system, (h) spent CuO/Al_2O_3 in isopropanol/water system.
□ cubic $CuAl_2O_4$ ▽ Al_2O_3 • CuO △ Cu^0 ⍰ Cu_2O

Upon the reduction process at 300 °C for 3 h, the diffraction peak assigned to metallic copper phase (PDF 00-004-0836) was clearly observed over $CuAl_2O_4$, while the structure of spinel $CuAl_2O_4$ still remained with lower intensity, apparently due to the incomplete reduction process (**Fig. 4c**). The partially reduced $CuAl_2O_4$ could improve a catalytic activity in hydrogenation reactions, involving reversible hydrogen adsorption (see H_2-TPD result in **Fig. 3** and **Table 1).** For CuO/Al_2O_3 catalyst, CuO was completely reduced to Cu as confirmed by XRD result in **Fig. 4d**. It should be noted that Cu^{2+} was more difficult to be reduced in cubic spinel structure of $CuAl_2O_4$ catalyst compared to CuO/Al_2O_3 (Luo *et al.*, 2005; Kwak *et al.*, 2012; Chiang and Lin, 2017; Qin *et al.*, 2017), (Jose´ A. Rodriguez a;*, 2003; Hu *et al.*, 2010), which were consistent with the TPR results. The crystalline phases of the catalysts after the reaction tests will be discussed in the next section.

Oxidation state of Cu element was determined by XPS as the results shown in **Fig. 5**. The calcined catalysts presented the principal $Cu2p_{3/2}$ peak around 925-965 eV and Cu LMM peak around 890−925 eV. In **Fig. 5a**, the main peaks of CuO/Al_2O_3 and $CuAl_2O_4$ were ca. 933.5 eV, corresponding to Cu^{2+} species. The satellite peak of Cu^{2+} species was also observed at 944.1 eV and 963 eV. In **Fig. 5b**, the Cu LMM spectra of both samples exhibited a single peak at 917.8 eV, which should be assignable to a characteristic peak for Cu^{2+} species (Zhang *et al.*, 2015; Han *et al.*, 2018; Li, X. *et al.*, 2019; Ponmudi *et al.*, 2019).

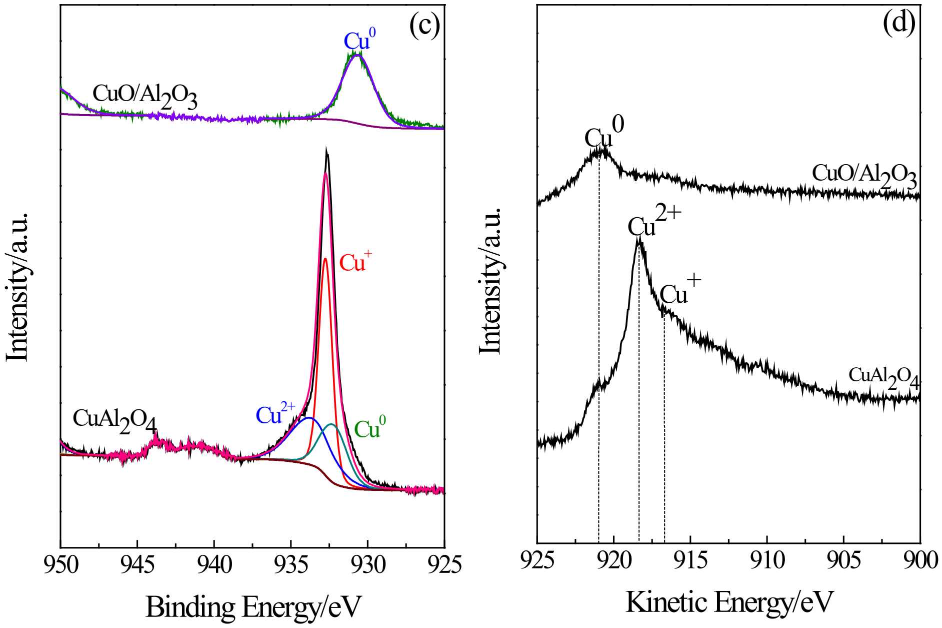

Fig. 5 XPS spectra of (a) Cu $2p_{3/2}$, (b) Cu LMM Auger spectra of as-prepared and XPS spectra of (c) Cu $2p_{3/2,}$ (d) Cu LMM Auger spectra of *in situ* reduced.

In situ XPS measurements after reduction process were carried out to evaluate the active surface species of copper. **Fig. 5c** and **Fig. 5c** show Cu $2p_{3/2}$ (a) and Cu LMM (b) spectra of the reduced catalysts and the characteristics of copper species are listed in the **Table 2**. Accordingly, the Cu $2p_{3/2}$ spectra of $CuAl_2O_4$ shifted the peak maxima from 933.5 to 932.8 eV, indicating the surface change from Cu^{2+}-rich surface to Cu^{1+}- rich one. In addition, Cu LMM spectra confirmed the reduction of Cu^{2+} to Cu^{1+} and Cu^0 species. It seems that Cu^{1+} and Cu^0 species are representing the reduced copper species, while Cu^{2+} is due to the unreduced spinel matrix. On the other hand, the satellite peak of CuO/Al_2O_3 was not detectable after the reduction process due to the fact that the divalent copper species was completely reduced to zero valent copper (Cu^0) as confirmed by the $Cu2p_{3/2}$ and Cu LMM in **Fig. 5c** and **5d**.

Table 2 The characteristics of CuO, Cu^0, Cu_2O, and $Cu(OH)_2$.

Catalyst	Cu $2p_{3/2}$ Biding energy(eV) Main peak	Cu $2p_{3/2}$ Biding energy(eV) Satellite	Cu LMM Kinetic energy(eV) Cu^0	Cu LMM Kinetic energy(eV) Cu^{1+}	Cu LMM Kinetic energy(eV) Cu^{2+}
CuO/Al_2O_3	933.5	d	n	n	917.8
CuO/Al_2O_3 (*in situ* reduced)	931.5	n	921.4	916.7	n
$CuAl_2O_4$	933.5	d	n	n	917.8
$CuAl_2O_4$ (*in situ* reduced)	932.8	d	921.4	916.7	918.0

d Detected
n Not detected

The in situ XAS measurement under the reduction condition was performed to further confirm the oxidation state changes of Cu species in Cu-based catalysts. The normalized Fe K-edge absorption spectra together with an amplified inset, showing the spectra of iron oxide species and Fe foil standard, are displayed in **Fig. 6**. During the reduction process of Cu-based catalysts, it was observed the phase transformation in the corresponding normalized Cu K-edge XANES spectrum. As the, a small absorption peak appears at ~ 8,981 eV in the spectrum (), indicating the formation of Cu(I). Another peak at ~ 8,980 eV corresponded to Cu(0). The compositions of Cu species analyzed from the corresponding spectra by linear combination fitting (LCF) analysis using the Athena program are summarized in **Table 3** with R factor and Reduced R^2 < 0.015 (see **Table S1)**. Before the reduction process, all calcined catalysts exhibited three main phases of copper oxide species including Cu_2O, CuO and $CuAl_2O_4$ as the compositions of both catalysts were almost similar which were 27.1-31.6 wt. %, 18.1-21.5 wt. %, and 50.2-51.4 wt. %, respectively. However, after the reduction process, Cu^0 was observed on reduced catalyst mixed with copper oxide species, suggesting that copper oxides were partially transformed to Cu^0. The main phase of reduced $CuAl_2O_4$ catalyst was $CuAl_2O_4$ (64.5 %) while that of reduced CuO/Al_2O_3 catalyst was Cu^0 (71.4 %), as were confirmed by XRD. N_2O pulse chemisorption technique was used to investigate the active sites of catalysts which referred to only Cu^0 phase. In **Table 3**, it was observed that the active Cu^0 sites of CuO/Al_2O_3 catalyst were 12.4 μmol/g which were 1.4 times higher than $CuAl_2O_4$ catalyst (8.7 μmol/g).

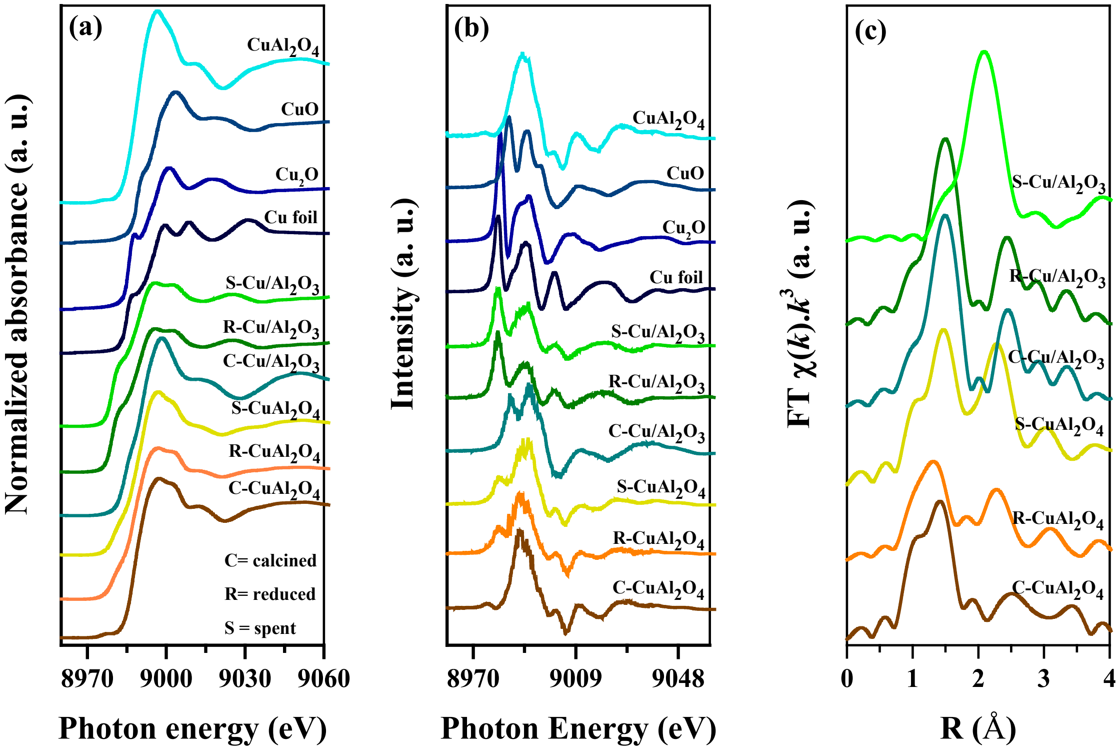

Fig. 6 In situ XAS results (a) Cu K-edge XANES spectra, (b) first-order derivatives of the XANES spectra, and (c) Fourier-transformed Cu K-edge EXAFS spectra of $CuAl_2O_4$ and Cu/Al_2O_3 catalysts before and after reduction process.

Table 3 Results from linear combination fitting (LCF) analysis before and after reduction process at 300 °C for 3 h, active Cu^0 sites and TOF of Cu-based catalysts.

Catalysts	Mass fraction[a], *w*/%				Active Cu^0 sites[b] (µmol/g)	TOF (s^{-1})[c]
	Cu foil	Cu_2O	CuO	$CuAl_2O_4$		
Calcined $CuAl_2O_4$	0.0	27.1	21.5	51.4	-	-
Reduced $CuAl_2O_4$	25.9	0.0	16.4	64.5	8.7	92.2
Spent $CuAl_2O_4$	14.4	0.0	21.1	64.5	-	-
Calcined Cu/Al_2O_3	0	31.6	18.1	50.2	-	-
Reduced Cu/Al_2O_3	71.4	13.1	5.4	10.1	12.4	66.1
Spent Cu/Al_2O_3	67.7	12.3	14.1	5.9	-	-

[a] R factor and Reduced R^2 are listed in Table S1

[b] Calculated from the N_2O pulse chemisorption.

[c] Calculated based on Cu^0 and the catalytic activity at 170 °C; catalyst weight, 0.5 g; furfural solution, 1.5 M; H_2 pressure, 40 bar; 1 h; 2-propanol solvent.

Table S1 R factor and Reduced R^2 from linear combination fitting (LCF) analysis of Cu-based catalysts before and after reduction process at 300 °C for 3 h.

Catalysts	Mass fraction[a], *w*/%				R factor	Reduced R^2
	Cu foil	Cu_2O	CuO	$CuAl_2O_4$		
Calcined $CuAl_2O_4$	0.0	27.1	21.5	51.4	0.0030	0.0008
Reduced $CuAl_2O_4$	25.9	0.0	16.4	64.5	0.0258	0.0058
Spent $CuAl_2O_4$	14.4	0.0	21.1	64.5	0.0149	0.0037
Calcined Cu/Al_2O_3	0.0	31.6	18.1	50.2	0.0005	0.0001
Reduced Cu/Al_2O_3	71.4	13.1	5.4	10.1	0.0018	0.0002
Spent Cu/Al_2O_3	67.7	12.3	14.1	5.9	0.0012	0.0001

- *Catalytic activity of Cu-based catalysts in furfural hydrogenation*

Fig. 7 shows the catalytic performance of $CuAl_2O_4$ in furfural hydrogenation to furfuryl alcohol as a function of temperature and time. In **Fig. 7a**, furfural conversion and furfuryl alcohol yield increased with respect to the increment of reaction temperature, suggesting its endothermic nature. The reaction temperature above 170 °C gave a similar yield above 95%. In **Fig. 7b**, furfural conversion and furfuryl alcohol yield increased monotonously with the increase in reaction time. The conversion and yield were achieved at 99.3% and 96.2%, respectively, within 60 min. The selectivity toward furfuryl alcohol was extremely high for all cases signifying that the side reactions was not flavored over the spinel catalysts. The small amount of by-products including 2-methyl furan (2MF) and tetrahydrofurfuryl alcohol (THFOL) was detected (< 2 %) as the reaction mechanism of by-products was reported by Nagaraja et. al (Nagaraja *et al.*, 2007).

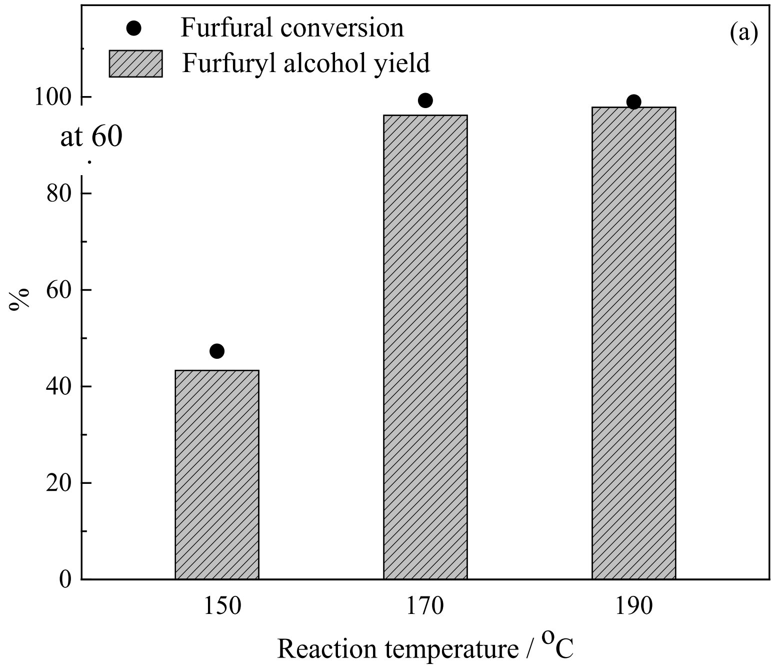

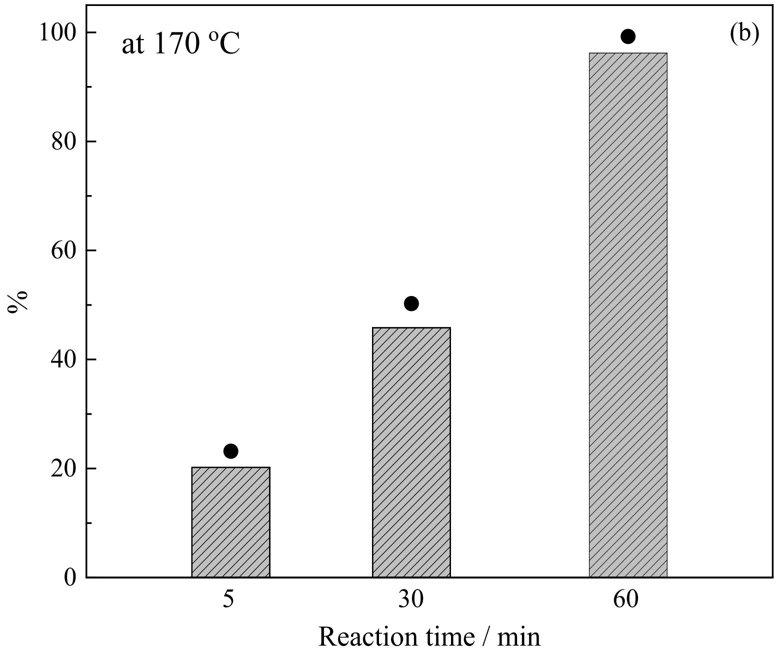

Fig. 7 Catalytic performance in term of furfural conversion and furfuryl alcohol yield as a function of reaction temperature (a) and time (b) over $CuAl_2O_4$ catalyst. Reaction condition: catalyst weight, 0.5 g; furfural solution, 1.5 M; H_2 pressure, 40 bar.

Next, the effect of initial hydrogen pressure (20, 30, and 40 bars) on furfural hydrogenation was studied at temperature of 170 °C and time of 60 min (**Fig. 8)**. It was found that with the increase in H_2 pressure from 20 to 30 bar would enhance the conversion and yield. However, the furfuryl alcohol yield slightly dropped when H_2 pressure was further increased to 40 bar, presumably due to the over-hydrogenation reaction. In addition, the reaction rate could be enhanced by increasing total pressure from 20 (pure H_2) to 40 bar (H_2:N_2 at 1:1). However, the activity from the mixed gas system was not as high as that from the pure H_2 system. The results suggested that the conversion and yield can be enhanced by increasing total pressure or partial hydrogen pressure, likely due to the improved solubility of hydrogen in the liquid phase.

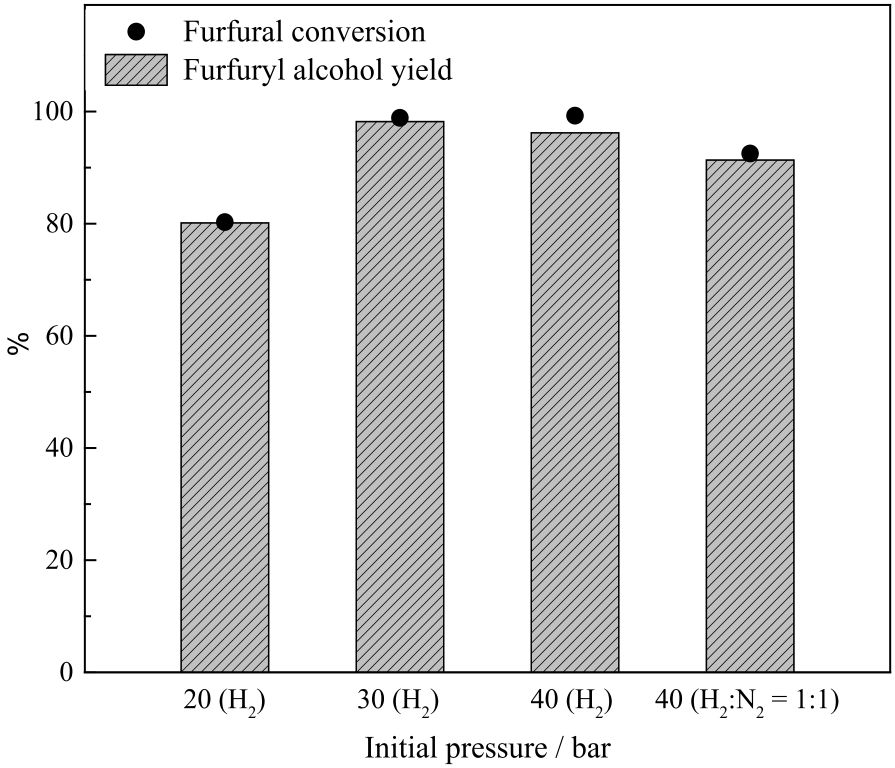

Fig. 8 Influence of initial reaction pressure on catalytic activity of $CuAl_2O_4$ catalyst. Reaction condition: catalyst weight, 0.5 g; furfural solution, 1.5 M; reaction temperature, 170 ^oC; reaction time, 1 h.

It is worth investigating the effect of water content in the furfural hydrogenation since water is basically used as a solvent in xylose dehydration to furfural. It is hard to remove all water from furfural by a conventional distillation process because they are azeotrope. In this section, the catalytic hydrogenation of furfural to furfuryl alcohol was studied at various water contents in a range of 0-30% v/v of 1.5 M of furfural solution. Moreover, the reaction was tested on CuO/Al_2O_3 for performance comparison (**Fig. 9**). Without water, $CuAl_2O_4$ catalyst showed complete conversion with furfuryl alcohol yield of 98.6%, which were much higher than CuO/Al_2O_3. The higher water content typically resulted in lower conversion and yield. The yield decreased to 94.3, 79.3 and 23.6% with the water contents of 10, 20, and 30% v/v, respectively. However, the more severe decline in activity was observed on CuO/Al_2O_3 when the water content was increased. As seen in **Fig. 9b**, the furfural yields drastically dropped to 57.7, and 11.7 % at water content of 20, and 30% v/v, respectively. The result suggested that the higher content of water leads to more side reactions. In addition, water would bring about *catalyst deactivation as oxidation of copper was* confirmed by XRD analysis. The spent $CuAl_2O_4$ and CuO/Al_2O_3 catalysts in the reaction with water addition demonstrated the XRD characteristics of Cu_2O phase (**Fig. 4**). It was observed that the reduced $CuAl_2O_4$ was more stable than the reduced CuO/Al_2O_3 at all water contents. The suggested condition of furfural solution should not contain more than 10 % v/v of water to achieve complete furfural conversion and furfuryl alcohol yield at or above 94%.

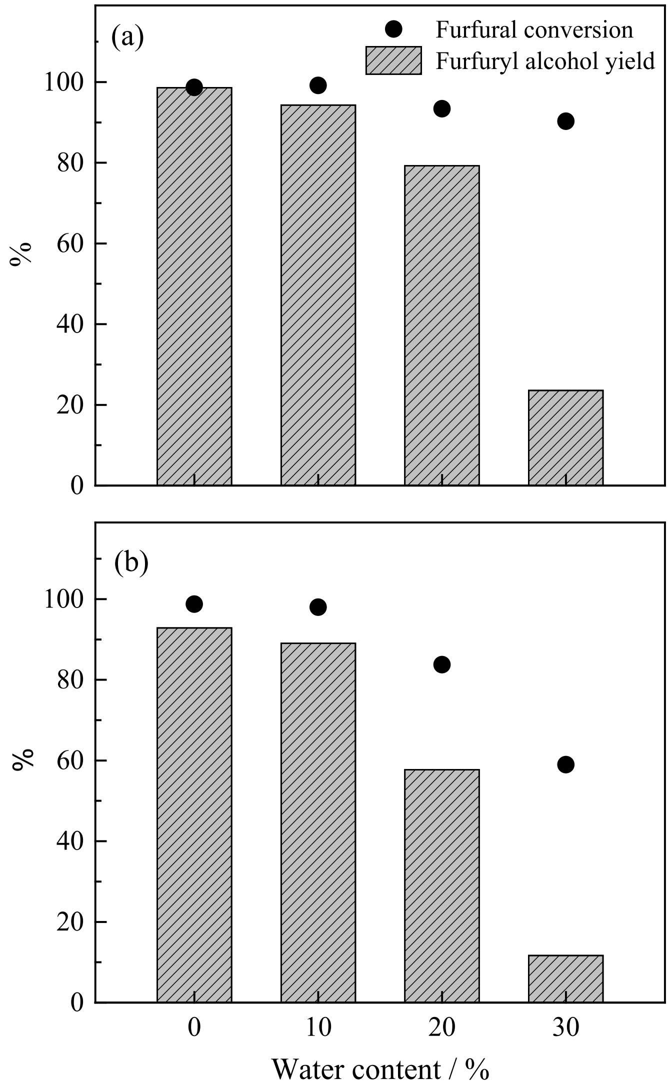

Fig. 9 The catalytic performance in term of furfural conversion and furfuryl alcohol yield as a function of water content over (a) $CuAl_2O_4$ and (b) CuO/Al_2O_3 catalysts. Reaction condition: catalyst weight, 0.5 g; furfural solution, 1.5 M; H_2 pressure, 20 bar; reaction temperature, 170 ^oC; reaction time, 5 h.

The TOF of reaction on Cu-based catalysts was calculated based on the active Cu^0 sites at the conditions which gave the highest catalytic activity. It was found that the TOF of spinel $CuAl_2O_4$ catalyst was 1.4 times higher than CuO/Al_2O_3 catalyst, implying that furfuryl alcohol flavored to produce over $CuAl_2O_4$ catalyst even though there is lower active Cu^0 sites. Accordingly, it was considered that the spinel structure along with the high H_2 adsorption and desorption ability in $CuAl_2O_4$ catalyst played a positive role in the hydrogenation reaction. In spite of the low surface area and pore volume, $CuAl_2O_4$ exhibited higher activity than CuO/Al_2O_3. Upon the H_2 activation process, isolated Cu-aluminate or Cu^{2+} ions were formed on the $CuAl_2O_4$ spinel host, and the interaction between them was anticipated to correlate to the excellent catalytic activity. It should be noted that the Cu^{2+} ions incorporated in octahedralsites of Al_2O_3 or vicariant in aluminate were the active sites which provided the H_2 dissociation and adsorbate for dissociated H_2 molecule, respectively, leading to the high catalytic activity in hydrogenation reaction (Bahmanpour *et al.*, 2019). Mainly Cu^0 on Cu/Al_2O_3 was inactive compared to the spinel catalyst containing both Cu^0 and $CuAl_2O_4$ (Cu^{2+}). Moreover, according to XRD results of spent catalyst (**Fig. 4**), metallic copper species on cubic spinel structure ($CuAl_2O_4$) remained quite stable, suggesting that these copper particles was more stable than the copper particles impregnated on γ-Al_2O_3. Comparing the catalytic activity of this research with the previous works from literatures as shown in **Table 4**, the spinel catalyst in the present work was among the top-list which gave the higher furfural yield (95-99%) than those of other works (50-98%). This result indicated that $CuAl_2O_4$ catalyst was effective for furfuryl alcohol production since the spinel structure was proved to provide the high tolerance against water in the liquid-phase hydrogenation reaction.

Table 4 Catalytic activity of this research compared to other literatures.

Catalysts	**Condition**	**Furfural conversion (%)**	**furfuryl alcohol yield (%)**	**TOF (s^{-1})**	**Ref.**
$CuAl_2O_4$	170 °C; 1 h; 1.5 M of furfural; 30 bars H_2; 0.5 g catalysts; 2-propanol solvent	100	>95	93.0	This work
$CuAl_2O_4$	170 °C; 5 h; 1.5 M of furfural; 20 bars H_2; 0.5 g catalysts; 10 %v/v water content in 2-propanol solvent	99	94	18.4	This work
35wt%CuO/ Al_2O_3	170 °C; 1 h; 1.5 M of furfural; 30 bars H_2; 0.5 g catalysts; 2-propanol solvent	98	89	66.1	This work
15wt%Cu/SBA-15	170 °C; 5 h; 0.1875 ml/h of furfural; 10 ml/min of H_2; 0.15 g catalyst; 5 vol.% cyclopentyl methyl ether solvent	54	Selectivity 95	0.002	(Vargas-Hernández *et al.*, 2014)

Pt/TiO$_2$/SiO$_2$	150 ^oC; 1 atm; HLSV 2 g/gcat h; H$_2$/furfural 2 mol/mol	68	Selectivity 94	-	(Jacek Kije´Nski A and Andrzej Lewicki B, 2002)
Cu–Fe	220 ^oC; 14 h; 2.0mL of furfural; 90 bars H$_2$; 0.2 g catalyst; 5 mL octane solvent	99	51	-	(Yan and Chen, 2014)
16wt.%Cu–MgO	180 ^oC; 1 atm H$_2$; 2.5 molar ratio H$_2$/furfural; furfural feed rate of 1.2 mlh^{-1}; GHSV 0.05 molh^{-1}gca^{-1}	98	Selectivity 98	0.005	(Nagaraja *et al.*, 2007)
10%Cu/SiO$_2$	230 ^oC; 1 atm H$_2$; 25 H$_2$/Feed ratio; 15 min; 41.3 gcat/furfural (mol/h)	69	Selectivity 98	1.3	(Sitthisa and Resasco, 2011)
1%Pd/SiO$_2$		69	Selectivity 14	265.8	
5%Ni/SiO$_2$		72	Selectivity 25	76.5	

In addition, the CuAl$_2$O$_4$ catalysts were found to be rapidly deactivated by coke deposition which could be regenerated by burning off at high temperature (Qin *et al.*). In order to reduce the production cost in large-scale, the CuAl$_2$O$_4$ catalyst stability and reusability was investigated in the hydrogenation of furfural. In **Fig. 10**, after 3rd cycle, the furfural conversion were almost similar to fresh catalyst while furfuryl yield was dropped approximately 25 % due to the coke deposition on the catalyst surface (from the element analysis, the carbon content was lower than 5 wt. %). However, after regeneration by calcination at 900 ^oC for 4 h, the catalytic performance was comparable to the fresh form (furfural conversion of 97.1 % and furfuryl alcohol yield of 91.6 %). The DFT calculations on the two catalytic systems including Cu/CuAl$_2$O$_4$ and Cu/γ-Al$_2$O$_3$ are carried out, and discussed in the next section.

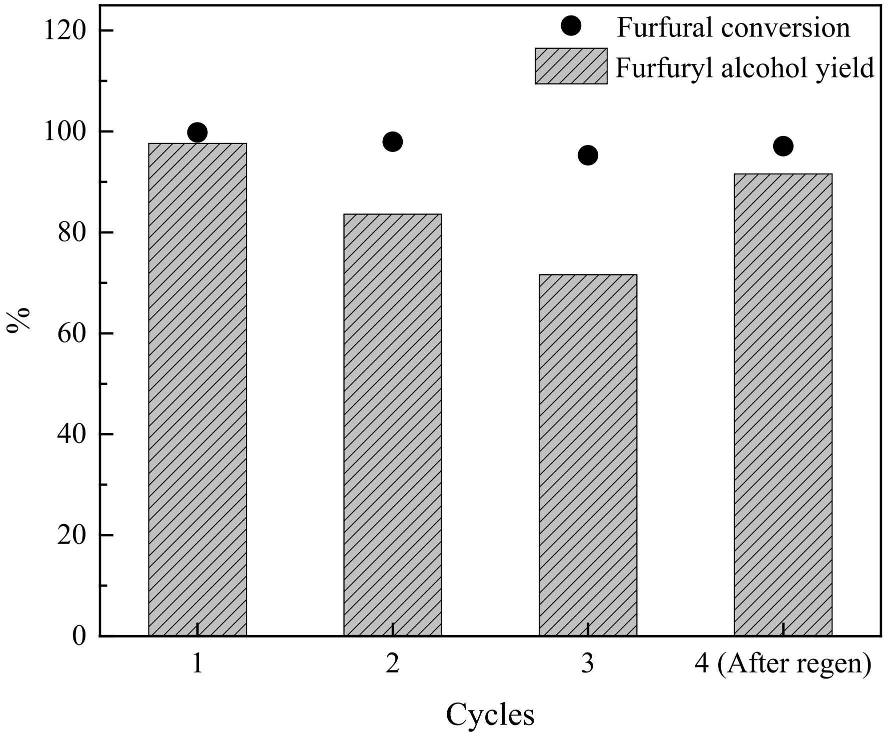

Fig. 10 Stability and reusability of $CuAl_2O_4$ catalyst in furfural conversion to furfuryl alcohol. Reaction conditions: catalyst weight, 0.5 g; furfural solution, 1.5 M; H_2 pressure, 20 bar; reaction temperature, 170 °C; reaction time, 1 h.

- *Furfural, furfuryl alcohol, hydrogen adsorption and furfural hydrogenation reaction mechanism*

In this section, DFT calculations were performed to investigate catalytic active sites, interaction between key species and catalyst surfaces, and furfural hydrogenation mechanisms on $Cu_{13}/CuAl_2O_4$ (311) and $Cu_{13}/\gamma\text{-}Al_2O_3$ (110) catalysts in order to obtain physical insight into different catalytic reactivity observed experimentally. The adsorption energy can be used as a preliminary probe of interaction strength between adsorbates and surfaces. The adsorption energy (E_{ad}) was calculated by

$$E_{ad} = E_{total} - E_{clean\,surface} - E_{adsorbate(isolated)} \qquad (5)$$

where E_{total} is the energy of the adsorption structure, $E_{clean\,surface}$ is the energy of the clean surface structure, and $E_{adsorbate(isolated)}$ is the energy of isolated adsorbate molecule. The more negative value of E_{ad} indicates the stronger adsorption. Furfural and furfuryl alcohol adsorption were initially located at three sites; (i) at Cu site (ii) at Al site and (iii) at the interface Cu-Al site. H_2 and 2H dissociative adsorption was also investigated at three sites of (i) Cu site (ii) at O site and (iii) at the interface Cu-O site. Here, we report only the most stable adsorption structures which are shown in **Fig. S3** and **S4** in supporting information and the adsorption energies are summarized in **Table 5**.

Table 5 The most stable adsorption energies, energy barriers and reaction free energies

	$Cu_{13}/CuAl_2O_4(311)$	$Cu_{13}/\gamma\text{-}Al_2O_3(110)$
Charges (e^-)		
Cu_{13}	-0.19	+0.27
Adsorption energy, E_{ad} (eV)		
Furfural	-3.26	-1.93
Furfuryl alcohol	-2.64	-1.92
H_2 molecule	-0.64 (at O site)	-0.38 (at Cu site)
Dissociative H atoms	-1.80 (at O site)	-1.04 (at Cu site)
Energy barriers (eV)		
H_2 dissociation	0.20	0.26
1st H addition	0.53	0.47
2nd H addition	0.58	1.02
Reaction free energies (eV)		
H_2 dissociation	-0.64 (at O site)	-0.66 (at Cu site)
Hydrogenation of furfural to furfuryl alcohol	-3.40	-2.47

(a) furfural adsorption (b) furfuryl alcohol adsorption

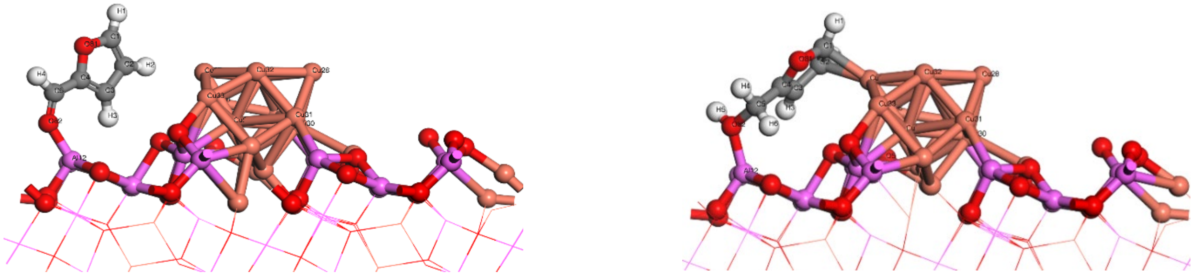

(c) molecular H_2 adsorption (d) dissociative 2H atoms adsorption

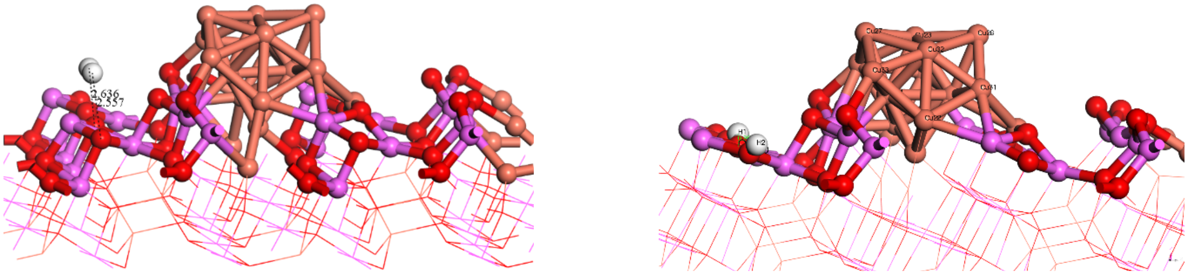

Fig. S3. Most stable adsorption structures of (a) furfural, (b) furfuryl alcohol, (c) H_2, and (d) dissociative 2H atoms on $Cu_{13}/CuAl_2O_4(311)$ surface.

(a) furfural adsorption (b) furfuryl alcohol adsorption

(c) molecular H_2 adsorption (d) dissociative 2H atoms adsorption

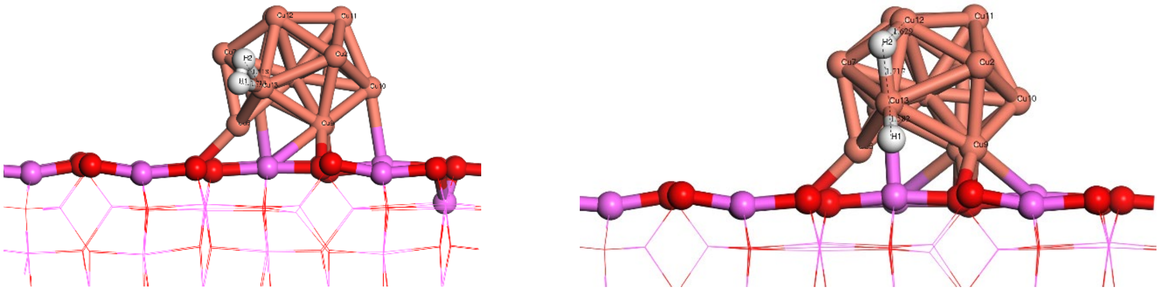

Fig. S4. Most stable adsorption structures of (a) furfural, (b) furfuryl alcohol, (c) H_2, and (d) dissociative 2H atoms on $Cu_{13}/\gamma\text{-}Al_2O_3(110)$ surface.

$Cu_{13}/CuAl_2O_4$ (311) adsorbs furfural, furfuryl alcohol, H_2, and dissociative 2H significantly stronger than Cu_{13}/γ-Al_2O_3 (110) catalyst. Oxygen of furfural and furfuryl alcohol bind to both catalysts at Al site adjacent to Cu cluster where their carbon atoms also interact with Cu cluster (see **Figure S3-S4** in supporting information). Therefore, the interface site between Al site of support and Cu cluster is important for furfural hydrogenation. Furthermore, the atomic partial charge from a Bader analysis of the Cu atom that involved in furfural and furfuryl alcohol adsorption on $Cu_{13}/CuAl_2O_4$ and on Cu_{13}/γ-Al_2O_3 are +0.06 and -0.05, respectively. This indicates the different Cu oxidation state at the active site on the two catalysts. Thus, the calculation results add support that the active Cu site on $Cu_{13}/CuAl_2O_4$ could be at the higher oxidation state than that on Cu_{13}/γ-Al_2O_3. We note that the charge associated with the Cu atom is delocalized from the Cu center, and so the Bader charge on Cu can only provide the relative and not the absolute value of the Cu charge state as Cu^0, Cu^{+1} or Cu^{2+} (Henkelman and Jónsson, 1999; Henkelman *et al.*, 2006; Sanville *et al.*, 2007; Tang *et al.*, 2009b; Han *et al.*, 2018). Interestingly, the favorable sites for H_2 dissociation are different, yet the energy barriers of H_2 dissociation on both catalysts are comparable (see **Table 5**). The Cu_{13} cluster acts as an active site for H_2 dissociation on Cu_{13}/γ-Al_2O_3 (110) while O sites are the active sites for H_2 dissociation on $Cu_{13}/CuAl_2O_4$ (311). The larger amount of H_2 desorption observed in the experiment (see **Table 1**) on $CuAl_2O_4$ could be ascribed to the higher amount of O sites on $CuAl_2O_4$ for H_2 adsorption and H_2 dissociation compared to amount of Cu sites on Cu/γ-Al_2O_3. The amount of H_2 on Cu_{13}/γ-Al_2O_3 (110) catalyst may be more dependent on Cu cluster dispersion due to Cu is the active site for H_2 adsorption and dissociation. In addition, Bader charge analysis shows the distinct characteristic of the supported Cu_{13} cluster that it loses electrons to γ-Al_2O_3 support whereas it gains electron from $CuAl_2O_4$ (see **Table 5**).

Table 5. Bader charge analysis of supported Cu_{13} cluster on $Cu_{13}/CuAl_2O_4$ (311) and Cu_{13}/γ-Al_2O_3 (110), the most stable adsorption energies of furfural, furfuryl alcohol, H_2 molecule and 2H atoms upon H_2 dissociation, energy barriers and reaction free energies of H_2 dissociation and the most favorable furfural hydrogenation pathways on $Cu_{13}/CuAl_2O_4$ (311) and Cu_{13}/γ-Al_2O_3(110). The corresponding adsorption structures and transition state structures are shown in **Fig. S3-S5** in supplementary information.

(a) 1st H addition step (TS1)

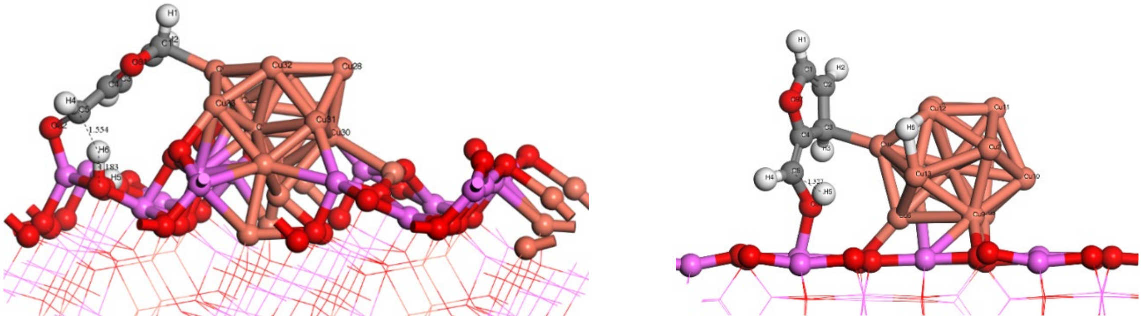

Cu$_{13}$/CuAl$_2$O$_4$(311) Cu$_{13}$/γ-Al$_2$O$_3$(110)

(b) 2nd H addition (TS2)

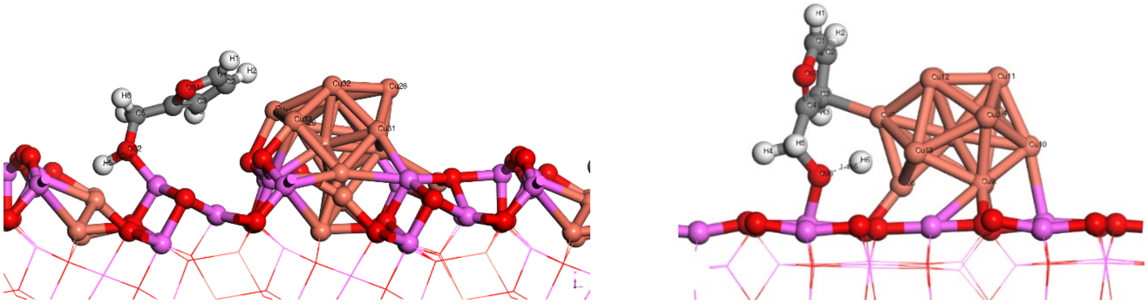

Cu$_{13}$/CuAl$_2$O$_4$(311) Cu$_{13}$/γ-Al$_2$O$_3$(110)

Fig. S5. Transition states structures of (a) 1st H addition step (TS1) and (b) 2nd H addition step (TS2) on Cu$_{13}$/CuAl$_2$O$_4$(311) and Cu$_{13}$/γ-Al$_2$O$_3$(110) surfaces.

Furfural hydrogenation to furfuryl alcohol reaction mechanism was investigated using DFT calculations to determine reaction free energies and energy barriers on Cu$_{13}$/CuAl$_2$O$_4$ (311) and Cu$_{13}$/γ-Al$_2$O$_3$ (110). Furfural molecule and dissociative H$_2$ firstly adsorbs on catalyst surface, then two hydrogen atom addition steps are required. The two H addition steps occur at carbon atom and O atom as illustrated in **Figure 11a**. The free energy diagrams of the most favorable pathway on the catalysts are shown in **Figure 11b**. The first H addition is favorable to occur at carbon atom on Cu$_{13}$/CuAl$_2$O$_4$ (311), however it is favorable to take place at O atom on Cu$_{13}$/γ-Al$_2$O$_3$ (110). The reaction free energies are -3.40 and -2.47 eV and the highest energy barriers are 0.58 and 1.02 eV on Cu$_{13}$/CuAl$_2$O$_4$(311) and Cu$_{13}$/γ-Al$_2$O$_3$(110), respectively (see **Table 5**). Thus, furfural hydrogenation is more thermodynamically and kinetically favorable on Cu$_{13}$/CuAl$_2$O$_4$ (311) surface. All in all, the DFT results suggest that catalytic activity increase of furfural hydrogenation on Cu/CuAl$_2$O$_4$ compared to Cu/Al$_2$O$_3$ catalysts could significantly be contributed by the factors of (i) the stronger interaction with furfural, furfuryl alcohol, (ii) the higher amount of active sites for H$_2$ dissociation and (iii) the lower reaction free energy and energy barriers for hydrogenation.

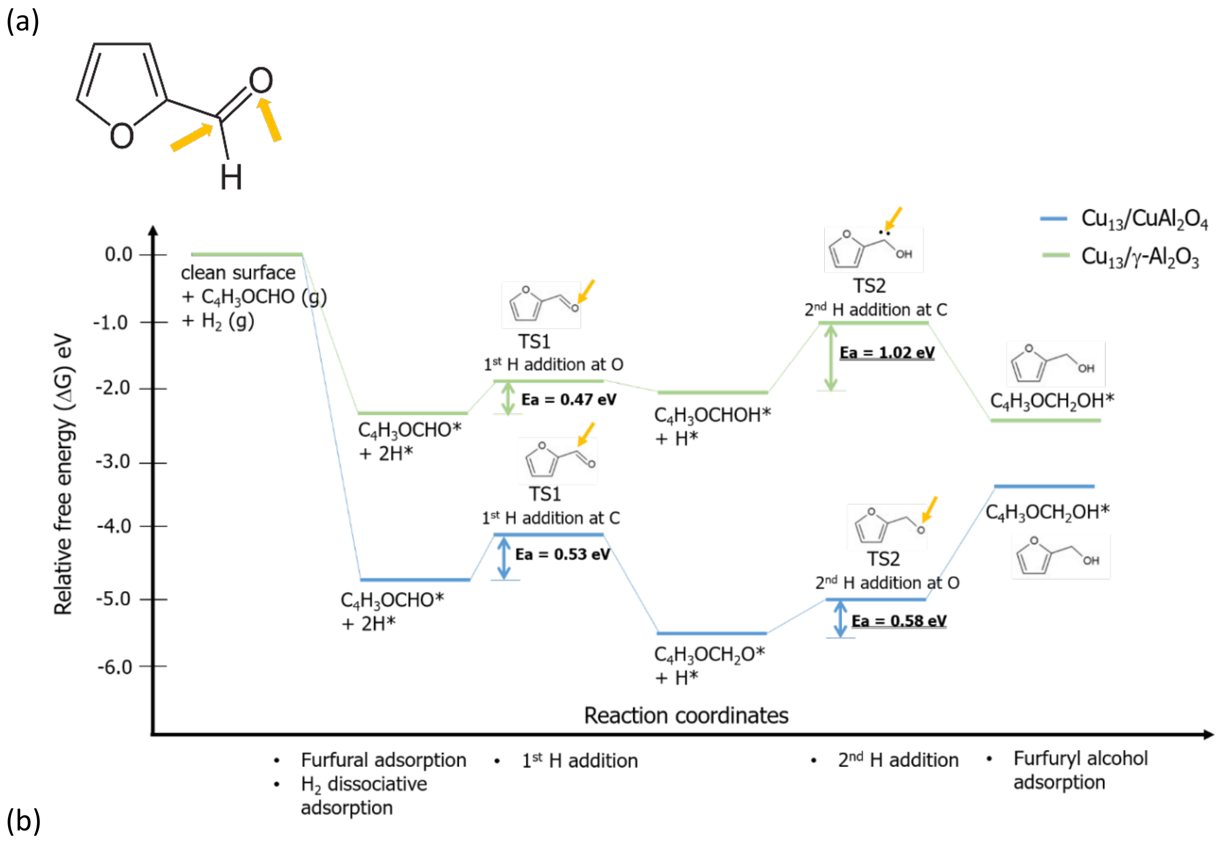

Fig. 11 Illustration of (a) H addition location at C atom and at O atom of furfural and (b) free energy diagrams of furfural hydrogenation to furfuryl alcohol on $Cu_{13}/CuAl_2O_4(311)$ (blue line) and $Cu_{13}/\gamma\text{-}Al_2O_3(110)$ (green line). The corresponding transition state structures (TS1 and TS2 are shown in **Fig. S5** in supporting information).

Conclusions

In this work, the spinel $CuAl_2O_4$ was proposed as a catalyst for liquid-phase hydrogenation of furfural to furfuryl alcohol. Compared to the impregnated Cu/Al_2O_3 and reported non-noble metal catalysts, the $CuAl_2O_4$ showed excellent performance in term of conversion, yield, selectivity and stability. The reaction temperature, time, and H_2 initial pressure strongly affected the conversion and yield of the product. The yield could be maximized at 98-99% over $CuAl_2O_4$. The spinel structure and high hydrogen uptake of $CuAl_2O_4$ correlated well with the high catalytic performance. DFT calculations revealed that that the spinel catalyst would give active sites for H_2 dissociation and stronger interaction with furfural/furfuryl alcohol. As a result, the lower reaction free energy and energy barriers were found on the hydrogenation over the spinel system.

Acknowledgements

We would like to thank computational resources from NSTDA Supercomputer Center (ThaiSC) and National Nanotechnology Center (NANOTEC). The financial support from the Thailand Research Fund (TRF), the NANOTEC, and the Synchrotron Light Research Institute (SLRI), Thailand (BRG6080015) is also acknowledged. Parts of the results are from a joint project with PTT Global Chemical Public Company Limited under the technical guidance of Dr.Wikanda Techanan and Dr. Papapida Pornsuriyasak.

References

ALLEN, G.; BERNSTEIN, H. Internal rotation: VIII. The infrared and raman spectra of furfural. **Canadian Journal of Chemistry,** v. 33, n. 6, p. 1055-1061, 1955. ISSN 0008-4042.

ALONSO-FAGúNDEZ, N. et al. Gas phase oxidation of furfural to maleic anhydride on V2O5/γ-Al2O3 catalysts: reaction conditions to slow down the deactivation. **Journal of Catalysis,** v. 348, p. 265-275, 2017. ISSN 0021-9517.

BAHMANPOUR, A. M. et al. Cu–Al Spinel as a Highly Active and Stable Catalyst for the Reverse Water Gas Shift Reaction. **ACS Catalysis,** v. 9, n. 7, p. 6243-6251, 2019. ISSN 2155-5435, 2155-5435.

BLöCHL, P. E. Projector Augmented-Wave Method. **Physical Review B,** v. 50, n. 24, p. 17953-17979, 1994.

CHEN, S.; CHEN, X.; ZHANG, H. Probing the activity of Ni13, Cu13, and Ni12Cu clusters towards the ammonia decomposition reaction by density functional theory. **Journal of Materials Science,** v. 52, n. 6, p. 3162-3168, March 01 2017. ISSN 1573-4803.

CHEN, X. et al. Highly selective hydrogenation of furfural to furfuryl alcohol over Pt nanoparticles supported on g-C3N4 nanosheets catalysts in water. **Sci Rep,** v. 6, p. 28558, Jun 22 2016.

CHIANG, C.-L.; LIN, K.-S. Preparation and characterization of CuO Al 2 O 3 catalyst for dimethyl ether production via methanol dehydration. **International Journal of Hydrogen Energy,** v. 42, n. 37, p. 23526-23538, 2017.

CHOU, J. P. et al. 13-atom metallic clusters studied by density functional theory: Dependence on exchange-correlation approximations and pseudopotentials. **Physical Review B,** v. 80, n. 16, p. 165412, 10/16/ 2009.

CHUNJIE HUANG, S. C., XIAOYAO FEI, DAI LIU AND YONGCHUN ZHANG. <Catalytic_Hydrogenation_of_CO2_to_Methanol_Study_o.pdf>. **Catalysts,** v. 5, p. 1846-1861, 2015.

DENG, Y. et al. Solvent tunes the selectivity of hydrogenation reaction over α-MoC catalyst. **Journal of the American Chemical Society,** v. 140, n. 43, p. 14481-14489, 2018. ISSN 0002-7863.

DESSAL, C. et al. Atmosphere-dependent stability and mobility of catalytic Pt single atoms and clusters on γ-Al2O3. **Nanoscale,** v. 11, n. 14, p. 6897-6904, 2019. ISSN 2040-3364.

DIGNE, M. et al. Use of DFT to achieve a rational understanding of acid–basic properties of γ-alumina surfaces. **Journal of Catalysis,** v. 226, n. 1, p. 54-68, 2004. ISSN 0021-9517.

FU, C. L.; HO, K. M. First-principles calculation of the equilibrium ground-state properties of transition metals: Applications to Nb and Mo. **Physical Review B,** v. 28, n. 10, p. 5480-5486, 1983.

FULAJTáROVA, K. et al. Aqueous phase hydrogenation of furfural to furfuryl alcohol over Pd–Cu catalysts. **Applied Catalysis A: General,** v. 502, p. 78-85, 2015/08/05/ 2015.

GAO, B.; ZHANG, J.; YANG, J.-H. Bimetallic Cu-Ni/MCM-41 catalyst for efficiently selective transfer hydrogenation of furfural into furfural alcohol. **Molecular Catalysis,** v. 517, p. 112065, 2022.

GAO, H. A first principles investigation of the NO oxidation mechanism on Pt/γ-Al2O3. **RSC Advances,** v. 6, n. 105, p. 102914-102923, 2016.

GAO, X. et al. Bimetallic PtFe-Catalyzed Selective Hydrogenation of Furfural to Furfuryl Alcohol: Solvent Effect of Isopropanol and Hydrogen Activation. **ACS Sustainable Chemistry & Engineering,** v. 8, n. 33, p. 12722-12730, 2020. ISSN 2168-0485, 2168-0485.

GIORGIANNI, G. et al. Effect of the Solvent in Enhancing the Selectivity to Furan Derivatives in the Catalytic Hydrogenation of Furfural. **ACS Sustainable Chemistry & Engineering,** v. 6, n. 12, p. 16235-16247, 2018. ISSN 2168-0485, 2168-0485.

GóMEZ MILLáN, G.; SIXTA, H. Towards the green synthesis of furfuryl alcohol in a one-pot system from xylose: A review. **Catalysts,** v. 10, n. 10, p. 1101, 2020.

GRIMME, S. Semiempirical GGA-type density functional constructed with a long-range dispersion correction. **Journal of Computational Chemistry,** v. 27, n. 15, p. 1787-1799, 2006.

GRIMME, S. et al. A consistent and accurate ab initio parametrization of density functional dispersion correction (DFT-D) for the 94 elements H-Pu. **The Journal of Chemical Physics,** v. 132, n. 15, p. 154104, 2010.

HAJDUK, Š. et al. COx-free hydrogen production via decomposition of ammonia over Cu–Zn-based heterogeneous catalysts and their activity/stability. **Applied Catalysis B: Environmental,** v. 211, p. 57-67, 2017.

HAN, M. et al. Physical properties of MgAl 2 O 4 , CoAl 2 O 4 , NiAl 2 O 4 , CuAl 2 O 4 , and ZnAl 2 O 4 spinels synthesized by a solution combustion method. **Materials Chemistry and Physics,** v. 215, p. 251-258, 2018.

HENKELMAN, G.; ARNALDSSON, A.; JóNSSON, H. A fast and robust algorithm for Bader decomposition of charge density. **Computational Materials Science,** v. 36, n. 3, p. 354-360, 2006.

HENKELMAN, G.; JóNSSON, H. A dimer method for finding saddle points on high dimensional potential surfaces using only first derivatives. **The Journal of Chemical Physics,** v. 111, n. 15, p. 7010-7022, 1999/10/15 1999.

HEYDEN, A.; BELL, A. T.; KEIL, F. J. Efficient methods for finding transition states in chemical reactions: Comparison of improved dimer method and partitioned rational function optimization method. **The Journal of Chemical Physics,** v. 123, n. 22, p. 224101, 2005/12/08 2005.

HIRUNSIT, P. et al. Cooperative H2 Activation at Ag Cluster/θ-Al2O3(110) Dual Perimeter Sites: A Density Functional Theory Study. **The Journal of Physical Chemistry C,** v. 118, n. 15, p. 7996-8006, 2014/04/17 2014.

HU, C. Y.; SHIH, K.; LECKIE, J. O. Formation of copper aluminate spinel and cuprous aluminate delafossite to thermally stabilize simulated copper-laden sludge. **J Hazard Mater,** v. 181, n. 1-3, p. 399-404, Sep 15 2010.

HUANG, W. et al. Selective hydrogenation of furfural to furfuryl alcohol over catalysts prepared via sonochemistry. **Ultrason Sonochem,** v. 14, n. 1, p. 67-74, Jan 2007.

IVANIŠ, G. et al. Hydrogen solubility in bio-based furfural and furfuryl alcohol at elevated temperatures and pressures relevant for hydrodeoxygenation. **Fuel,** v. 290, p. 120021, 2021.

JACEK KIJE´NSKI A, PIOTR WINIAREK A, TADEUSZ PARYJCZAK B,; ANDRZEJ LEWICKI B, A. M. A. Platinum deposited on monolayer supports in selective hydrogenation of furfural to furfuryl alcohol. **Applied Catalysis A: General** v. 233 p. 171–182, 2002.

JIA, P. et al. Highly selective hydrogenation of furfural to cyclopentanone over a NiFe bimetallic catalyst in a methanol/water solution with a solvent effect. **ACS Sustainable Chemistry & Engineering,** v. 7, n. 18, p. 15221-15229, 2019.

JIMéNEZ-GóMEZ, C. P. et al. Promotion effect of Ce or Zn oxides for improving furfuryl alcohol yield in the furfural hydrogenation using inexpensive Cu-based catalysts. **Molecular Catalysis,** v. 455, p. 121-131, 2018.

JOSE´ A. RODRIGUEZ A;*, J. Y. K. A., JONATHAN C. HANSON A,MANUEL PE´REZ B,AND ANATOLY I. FRENKEL C. Reduction of CuO in H2: in situ time-resolved XRD studies. **Catalysis Letters** v. 85, p. 247-254, 2003.

KäSTNER, J.; SHERWOOD, P. Superlinearly converging dimer method for transition state search. **The Journal of Chemical Physics,** v. 128, n. 1, p. 014106, 2008/01/07 2008.

KRESSE, G.; FURTHMüLLER, J. Efficiency of Ab initio Total Energy Calculations for Metals and Semiconductors Using a Plane-Wave Basis Set. **Computational Materials Science,** v. 6, n. 1, p. 15-50, 1996a.

______. Efficient Iterative Schemes for Ab initio Total-Energy Calculations Using a Plane-Wave Basis Set. **Physical Review B,** v. 54, n. 16, p. 11169-11186, 1996b.

KRESSE, G.; JOUBERT, D. From Ultrasoft Pseudopotentials to the Projector Augmented-Wave Method. **Physical Review B,** v. 59, n. 3, p. 1758-1775, 1999.

KWAK, B. K. et al. Preparation and characterization of nanocrystalline CuAl2O4 spinel catalysts by sol–gel method for the hydrogenolysis of glycerol. **Catalysis Communications,** v. 24, p. 90-95, 2012/07/05/ 2012. ISSN 1566-7367.

LEE, C. B. T. L.; WU, T. Y. A review on solvent systems for furfural production from lignocellulosic biomass. **Renewable and Sustainable Energy Reviews,** v. 137, p. 110172, 2021.

LEE, J. et al. Cu2O (100) surface as an active site for catalytic furfural hydrogenation. **Applied Catalysis B: Environmental,** v. 282, p. 119576, 2021.

LI, T. T. et al. Enhanced catalytic CO oxidation by Cu13-mNim (m = 0, 1, 13) clusters at ambient temperatures with more active sites and distinct mechanistic pathways. **Applied Surface Science,** v. 479, p. 39-46, 2019/06/15/ 2019. ISSN 0169-4332.

LI, X. et al. The Support Effects on the Direct Conversion of Syngas to Higher Alcohol Synthesis over Copper-Based Catalysts. **Catalysts,** v. 9, n. 2, 2019.

LIU, B.; ZHANG, Z. Catalytic conversion of biomass into chemicals and fuels over magnetic catalysts. **Acs Catalysis,** v. 6, n. 1, p. 326-338, 2016.

LUO, M.-F. et al. In situ XRD, Raman, and TPR studies of CuO/Al2O3 catalysts for CO oxidation. **Journal of Molecular Catalysis A: Chemical,** v. 239, n. 1-2, p. 243-248, 2005.

MONGKOLCHANOK PRAMOTTANA, P. P. A. B. N. Copper Chromite Catalyst for the Selective Hydrogenation of Furfural to Furfuryl Alcohol **J. Chin. Inst. Chem. Engrs.,,** v. 33, n. 5, p. 477-481, 2002.

MONKHORST, H. J.; PACK, J. D. Special points for Brillouin-zone integrations. **Phys. Rev. B,** v. 13, n. 12, p. 5188-5192, 1976.

NAGARAJA, B. M. et al. Vapor phase selective hydrogenation of furfural to furfuryl alcohol over Cu–MgO coprecipitated catalysts. **Journal of Molecular Catalysis A: Chemical,** v. 265, n. 1-2, p. 90-97, 2007.

NAGARAJA, B. M. et al. A highly efficient Cu/MgO catalyst for vapour phase hydrogenation of furfural to furfuryl alcohol. **Catalysis Communications,** v. 4, n. 6, p. 287-293, 2003/06/01/ 2003.

NORTIER, P. et al. Effects of crystallinity and morphology on the surface properties ofalumina. **Applied Catalysis,** v. 61, n. 1, p. 141-160, 1990.

OUYANG, M. et al. Organogelator based on long alkyl chain attached excimer precursor: Two channels of TICT, highly efficient and switchable luminescence. **Dyes and Pigments,** v. 180, p. 108433, 2020.

PANTALEO, G. et al. Support effect on the structure and CO oxidation activity of Cu-Cr mixed oxides over Al2O3 and SiO2. **Materials Chemistry and Physics,** v. 114, n. 2-3, p. 604-611, 2009.

PERDEW, J. P.; BURKE, K.; ERNZERHOF, M. Generalized Gradient Approximation Made Simple. **Physical Review Letters,** v. 77, n. 18, p. 3865-3868, 1996.

PIOTROWSKI, M. J.; PIQUINI, P.; DA SILVA, J. L. F. Density functional theory investigation of 3d, 4d, and 5d 13-atom metal clusters. **Physical Review B,** v. 81, n. 15, p. 155446, 04/22/ 2010.

PONMUDI, S. et al. Facile fabrication of spinel structured n-type CuAl2O4 thin film with nano-grass like morphology by sputtering technique. **Applied Surface Science,** v. 483, p. 601-615, 2019.

PUDI, S. M. et al. Selective Hydrogenolysis of Glycerol to 1,2-Propanediol Over Bimetallic Cu-Ni Catalysts Supported on γ-Al2O3. **Journal of the Brazilian Chemical Society**, 2015.

QIN, F.-J. et al. Cu-Al spinel as a sustained release catalyst for H 2 production from methanol steam reforming: Effects of different copper sources. **Journal of Fuel Chemistry and Technology,** v. 45, n. 12, p. 1481-1488, 2017.

RAMIREZ-BARRIA, C. et al. Optimization of ruthenium based catalysts for the aqueous phase hydrogenation of furfural to furfuryl alcohol. **Applied Catalysis A: General,** v. 563, p. 177-184, 2018.

SALAVATI-NIASARI, M.; DAVAR, F.; FARHADI, M. Synthesis and characterization of spinel-type CuAl2O4 nanocrystalline by modified sol–gel method. **Journal of Sol-Gel Science and Technology,** v. 51, n. 1, p. 48-52, 2009. 1573-4846.

SALNIKOVA, K. et al. The liquid phase catalytic hydrogenation of the furfural to furfuryl alcohol. **Chemical Engineering Transactions,** v. 70, p. 379-384, 2018.

SANVILLE, E. et al. Improved grid-based algorithm for Bader charge allocation. **Journal of Computational Chemistry,** v. 28, n. 5, p. 899-908, 2007.

SCHUDDEBOOM, W. et al. Excited-state dipole moments of dual fluorescent 4-(dialkylamino) benzonitriles: influence of alkyl chain length and effective solvent polarity. **The Journal of Physical Chemistry,** v. 96, n. 26, p. 10809-10819, 1992.

SHEPPARD, D.; HENKELMAN, G. Paths to which the nudged elastic band converges. **Journal of Computational Chemistry,** v. 32, n. 8, p. 1769-1771, 2011/06/01 2011.

SHEPPARD, D.; TERRELL, R.; HENKELMAN, G. Optimization methods for finding minimum energy paths. **The Journal of Chemical Physics,** v. 128, n. 13, p. 134106, 2008/04/07 2008.

SHEPPARD, D. et al. A generalized solid-state nudged elastic band method. **The Journal of Chemical Physics,** v. 136, n. 7, p. 074103, 2012/02/21 2012.

SIERRA, J. C. Solvent effects based on pure solvent scales. Handbook of solvents, 2001, ChemTec Publishing. p.583-616.

SINGH, G. et al. Catalytic hydrogenation of furfural to furfuryl alcohol over chromium-free catalyst: Enhanced selectivity in the presence of solvent. **Molecular Catalysis,** v. 500, p. 111339, 2021.

SITTHISA, S.; RESASCO, D. E. Hydrodeoxygenation of Furfural Over Supported Metal Catalysts: A Comparative Study of Cu, Pd and Ni. **Catalysis Letters,** v. 141, n. 6, p. 784-791, 2011.

SITTHISA, S. et al. Kinetics and mechanism of hydrogenation of furfural on Cu/SiO2 catalysts. **Journal of catalysis,** v. 277, n. 1, p. 1-13, 2011.

SRIVASTAVA, S. et al. Cr-free Co–Cu/SBA-15 catalysts for hydrogenation of biomass-derived α-, β-unsaturated aldehyde to alcohol. **Chinese Journal of Catalysis,** v. 36, n. 7, p. 933-942, 2015.

TANG, W.; SANVILLE, E.; HENKELMAN, G. A grid-based Bader analysis algorithm without lattice bias. **Journal of Physics: Condensed Matter,** v. 21, n. 8, p. 084204, 2009a.

______. A grid-based Bader analysis algorithm without lattice bias. **J Phys Condens Matter,** v. 21, n. 8, p. 084204, Feb 25 2009b.

TANG, X. et al. Conversion of biomass to γ-valerolactone by catalytic transfer hydrogenation of ethyl levulinate over metal hydroxides. **Applied Catalysis B: Environmental,** v. 147, p. 827-834, 2014.

THONGRATKAEW, S. et al. Cu-Al spinel-oxide catalysts for selective hydrogenation of furfural to furfuryl alcohol. **Catalysis Today,** v. 367, p. 177-188, 2021.

TOLEK, W. et al. Flame spray-synthesized Pt-Co/TiO2 catalysts for the selective hydrogenation of furfural to furfuryl alcohol. **Catalysis Communications,** v. 149, p. 106246, 2021.

TONG, Z. et al. Adsorption configuration-determined selective hydrogenative ring opening and ring rearrangement of furfural over metal phosphate. **ACS Catalysis,** v. 11, n. 11, p. 6406-6415, 2021.

VAN DER WAAL, J. et al. Zeolite titanium beta: A selective catalyst for the gas-phase Meerwein–Ponndorf–Verley, and Oppenauer reactions. **Journal of Catalysis,** v. 173, n. 1, p. 74-83, 1998.

VARGAS-HERNáNDEZ, D. et al. Furfuryl alcohol from furfural hydrogenation over copper supported on SBA-15 silica catalysts. **Journal of Molecular Catalysis A: Chemical,** v. 383-384, p. 106-113, 2014.

VILLAVERDE, M. M. et al. Selective liquid-phase hydrogenation of furfural to furfuryl alcohol over Cu-based catalysts. **Catalysis today,** v. 213, p. 87-92, 2013.

VILLAVERDE, M. M.; GARETTO, T. F.; MARCHI, A. J. Liquid-phase transfer hydrogenation of furfural to furfuryl alcohol on Cu–Mg–Al catalysts. **Catalysis Communications,** v. 58, p. 6-10, 2015.

WANG, Z. et al. Selective hydrogenation of furfural to furfuryl alcohol over Pd/TiH2 catalyst. **Molecular Catalysis,** v. 508, p. 111599, 2021.

WEERACHAWANASAK, P. et al. Development of bimetallic Ni-Cu/SiO2 catalysts for liquid phase selective hydrogenation of furfural to furfuryl alcohol. **Catalysis Communications,** v. 149, p. 106221, 2021.

XIAO, P. et al. Solid-state dimer method for calculating solid-solid phase transitions. **The Journal of Chemical Physics,** v. 140, n. 17, p. 174104, 2014/05/07 2014.

XU, Y. et al. Mechanism and kinetics of catalytic ozonation for elimination of organic compounds with spinel-type CuAl2O4 and its precursor. **Sci Total Environ,** v. 651, n. Pt 2, p. 2585-2596, Feb 15 2019.

YAN, K.; CHEN, A. Selective hydrogenation of furfural and levulinic acid to biofuels on the ecofriendly Cu–Fe catalyst. **Fuel,** v. 115, p. 101-108, 2014.

YAN, K. et al. A noble-metal free Cu-catalyst derived from hydrotalcite for highly efficient hydrogenation of biomass-derived furfural and levulinic acid. **RSC advances,** v. 3, n. 12, p. 3853-3856, 2013.

YAN, K. et al. Production, properties and catalytic hydrogenation of furfural to fuel additives and value-added chemicals. **Renewable and Sustainable Energy Reviews,** v. 38, p. 663-676, 2014.

YU, M.; TRINKLE, D. R. Accurate and efficient algorithm for Bader charge integration. **The Journal of Chemical Physics,** v. 134, n. 6, p. 064111, 2011/02/14 2011.

ZENG, W. et al. Density functional theory (DFT) studies of CO oxidation reaction on M13 and Au18M clusters (M = Au, Ag, Cu, Pt and Pd): the role of co-adsorbed CO molecule. **RSC Advances,** v. 6, n. 61, p. 55867-55877, 2016.

ZHANG, J. et al. Selective transfer hydrogenation of furfural into furfuryl alcohol on Zr-containing catalysts using lower alcohols as hydrogen donors. **ACS omega,** v. 3, n. 6, p. 6206-6216, 2018.

ZHANG, J. et al. Electrospun CuAl 2 O 4 hollow nanofibers as visible light photocatalyst with enhanced activity and excellent stability under acid and alkali conditions. **CrystEngComm,** v. 20, n. 3, p. 312-322, 2018.

ZHANG, J.; WU, D. Aqueous phase catalytic hydrogenation of furfural to furfuryl alcohol over in-situ synthesized Cu–Zn/SiO2 catalysts. **Materials Chemistry and Physics,** v. 260, p. 124152, 2021.

ZHANG, L. et al. Effect of precursor and precipitant concentrations on the catalytic properties of CuO/ZnO/CeO2-ZrO2 for methanol steam reforming. **Journal of Fuel Chemistry and Technology,** v. 43, n. 11, p. 1366-1374, 2015.

3.4 Solvent Effects in Integrated Reaction-Separation Process of Liquid-Phase Hydrogenation of Furfural to Furfuryl Alcohol over $CuAl_2O_4$ Catalysts

Sutarat Thongratkaew[a], Sirapassorn Kiatphuengporn[a], Anchalee Jankaew[a], Sanchai Kuboon[a], Narong Chanlek[b], Anusorn Seubsai[c], Bunyarat Rungtaweevoranit[a] and Kajornsak Faungnawakij[a,*]

[a] *National Nanotechnology Center (NANOTEC), National Science and Technology Development Agency (NSTDA), Pathum Thani 12120, Thailand*
[b] *Synchrotron Light Research Institute, 111 University Avenue, Muang, Nakhon Ratchasima, 30000, Thailand*
[c] *Research Network of NANOTEC–KU on NanoCatalysts and NanoMaterials for Sustainable Energy and Environment, Kasetsart University, Bangkok 10900, Thailand*

ABSTRACT: Selective hydrogenation of furfural to furfuryl alcohol over $CuAl_2O_4$ catalysts is studied in a batch reactor using a range of solvents of varying chemical properties. We find that the reactions in branched alcohols provide higher furfuryl alcohol yields compared to linear alcohols. Besides, the reactions performed in nonane and decane provide excellent furfuryl alcohol yields of 96%. In situ FTIR analysis indicates that the carbonyl group of furfural is preferentially adsorbed leading to such high catalyst performance. Importantly, the efficient production of furfuryl alcohol in immiscible solvents minimizing downstream process is achieved in this integrative reaction-separation concept.

Introduction

Biomass has the potential to be a viable replacement for finite fossil fuels to manufacture a range of commodities and liquid fuels (Liu and Zhang, 2016). Among biomass-derived chemicals, furfural (FF) is listed as one of the most important platform chemicals which can be converted to several chemicals such as furfuryl alcohol (FFA), tetrahydrofurfuryl alcohol (THFA), 2-methyl furan (2-MF), tetrahydrofurfural (THFF) and 2-methyl tetrahydrofuran(2-MTHF) **(Scheme S1)** (Zhang and Wu, 2021). The synthetic versatility of FF stems from its structure which is composed of a carbonyl (C=O) fragment, a π-conjugated (C=C–C=C) moiety, and a five-membered ring structure enabling several chemical transformations. In this aspect, selective hydrogenation of the carbonyl moiety of furfural to furfuryl alcohol (FFA) is an important process that consumes more than 60% of the furfural produced to make fine chemicals, resins, lubricants, fragrances, dispersants, and plasticizers (Fulajtárova *et al.*, 2015; Deng *et al.*, 2018). Industrially, FFA is manufactured both in liquid and gas phases(Gómez Millán and Sixta, 2020). While the reactions in the gas phase generally provide FFA in good yields, the reactions in the liquid phase offer additional control by using the property of solvents to tune reaction performance.

Several metal catalysts such as Ru (Ramirez-Barria *et al.*, 2018), Pd (Salnikova *et al.*, 2018), and Pt (Chen *et al.*, 2016) have been reported as highly active catalysts while base metal catalysts Cu, Co, Ni, Zr, Mg, Fe, Ce, and Zn have also been documented to show hydrogenation activity toward FF (Villaverde *et al.*, 2015; Jiménez-Gómez *et al.*, 2018; Tolek *et al.*, 2021;

Weerachawanasak *et al.*, 2021). Particularly, Cu catalysts show good selectivity for the hydrogenation of the carbonyl group of the FF (Villaverde *et al.*, 2013). Depending on the local configuration of the Cu active sites in alcoholic solvents are commonly reported in the literature, the catalytic activity and selectivity can vary greatly (**Table S1**). We recently reported $CuAl_2O_4$ spinel as a low-cost and high-performance catalyst for FF hydrogenation to FFA using isopropanol and water as a solvent mixture obtaining FFA with a remarkable yield of 94%. However, the effects of solvents in such a catalytic system remain unknown which could drastically affect the reaction efficiency. Previous studies on the solvent effects of FF hydrogenation to FFA generally agree that higher hydrogen donating ability and polarity of the solvents promote FF conversions; and secondary alcohols such as 2-propanol have been concluded as the optimal solvent (Deng *et al.*, 2018; Zhang, Jun *et al.*, 2018; Jia *et al.*, 2019). However, the solvents studied are limited to some selected solvents prompting us to investigate the possibility of using other solvent systems to improve reaction efficacy (Lee and Wu, 2021).

Table S1. Examples of Cu-based catalysts for furfural hydrogenation.

Catalyst	**Solvent**	**Condition**			**Conversion (%)**	**Selectivity (%)**		**Ref.**
		T (°C)	**t (h)**	**P_{H2} (bar)**		**FA (%)**	**Others (%)**	
m-CuO	Isopropanol	180	5	20	37	79	21	(Lee *et al.*, 2021)
Cu-Cr	Octane	200	4	60	94	83	0.3	(Yan *et al.*, 2013)
15wt%Cu-15wt%Ni/ MCM-41	2-propanol	160	4		95	99	-	(Gao *et al.*, 2022)
2wt%Ni-5wt%Cu/SiO_2	Methanol	100	2	20	94	60	37	(Weerachawanasak *et al.*, 2021)
10wt%Co-10wt%Cu/SBA-15	Isopropanol	170	4	20	99	80	8	(Srivastava *et al.*, 2015)

Here, we comprehensively investigated the roles of solvents including protic solvents such as methanol, ethanol, 1-butanol, isopropanol, and 2-butanol; and aprotic solvents including pentane, hexanes, heptane, octane, nonane and decane for the hydrogenation of FF to FFA over $CuAl_2O_4$ spinel catalysts. Such an extensive list of solvents allowed us to correlate the properties of the solvents such as hydrogen donating ability and polarity with the FFA yields. For protic solvents, we found that the reactions in branched alcohols provide better FFA yields. In contrast to previous reports, excellent FFA yields of 96% were obtained when nonane and decane were used as solvents despite the low hydrogen solubility in these solvents. The immiscibility of the FFA product is immiscible in these solvents facilitating the easy and rapid isolation of FFA by a simple extraction and the solvents can be reused in this integrated reaction-separation approach. Additionally, insights on the high selectivity of FFA production have been studied by in situ FTIR analysis of adsorbed FF on the catalyst.

Experimental

- *Materials*

2-Propanol (99.5%), 2-butanol (99%), nonane (99%), decane (95%), isopropanol (≥99.5%), furfural (99%), furfuryl alcohol (98%), copper nitrate hemi(pentahydrate) (98%), aluminum nitrate nonahydrate (98%) and citric acid (99.5%) were obtained from Sigma-Aldrich. Hexanes (99%), methanol (99.99%), and pentane (97%) were purchased from Fisher chemicals. Heptane (99%) was obtained from Quick. Octane (98%) and 1-butanol (99.9%) were purchased from RCI Labscan. Ethanol (99.9%) was obtained from DUKSAN.

- *Catalyst Preparation*

$CuAl_2O_4$ was prepared by a sol-gel combustion method. Specifically, copper nitrate hemi(pentahydrate) (11.87 g) was dissolved in deionized water (100 mL) and stirred at 60 °C until completely dissolved. Then, aluminum nitrate nonahydrate (38.28 g) was introduced to the copper nitrate hemi(pentahydrate) solution and the solution was stirred at 60 °C for 2 h. After that, citric acid (44.35 g) was added to the solution and stirred at 60 °C for 1 h. The solution was then heated to 100 °C while stirring until all the water was evaporated resulting in a gel-like substance. The temperature was then increased to 300 °C to initiate the combustion process, yielding a fine black powder. Finally, the solid product was calcined for 4 h at 900 °C in the air (Thongratkaew *et al.*, 2021).

- *Catalysts Characterization*

The phase of the catalyst was investigated by powder X-ray diffraction (PXRD, Bruker D8 ADVANCE) using Cu Kα radiation operated at 40 kV and 40 mA. The data was collected using a step size of 0.02° in the 2θ range of 20°–80°. The temperature-programmed reduction was used to investigate the reducibility of catalysts (TPR, Dynamic Flow Chemisorption Quantachrome Instruments). In each TPR experiment, the catalyst (0.2 g) was pretreated in a He flows (30 mL/min) at 150 °C for 1 h with a ramp rate of 5 °C/min. The catalyst was cooled to 60 °C under He flow (30 mL/min). Finally, the catalyst was performed using a TPR setup. Finally, the H_2 temperature-programmed reduction (TPR) experiment was carried out using 10% H_2/Ar in the temperature range of 45–800 °C at a ramp rate of 5 °C/min. Thermogravimetric Analysis (TGA, METTLER TOLEDO) experiments on spent catalysts were carried out under airflow at temperatures from room temperature to 900 °C at 10 °C/min to analyze the extent of catalyst coking.

- *Catalysis test*

The Cu-based catalyst was tested for FF hydrogenation reaction in a stainless-steel batch reactor with a magnetic stirrer. The catalyst was activated immediately before each experiment by reducing it to 10% H_2/N_2 at 350 °C for 3 h. After the catalyst activation, 5 mL of FF in 25 mL of selected organic solvents and 0.5 g of the pre-reduced catalyst were added to the reactor. The reaction was carried out at 170 °C and an initial H_2 pressure of 20 bar. The autoclave was cooled to room temperature using an ice-water bath after the reaction. The liquid phase product was collected and the solid catalyst was removed by centrifugation. Then the liquid samples were analyzed by gas chromatography (GC-2010, Shimadzu) with a flame ionization detector using a capillary column (DB-WAX, Agilent Technologies). The FF conversion, FFA yields, and isolated yields are calculated using the following equations:

$$\text{Conversion (\%)} = \left(\frac{\text{moles of furfural consumed}}{\text{moles of furfural initially charged}}\right) \times 100\ \% \qquad (1)$$

$$\text{Yield (\%)} = \left(\frac{\text{moles of furfuryl alcohol produced}}{\text{theoretical moles of furfuryl alcohol}}\right) \times 100\ \% \qquad (2)$$

For the isolation of FFA, the catalysis was conducted using decane as a solvent. After the reaction, the solid catalyst was removed by centrifugation. The liquid phase containing FFA and decane layers was separated by a separatory funnel and the amount of FFA was determined by an analytical balance.

- *In situ infrared spectroscopy of furfural adsorbed on $CuAl_2O_4$ catalyst*

The adsorption of FF on the catalyst surface was investigated using a Nicolet iS50 infrared spectrometer (Thermo Scientific, Waltham, MA, USA) equipped with a mercury-cadmium-telluride (MCT) detector, a diffuse reflection attachment Praying Mantis^{TM} and a high-temperature reaction cell. The catalyst sample was reduced to 350 °C for 3 h in the reaction cell with 10% H_2/Ar (30 mL/min) and then cooled down to 30 °C. The cell was purged with Ar (30 mL/min) for 1 h to remove physisorbed H_2. Then, FF (40 µL) was added to the catalyst dropwise using a microsyringe and the time counter was started. The spectrum was recorded at 30–150 °C until all the physisorbed species were removed (Wang *et al.*, 2021).

Results and discussion

The textural and chemical property of the Cu-based catalysts.

The physical properties of the catalyst were studied by PXRD analysis (**Fig. 1(a)**). The fresh $CuAl_2O_4$ shows the diffraction peaks at 19.0°, 31.3°, 36.9°, 44.8°, 49.1°, 55.7°, 59.4°, 65.3°, 74.2°, 77.4°, and 78.5° which can be indexed to the cubic structure of the $CuAl_2O_4$ spinel phase (JCPDS 01-071-0966). After the reduction in H_2 at 350 °C, the peaks belonging to the $CuAl_2O_4$ spinel phase are broadened suggesting the reduction in crystallite size of the spinel phase. In addition, we observed the appearance of the peaks at 43.3°, 50.5°, and 74.2° (JCPDS 00-001-1242) which is attributed to the partial reduction of $CuAl_2O_4$ to Cu.

The H_2-TPR measurements were conducted to investigate the reduction characteristics of the catalyst **(Fig. 1(b)).** Three peaks were observed in the H_2-TPR profile: i) 260 –300 °C, ii) 500–600 °C and iii) 630–750 °C. The first reduction peak was assigned to the reduction of Cu^{2+} in the $CuAl_2O_4$ to metallic Cu on the catalyst surface (Kwak *et al.*, 2012). The peaks found at higher temperatures were attributed to the reduction of bulk CuO or metal oxide composite of $CuAl_2O_4$ (Bahmanpour *et al.*, 2019).

The electronic state of Cu species in the fresh and reduced $CuAl_2O_4$ was probed by X-ray photoelectron spectroscopy (XPS). **Fig. 1(c)** shows XPS spectra in the $Cu2p_{3/2}$ region of the fresh and reduced $CuAl_2O_4$ catalysts. In the fresh catalyst, the primary peak located at 933.5 eV was observed corresponding to Cu^{2+} species. The satellite peaks of Cu^{2+} species were also noticed at 943.0 eV further confirming the presence of Cu^{2+} in the fresh catalyst. In situ, XPS measurements after the reduction process at 350 °C indicate mixed-valence Cu including Cu^0 and Cu^{2+} as evidenced by peaks appearing at 932.8 and 933.5 eV, respectively (Zhang, Jian *et al.*, 2018; Xu *et al.*, 2019).

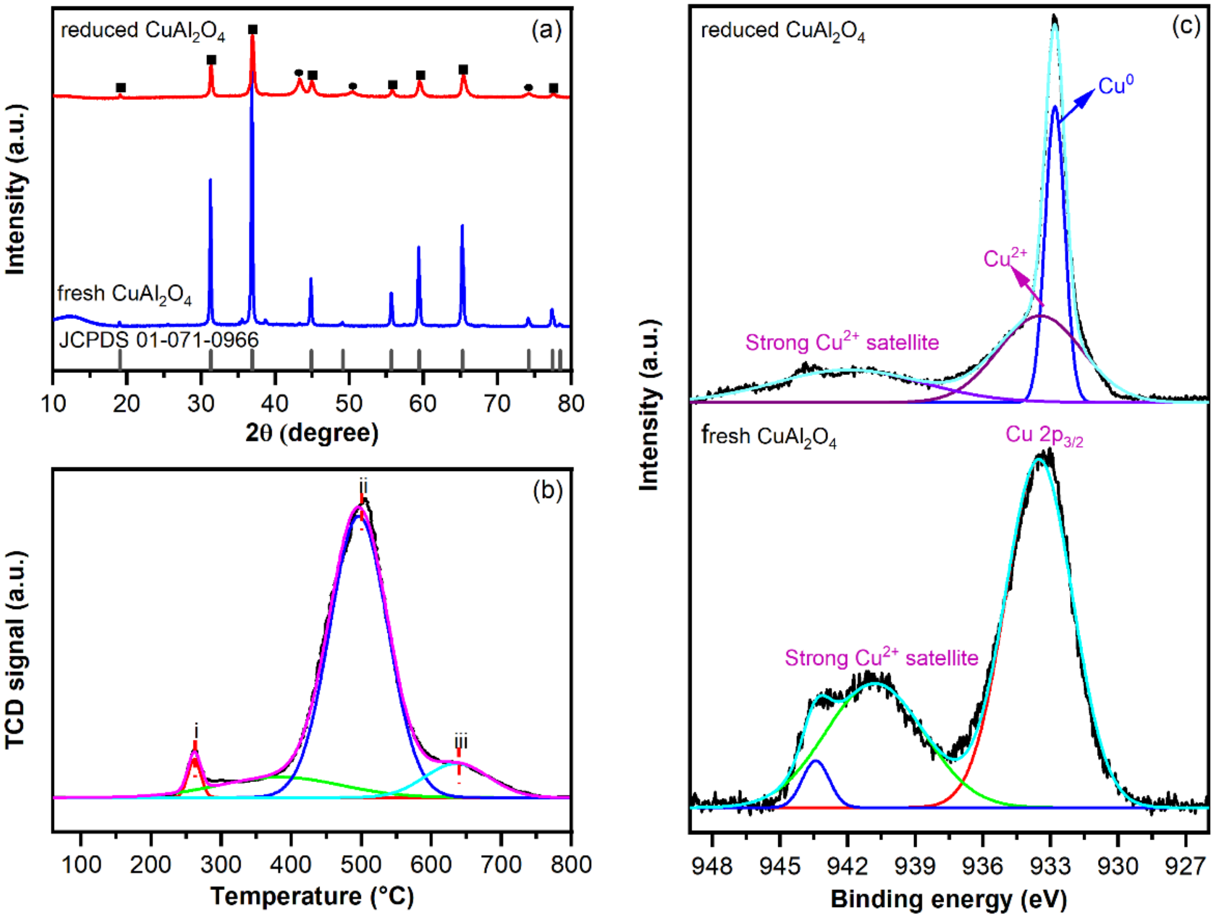

Fig. 1. (a) PXRD patterns of fresh and reduced $CuAl_2O_4$. ■ $CuAl_2O_4$ spinel ● Cu^0, (b) The H_2-TPR profile, and (C) XPS in the Cu $2p_{3/2}$ region of the $CuAl_2O_4$ catalyst before and after the in-situ reduction.

The catalytic activity of Cu-based catalysts in furfural hydrogenation

Next, we studied the effects of organic solvents for FF hydrogenation at 170 °C and 20 bar of H_2. We selected two classes of organic solvents including alcohols and alkanes to understand the effects of the hydrogen donor ability of alcohol and the effects of biphasic systems.

- *Effects of alcohol solvents*

Alcohol solvents are typically used in the hydrogenation of FF because of their ability to generate hydrogen in situ via the catalytic transfer hydrogenation route and the solubility of FF in alcohol solvents (Gao *et al.*, 2020; Singh *et al.*, 2021). We thus investigated such effects on the reduced $CuAl_2O_4$ catalyst by using a range of alcohol solvents including linear alcohols: methanol, ethanol, and 1-butanol; and branched alcohols: isopropanol and 2-butanol (**Fig. 2**). The highest FFA yield of 96% was obtained from the reaction using 2-butanol as a solvent followed by isopropanol (95%), ethanol (77%), 1-butanol (76%), and methanol (36%). To understand this trend, we first focus on the correlation with hydrogen donation ability. Such property has been reported to inversely correlate with the reduction potential of the alcohol ($\Delta_f H^\circ$) (Tang *et al.*, 2014). The reduction potential of alcohols increases in the order of: methanol (130.1 kJ/mol) >> ethanol (85.4 kJ/mol) > 1-butanol (79.7 kJ/mol) > isopropanol (70.0 kJ/mol) ≈ 2-butanol (69.3 kJ/mol) (Van Der Waal *et al.*, 1998; Tang *et al.*, 2014). Such a trend on the hydrogen donation property of alcohols is remarkably close to the FFA yields observed. Another factor that could affect the FFA yield is the solvent polarity which could be mapped with the π* value. The plot between FFA yields and π* values does not display any correlation (**Fig. S1**) suggesting that polarity is not the main factor in this catalytic system.

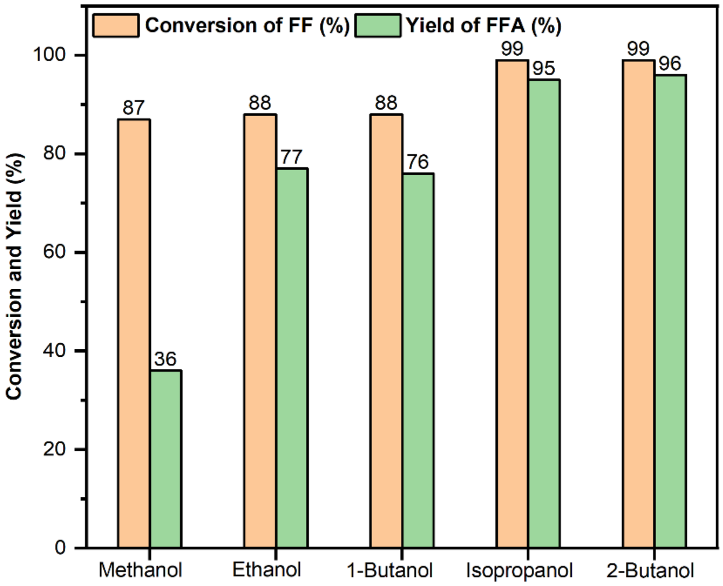

Fig. 2. Effects of alcohol solvents on FF hydrogenation over the reduced $CuAl_2O_4$ catalyst. Reaction conditions: 0.5 g of reduced $CuAl_2O_4$, 2 mL of FF, 25 mL of solvent, 170 °C, 20 bar H_2, and 5 h.

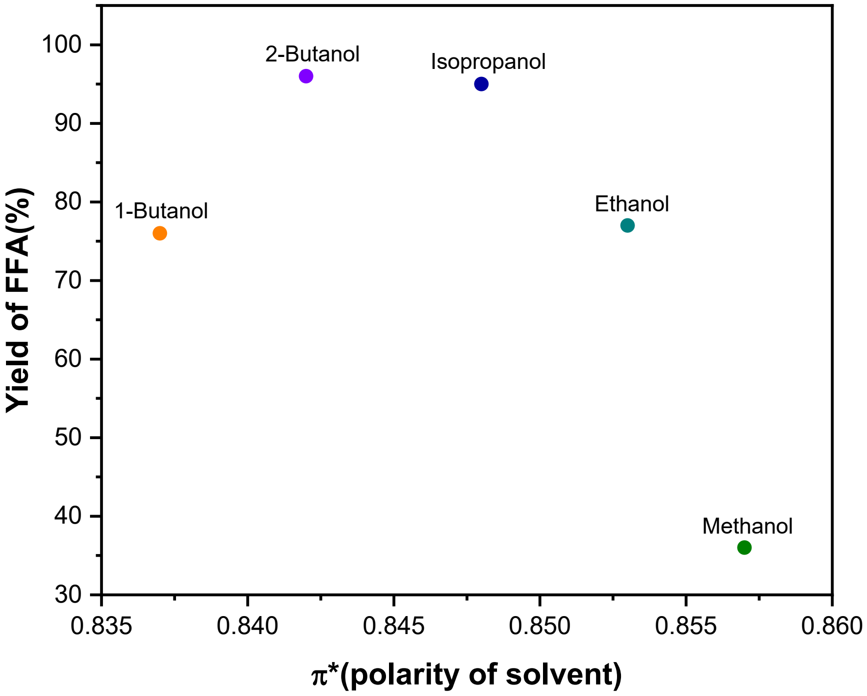

Fig. S1. The plot between FFA yields and π* values

- *Effects of alkane solvents*

Alkane solvents have not been widely used in the hydrogenation of FF which is likely due to the limited solubility of H_2 and FF in these solvents. Despite this, we previously found that the reduced $CuAl_2O_4$ catalyst has excellent H_2 sorption ability which could overcome the H_2 solubility issue. Accordingly, we performed the catalytic tests in solvents including pentane, hexanes, heptane, octane, nonane, and decane. There are several benefits of performing the reaction in these solvents. First, FF is sparingly soluble while FFA is insoluble in these solvents. During the reaction, FF will be reduced in the alkane phase to FFA where FFA is segregated from the alkane phase and thereby shifting the reaction equilibria toward FFA providing better FFA yield. Second, since FFA is separated from alkane solvent, FFA can be conveniently isolated from the solvent by a simple liquid-liquid separation without additional solvent. Third, phase-separated alkane solvents can then be reused for the next reaction.

From the catalytic test, we found that the FF conversions in the alkane solvents were high in the range of 88–98% (**Fig. 3(a)**). However, we found that the FFA yields increase monotonically as a function of solvent chain length in the order: pentane (59%) < hexane (86%) < heptane (91%) < octane (95%) ~ nonane (96%) ~ decane (96%). We ruled out hydrogen solubility as the main factor because H_2 solubility is similarly low in these solvents (Ivaniš *et al.*, 2021). Another parameter that could influence the FFA yield is the polarity of the solvent. As such, FFA yields from the reactions using different solvents were plotted against the polarity of the respective solvents (**Fig. 3b**) (Sierra, 2001). From this graph, we observe a correlation between higher solvent polarity providing higher FFA yield. Therefore, increasing polarity of the longer alkyl chain of the solvents is likely the main factor for this observed trend (Schuddeboom *et al.*, 1992; Ouyang *et al.*, 2020). After the reactions, the spent catalysts were characterized by PXRD where the patterns are comparable to the pattern of the reduced $CuAl_2O_4$ (**Fig S2**).

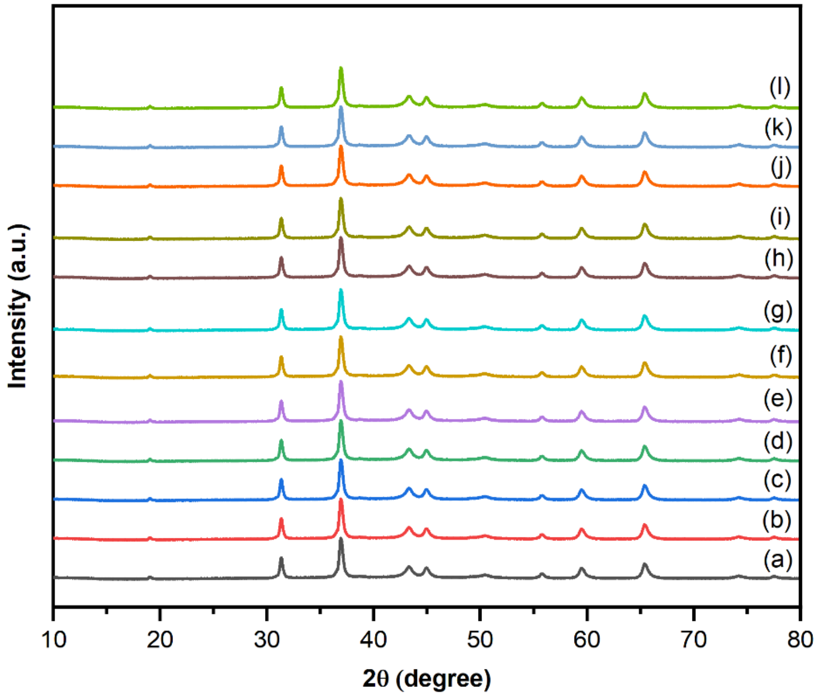

Fig. S2. PXRD patterns of the reduced $CuAl_2O_4$ (a) and spent catalysts after the reactions carried out in methanol (b), ethanol (c), 1-butanol (d), isopropanol (e), 2-butanol (f), pentane (g), hexanes (h), heptane (i), octane (j), nonane (k) and decane (l).

As expected, the reactions carried out in these alkane solvents yield two separated phases including alkane and FFA (**Fig 3**). Remarkably, the FFA phase obtained from the reactions in octane, nonane, and decane contains only FFA without any typical reaction by-products such as 2-MF, THF, THFF, and 2-MTHF as indicated by the GC analysis (Giorgianni *et al.*, 2018). This catalytic system thus provides excellent FFA yield with ease of FFA isolation.

To demonstrate the ease of product isolation, after the catalysis using decane as a solvent, the FFA layer was separated from the decane layer using a separatory funnel. The isolated FFA yield was 50%. This value is lower than the value determined by GC analysis because FFA is lost during the catalyst removal and the product transfer in such a small-scale reaction.

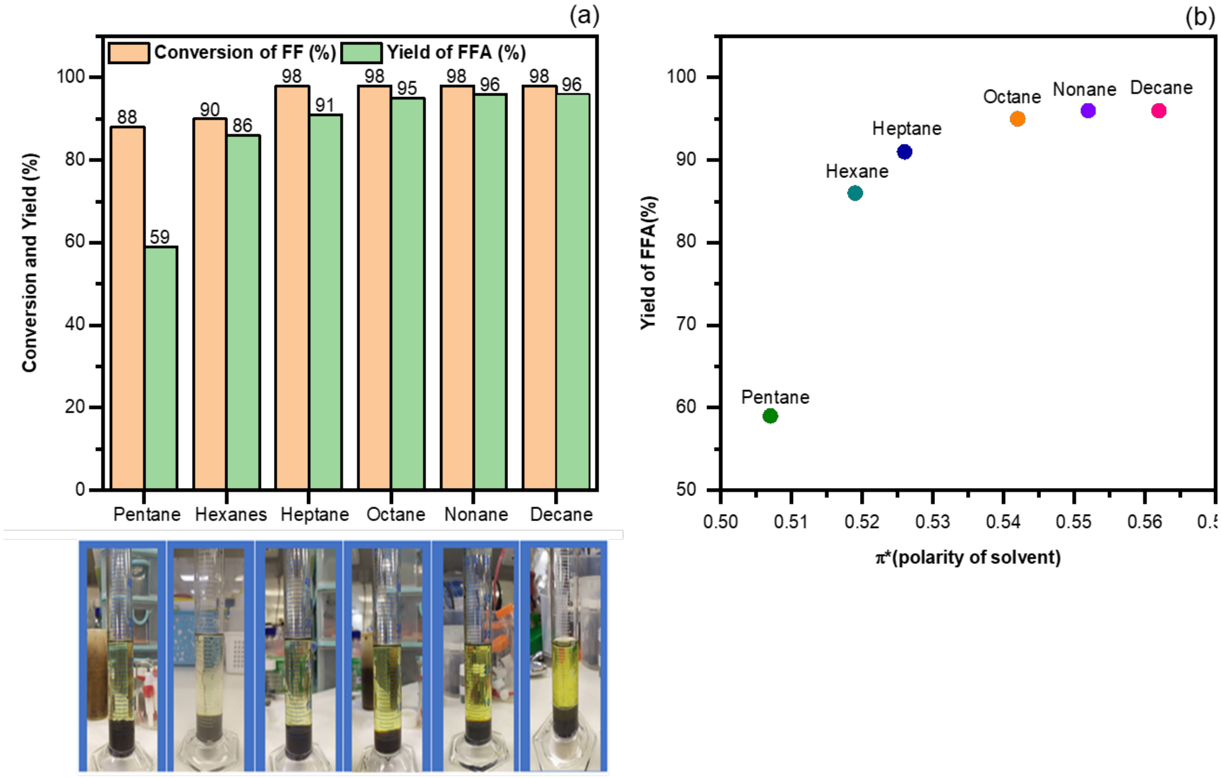

Fig. 3. (a) Effects of alkane solvents on the catalytic activity of reduced $CuAl_2O_4$ catalyst. Pictures of the reactions after the catalysis showing phase separation of FFA (bottom layer) from the alkane solvents (top layer). Reaction conditions: 0.5 g of reduced $CuAl_2O_4$, 2 mL of FF, 25 mL of solvent, 170 °C, 20 bar H_2 and 5 h. (b) The FFA yields from the reactions using different solvents were plotted against the polarity of the respective solvents.

We then assessed the recyclability of the $CuAl_2O_4$ catalyst under optimal conditions using decane as a solvent (**Fig. S3**). After each run, the catalyst was isolated by centrifugation, washed several times with decane, dried at 105 °C overnight, and reduced to 10% H_2/N_2 at 350 °C for 3 h. The FF conversions and FFA yields decrease gradually in the second and third cycles. The reduction in catalyst performance is attributable to the deposition of coke formation on the catalyst as indicated by TGA analysis (**Fig S4**). Distinct weight loss between 100–600 °C was observed corresponding to the loss of solvent and carbon deposit on the catalyst. The catalyst was then regenerated in static air at 900 °C to remove the carbon deposit. After regeneration, the catalyst exhibited FF conversion of 89% and FFA yield of 80% which is close to the performance obtained from the second cycle. After the regenerated catalytic 900°C in ambient, FF conversion and the yield of FFA were 89% and 80%, respectively.

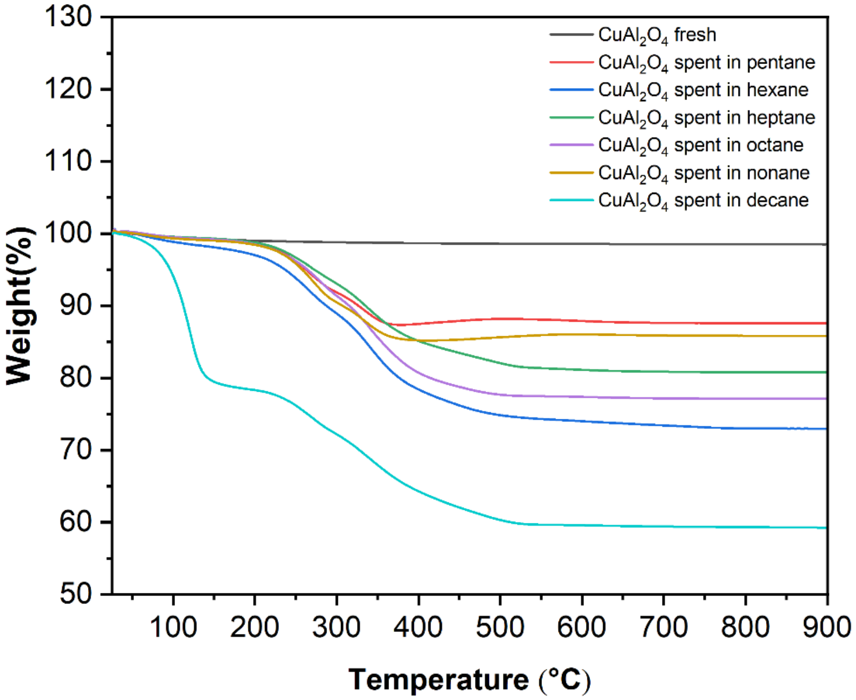

Fig. S3. The TGA curve of $CuAl_2O_4$ fresh catalytic and spent catalytic.

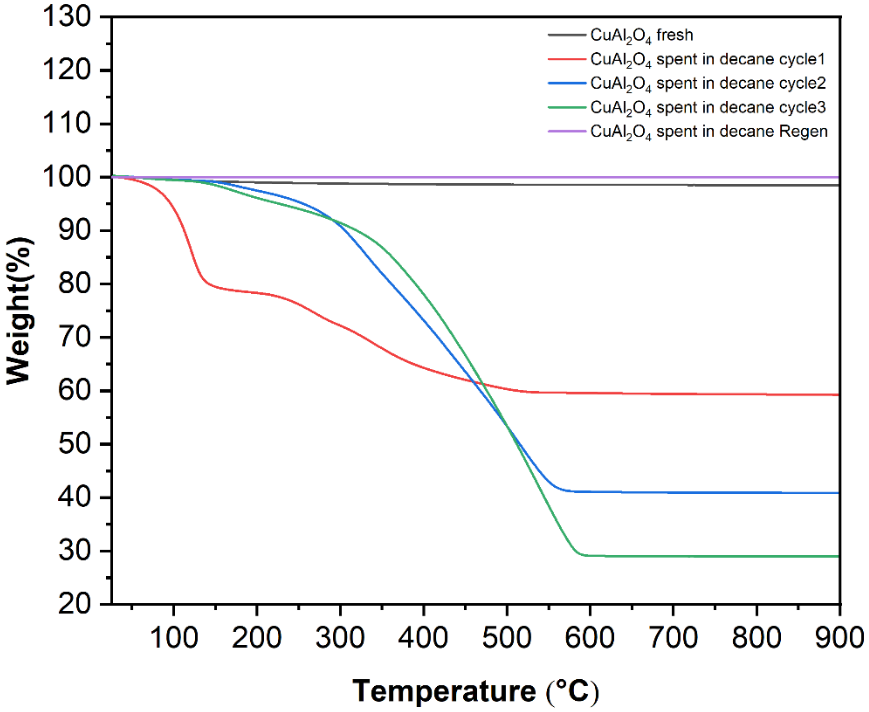

Fig. S4. The TGA curve of $CuAl_2O_4$ fresh catalytic and spent catalytic for stability catalyst in 3 cycles experiments.

- *Infrared absorption spectroscopy of furfural adsorbed on reduced $CuAl_2O_4$ catalyst.*

To understand the origin of high catalytic selectivity toward FFA over reduced $CuAl_2O_4$, in situ diffuse reflectance infrared Fourier transform spectroscopy (DRIFTS) was performed (**Fig 4**). At 150 °C, peaks located at 1723, 1703, 1693, 1679, and 1673 cm^{-1} were observed which can be assigned to the C=O stretch of furfural. Upon heating to 200 °C which is above the boiling point of furfural, the peaks appearing at 1693 and 1676 cm^{-1} remain which belongs to the C=O stretch of furfural chemisorbed on the catalyst η^1(O) configuration (Sitthisa *et al.*, 2011). Such red-shift compared to the gas phase furfural (1720 cm^{-1}) indicates the activation of the C=O group. Notably, the IR bands of the furan skeleton (1569, 1475, and 1464 cm^{-1}) are similar to those of FF in the gas phase hinting that the furan group does not have significant interaction with the catalyst (Allen and Bernstein, 1955; Alonso-Fagúndez *et al.*, 2017; Tong *et al.*, 2021). Overall, FF is adsorbed on the reduced $CuAl_2O_4$ catalyst with the C=O group alone interacting with the catalyst which could explain the selective hydrogenation of the carbonyl group of FF to produce FFA.

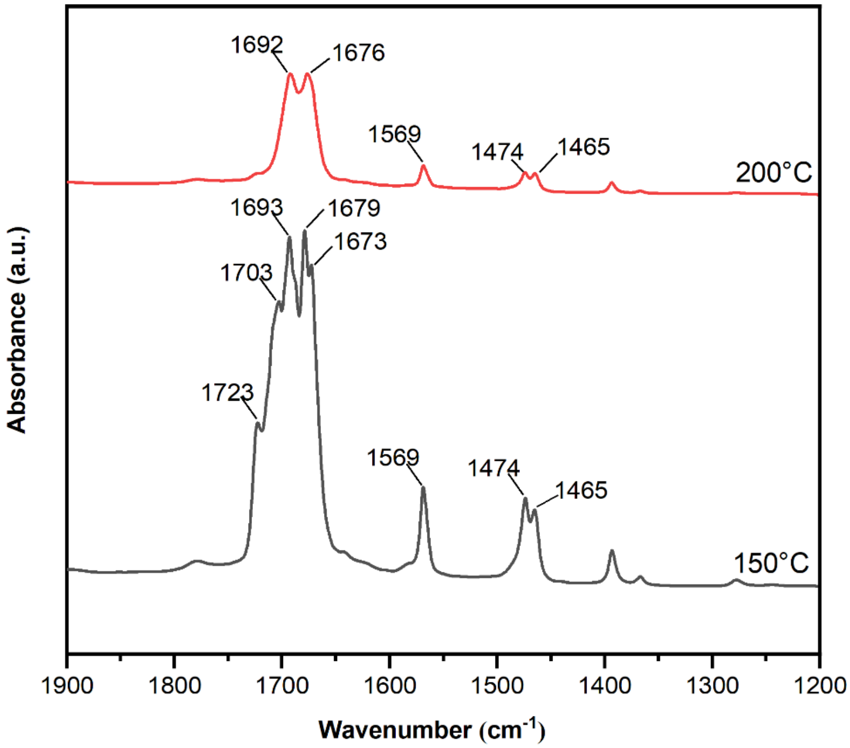

Fig. 4. In situ DRIFTS of adsorbed furfural on reduced $CuAl_2O_4$ collected at 150 °C and 200 °C after pretreatment in H_2 at 350 °C for 3 h.

Conclusions

In this study, we studied the effects of solvents on the hydrogenation of furfural over $CuAl_2O_4$ catalysts. High FF conversions (maximum of 98%) and FFA yields (maximum of 95%) were achieved in the reactions using branched alcohols such as isopropanol and 2-butanol and long alkanes such as octane, nonane, and decane as solvents. We found that the main factor contributing to the high FFA yields is different for different solvent systems. For alcohol solvents, the hydrogen donating ability of alcohols has been identified as a key parameter. In contrast, for alkane solvents, the combination of the high H_2 sorption property of $CuAl_2O_4$ catalyst and high solvent polarity seems to play a key role in providing high FFA yields. The use of alkane solvent systems is advantageous for scale-up production since FFA spontaneously separates from the alkane solvents facilitating the FFA isolation process. From in situ DRIFTS of adsorbed FF, selective hydrogenation of the carbonyl group of FF was attained by the preferred adsorption of the carbonyl portion over the furan ring of FF on the catalyst surface.

Acknowledgments

This work was supported by the National Research Council of Thailand and the National Nanotechnology (NRCT5-RSA63026-02) and the CAS-NSTDA Joint Research Program (P1952712). We acknowledge Dr. Tanasan Intana for his technical support of this work.

References

ALLEN, G.; BERNSTEIN, H. Internal rotation: VIII. The infrared and raman spectra of furfural. **Canadian Journal of Chemistry,** v. 33, n. 6, p. 1055-1061, 1955.

ALONSO-FAGúNDEZ, N. et al. Gas phase oxidation of furfural to maleic anhydride on V2O5/γ-Al2O3 catalysts: reaction conditions to slow down the deactivation. **Journal of Catalysis,** v. 348, p. 265-275, 2017.

BAHMANPOUR, A. M. et al. Cu–Al Spinel as a Highly Active and Stable Catalyst for the Reverse Water Gas Shift Reaction. **ACS Catalysis,** v. 9, n. 7, p. 6243-6251, 2019. 2155-5435.

BLöCHL, P. E. Projector Augmented-Wave Method. **Physical Review B,** v. 50, n. 24, p. 17953-17979, 1994.

CHEN, S.; CHEN, X.; ZHANG, H. Probing the activity of Ni13, Cu13, and Ni12Cu clusters towards the ammonia decomposition reaction by density functional theory. **Journal of Materials Science,** v. 52, n. 6, p. 3162-3168, March 01 2017.

CHEN, X. et al. Highly selective hydrogenation of furfural to furfuryl alcohol over Pt nanoparticles supported on g-C3N4 nanosheets catalysts in water. **Sci Rep,** v. 6, p. 28558, Jun 22 2016. 2045-2322.

CHIANG, C.-L.; LIN, K.-S. Preparation and characterization of CuO Al 2 O 3 catalyst for dimethyl ether production via methanol dehydration. **International Journal of Hydrogen Energy,** v. 42, n. 37, p. 23526-23538, 2017.

CHOU, J. P. et al. 13-atom metallic clusters studied by density functional theory: Dependence on exchange-correlation approximations and pseudopotentials. **Physical Review B,** v. 80, n. 16, p. 165412, 10/16/ 2009.

CHUNJIE HUANG, S. C., XIAOYAO FEI, DAI LIU AND YONGCHUN ZHANG. <Catalytic_Hydrogenation_of_CO2_to_Methanol_Study_o.pdf>. **Catalysts,** v. 5, p. 1846-1861, 2015.

DENG, Y. et al. Solvent tunes the selectivity of hydrogenation reaction over α-MoC catalyst. **Journal of the American Chemical Society,** v. 140, n. 43, p. 14481-14489, 2018.

DESSAL, C. et al. Atmosphere-dependent stability and mobility of catalytic Pt single atoms and clusters on γ-Al2O3. **Nanoscale,** v. 11, n. 14, p. 6897-6904, 2019. ISSN 2040-3364.

DIGNE, M. et al. Use of DFT to achieve a rational understanding of acid–basic properties of γ-alumina surfaces. **Journal of Catalysis,** v. 226, n. 1, p. 54-68, 2004.

FU, C. L.; HO, K. M. First-principles calculation of the equilibrium ground-state properties of transition metals: Applications to Nb and Mo. **Physical Review B,** v. 28, n. 10, p. 5480-5486, 1983.

FULAJTáROVA, K. et al. Aqueous phase hydrogenation of furfural to furfuryl alcohol over Pd–Cu catalysts. **Applied Catalysis A: General,** v. 502, p. 78-85, 2015/08/05/ 2015.

GAO, B.; ZHANG, J.; YANG, J.-H. Bimetallic Cu-Ni/MCM-41 catalyst for efficiently selective transfer hydrogenation of furfural into furfural alcohol. **Molecular Catalysis,** v. 517, p. 112065, 2022.

GAO, H. A first principles investigation of the NO oxidation mechanism on Pt/γ-Al2O3. **RSC Advances,** v. 6, n. 105, p. 102914-102923, 2016.

GAO, X. et al. Bimetallic PtFe-Catalyzed Selective Hydrogenation of Furfural to Furfuryl Alcohol: Solvent Effect of Isopropanol and Hydrogen Activation. **ACS Sustainable Chemistry & Engineering,** v. 8, n. 33, p. 12722-12730, 2020. 2168-0485.

GIORGIANNI, G. et al. Effect of the Solvent in Enhancing the Selectivity to Furan Derivatives in the Catalytic Hydrogenation of Furfural. **ACS Sustainable Chemistry & Engineering,** v. 6, n. 12, p. 16235-16247, 2018. 2168-0485.

GóMEZ MILLáN, G.; SIXTA, H. Towards the green synthesis of furfuryl alcohol in a one-pot system from xylose: A review. **Catalysts,** v. 10, n. 10, p. 1101, 2020.

GRIMME, S. Semiempirical GGA-type density functional constructed with a long-range dispersion correction. **Journal of Computational Chemistry,** v. 27, n. 15, p. 1787-1799, 2006.

GRIMME, S. et al. A consistent and accurate ab initio parametrization of density functional dispersion correction (DFT-D) for the 94 elements H-Pu. **The Journal of Chemical Physics,** v. 132, n. 15, p. 154104, 2010.

HAJDUK, Š. et al. COx-free hydrogen production via decomposition of ammonia over Cu–Zn-based heterogeneous catalysts and their activity/stability. **Applied Catalysis B: Environmental,** v. 211, p. 57-67, 2017.

HAN, M. et al. Physical properties of MgAl 2 O 4 , CoAl 2 O 4 , NiAl 2 O 4 , CuAl 2 O 4 , and ZnAl 2 O 4 spinels synthesized by a solution combustion method. **Materials Chemistry and Physics,** v. 215, p. 251-258, 2018.

HENKELMAN, G.; ARNALDSSON, A.; JóNSSON, H. A fast and robust algorithm for Bader decomposition of charge density. **Computational Materials Science,** v. 36, n. 3, p. 354-360, 2006. ISSN 0927-0256.

HENKELMAN, G.; JóNSSON, H. A dimer method for finding saddle points on high dimensional potential surfaces using only first derivatives. **The Journal of Chemical Physics,** v. 111, n. 15, p. 7010-7022, 1999/10/15 1999. ISSN 0021-9606.

HEYDEN, A.; BELL, A. T.; KEIL, F. J. Efficient methods for finding transition states in chemical reactions: Comparison of improved dimer method and partitioned rational function optimization method. **The Journal of Chemical Physics,** v. 123, n. 22, p. 224101, 2005/12/08 2005.

HIRUNSIT, P. et al. Cooperative H2 Activation at Ag Cluster/θ-Al2O3(110) Dual Perimeter Sites: A Density Functional Theory Study. **The Journal of Physical Chemistry C,** v. 118, n. 15, p. 7996-8006, 2014.

HU, C. Y.; SHIH, K.; LECKIE, J. O. Formation of copper aluminate spinel and cuprous aluminate delafossite to thermally stabilize simulated copper-laden sludge. **J Hazard Mater,** v. 181, n. 1-3, p. 399-404, 2010.

HUANG, W. et al. Selective hydrogenation of furfural to furfuryl alcohol over catalysts prepared via sonochemistry. **Ultrason Sonochem,** v. 14, n. 1, p. 67-74, 2007.

IVANIŠ, G. et al. Hydrogen solubility in bio-based furfural and furfuryl alcohol at elevated temperatures and pressures relevant for hydrodeoxygenation. **Fuel,** v. 290, p. 120021, 2021.

JACEK KIJE´NSKI A, PIOTR WINIAREK A, TADEUSZ PARYJCZAK B,; ANDRZEJ LEWICKI B, A. M. A. Platinum deposited on monolayer supports in selective hydrogenation of furfural to furfuryl alcohol. **Applied Catalysis A: General** v. 233 p. 171–182, 2002.

JIA, P. et al. Highly selective hydrogenation of furfural to cyclopentanone over a NiFe bimetallic catalyst in a methanol/water solution with a solvent effect. **ACS Sustainable Chemistry & Engineering,** v. 7, n. 18, p. 15221-15229, 2019.

JIMéNEZ-GóMEZ, C. P. et al. Promotion effect of Ce or Zn oxides for improving furfuryl alcohol yield in the furfural hydrogenation using inexpensive Cu-based catalysts. **Molecular Catalysis,** v. 455, p. 121-131, 2018.

JOSE´ A. RODRIGUEZ A;*, J. Y. K. A., JONATHAN C. HANSON A,MANUEL PE´REZ B,AND ANATOLY I. FRENKEL C. Reduction of CuO in H2: in situ time-resolved XRD studies. **Catalysis Letters** v. 85, p. 247-254, 2003.

KäSTNER, J.; SHERWOOD, P. Superlinearly converging dimer method for transition state search. **The Journal of Chemical Physics,** v. 128, n. 1, p. 014106, 2008.

KRESSE, G.; FURTHMüLLER, J. Efficiency of Ab initio Total Energy Calculations for Metals and Semiconductors Using a Plane-Wave Basis Set. **Computational Materials Science,** v. 6, n. 1, p. 15-50, 1996a.

______. Efficient Iterative Schemes for Ab initio Total-Energy Calculations Using a Plane-Wave Basis Set. **Physical Review B,** v. 54, n. 16, p. 11169-11186, 1996b.

KRESSE, G.; JOUBERT, D. From Ultrasoft Pseudopotentials to the Projector Augmented-Wave Method. **Physical Review B,** v. 59, n. 3, p. 1758-1775, 1999.

KWAK, B. K. et al. Preparation and characterization of nanocrystalline CuAl2O4 spinel catalysts by sol–gel method for the hydrogenolysis of glycerol. **Catalysis Communications,** v. 24, p. 90-95, 2012.

LEE, C. B. T. L.; WU, T. Y. A review on solvent systems for furfural production from lignocellulosic biomass. **Renewable and Sustainable Energy Reviews,** v. 137, p. 110172, 2021. ISSN 1364-0321.

LEE, J. et al. Cu2O (100) surface as an active site for catalytic furfural hydrogenation. **Applied Catalysis B: Environmental,** v. 282, p. 119576, 2021.

LI, T. T. et al. Enhanced catalytic CO oxidation by Cu13-mNim (m = 0, 1, 13) clusters at ambient temperatures with more active sites and distinct mechanistic pathways. **Applied Surface Science,** v. 479, p. 39-46, 2019.

LI, X. et al. The Support Effects on the Direct Conversion of Syngas to Higher Alcohol Synthesis over Copper-Based Catalysts. **Catalysts,** v. 9, n. 2, 2019.

LIU, B.; ZHANG, Z. Catalytic conversion of biomass into chemicals and fuels over magnetic catalysts. **Acs Catalysis,** v. 6, n. 1, p. 326-338, 2016.

LUO, M.-F. et al. In situ XRD, Raman, and TPR studies of CuO/Al2O3 catalysts for CO oxidation. **Journal of Molecular Catalysis A: Chemical,** v. 239, n. 1-2, p. 243-248, 2005.

MONGKOLCHANOK PRAMOTTANA, P. P. A. B. N. Copper Chromite Catalyst for the Selective Hydrogenation of Furfural to Furfuryl Alcohol **J. Chin. Inst. Chem. Engrs.,,** v. 33, n. 5, p. 477-481, 2002.

MONKHORST, H. J.; PACK, J. D. Special points for Brillouin-zone integrations. **Phys. Rev. B,** v. 13, n. 12, p. 5188-5192, 1976.

NAGARAJA, B. M. et al. Vapor phase selective hydrogenation of furfural to furfuryl alcohol over Cu–MgO coprecipitated catalysts. **Journal of Molecular Catalysis A: Chemical,** v. 265, n. 1-2, p. 90-97, 2007.

NAGARAJA, B. M. et al. A highly efficient Cu/MgO catalyst for vapour phase hydrogenation of furfural to furfuryl alcohol. **Catalysis Communications,** v. 4, n. 6, p. 287-293, 2003/06/01/ 2003. ISSN 1566-7367.

NORTIER, P. et al. Effects of crystallinity and morphology on the surface properties ofalumina. **Applied Catalysis,** v. 61, n. 1, p. 141-160, 1990.

OUYANG, M. et al. Organogelator based on long alkyl chain attached excimer precursor: Two channels of TICT, highly efficient and switchable luminescence. **Dyes and Pigments,** v. 180, p. 108433, 2020.

PANTALEO, G. et al. Support effect on the structure and CO oxidation activity of Cu-Cr mixed oxides over Al2O3 and SiO2. **Materials Chemistry and Physics,** v. 114, n. 2-3, p. 604-611, 2009.

PERDEW, J. P.; BURKE, K.; ERNZERHOF, M. Generalized Gradient Approximation Made Simple. **Physical Review Letters,** v. 77, n. 18, p. 3865-3868, 1996.

PIOTROWSKI, M. J.; PIQUINI, P.; DA SILVA, J. L. F. Density functional theory investigation of 3d, 4d, and 5d 13-atom metal clusters. **Physical Review B,** v. 81, n. 15, p. 155446, 2010.

PONMUDI, S. et al. Facile fabrication of spinel structured n-type CuAl2O4 thin film with nano-grass like morphology by sputtering technique. **Applied Surface Science,** v. 483, p. 601-615, 2019.

PUDI, S. M. et al. Selective Hydrogenolysis of Glycerol to 1,2-Propanediol Over Bimetallic Cu-Ni Catalysts Supported on γ-Al2O3. **Journal of the Brazilian Chemical Society**, 2015.

QIN, F.-J. et al. Cu-Al spinel as a sustained release catalyst for H 2 production from methanol steam reforming: Effects of different copper sources. **Journal of Fuel Chemistry and Technology,** v. 45, n. 12, p. 1481-1488, 2017.

RAMIREZ-BARRIA, C. et al. Optimization of ruthenium based catalysts for the aqueous phase hydrogenation of furfural to furfuryl alcohol. **Applied Catalysis A: General,** v. 563, p. 177-184, 2018.

SALAVATI-NIASARI, M.; DAVAR, F.; FARHADI, M. Synthesis and characterization of spinel-type CuAl2O4 nanocrystalline by modified sol–gel method. **Journal of Sol-Gel Science and Technology,** v. 51, n. 1, p. 48-52, 2009. 1573-4846.

SALNIKOVA, K. et al. The liquid phase catalytic hydrogenation of the furfural to furfuryl alcohol. **Chemical Engineering Transactions,** v. 70, p. 379-384, 2018.

SANVILLE, E. et al. Improved grid-based algorithm for Bader charge allocation. **Journal of Computational Chemistry,** v. 28, n. 5, p. 899-908, 2007.

SCHUDDEBOOM, W. et al. Excited-state dipole moments of dual fluorescent 4-(dialkylamino) benzonitriles: influence of alkyl chain length and effective solvent polarity. **The Journal of Physical Chemistry,** v. 96, n. 26, p. 10809-10819, 1992.

SHEPPARD, D.; HENKELMAN, G. Paths to which the nudged elastic band converges. **Journal of Computational Chemistry,** v. 32, n. 8, p. 1769-1771, 2011.

SHEPPARD, D.; TERRELL, R.; HENKELMAN, G. Optimization methods for finding minimum energy paths. **The Journal of Chemical Physics,** v. 128, n. 13, p. 134106, 2008.

SHEPPARD, D. et al. A generalized solid-state nudged elastic band method. **The Journal of Chemical Physics,** v. 136, n. 7, p. 074103, 2012.

SIERRA, J. C. Solvent effects based on pure solvent scales. Handbook of solvents, 2001, ChemTec Publishing. p.583-616.

SINGH, G. et al. Catalytic hydrogenation of furfural to furfuryl alcohol over chromium-free catalyst: Enhanced selectivity in the presence of solvent. **Molecular Catalysis,** v. 500, p. 111339, 2021.

SITTHISA, S.; RESASCO, D. E. Hydrodeoxygenation of Furfural Over Supported Metal Catalysts: A Comparative Study of Cu, Pd and Ni. **Catalysis Letters,** v. 141, n. 6, p. 784-791, 2011.

SITTHISA, S. et al. Kinetics and mechanism of hydrogenation of furfural on Cu/SiO2 catalysts. **Journal of catalysis,** v. 277, n. 1, p. 1-13, 2011.

SRIVASTAVA, S. et al. Cr-free Co–Cu/SBA-15 catalysts for hydrogenation of biomass-derived α-, β-unsaturated aldehyde to alcohol. **Chinese Journal of Catalysis,** v. 36, n. 7, p. 933-942, 2015.

TANG, W.; SANVILLE, E.; HENKELMAN, G. A grid-based Bader analysis algorithm without lattice bias. **Journal of Physics: Condensed Matter,** v. 21, n. 8, p. 084204, 2009a.

______. A grid-based Bader analysis algorithm without lattice bias. **J Phys Condens Matter,** v. 21, n. 8, p. 084204, Feb 25 2009b.

TANG, X. et al. Conversion of biomass to γ-valerolactone by catalytic transfer hydrogenation of ethyl levulinate over metal hydroxides. **Applied Catalysis B: Environmental,** v. 147, p. 827-834, 2014.

THONGRATKAEW, S. et al. Cu-Al spinel-oxide catalysts for selective hydrogenation of furfural to furfuryl alcohol. **Catalysis Today,** v. 367, p. 177-188, 2021.

TOLEK, W. et al. Flame spray-synthesized Pt-Co/TiO2 catalysts for the selective hydrogenation of furfural to furfuryl alcohol. **Catalysis Communications,** v. 149, p. 106246, 2021.

TONG, Z. et al. Adsorption configuration-determined selective hydrogenative ring opening and ring rearrangement of furfural over metal phosphate. **ACS Catalysis,** v. 11, n. 11, p. 6406-6415, 2021.

VAN DER WAAL, J. et al. Zeolite titanium beta: A selective catalyst for the gas-phase Meerwein–Ponndorf–Verley, and Oppenauer reactions. **Journal of Catalysis,** v. 173, n. 1, p. 74-83, 1998.

VARGAS-HERNáNDEZ, D. et al. Furfuryl alcohol from furfural hydrogenation over copper supported on SBA-15 silica catalysts. **Journal of Molecular Catalysis A: Chemical,** v. 383-384, p. 106-113, 2014.

VILLAVERDE, M. M. et al. Selective liquid-phase hydrogenation of furfural to furfuryl alcohol over Cu-based catalysts. **Catalysis today,** v. 213, p. 87-92, 2013.

VILLAVERDE, M. M.; GARETTO, T. F.; MARCHI, A. J. Liquid-phase transfer hydrogenation of furfural to furfuryl alcohol on Cu–Mg–Al catalysts. **Catalysis Communications,** v. 58, p. 6-10, 2015.

WANG, Z. et al. Selective hydrogenation of furfural to furfuryl alcohol over Pd/TiH2 catalyst. **Molecular Catalysis,** v. 508, p. 111599, 2021.

WEERACHAWANASAK, P. et al. Development of bimetallic Ni-Cu/SiO2 catalysts for liquid phase selective hydrogenation of furfural to furfuryl alcohol. **Catalysis Communications,** v. 149, p. 106221, 2021.

XIAO, P. et al. Solid-state dimer method for calculating solid-solid phase transitions. **The Journal of Chemical Physics,** v. 140, n. 17, p. 174104, 2014.

XU, Y. et al. Mechanism and kinetics of catalytic ozonation for elimination of organic compounds with spinel-type CuAl2O4 and its precursor. **Sci Total Environ,** v. 651, n. Pt 2, p. 2585-2596, 2019.

YAN, K.; CHEN, A. Selective hydrogenation of furfural and levulinic acid to biofuels on the ecofriendly Cu–Fe catalyst. **Fuel,** v. 115, p. 101-108, 2014.

YAN, K. et al. A noble-metal free Cu-catalyst derived from hydrotalcite for highly efficient hydrogenation of biomass-derived furfural and levulinic acid. **RSC advances,** v. 3, n. 12, p. 3853-3856, 2013.

YAN, K. et al. Production, properties and catalytic hydrogenation of furfural to fuel additives and value-added chemicals. **Renewable and Sustainable Energy Reviews,** v. 38, p. 663-676, 2014.

YU, M.; TRINKLE, D. R. Accurate and efficient algorithm for Bader charge integration. **The Journal of Chemical Physics,** v. 134, n. 6, p. 064111, 2011.

ZENG, W. et al. Density functional theory (DFT) studies of CO oxidation reaction on M13 and Au18M clusters (M = Au, Ag, Cu, Pt and Pd): the role of co-adsorbed CO molecule. **RSC Advances,** v. 6, n. 61, p. 55867-55877, 2016.

ZHANG, J. et al. Selective transfer hydrogenation of furfural into furfuryl alcohol on Zr-containing catalysts using lower alcohols as hydrogen donors. **ACS omega,** v. 3, n. 6, p. 6206-6216, 2018.

ZHANG, J. et al. Electrospun CuAl 2 O 4 hollow nanofibers as visible light photocatalyst with enhanced activity and excellent stability under acid and alkali conditions. **CrystEngComm,** v. 20, n. 3, p. 312-322, 2018.

ZHANG, J.; WU, D. Aqueous phase catalytic hydrogenation of furfural to furfuryl alcohol over in-situ synthesized Cu–Zn/SiO2 catalysts. **Materials Chemistry and Physics,** v. 260, p. 124152, 2021.

ZHANG, L. et al. Effect of precursor and precipitant concentrations on the catalytic properties of CuO/ZnO/CeO2-ZrO2 for methanol steam reforming. **Journal of Fuel Chemistry and Technology,** v. 43, n. 11, p. 1366-1374, 2015.

3.5 Kinetics Study of the Selective Hydrogenation of Furfural to Furfuryl Alcohol over $CuAl_2O_4$ Spinel Catalysts

Tanasan Intana[a], Sutarat Thongratkaew[a], Jeeranan Nonkumwong[a], Waleeporn Donphai[b,c], Thongthai Witoon[b,c], Metta Chareonpanich[b,c], Kajornsak Faungnawakij[a,c], and Sirapassorn Kiatphuengporn[a,*]

[a]National Nanotechnology Center (NANOTEC), National Science and Technology Development Agency (NSTDA), Pathumthani 12120, Thailand
[b]Center of Excellence on Petrochemical and Materials Technology, Department of Chemical Engineering, Faculty of Engineering, Kasetsart University, Bangkok 10900, Thailand
[c]Research Network of NANOTEC–KU on NanoCatalysts and NanoMaterials for Sustainable Energy and Environment, Kasetsart University, Bangkok 10900, Thailand

Abstract

The catalytic hydrogenation of furfural is an important process that produce value-added furfural derivatives, especially furfuryl alcohol. In this work, the kinetics of the catalytic furfural hydrogenation over copper aluminate spinel ($CuAl_2O_4$) was studied in a batch-type reactor under various reaction parameters including the stirring speed, initial furfural concentration, H_2 pressure, and reaction temperature. The $CuAl_2O_4$ catalyst showed excellent performance in furfuryl alcohol production as the furfural conversion could reach 100% and the furfuryl alcohol yield was >98%. The furfural concentration and the reaction temperature were found to significantly impact on the reaction rate, while other parameters showed less contributions leading to a flexible operation window. It was determined that the reaction rate expression followed the equation $r = kC_{furfural}^{0.355}$ with the apparent activation energy of 45.6 kJ/mol. The developed kinetic model for hydrogenation of furfural to furfuryl alcohol were in good agreement with the experimental results. The kinetic model presented here could be useful for process design and scale-up of the hydrogenation reactor in the industrial application.

Introduction

Furfuryl alcohol (FA) is one of the valuable platform chemicals in various industries including the production of vitamin C, lysine, plasticizer (Vaidya and Mahajani, 2003), dispersing agent (Rao et al., 1997), thermostatic resins (Li et al., 2006), acid proof bricks (Sharma et al., 2013) and so forth. Typically, FA can be produced via selective hydrogenation of furfural (FF) in the gas or liquid phase (Li et al., 2003; Li et al., 2016; Liu et al., 2013; Nagaraja et al., 2003; Wu et al., 2005). In order to improve productivity and enhance catalytic activity of FF hydrogenation, many variables such as types of metal, promoter, support, and catalyst preparation technique have to be considered. Generally, Cu-based catalysts have been widely used in the production of FA via FF hydrogenation (Liu et al., 2013; Rao et al., 1997). For the gas-phase reaction, the catalysts–i.e., Cu–Ca/SiO_2 (Wu et al., 2005), Cu/MgO (Nagaraja et al., 2003)–provided high FA yield of >95% and high FF conversion of >97%. However, the gas phase reaction has some drawbacks such as low production rate and energy efficiency. Meanwhile, for the liquid-phase furfural hydrogenation, the catalysts–i.e., Zr_xB_yFeO (Li et al., 2021), Ni–Fe–B (Li et al., 2003), Pd–Cu/MgO (Fulajtárova et al., 2015), Ir–ReO_x/SiO_2 (Liu et al., 2014), Pt–Sn/SiO_2 (Merlo et al., 2009), Ru/UiO-66 (Yuan et al., 2015), Fe(NiFe)O_4–SiO_2 (Halilu et al., 2016)–gave high FA yield of >90% and FF conversion of >95%. Although the high catalytic performance was achieved using those catalysts, the synthesis process of catalysts was complicated and needs improvement. In addition, avoiding the high-cost materials especially precious metals could be one of interesting alternatives to minize the cost of processing. Among several catalysts, the spinel-type oxides have been of interest for many reactions since these materials could provide a high dispersion of metal species that would lead to an excellent catalytic performance (Faungnawakij et al., 2008). They were synthesized by a sol-gel combustion technique which was simple and cost-effective. Our previous work firstly reported the application of $CuAl_2O_4$ spinel catalyst for FA production from FF. It gave the excellent activity in furfural conversion (>99%) and yield of furfuryl alcohol (>95%) comparing to the different types of spinels studied and the reported non-noble metal catalysts, according to the synergistic effect induced by the interaction between the reduced copper species (Cu^0) and the copper spinel host (Cu^{2+}) along with the high H_2 sorption ability (Thongratkaew et al., 2021).

In addition, comprehension of reaction kinetic is one of the important factors for the process design which can help to predict the extent of the reaction under particular reaction conditions at any time. However, there are limited numbers of researches that reported the study of the kinetic and optimization for the FF hydrogenation to FA. In recent years, reaction order and activation energy have been investigated via the reaction over some catalysts including copper chromite, Pt/C, Co-Cu/SBA-15 and Cu-MgO through liquid phase and gas phase conditions. For the liquid phase, the copper chromite catalyst was found to follow the first order kinetic with respect to furfural and second order with respect to hydrogen as expressed by M.S. Borts et al. (Borts et al., 1986). R. Rao et al. (Rao et al., 1997) reported that reaction orders on FF and hydrogen were near unity when the reaction was performing, and selectivity of FF to FA was obtained in the range from 35–80%. For the Pt/C catalyst, reaction order with respect to furfuraldehyde was varied from zero to 0.86 depending on initial concentration of furfuraldehyde reported by P.D. Vaidya and V.V. Mahajani (2003) (Vaidya and Mahajani, 2003). Pseudo-first order with respect to initial concentration of FF in liquid phase with an activation energy of 48.3 and 38.5 kJ/mol was investigated over Zr_1B_3FeO and Co-Cu/SBA-15, respectively (Li et al., 2021; Srivastava et al., 2015). For the gas phase, the reaction mechanisms and macro-kinetics on Cu-MgO catalyst were deduced that a reaction order of near zero with respect to furfural showed as excellent agreement with the reactivity data and the activation energy of 25.5 kJ/mol was obtained as in the report by M. Ghashghaee et al. (2017) (Ghashghaee et al., 2017).

To the best of our knowledge, the kinetic study on $CuAl_2O_4$ spinel catalyst via the selective hydrogenation of FF to FA has not been studied and reported yet. Therefore, the aim of this present work was to investigate the kinetic model for the FF hydrogenation to FA using $CuAl_2O_4$ spinel catalyst. A sensitivity study was performed by varying the reaction conditions (stirring speed, furfural concentration, H_2 pressure, and reaction temperature) to analyze the kinetic model of the reaction.

Experimental

- *Catalyst preparation*

$CuAl_2O_4$ spinel catalyst was prepared by a sol-gel combustion method following the protocal reported in our previous publications (Luadthong et al., 2016; Luadthong et al., 2017). Briefly, copper (II) nitrate hemi(pentahydrate) ($Cu(NO_3)_2.2.5H_2O$: 98%, Ajax (Australia)) and aluminum nitrate nonahydrate ($Al(NO_3)_3.9H_2O$: 98%, Ajax (Australia)) were mixed in a molar ratio of 1:2 by dissolving in deionized water under continuous stirring at 60 ^oC for 2 h. After that, excess amounts of citric acid (44.35 g) ($C_6H_8O_7$: 98%, Ajax (Australia)) were added into the aqueous solution, before it was further stirred at 60 ^oC for 1 h. The water in the solution has been evaporated by heating up to 100 ^oC until the solution turned to gel. Then, the temperature was raised up to ca. 300 ^oC to combust the gel to black fine powder. Finally, the black powder were grounded and calcined in air at 900 ^oC for 4 h to obtain brown $CuAl_2O_4$ spinel catalyst. For a comparison of the catalytic performance, other aluminate spinel catalysts (BAl_2O_4 where B = Ni, NiCu, Zn, Mg) were also synthesized using their corresponding nitrate salts ($Ni(NO_3)_2.6H_2O$, $Zn(NO_3)_2.6H_2O$ and $Mg(NO_3)_2.6H_2O$), respectively, as divalent metal resource instead of copper (II).

- *Catalyst characterization*

Phase identification of the catalysts was performed using the powder X-ray diffractometer (XRD; D8 ADVANCE, Bruker, Ltd., Germany) with Cu Kα radiation. The measurement was operated at 40 kV and 40 mA, and in steps of 0.02^o s^{-1} with a step time of 0.5 s over the range of $20^o < 2\theta < 80^o$. Morphology of $CuAl_2O_4$ catalyst was revealed using transmission electron microscopy (TEM; JEM-2100 JEOL, Japan). The specific surface area was performed by conventional nitrogen adsorption-desorption technique (Nova 2000e, Quantachrome Instruments, Germany). Prior to the measurement, the sample was degassed at 300 ^oC for 3 h. The specific surface area of the catalysts was examined using the Brunauer-Emmett-Teller (BET) analysis in a relative pressure (p/p_0) range between 0.05 and 0.95, where the specific pore volume was measured at a relative pressure of 0.995. Pore diameters and volumes were calculated using Barrett- Joyner- Halenda (BJH) method. Temperature programmed reduction (TPR) was conducted using CHEMBET-Pulsar (Quantachrome Instruments, Germany). In each TPR experiment, the catalyst was heated in a flow of gas mixture of hydrogen (H_2) and argon (Ar). The experiment was carried out in the temperature range of 45-800 ^oC with a heating rate of 5 ^oC/min.

- *Catalytic performance and kinetic study*

Catalytic performance tests for analyzing the kinetic model in the FF hydrogenation to FA using $CuAl_2O_4$ spinel catalyst were carried out in a 130 mL stainless steel autoclave with a magnetic stirrer under the reaction condition as follows: stirring speed (0, 400, 950 and 1,500 rpm), initial FF concentration (1, 2, 3 and 4 M), H_2 pressure (10, 20 and 30 bar) and reaction temperature (150, 170 and 190 ^oC). Note that the stirring speed above 400 rpm provided the condition without the mass transport limitation. Prior to the reaction, 0.5 g of catalyst was reduced with 10% H_2 balanced in N_2 at 300 ^oC for 3 h in a packed bed reactor, and then the reduced catalyst was transferred to the autoclave just prior to the reaction under ambient atmosphere. Furfural ($C_5H_6O_2$: 99%, Sigma-Aldrich) and 2-propanol (C_3H_8O: 99.98%, Fisher Scientific) were then mixed at the designed initial FF concentration in the autoclave with the total volume of 30 mL. The mixture was continuously stirred at the designed stirring speed, and heated up to the designed reaction temperature with a heating rate of 5 ^oC/min. In the beginning, the initial pressure increased with the elevated temperature. When the temperature achieved the desired value, the autoclave was pressurized to a greater extent by filling hydrogen gas (H_2: 99.99%, Praxair). Then the liquid sample was collected as a function of time for further investigation. During the reaction, the total pressure in the reactor was found to slowly decrease due to the H_2 consumption. So, the H_2 gas supply was connected to the system to keep the total pressure in the reactor identical to the initial value all the time. Note that the transfer hydrogenation was minor as compared to the direct hydrogenation in the present conditions. The samples were collected at the reaction time of 15, 30, 45, 60, 90, 120, 180, 240 and 300 min and analyzed by gas chromatography (GC-2010, Shimadzu) using a flame ionization detector and a capillary column (DB-WAX, Agilent technologies, 30 m in length with 0.25 mm i.d. and 0.25 µm film thickness). The furfural conversion and furfuryl alcohol yield are calculated using the following equations:

$$\text{FF Conversion (\%)} = \left(\frac{\text{The number of moles of furfural consumption}}{\text{The number of moles of initially charged furfural}}\right) \times 100 \qquad (1)$$

$$\text{FA Yield (\%)} = \left(\frac{\text{The number of moles of furfuryl alcohol generation}}{\text{The number of moles of initially charged furfural}}\right) \times 100 \qquad (2)$$

Results and discussion

Characterization of catalysts

The XRD pattern of the as-synthesized $CuAl_2O_4$ as illustrated at the top panel of **Fig. 1a** indicated cubic spinel structure via an evidence of 2θ around 31.2, 36.8, 44.7, 55.6, 59.3, 65.2, 74.0 and 77.3°. These are corresponded to the reflections of (220), (311), (400), (422), (511), (440), (620) and (533) planes (PDF 01-075-4256), respectively. Similarly, the as-synthesized $NiAl_2O_4$, $MgAl_2O_4$ and 5%Ni-$ZnAl_2O_4$ also possess cubic spinel structure, as shown in Supplementary **Fig. S1**. After reduction process with 10% H_2 balanced in N_2 for 3 h, the $CuAl_2O_4$ catalyst partially transformed to metallic copper, Cu^0 (PDF 00-004-0836), as marked in the middle panel of **Fig. 1**, while the major phase is still $CuAl_2O_4$. No phase transformation was observed after the reaction test as the XRD pattern of the spent catalyst remained unchanged, suggesting its good stability in the operating reaction conditions. It was reported that an oxidation of Cu^0 to copper oxides could sometimes occur when using water as the solvent (Sádaba et al., 2015).

Fig. 1b illustrated a TEM image of the as-synthesized $CuAl_2O_4$. It was found that the catalyst was pseudo-cubic-like in shape with nanoscale to submicron particles. The specific surface area, pore diameter and total pore volume of the $CuAl_2O_4$ were found to be 1.8 m^2/g, 0.02 cm^3/g and 11.4 nm, respectively. The TPR profile of the $CuAl_2O_4$ (**Fig. 1c**) demonstrated the tiny peak appeared at around 260 °C which should be assigned to the reduction of dispersed CuO particles to Cu^0 (Kwak et al., 2012). The stronger reduction peak was observed in the temperature range of 350-600 °C, corresponded to reduction of $CuAl_2O_4$ to Cu^0 (Luadthong et al., 2017). As observed in our previous study, the higher temperature led more complete reduction behavior of Cu oxide to metallic Cu, however, the activity of $CuAl_2O_4$ catalyst was decreased since the Cu particles were sintered at the reduction temperature higher than 300 °C (Thongratkaew et al., 2021). Therefore, the suitable reduction temperature was 300 °C.

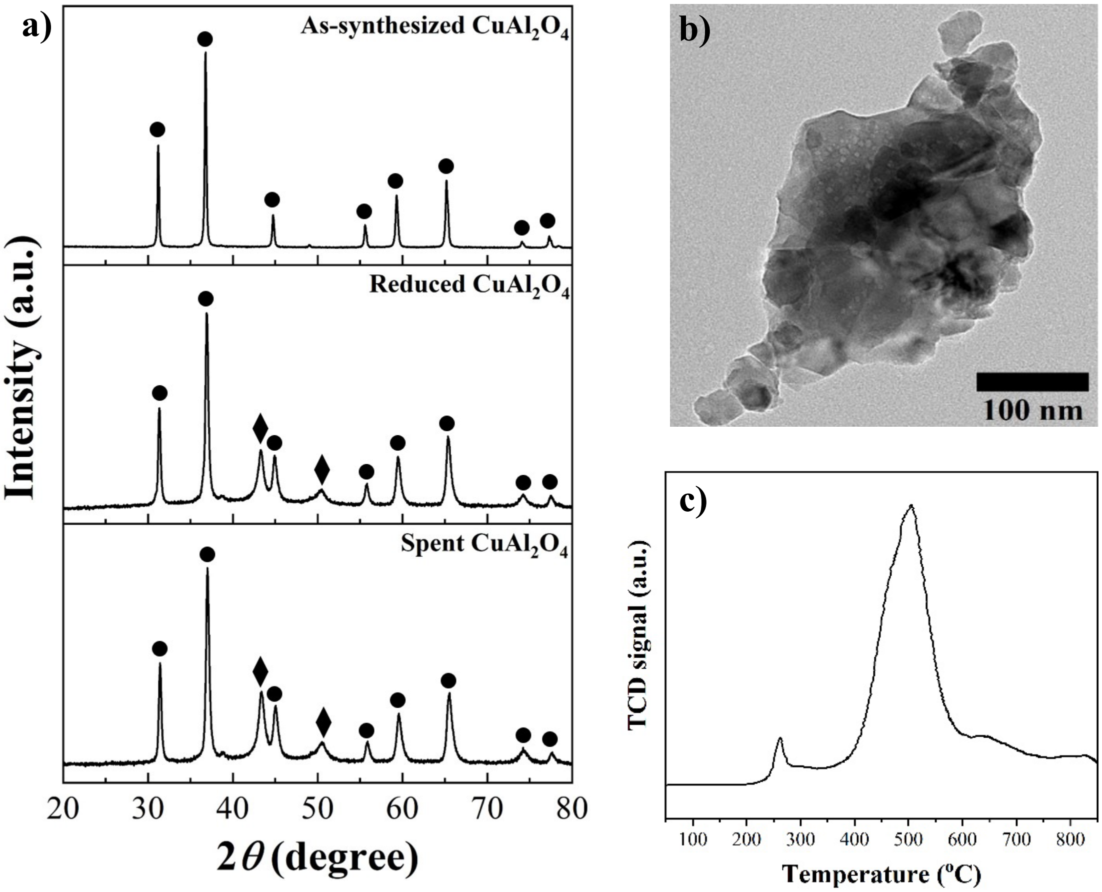

Fig. 1 a) XRD patterns of the as-synthesized $CuAl_2O_4$, reduced $CuAl_2O_4$ and spent $CuAl_2O_4$: cubic $CuAl_2O_4$ (●) and Cu^0 (♦), b) TEM image and c) TPR profile of the $CuAl_2O_4$ catalyst.

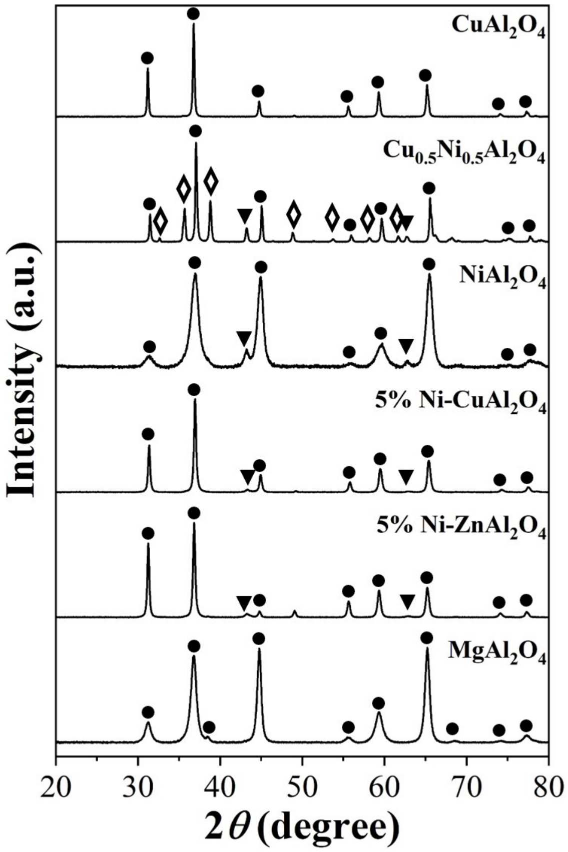

Fig. S1. XRD patterns of the $CuAl_2O_4$, $NiAl_2O_4$ $Ni_{0.5}Cu_{0.5}Al_2O_4$, 5%Ni-$CuAl_2O_4$ 5%Ni-$ZnAl_2O_4$ and $MgAl_2O_4$: cubic spinel (●), CuO (◊) and NiO (▼). 5%Ni-$CuAl_2O_4$ and 5%Ni-$ZnAl_2O_4$ were prepared by impregnating 5 wt% of Ni onto $CuAl_2O_4$ or $ZnAl_2O_4$ spinels in order to see the role of Ni species.

Catalytic performance of BAl_2O_4 *(B = Cu,* $Cu_{0.5}Ni_{0.5}$*, Ni, Zn, Mg)*

Various aluminate spinel catalysts with different divalent metals, BAl_2O_4 (B = Cu, $Cu_{0.5}Ni_{0.5}$, Ni, Zn, Mg), were initially screened to evaluate their catalytic performance. It was found that, among all catalysts, $CuAl_2O_4$ was selectively produce furfuryl alcohol (**Fig. S2a**) with highest FF conversion of ~100% (**Fig. S2b**) and FA yield of >98% (**Fig. S2c)**. Althought it is widely known that Ni-based catalysts would be active for hydrogenation reaction, the Ni or Ni-Cu aluminate spinels clearly showed lower activity compared to the Cu aluminate spinel. Therefore, $CuAl_2O_4$ was focused for further study and kinetic parameter evaluation.

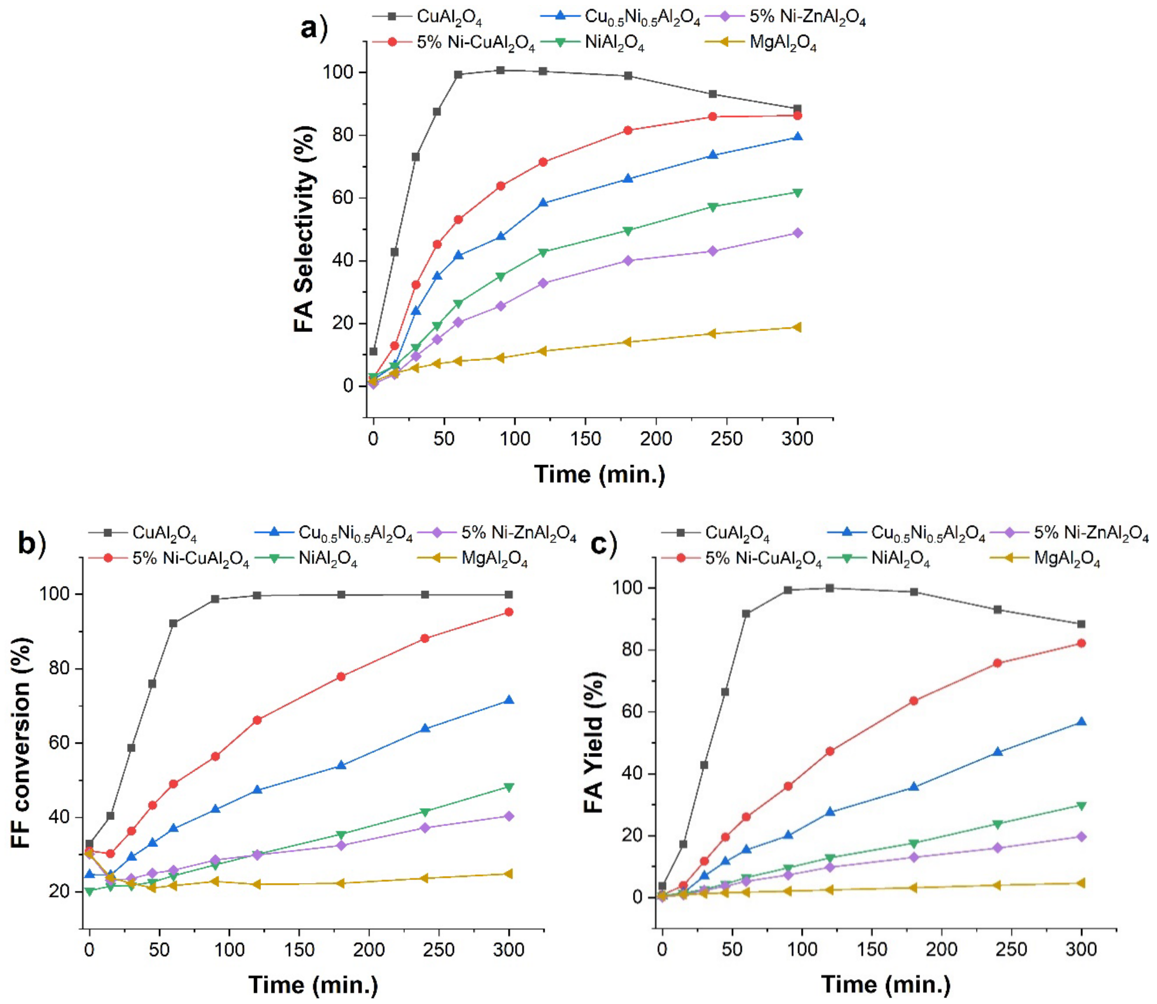

Fig. S2. Time-dependence of a) FF conversion, b) FA yield and c) FA selectivity on various aluminate spinel catalysts. Reaction condition: stirring speed of 400 rpm; initial FF concentration of 2 M; H_2 pressure of 20 bar; reaction temperature of 170 °C; each of the data is from the reaction time of 0, 15, 30, 45, 60, 90, 120, 180, 240 and 300 min. The copper aluminate spinel ($CuAl_2O_4$) showed the best performance among the catalysts. The Ni catalysts (spinel phases - $NiAl_2O_4$ and $Ni_{0.5}Cu_{0.5}Al_2O_4$) or Ni-impregated on the spinels (5% Ni-$ZnAl_2O_4$ and 5% Ni-$CuAl_2O_4$) all showed lower hydrogenation activity compared to the pre phase of $CuAl_2O_4$ spinel.

Optimization of reaction conditions for FF hydrogenation over $CuAl_2O_4$ catalyst

- *Effect of stirring speed*

Basically, the gas phase mass-transfer resistance in the FF hydrogenation reaction can be neglected due to the low vapor pressure of the solution and the low selectivity to gas products, resulting in the instantaneous gas-liquid interface saturation with H_2 (Gabrysch et al., 2019; Vasiliadou and Lemonidou, 2013). The external mass transfer limitations –H_2 transfer to the bulk liquid and reactant transport to catalyst surface– may differ depening on the experimental setup. Here, the effect of stirring speed (0, 400, 950 and 1,500 rpm) on the catalytic activity was studied at the reaction temperature of 170 °C, H_2 pressure of 20 bar and initial FF concentration of 2 M (see in **Fig. 2**). The results showed that the initial reaction rate in the system without stirring was remarkably low as compared to that in the stirring modes. Increasing the stirried speed to 400 rpm could enhance the reaction rate drastically, while further increase in stirring speed did not significantly affect the initial reaction rate. It was clearly shown that the influence of external diffusion resistance can be neglected when stirring at or above 400 rpm. The stirring speed of 400 rpm gave the highest FF conversion and FA yield of 89.4% and 92%, and was chosen for further experiments.

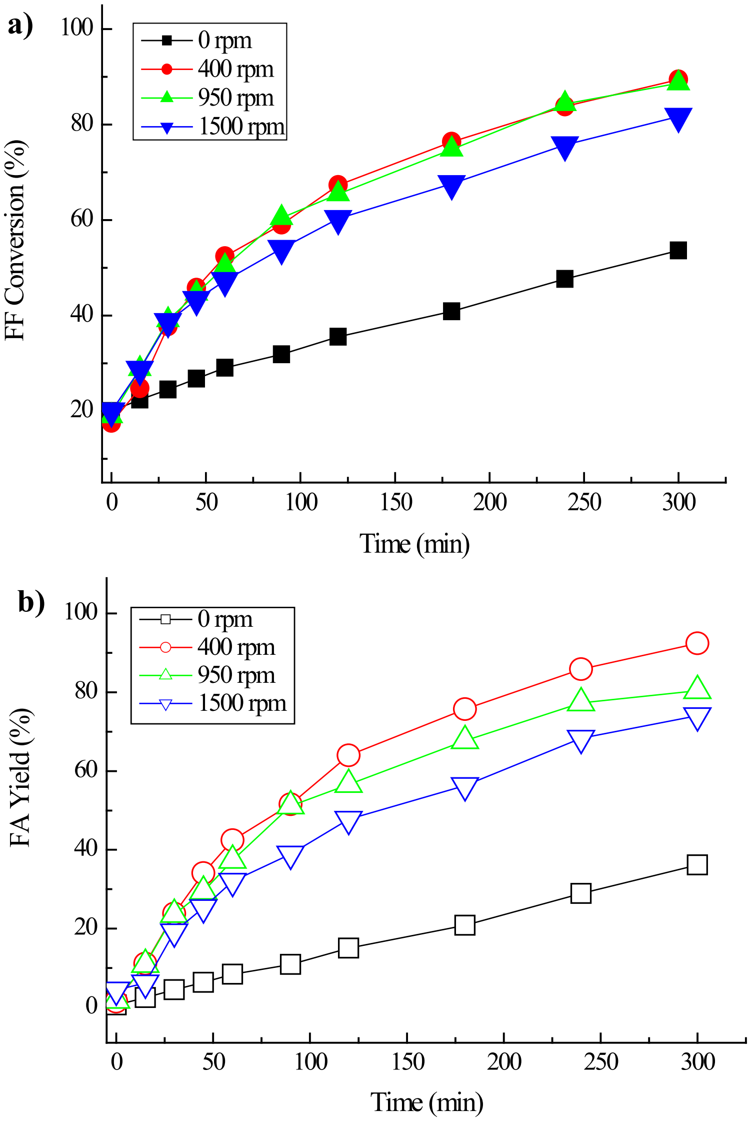

Fig. 2. Time-dependence of a) FF conversion and b) FA yield during FF hydrogenation over $CuAl_2O_4$ at various stirring speed. Reaction condition: stirring speed of 0, 400, 950 and 1,500 rpm; initial FF concentration of 2 M; H_2 pressure of 20 bar; reaction temperature of 170 °C.

- *Effect of furfural concentration*

Principally, reactant concentrations are one of the factors affecting the reaction rate and the rate law if the order of reaction is not zero (Dai et al., 2016; Sheng et al., 2017). The influence of FF concentration on catalytic performance over $CuAl_2O_4$ was studied in the batch reactor by varying the initial concentrations of 1, 2, 3 and 4 M at temperature of 170 ^oC and H_2 pressure of 20 bar (see in **Fig. 3**). The results demonstrated that the FF conversion increased rapidly with different slopes, at the beginning of the reaction. These referred to differences in initial reaction rates upon varied furfural concentrations. On the other hand, the result also indicated that the kinetic of the reaction was strongly impacted by the furfural concentration which would be taken into account as a kinetic parameter in the model. Moreover, the FF conversion could reach 100% within 300 min for all concentration variations. Meanwhile, the FA yield sharply increased as a function of time until it reached the maximum value of >98%. The increasing rates of the yield corresponded well with those of the conversion. However, prolonging reaction time decreased the FA yield, suggesting the over-hydrogenation of furfuryl alcohol to other products e.g., 2-methyltetrahydrofuran, methylfuran and pentanol. The decrease in FA yield was more severe at lower initial FF concentration. The initial FF concentration of 2–3 M seems to be the optimal conditions exhibiting high FA yield and wide operation window in the present study.

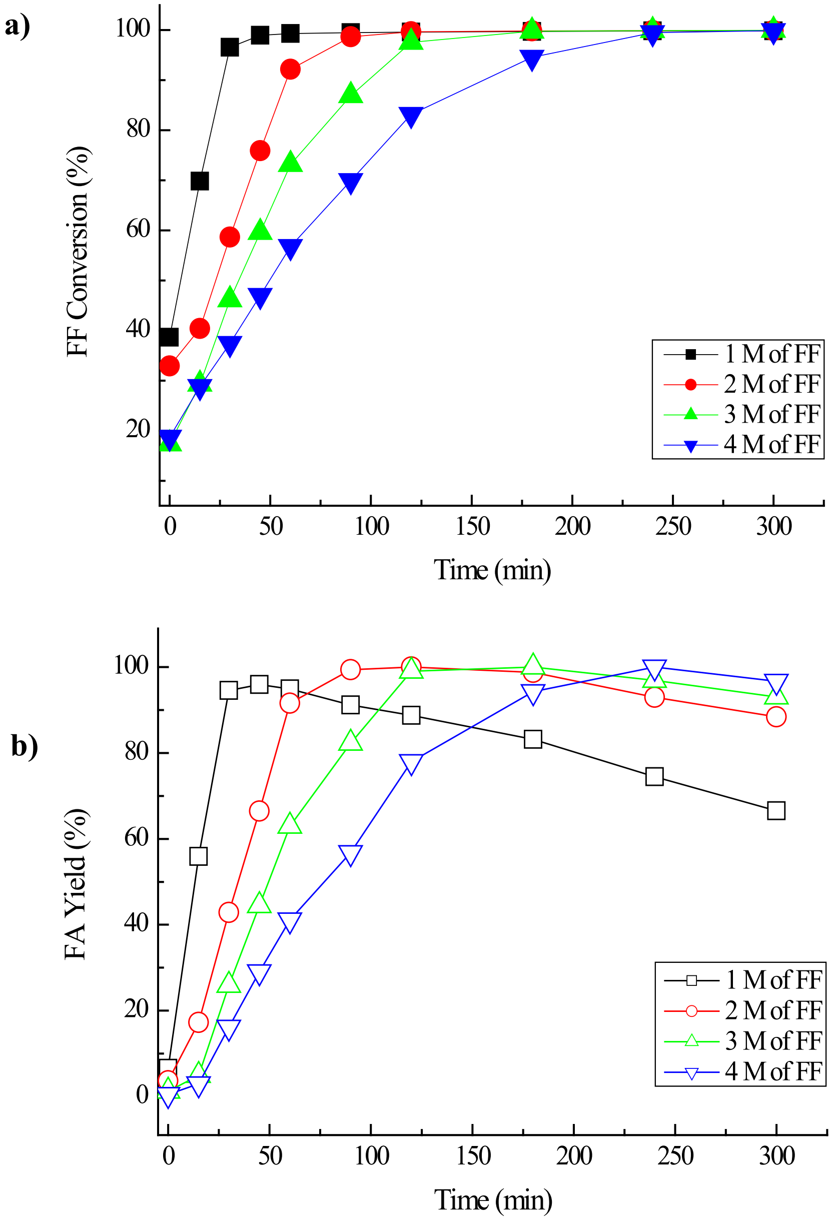

Fig. 3. Time-dependence of a) FF conversion and b) FA yield during FF hydrogenation over $CuAl_2O_4$ at various initial FF concentrations. Reaction condition: stirring speed at 400 rpm; initial FF concentration of 1, 2, 3 and 4 M; H_2 pressure of 20 bar; reaction temperature of 170 °C.

- *Effect of H_2 pressure*

The effect of H_2 partial pressure was investigated since H_2 is the co-reactant in the furfural hydrogenation reaction. It is known that the amount of dissolved H_2 in solution mixture is directly proportional to the H_2 partial pressure, and the use of external H_2 supply usually requires high H_2 pressure due to the soluble limitation of H_2 in the liquid phase (Gabrysch et al., 2019; Vasiliadou and Lemonidou, 2013). The catalytic performance over $CuAl_2O_4$ at various H_2 pressures of 10, 20 and 30 bar was shown in **Fig. 4**. It turned out that the increase of H_2 pressure from 10 to 20 bar clearly enhanced the initial rate of FF conversion to FA. However, no signicant change in the reaction rate was observed in the pressure range of 20-30 bar. The lower solubility of H_2 in the liquid phase at lower pressure would reduce the driving force in term of mass transport. In the present study, the high-pressure above 20 bar would drive the reaction outside the H_2 mass-transfer limitation zone. Therefore, it could be deduced that a zero-order with respect to H_2 partial pressure could be applied in the reaction rate expression. The long reaction time at high pressure of 30 bar would also lead to over-hydrogenation, lowering the FA yield.

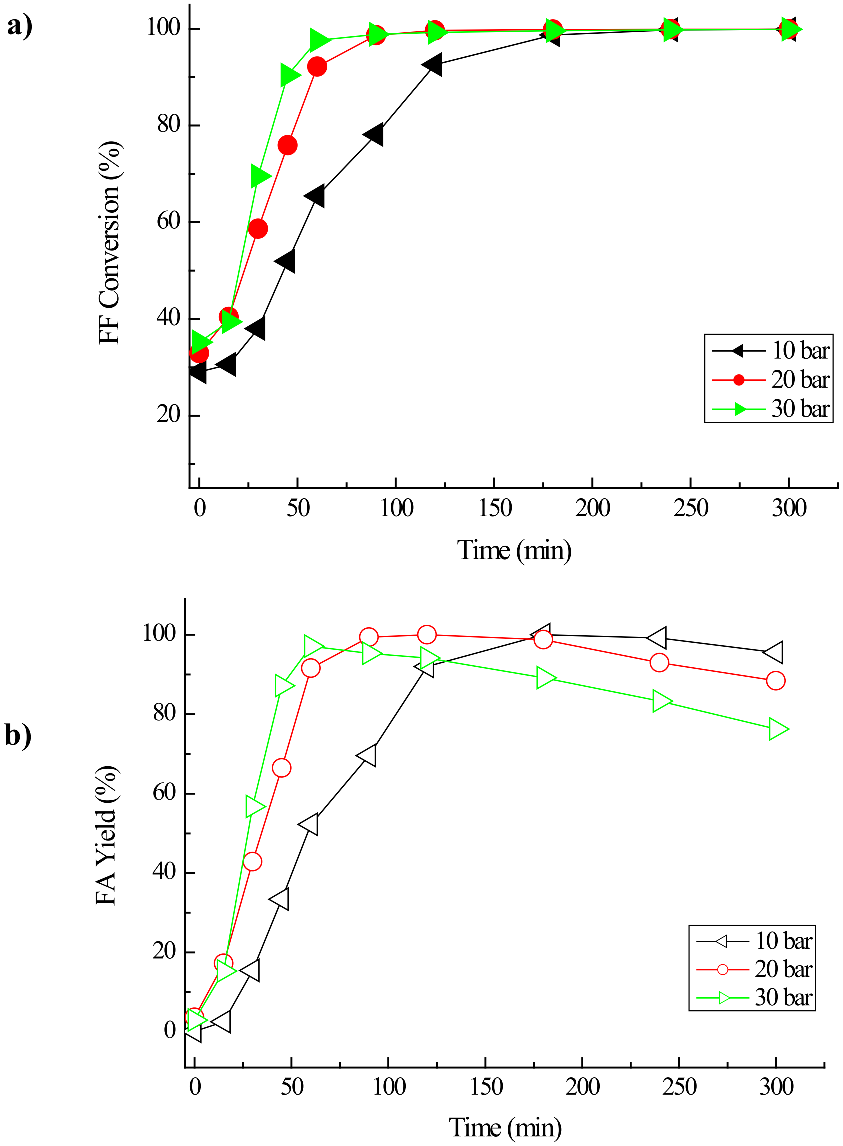

Fig. 4. Time-dependence of a) FF conversion and b) FA yield during FF hydrogenation over $CuAl_2O_4$ at various H_2 pressures. Reaction condition: stirring speed at 400 rpm; initial FF concentration of 2 M; H_2 pressure of 10, 20, and 40 bar; reaction temperature of 170 °C.

- *Effect of reaction temperature*

Reaction temperature is the important parameter for the kinetic analysis in order to investigate the apparent activation energy of the reaction. The influence of reaction temperature (150, 170 and 190 °C) on the catalytic performance over $CuAl_2O_4$ was studied under the H_2 pressure of 20 bar, initial FF concentration of 2 M and stirring speed of 400 rpm as the results shown in **Fig. 5**. It was observed that the reaction temperature remarkedly influenced the catalytic behaviors. The FF conversion could reach nearly 100% much faster at higher reaction temperatures. At 170 °C, the FA yield of 98-99% could remain stable in a reaction time period of 90–180 min, suggesting the promising operation window. Althought, at 190 °C, the maximum FA yield of 99% could be obtained within 45 min of the reaction. The FA yield suddenly decreased at longer time – the yield was 85% at 90 min and 45% at 300 min, suggesting that FA could be easily converted to other chemicals over the catalyst at high temperature (190 °C) such as 2-methyltetrahydrofuran and methylfuran which were observed in the GC chromatogram (**Fig. S3**) and consistent with our previous report (Thongratkaew et al., 2021). Moreover, these results also confirmed that the reaction temperature variation was the key parameter affecting the initial reaction rate, and the kinetic of FF hydrogenation.

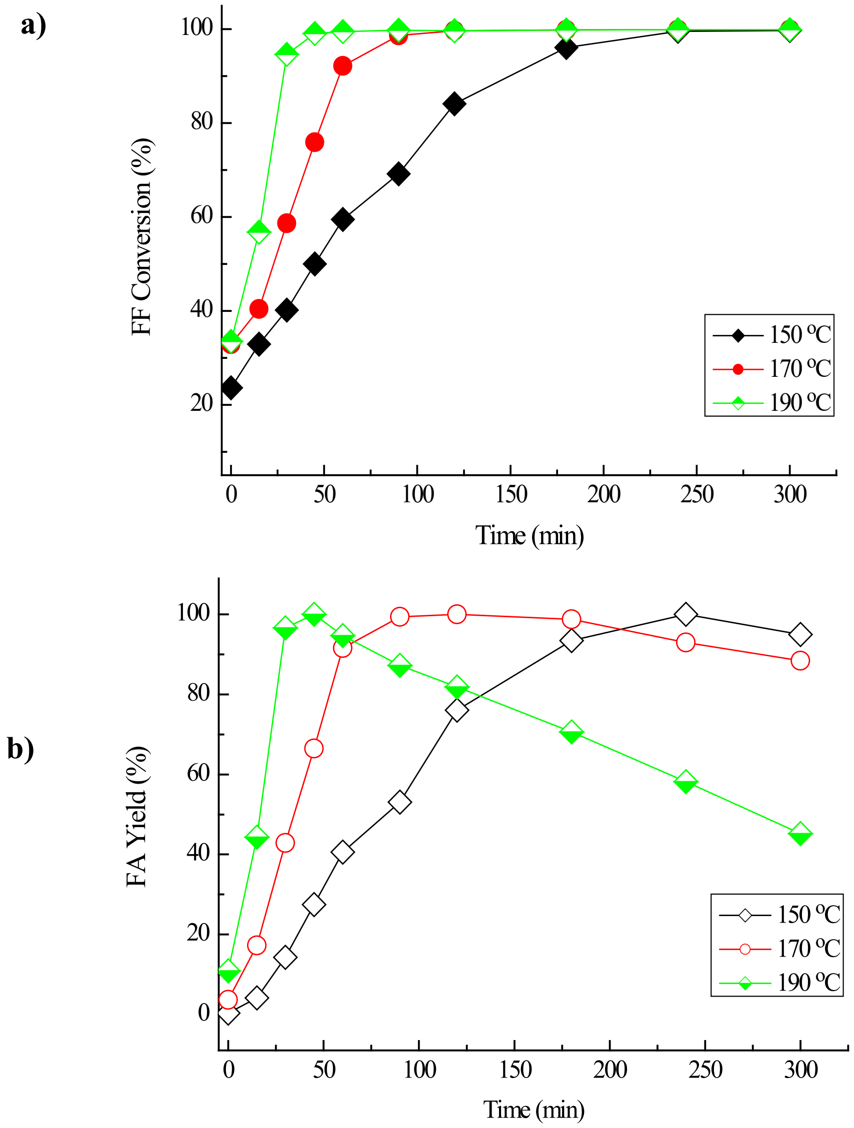

Fig. 5. Time-dependence of a) FF conversion and b) FA yield during FF hydrogenation over $CuAl_2O_4$ at various reaction temperatures. Reaction condition: stirring speed of 400 rpm; initial FF concentration of 2 M; H_2 pressure of 20 bar; reaction temperature of 150, 170 and 190 °C.

Kinetic study

According to the catalytic performance tests in the previous section, the FF concentration and reaction temperature were the two significant factors affecting the initial reaction rate while the external mass-transfer limitations can be avoided by using appropriate H_2 pressure and stirring speed. The kinetic model was assumed as the rate raw of n^{th}-order with respect to the furfural concentration as expressed in the following equation (3),

$$-\frac{dC_{FF}}{dt} = r = kC_{FF}^{n} \qquad (3)$$

where r is reaction rate (mol/(L·min), C_{FF} is FF concentration (M), t is reaction time (min), k is reaction rate constant and n is order of reaction rate. The relationship between C_{FF} and t from the results of initial FF concentration and reaction temperature variations were analyzed. The reaction rate (r) was calculated from the differential method by applying the equation (3) as shown in **Table 1** when the H_2 pressure and stirring speed were fixed at 20 bar and 400 rpm, respectively. The reaction rate increased with the increment of initial FF concentration at all reaction tempertures. In order to find the reaction order (n), the equation (3) is rearranged to the linear equation (4),

$$\ln(\mathrm{r}) = \mathrm{n}\ln(\mathrm{C_{FF}}) + \ln(\mathrm{k}) \qquad (4)$$

By fitting the experimental relationship between $\ln(\mathrm{r})$ and $\ln(\mathrm{C_{FF}})$, it was determined that the reaction order was 0.355 (R^2 of 0.997; see in **Fig. 6**). The results indicated that the kinetic model for FF hydrogenation to FA over $CuAl_2O_4$ was a non-elementary reaction. In addition, the reaction rate constant of 0.0195 at 170 ^{o}C was also determined from the intersect value in **Fig. 6**.

For the reaction temperature variation, the reaction rate was remarkably increased with the elevated temperature at the initial FF concentration of 2 M (see in **Table 1)** due to the high kinetic energy at high temperature. Meanwhile, the reaction rate constant tended to increase when the temperature was raised up. The reaction rate constant (k) is a function of reaction temperature in accordance with the Arrhenius equation as described in equation (5),

$$\mathrm{k} = \mathrm{A}e^{\frac{-\mathrm{E_A}}{\mathrm{RT}}} \qquad (5)$$

where $\mathrm{E_A}$ is apparent activation energy (J/mol), A is pre-exponential factor, R is gas constant (J/(mol·K)) and T is reaction temperature (K). In order to investigate the $\mathrm{E_A}$, the Arrhenius equation is rearranged to linear equation (6).

$$\ln(\mathrm{k}) = \frac{-\mathrm{E_A}}{\mathrm{R}}\left(\frac{1}{\mathrm{T}}\right) + \ln(\mathrm{A}) \qquad (6)$$

The experimental data were fitted in the relationship between $\ln(\mathrm{k})$ and $\left(\frac{1}{\mathrm{T}}\right)$ having R^2 of 0.983 (see in **Fig. 7)**. As the result, the $\mathrm{E_A}$ of 45.6 kJ/mol was obtained from the slope fitting while the pre-exponential factor of 2867.7 was calculated from the intersect value. Therefore, the kinetic model in term of reaction rate expression for FF hydrogenation to FA over $CuAl_2O_4$ was determined from all kinetic parameters as following,

$$-\frac{\mathrm{dC_{FF}}}{\mathrm{dt}} = (2867.7e^{\frac{-45647.6}{\mathrm{RT}}})\mathrm{C_{FF}^{0.355}} \qquad (7)$$

Table 1 Reaction rate and rate constant with variation of initial FF concentration and reaction temperature at H_2 pressure of 20 bar and stirring speed of 400 rpm.

Initial FF concentration (M)	Reaction temperature (°C)	Reaction rate (r) (mol/(L·min))	k
1	170	0.0194	0.0195
2		0.0249	
3		0.0295	
4		0.0313	
2	150	0.0152	0.0130
	170	0.0249	0.0195
	190	0.0427	0.0379

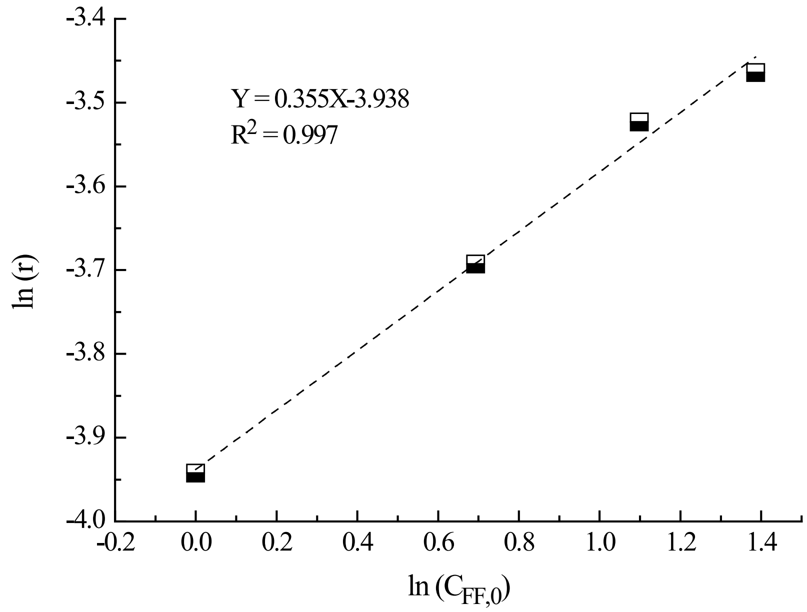

Fig. 6. Graph fitting of the experimental data applied with nth-order kinetic rate constant plots at 170 ºC.

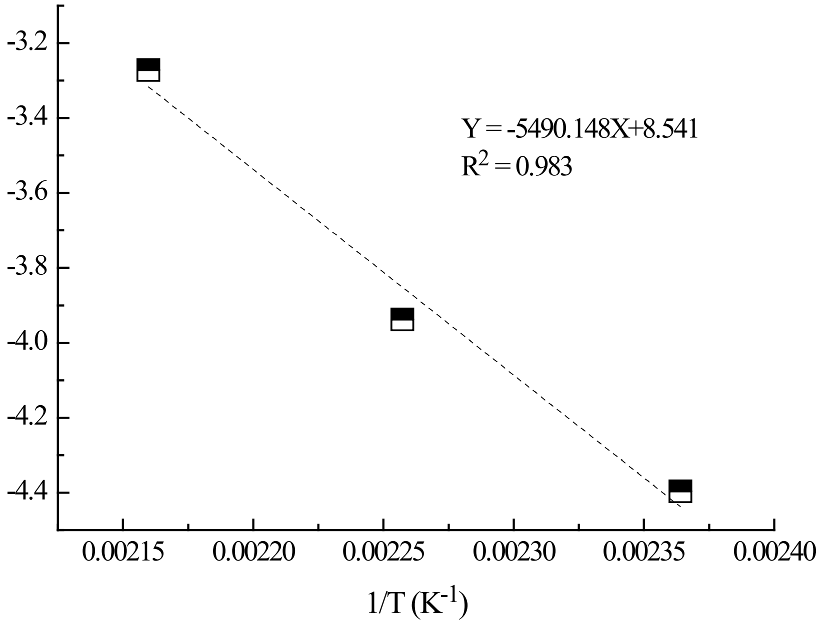

Fig. 7. Graph fitting of the experimental data applied with Arrhenius plots at initial FF concentration of 2 M.

The comparison of the obtained kinetic data (reaction order and activation energy) with known literature data derived from FA production via FF hydrogenation reaction was shown in **Table S1**. It was observed that reaction order with respect to FF and activation energy in this work was consistent with the literatures.

Table S1 Comparison of the obtained kinetic data with known literature data derived from furfuryl alcohol production via hydrogenation reaction.

Catalyst	Reaction condition	Reaction order with respect to FF	Activation energy (kJ/mol)	Ref.
$CuAl_2O_4$	Initial FF concentration of 1-4 M; H_2 pressure of 20 bar; Stirring speed of 400 rpm; reaction temperature of 170 °C; reaction time of 0-300 min	0.355	45.6	This work
Cu–Co/Al_2O_3	Initial FF concentration of ca. 1.75-3.25 M in 2-propanol; N_2 pressure of 20-50 bar; reaction temperature of 190-220 °C; reaction time of 3-6 h	0-0.86	50.2	(Srivastava et al., 2018)

5% Pt/C	Initial FF concentration of 0-0.13 M; H_2 pressure of 20.6 bar; reaction temperature of 150 ^oC	0-0.86	28	(Vaidya and Mahajani, 2003)
Co-Cu/SBA-15	FF/2-propanol mol ratio of 1:7; H_2 pressure of 30 bar; Stirring speed of 1000 rpm; reaction temperature of 130-190 ^oC; reaction time of 180 min	1	38.5	(Srivastava et al., 2015)
Zr_1B_3FeO	Initial FF concentration of ca. 0.08 M in 2-propanol; N_2 pressure of 10 bar; Stirring speed of 600 rpm; reaction temperature of 110-170 ^oC; reaction time of 20-120 min	1	48.3	(Li et al., 2021)
Copper chromite	FF pressure of 0.01 bar; H_2 pressure of 0.97 bar; reaction temperature of 150-200 ^oC	0.9	46.0 ± 8.4	Rao et al., 1997

The developed kinetic model leads to the advantages in the clarification and prediction the catalytic performance of the reaction over $CuAl_2O_4$ spinel catalyst in a batch reactor. Accordingly, the accuracy of the kinetic model was corroborated with the experimental data by curve fitting method (see in **Fig. 8)**. It was clear that the predicted data agreed well with the experimental ones. For the initial FF concentration variation (**Fig. 8a**), it was observed that the accuracy of the kinetic model was more precise at higher initial FF concentration as suggested by the increment of R^2. Meanwhile, the accuracy of the kinetic model for the reaction temperature variation was slightly lower at the elevated temperatures (**Fig. 8b**). The validation strongly confirmed that the developed kinetic model was acceptable, and should be a useful tool for advancing the reactor design and scale-up.

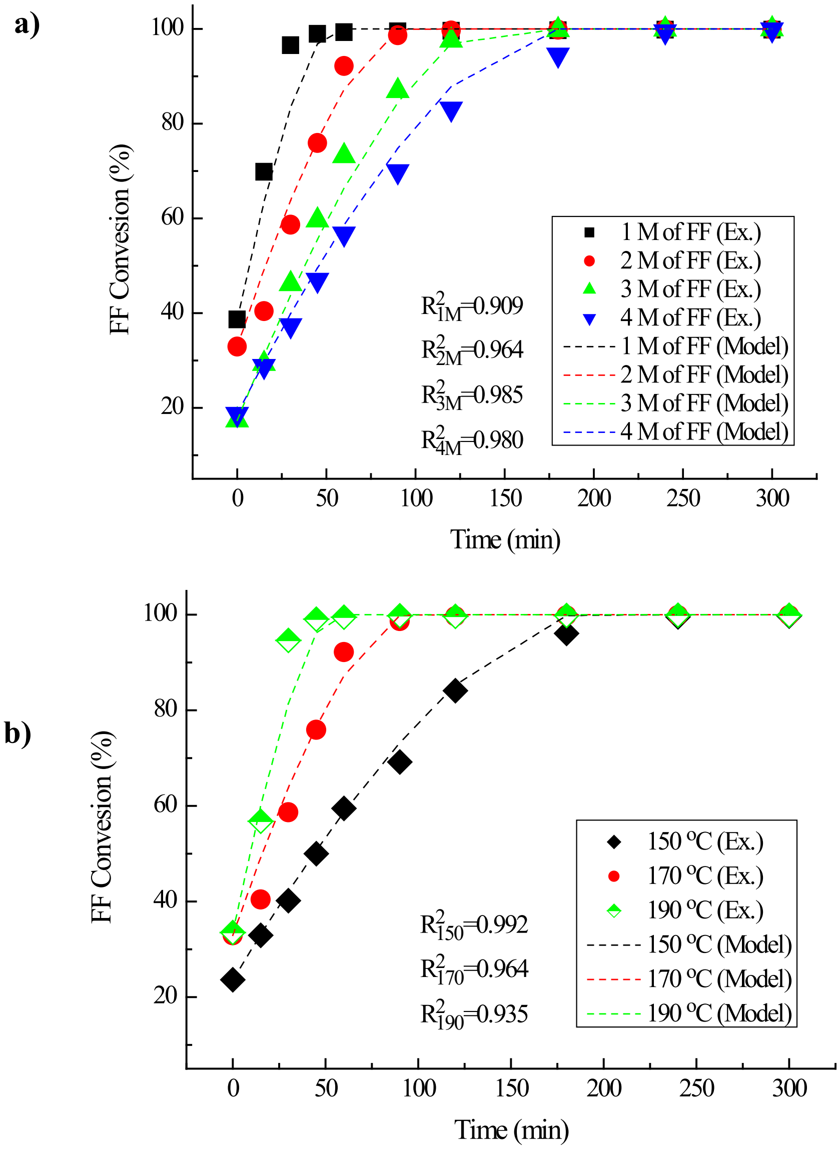

Fig. 8. Plots of validation curves between the predicted data from the kinetic model and the experimental data as a function of time with diferent initial FF concentrations and reaction tempertures. a) at initial furfural concentrations of 1, 2, 3 and 4 M and b) at reaction temperatures of 150, 170 and 190 °C.

Conclusions

The catalytic performance of furfural hydrogenation to furfuryl alcohol was studied over various aluminate spinel catalysts. The results showed that $CuAl_2O_4$ spinel outperformed the other BAl_2O_4 spinels (B = $Cu_{0.5}Ni_{0.5}$, Ni, Zn, Mg). The influence of reaction parameters including stirring speed, initial furfural concentration, H_2 pressure, and reaction temperature was investigated over $CuAl_2O_4$ spinel and the kinetic study was developed based on the experimental data. The results revealed that the external mass transfer limitations could be neglected when the batch reactor was operated at the appropriate stirring speed of 400 rpm and H_2 pressure of 20 bar. The catalytic performance was found to be highly sensitive to the furfural concentration and reaction temperature which are the important parameters for kinetic modelling. At the optimal condition, the $CuAl_2O_4$ showed excellent performance with the furfural conversion of 100% and the furfuryl alcohol yield of >98%. From the kinetic study, the 0.355-order with respect to furfural concentration was determined in the rate expression with the apparent activation energy of 45.6 kJ/mol. The predicted data were in good agreement with the experimental observation. The develop kinetic model provided a good prediction of the experimental results and also could be useful for development of the reactor, process design and scale-up in the industrial application.

Acknowledgements

This work was supported by the NANOTEC platform project (P1750381) and the CAS-NSTDA project (P1952712). This research is also supported in part by NANOTEC, the Ministry of Science and Technology, Thailand, through its program of Research Network of NANOTEC (RNN).

References

Borts, M.S., Gil'chenok, N.D., Gurevich, G.S., Ignat'ev, V.M., 1986. Kinetics of vapor-phase hydrogenation of furfural on a copper-chromium catalyst.

Dai, F., Wang, H., Gong, M., Li, C., Muhammad, Y., Li, Z., 2016. Modeling of kinetic-based catalyst grading for upgrading shale oil hydrogenation. Fuel 166, 19-23.

Faungnawakij, K., Shimoda, N., Fukunaga, T., Kikuchi, R., Eguchi, K., 2008. Cu-based spinel catalysts CuB2O4 (B=Fe, Mn, Cr, Ga, Al, Fe0.75Mn0.25) for steam reforming of dimethyl ether. Applied Catalysis A: General 341, 139-145.

Fulajtárova, K., Soták, T., Hronec, M., Vávra, I., Dobročka, E., Omastová, M., 2015. Aqueous phase hydrogenation of furfural to furfuryl alcohol over Pd–Cu catalysts. Applied Catalysis A: General 502, 78-85.

Gabrysch, T., Muhler, M., Peng, B., 2019. The kinetics of glycerol hydrodeoxygenation to 1,2-propanediol over Cu/ZrO2 in the aqueous phase. Applied Catalysis A: General 576, 47-53.

Ghashghaee, M., Shirvani, S., Ghambarian, M., 2017. Kinetic models for hydroconversion of furfural over the ecofriendly Cu-MgO catalyst: An experimental and theoretical study. Applied Catalysis A: General 545, 134-147.

Halilu, A., Ali, T.H., Atta, A.Y., Sudarsanam, P., Bhargava, S.K., Abd Hamid, S.B., 2016. Highly Selective Hydrogenation of Biomass-Derived Furfural into Furfuryl Alcohol Using a Novel Magnetic Nanoparticles Catalyst. Energy & Fuels 30, 2216-2226.

Kwak, B.K., Park, D.S., Yun, Y.S., Yi, J., 2012. Preparation and characterization of nanocrystalline CuAl2O4 spinel catalysts by sol–gel method for the hydrogenolysis of glycerol. Catalysis Communications 24, 90-95.

Li, D., Zhang, J., Liu, Y., Yuan, H., Chen, Y., 2021. Boron doped magnetic catalysts for selective transfer hydrogenation of furfural into furfuryl alcohol. Chemical Engineering Science 229.

Li, H., Chai, W.-M., Luo, H.-S., Li, H.-X., 2006. Hydrogenation of Furfural to Furfuryl Alcohol over Co-B Amorphous Catalysts Prepared by Chemical Reduction in Variable Media. Chinese Journal of Chemistry 24, 1704-1708.

Li, H., Luo, H., Zhuang, L., Dai, W., Qiao, M., 2003. Liquid phase hydrogenation of furfural to furfuryl alcohol over the Fe-promoted Ni-B amorphous alloy catalysts. Journal of Molecular Catalysis A: Chemical 203, 267-275.

Li, X., Jia, P., Wang, T., 2016. Furfural: A Promising Platform Compound for Sustainable Production of C4 and C5 Chemicals. ACS Catalysis 6, 7621-7640.

Liu, D., Zemlyanov, D., Wu, T., Lobo-Lapidus, R.J., Dumesic, J.A., Miller, J.T., Marshall, C.L., 2013. Deactivation mechanistic studies of copper chromite catalyst for selective hydrogenation of 2-furfuraldehyde. Journal of Catalysis 299, 336-345.

Liu, S., Amada, Y., Tamura, M., Nakagawa, Y., Tomishige, K., 2014. One-pot selective conversion of furfural into 1,5-pentanediol over a Pd-added Ir–ReOx/SiO2 bifunctional catalyst. Green Chemistry 16, 617-626.

Luadthong, C., Khemthong, P., Nualpaeng, W., Faungnawakij, K., 2016. Copper ferrite spinel oxide catalysts for palm oil methanolysis. Applied Catalysis A: General 525, 68-75.

Luadthong, C., Kuboon, S., Ratanatawanate, C., Nualpaeng, W., Viriya-Empikul, N., Faungnawakij, K., Pavasant, P., 2017. Cu-Based Spinels for Catalytic Hydrogenolysis of Glycerol to 1,2-Propanediol. Science of Advanced Materials 9, 34-41.

Merlo, A.B., Vetere, V., Ruggera, J.F., Casella, M.L., 2009. Bimetallic PtSn catalyst for the selective hydrogenation of furfural to furfuryl alcohol in liquid-phase. Catalysis Communications 10, 1665-1669.

Nagaraja, B.M., Siva Kumar, V., Shasikala, V., Padmasri, A.H., Sreedhar, B., David Raju, B., Rama Rao, K.S., 2003. A highly efficient Cu/MgO catalyst for vapour phase hydrogenation of furfural to furfuryl alcohol. Catalysis Communications 4, 287-293.

Rao, R., Dandekar, A., Baker, R.T.K., Vannice, M.A., 1997. Properties of Copper Chromite Catalysts in Hydrogenation Reactions. Journal of Catalysis 171, 406-419.

Sádaba, I., López Granados, M., Riisager, A., Taarning, E., 2015. Deactivation of solid catalysts in liquid media: the case of leaching of active sites in biomass conversion reactions. Green Chemistry 17, 4133-4145.

Sharma, R.V., Das, U., Sammynaiken, R., Dalai, A.K., 2013. Liquid phase chemo-selective catalytic hydrogenation of furfural to furfuryl alcohol. Applied Catalysis A: General 454, 127-136.

Sheng, Q., Wang, G., Zhang, Q., Gao, C., Duan, M., Gao, J., 2017. Kinetic model for liquid-phase liquefaction of asphaltene by hydrogenation with industrial distillate narrow fraction as hydrogen donor. Fuel 209, 54-61.

Srivastava, S., Solanki, N., Mohanty, P., Shah, K.A., Parikh, J.K., Dalai, A.K., 2015. Optimization and Kinetic Studies on Hydrogenation of Furfural to Furfuryl Alcohol over SBA-15 Supported Bimetallic Copper–Cobalt Catalyst. Catalysis Letters 145, 816-823.

Thongratkaew, S., Luadthong, C., Kiatphuengporn, S., Khemthong, P., Hirunsit, P., Faungnawakij, K., 2021. Cu-Al spinel-oxide catalysts for selective hydrogenation of furfural to furfuryl alcohol. Catalysis Today 367, 177-188.

Vaidya, P.D., Mahajani, V.V., 2003. Kinetics of Liquid-Phase Hydrogenation of Furfuraldehyde to Furfuryl Alcohol over a Pt/C Catalyst. Industrial & Engineering Chemistry Research 42, 3881-3885.

Vasiliadou, E.S., Lemonidou, A.A., 2013. Kinetic study of liquid-phase glycerol hydrogenolysis over Cu/SiO2 catalyst. Chemical Engineering Journal 231, 103-112.

Wu, J., Shen, Y., Liu, C., Wang, H., Geng, C., Zhang, Z., 2005. Vapor phase hydrogenation of furfural to furfuryl alcohol over environmentally friendly Cu–Ca/SiO2 catalyst. Catalysis Communications 6, 633-637.

Yuan, Q., Zhang, D., Haandel, L.v., Ye, F., Xue, T., Hensen, E.J.M., Guan, Y., 2015. Selective liquid phase hydrogenation of furfural to furfuryl alcohol by Ru/Zr-MOFs. Journal of Molecular Catalysis A: Chemical 406, 58-64.

6. Outputs

4.1 Publications

- Tanasan Intana; Sutarat Thongratkaew; Jeeranan Nonkumwong; Waleeporn Donphai; Thongthai Witoon; Metta Chareonpanich; Kajornsak Faungnawakij; Noriaki Sano; Sirapassorn Kiatphuengporn, Kinetics Study of the Selective Hydrogenation of Furfural to Furfuryl Alcohol over CuAl2O4 Spinel Catalysts, revision submitted 2023

- Soon-Chien Lu, Thakorn Wichidit, Thanitporn Narkkun, Kuo-Lun Tung, Kajornsak Faungnawakij, Chalida Klaysom, Aminosilane-Functionalized Zeolite Y in Pebax Mixed Matrix Hollow Fiber Membranes for CO2/CH4 Separation, Polymers, 15 (2022) 102

- Seth Sawatdiruk, Pongtorn Charoensuppanimit, Kajornsak Faungnawakij, Chalida Klaysom, POSS/PDMS composite pervaporation membranes for furfural recovery, Separation and Purification Technology 278 (2021) 119281

Proceeding

- Satienpong Pannawatwisut, Rungnapa Kaewmeesri, Toshiyuki Yokoi, Pakorn Opaprakasit, and Kajornsak Faungnawakij,Synthesis and Characterization of 2-Dimensional Zeolite Catalyst Using C22-6-6Br2 Template, Proceeding in Science and Technology of Emerging Materials (STEMa2022), Pattaya, THAILAND, 4-6 August 2022

- Nataphon Meeboonanake, Rungnapa Kaewmeesri, Toshiyuki Yokoi, Pakorn Opaprakasit, and Kajornsak Faungnawakij, Cobalt-based Catalysts Supported on Urea-Modified Sheet-Like ZSM-5 for Hydrodeoxygenation of FAMEs, Proceeding in Science and Technology of Emerging Materials (STEMa2022), Pattaya, THAILAND, 4-6 August 2022

- Pongkarn Chakthranont, Translating CO2 Reduction Testing from H-cell to Gas Diffusion Electrode”. International Conference on Materials for Humanity 2022 (MH 22), Singapore, September 2022 (Invited talk)

Award

- Dr. Kajornsak Faungnawakij was listed in The World's Top 2% Scientists List 2022 (in Physical Chemistry) by Stanford University and Elsevier
- Dr. Anchalee Jankaew, L'OREAL For Women in Science 2022

4.2 Exchange and Visitation

- JASTIP seminar was held online on March 24, 2021 with 24 participants from both Kyoto and Thailand.

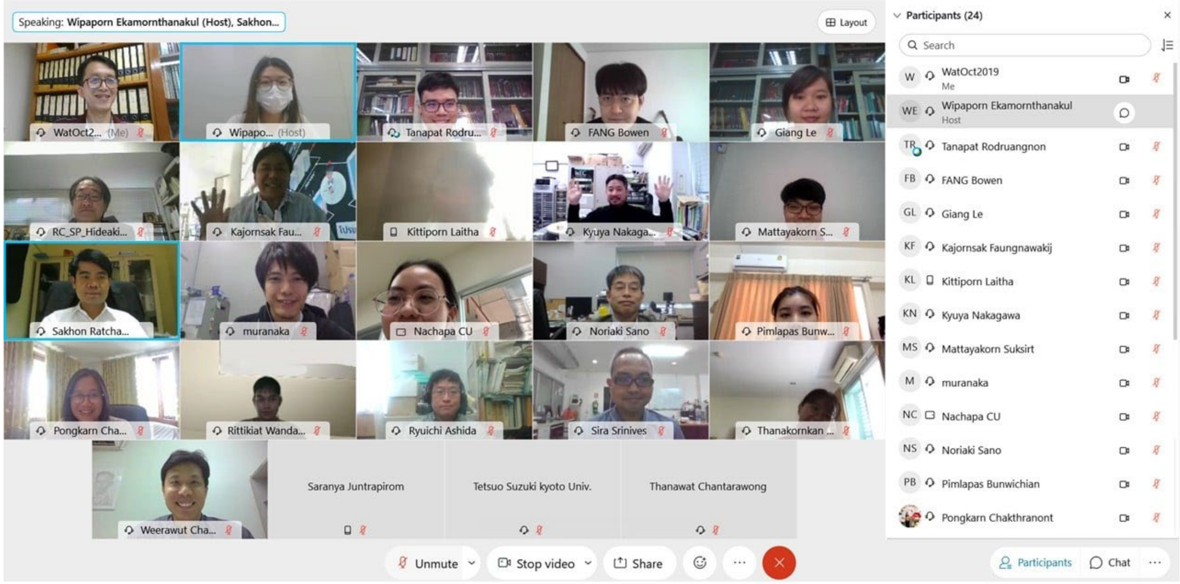
Speaking: Wipaporn Ekamornthanakul (Host), Sakhon...
Layout
WatOct2... (Me)
Wipapo... (Host)
Tanapat Rodru...
FANG Bowen
Giang Le
RC_SP_Hideaki...
Kajornsak Fau...
Kittiporn Laitha
Kyuya Nakaga...
Mattayakorn S...
Sakhon Ratcha...
muranaka
Nachapa CU
Noriaki Sano
Pimlapas Bunw...
Pongkarn Cha...
Rittikiat Wanda...
Ryuichi Ashida
Sira Srinives
Thanakornkan ...
Weerawut Cha...
Saranya Juntrapirom
Tetsuo Suzuki kyoto Univ.
Thanawat Chantarawong
Unmute
Stop video
Share
Participants (24)
Search
WatOct2019
Me
Wipaporn Ekamornthanakul
Host
Tanapat Rodruangnon
FANG Bowen
Giang Le
Kajornsak Faungnawakij
Kittiporn Laitha
Kyuya Nakagawa
Mattayakorn Suksirt
muranaka
Nachapa CU
Noriaki Sano
Pimlapas Bunwichian
Pongkarn Chakthranont
Participants
Chat

Catalytic pyrolysis process and hydrothermal liquefaction for bio-fuel production

Abstract

The ASEAN countries generate millions of cubic meters of agricultural waste products annually (e.g. palm kernel shells, rice husks, corn stover, coffee husks, sugarcane bagasse, etc.) that can potentially be tapped for bioenergy production. This large amount of residual biomass is widely available and can be converted to heat and power for agro-industrial processes. Studies have shown that lignocellulosic biomass can be converted to bioenergy using thermochemical, and biochemical processes such as fermentation, pyrolysis and gasification, among others. Development of alternative technologies for the productions of renewable energy from biomass found in ASEAN geographical locations could help stimulate widespread use of biomass as fuel source for industrial and residential heating needs in the region. Consequently, this could lead to the introduction of biomass fed furnaces, boilers and stoves for industrial and residential heating applications. In addition, the use of catalysts such as minerals can also enhance biomass conversion rate. This annual report highlights our recent works on the (1) techno-economics/environmental/societal/governmental (TESG) evaluation of thermochemical conversion of oil palm residues to alternative energies for ASEAN region, (2) aviation fuel production from palm fatty acid distillate by a single-step hydrotreating process and (3) hydrothermal conversion of empty fruit bunch lignin to fuels and chemicals.

Researchers

1. Prof Armando T. Quitain	Kumamoto University, Japan
2. Prof Suttichai Assabumrungrat	Chulalongkorn University, Thailand
3. Prof Ir. Suzana Yusup	Tenaga Nasional Berhad (TNB) Research, Malaysia
4. Dr Bridgid Chin Lai Fui	Curtin University Malaysia, Malaysia
5. Dr Yiin Chung Loong	Universiti Malaysia Sarawak, Malaysia
6. Dr Elisabeth Rianawati	Resilience Development Initiatives, Indonesia
7. Dr Worapon Kiatkittipong	Silpakorn University, Thailand
8. Mr Hj. Ismail Shariff	Tenaga Nasional Berhad (TNB) Research, Malaysia
9. Dr Atthapon Srifa	Mahidol University, Malaysia
10. Dr Apiluck Eiad-ua	King Mongkut's Institute of Technology Lakrabang, Thailand
11. Dr Jonas Karl Agutaya	Kumamoto University, Japan

1. Techno-economics/Environmental/Societal/Governmental (TESG) evaluation of thermochemical conversion of oil palm residues to alternative energies for ASEAN region

Abstract

This research project aims to compare different oil palm residues-to-fuel conversion technologies in terms of technical and economic efficiency, and environmental burdens to provide indications on the sustainability of such biorefineries. The materials and energy flows involved in these two processes for energy production will be analysed. Furthermore, the current status, challenges, and future policies related to oil palm residues to-fuel conversion technologies covering the techno-economics, environmental, and governmental (ESG) evaluations. Successful implementation of the project could help stimulate interest in the palm oil wastes for bio-oil, biofuel, heat and power production in ASEAN countries. Case study on the potential of utilising palm wastes as solid fuel for power generation is explored.

Research Summary

1. Renewable energy sources particularly in biomass energy had drew attention from public to researchers and scientists recently in seeking alternative solution to resolve the arising issues associated to climate change, unequal distribution of fossil fuels and fluctuation of fossil fuels prices faced globally. This study investigates the thermodynamic analysis and techno-economic feasibility of pyrolysis and gasification process for palm oil wastes in Malaysia. Empty fruit bunches (EFB), palm kernel shell (PKS), and palm mesocarp fibre (PMF) have been selected as the biomass feedstock in this current study.

   The model was developed by using Aspen Plus V10. The production of the biofuels includes the bio-char, bio-oil, and syngas. The operating conditions of the pyrolysis process involved and assessed in this study are as follows: Temperature (300-1,000°C), Pressure (1-10 bar) and carrier gas nitrogen (N_2)/biomass ratio (0.3-1.0). Furthermore, the operating conditions of the gasification process involved and assessed in this study are as follows: Temperature (500-1,500°C), air to biomass ratio and steam to biomass ratio (0.5-1.5). To assess the economic viability, there were four economic indicators used in the analysis which are project capital cost, operating cost, raw material cost and product sales. Fluctuation of biomass price was considered in the sensitivity studies of economic analysis. Payback period was estimated and compared for the thermochemical conversion of empty fruit bunches (EFB), palm kernel shell (PKS) and palm mesocarp fibres (PMF), via using cumulative cash flow diagram.

   According to the results generated from the simulation, temperature has the most obvious impact to the system. The char yield could be optimized at lower temperature, within 300℃-400℃ at yield of 55 wt%. Meanwhile, for the liquid and gaseous product yield peaked at 300℃ and 800℃ at yield of 15 wt% and 60 wt%, respectively. It is concluded that higher operating temperature favours in gas product. On the other hand, the parametric study for gasification process are temperature from 500℃ to 1500℃, and air/steam to biomass ratio from 0.5 to 1.5. The main products of gasification are char and syngas. It is concluded that temperature is favourable for the enhancement of gaseous product such as H_2 and CO. Techno-economic analysis revealed that the cost involved in the production of char by pyrolysis is generally lower than gasification process, cost per product for pyrolysis of EFB ($163/ton) is $33/ton lower than cost per product for gasification of EFB ($196/ton). However, the profitability of gasification is higher than pyrolysis due to high revenue per product of char. Apart from that, EFB is high profitable than PMF and PKS, despite in either gasification or pyrolysis process. This is because of cheaper feedstock price of EFB compared to PKS and PMF. These three biomass have very similar properties in term of proximate and ultimate analysis. Therefore, the product yield is insignificant affected by the type of palm oil biomass. On the other hand, the sensitivity analysis for economic study has concluded the profitability of pyrolysis and gasification process plant are sensitive to products price, and feedstock price, while the utilities and others input price impact the net present value (NPV) moderately. Furthermore, steam gasification has higher total project capital, operating cost than air gasification, thought it has high products sales to reduce high cost expenses.

2. The world's constant need for energy has significantly expanded as a result of population growth and economic expansion. Hence, many initiatives had been undertaken by Malaysia to seek renewable sources to replace the conventional fossil fuels. Biomass is said to be a potential source for renewable energy and production of value-added products. Additionally, biomass has gotten hold of global recognition in recent years owing to its natural abundance and low car-bon emission. In light of its availability and potential for renewable energy solutions, oil palm waste is a dependable resource. It is well known that palm oil rep-resents the cornerstone of Malaysia's economic growth, accounting for more than 5% of its Gross Domestic Product (GDP). The accumulation of oil palm wastes in the existing situation has caused many threats challenge that has an effect on the ecosystem. To achieve the optimal method for utilising oil palm wastes, technological, economic, and environmental concerns should be matched. As a result, optimising energy recovery from oil palm wastes is beneficial for both social and economic reasons. Alternative conversion strategies to achieve the maximum recovery comprise direct combustion, gasification, pyrolysis, liquefaction, fermentation, and anaerobic digestion. This could aid in promoting biomass consumption as a power source, in addition to protect the potential development of the biomass energy market within the country through practical utilization, simultaneously alleviating the poor waste management and indirectly generating employment. Hence, this work also aims to discuss on the possibilities of palm oil residues towards sustainable development in terms of social, technological, and economic aspects.

   It was found that bioenergy policy does not have great influence on the three main sustainability pillars namely, the economic, social and environment factors. It was found that economic factor is the predominant associated to the bioenergy policy. Nevertheless, both social and environmental factors also play a crucial role for the development of bioenergy structure of the country. In order to address these issues, effective regulations should be implemented and awareness from stakeholders, governments, industry players, and public could aid by synergising the bioenergy implementation which enables to create better under-standing and foster the relationship between the institutional governances in achieving the sustainable development for the bioenergy implementation.

3. As one of the major sources of greenhouse gases (GHG) emissions, the energy sector faces an urgent shift to cleaner energy sources. Currently, palm oil-based bioenergy has grown as a growing source of renewable energy, especially in the ASEAN region, where some of its members are the world's top palm oil producer nations. With recent technologies, the thermochemical conversion of oil palm residues has made it possible to develop alternatives for bioenergy sources. This research also aims to discover how thermochemical conversion can solve environmental, societal, and governance challenges in oil palm-based bioenergy.
   Whilst the oil palm industry gained attention for its high GHG emissions, utilizing its residues can solve recurring problems. Processed palm oil biomass using thermochemical conversion can serve as a substitute to produce lower emissions in combined heat and power (CHP) plants, as well as provide lower energy density, thus minimizing logistics costs. To perform this, investment incentives and strengthening supporting regulations become a strong foundation to boost the implementation of thermochemical conversion to further advance biomass as a sustainable energy source and decarbonization effort from the energy and industry sectors.

   The common challenges in oil palm-based biomass are related to greenhouse gases (GHGs) emissions from underutilized oil palm waste and land clearing throughout the plantation process, distribution cost of biomass products and inadequate processing method of oil palm waste among its practitioners. To perform successful thermochemical method adaptation in further the oil palm biomass industry, strengthening supporting regulations should become the cornerstone to enact the first movement and mainstreaming thermochemical conversion in oil palm biomass practices. For instance, the government will need to integrate conversion method options into the related action plan to achieve biomass development or even emission reduction targets. Additionally, investment incentives will also become essential to boost the implementation as research and technology development usually needs more cost to prove the feasibility, as well as to reach economies of scale during the technology shift.

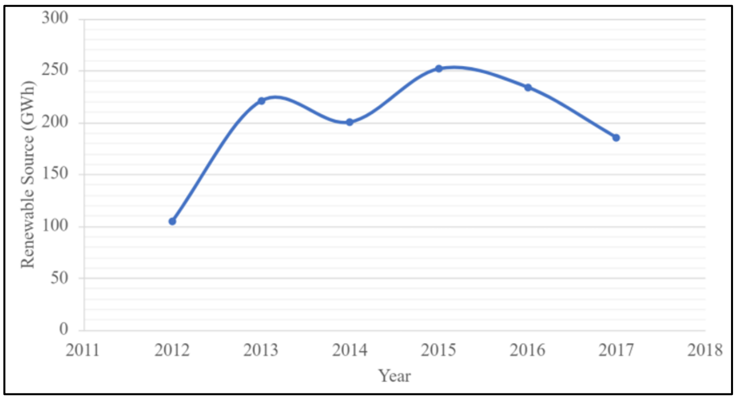

Figure 1: The renewable energy sources derived from biomass in Malaysia starting from year 2012-2018

4. The impact of co-firing of three types of oil palm wastes from Sarawak's oil palm plantation was explored as shown in Table 1, to test on their combustion performances and influence on co-firing combustion behaviour that influenced the utility boiler performance. The effect of solid fuel oil palm wastes on the slagging and fouling propensity, combustion temperature, plant efficiency, mill performance, percentage of unburnt carbon (UBC), and emission levels were determined through Computational Fluid Dynamics approach, for the in-furnace blending of the oil palm wastes and coal.

Table 1: Characterisation of Oil Palm Wastes (OPW)

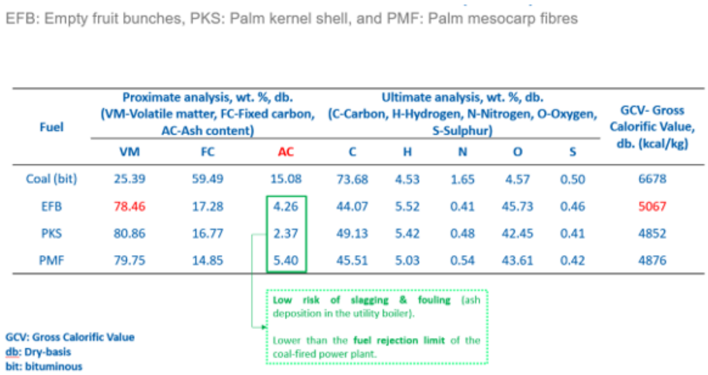

EFB: Empty fruit bunches, PKS: Palm kernel shell, and PMF: Palm mesocarp fibres

Fuel	Proximate analysis, wt. %, db. (VM-Volatile matter, FC-Fixed carbon, AC-Ash content)			Ultimate analysis, wt. %, db. (C-Carbon, H-Hydrogen, N-Nitrogen, O-Oxygen, S-Sulphur)					GCV- Gross Calorific Value, db. (kcal/kg)
	VM	FC	AC	C	H	N	O	S	
Coal (bit)	25.39	59.49	15.08	73.68	4.53	1.65	4.57	0.50	6678
EFB	78.46	17.28	4.26	44.07	5.52	0.41	45.73	0.46	5067
PKS	80.86	16.77	2.37	49.13	5.42	0.48	42.45	0.41	4852
PMF	79.75	14.85	5.40	45.51	5.03	0.54	43.61	0.42	4876

Low risk of slagging & fouling (ash deposition in the utility boiler).

Lower than the **fuel rejection limit** of the coal-fired power plant.

GCV: Gross Calorific Value
db: Dry-basis
bit: bituminous

In the study, it was calculated that for 20 cal% OPWs: 80 cal % coal, as indicated in Table 1, it would need approximately, 41tonne/hr of OPWs. Thus, in a day 24*4 t/hr= 984 tonne of OPWs would be needed for the stated ratio. Further, the OPWs ash contents (AC) were lower than the fuel rejection limit of the selected coal in this case the bituminous coal. These characteristics indicated that low risk of slagging and fouling by the ash deposition in the boiler. Figure 1 indicated the boiler nose temperatures for the baseline coal against each of the oil palm wastes. The nose area temperature must not exceed the initial deformation temperature of the fuel blends. Thus, the findings indicated that, co-firings of the understudied, types of OPWs are more suitable with sub-bituminous coal. In addition, higher volatiles matter compositions promote more combustion zones.

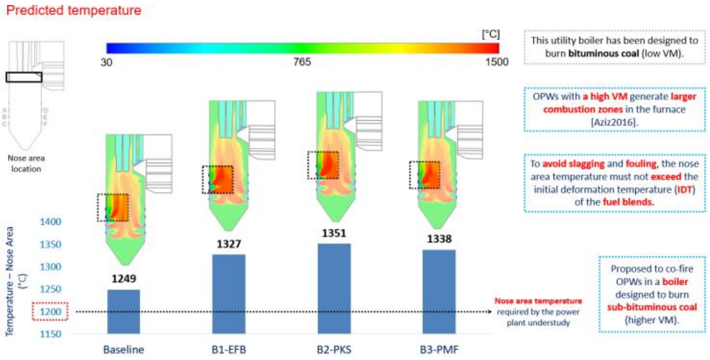

This utility boiler has been designed to burn **bituminous coal** (low VM).

OPWs with **a high VM** generate **larger combustion zones** in the furnace [Aziz2016].

To **avoid slagging** and **fouling**, the nose area temperature must not **exceed** the initial deformation temperature (**IDT**) of the **fuel blends.**

Proposed to co-fire OPWs in a **boiler** designed to burn **sub-bituminous coal** (higher VM).

The UBC levels were reduced when co-firing with OPWs because the OPWs-coal blends contain less Fixed Carbon than the pure coal blend. OPWs have lower FC than coal, resulting in lower CO and CO2 emissions when coal is co-fired with OPWs. Although OPWs contain less weight % db of N than the baseline coal, OPW co-firing cases were observed to produce more NOx than the baseline coal due to higher flame temperature generated, which resulted in an increase in thermal NOx. In conclusion, OPWs showed the potential to be co-fired with coal based on the computational fluid dynamic studies but further comprehensive analysis would be needed in finding the optimum blend and suitable partner coal to achieve desired power plant performance with efficient combustion in the utility boiler.

2. Aviation Fuel Production from Palm Fatty Acid Distillate by a Single-step Hydrotreating Process

Sustainable aviation fuel (SAF) is expected to play the largest role in the commitment of airlines to achieve net zero carbon by 2050 as called “Fly net zero”. In this study, industrial palm fatty acid distillate (PFAD), an inedible byproduct from the refining palm oil process, was used as a low-cost feedstock for SAF production.

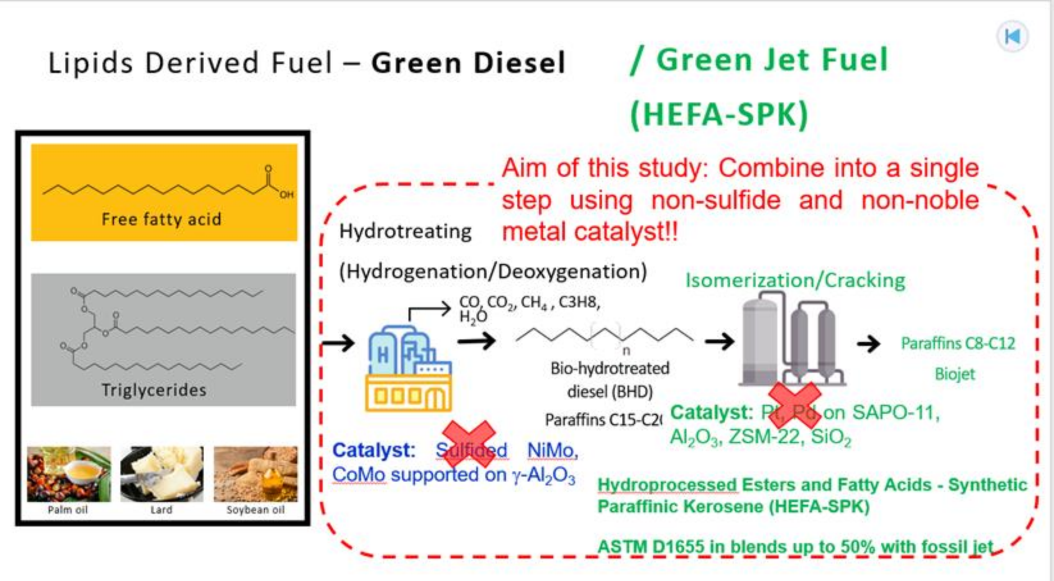

Lipids Derived Fuel – **Green Diesel** **/ Green Jet Fuel (HEFA-SPK)**

Aim of this study: Combine into a single step using non-sulfide and non-noble metal catalyst!!

Catalyst: ~~Sulfided~~ NiMo, CoMo supported on γ-Al_2O_3

Catalyst: ~~Pt, Pd~~ on SAPO-11, Al_2O_3, ZSM-22, SiO_2

Hydroprocessed Esters and Fatty Acids - Synthetic Paraffinic Kerosene (HEFA-SPK)

ASTM D1655 in blends up to 50% with fossil jet

Figure 2. Pictorial representation providing concept and advantages of a single-step hydrotreating process using non-sulfide and non-noble metal catalyst.

Hydroprocessed Esters and Fatty Acids - Synthetic Paraffinic Kerosene (HEFA-SPK) which also referred to hydrotreated renewable jet (HRJ) is powered the highest contribution of all SAF flights to date. Part of HEFA-SPK is based on the HEFA technology which is deoxygenation and isomerization. However, since the fuel specifications for aviation fuels are very stringent in comparing with diesel due to critical safety concerns and especially on cold flow properties, the liquid product is then cracked and isomerized (Figure 1) under the condition that maximizes jet fuel production. The aim of this study is to combine these two steps into a single step using non-sulfide and non-noble metal catalyst. The catalyst screening was performed in a 100-cm3 batch reactor (Figure 2a). The best catalyst could offer the highest conversion of 96% with the highest bio-jet yield of 51%. The catalyst stability was further studied in continuous flow reactor (Figure 2b) and the results showed that no catalyst deactivation could be observed for 48 h time-on-stream.

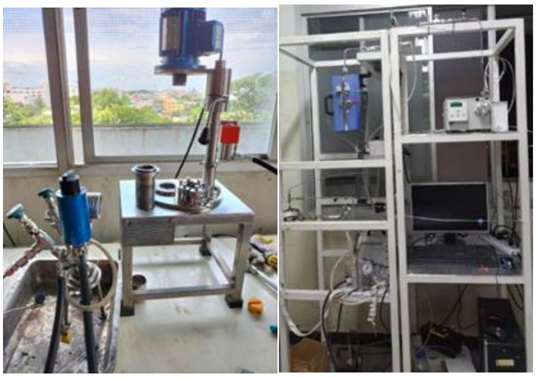

Figure 3. Experimental apparatus for HEFA-SPK production a) 100 cm3 batch reactor b) continuous trickle bed reactor.

3. Hydrothermal conversion of empty fruit bunch lignin to fuels and chemicals

One of the greatest challenges in biorefinery is to modify lignin structure with the purpose to reduce biomass' recalcitrance and enable lignin valorization such as conversion to higher value compounds. The search for a viable, sustainable and cost-efficient pretreatment method of lignocellulosic biomass is still considered a big challenge. Biomass delignification using LTTMs is still an underdefined process without considering the potential of bio-based fuels that can be produced from the green solvents-extracted lignin through hydrothermal liquefaction technology.

Figure 4 shows the steps for the conversion of lignin obtained from palm empty fruit bunch to useful chemicals and fuels. The obtained bio-oil was characterized using GC-MS analyses showing production of the target phenolic compounds in large amount at an optimum temperature of 250 ^{o}C and P = 20 MPa. The highest bio-oil yield of 77.42% was achieved at 20MPa, 275 degree and 5mL water per gram of lignin. From the GC-MS analysis of all the runs, phenolic compounds were confirmed to be present in the HTL product.

Hydrothermal liquefaction（HTL）

Extraction of bio-oil layer

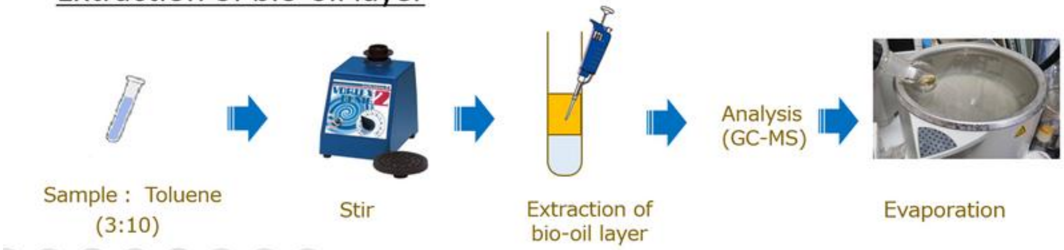

Figure 4. Steps for hydrothermal conversion of EFB lignin to useful chemicals and fuels

Publications and Presentation

1. Yiin, C.L., Odita, E.B., Lock, S.S.M., Cheah, K.W., Chan, Y.H., Wong, M.K., Chin, B.L.F., Quitain, A.T., Loh, S.K., S. Yusup, 2022. A review on potential of green solvents in hydrothermal liquefaction (HTL) of lignin, Bioresource Technology 364, 128075, doi: 0.1016/j.biortech.2022.128075. doi: 0.1016/j.biortech.2022.128075.

2. Suherrto, N.A.N., Chin, B.L.F., Salsabilla, A.H., Izzatunnisaa, Widiastomo, A., Rianawati, E., Yusup, S., Quitain, A.T., Agutaya, J. K., Shariff, H.I., Yiin, C.Y., Assabumrungrat S., Kiatkittipong, W., Srifa, A., Eiad-ua,. A., 2023. Utilisation of Oil Palm Residues for Malaysia's Sustainable Bioenergy Transition, World Integrated Chemical and Material Engineering Technology Conference 2023 (WiCMETC 2023), Thailand Bangkok.

3. Salsabilla, A.H., Izzatunnisaa, Widiastomo, A., Rianawati, E.,Chin, B.L.F., Yusup, S., Quitain, A.T. Agutaya, J.K., Shariff, H.I., Yiin, C.L., Assabumrungrat, S.Kiatkittipong, W., Srifa, A., Eiad-ua, A., 2023. Thermochemical conversion for enhancing oil palm biomass utilization as an energy source in ASEAN: Facing the challenges from policy perspective, Utilisation of Oil Palm Residues for Malaysia's Sustainable Bioenergy Transition, World Integrated Chemical and Material Engineering Technology Conference 2023 (WiCMETC 2023). Thailand Bangkok.

4. Chee, A.L.K., Chin, B.L.F., Goh, S.M.X., Chai, Y.H., Loy, A.C.M., Cheah, K.W., Yiin, C.L., Lock, S.S.M., 2023. Thermo-catalytic co-pyrolysis of palm kernel shell and plastic waste mixtures using bifunctional HZSM-5/limestone catalyst: Kinetic and

thermodynamic insights, Journal of the Energy Institute, 101194, doi: 10.1016/j.joei.2023.101194 (In Press, Journal Pre-proof).

5. Kumar, A.N., Chin, B.L.F., Chee, A.L.K., 2022. Kinetic analysis for catalytic co-pyrolysis of palm kenel shell and plastic waste mixtures with bifunctional HZSM-5 and mussel shell catalyst, IOP Conf. Series: Materials Science and Engineering 257 (2022) 012016, doi:10.1088/1757-899X/1257/1/012016.

Group Workshops, Meetings, and Research Exchange

1. **Special Symposium on "Materials for Environment Applications" in the Third International Conference on Science and Technology of Emerging Materials (STEMa2022), Thailand on the 5th August 2022 (Hybrid session).**

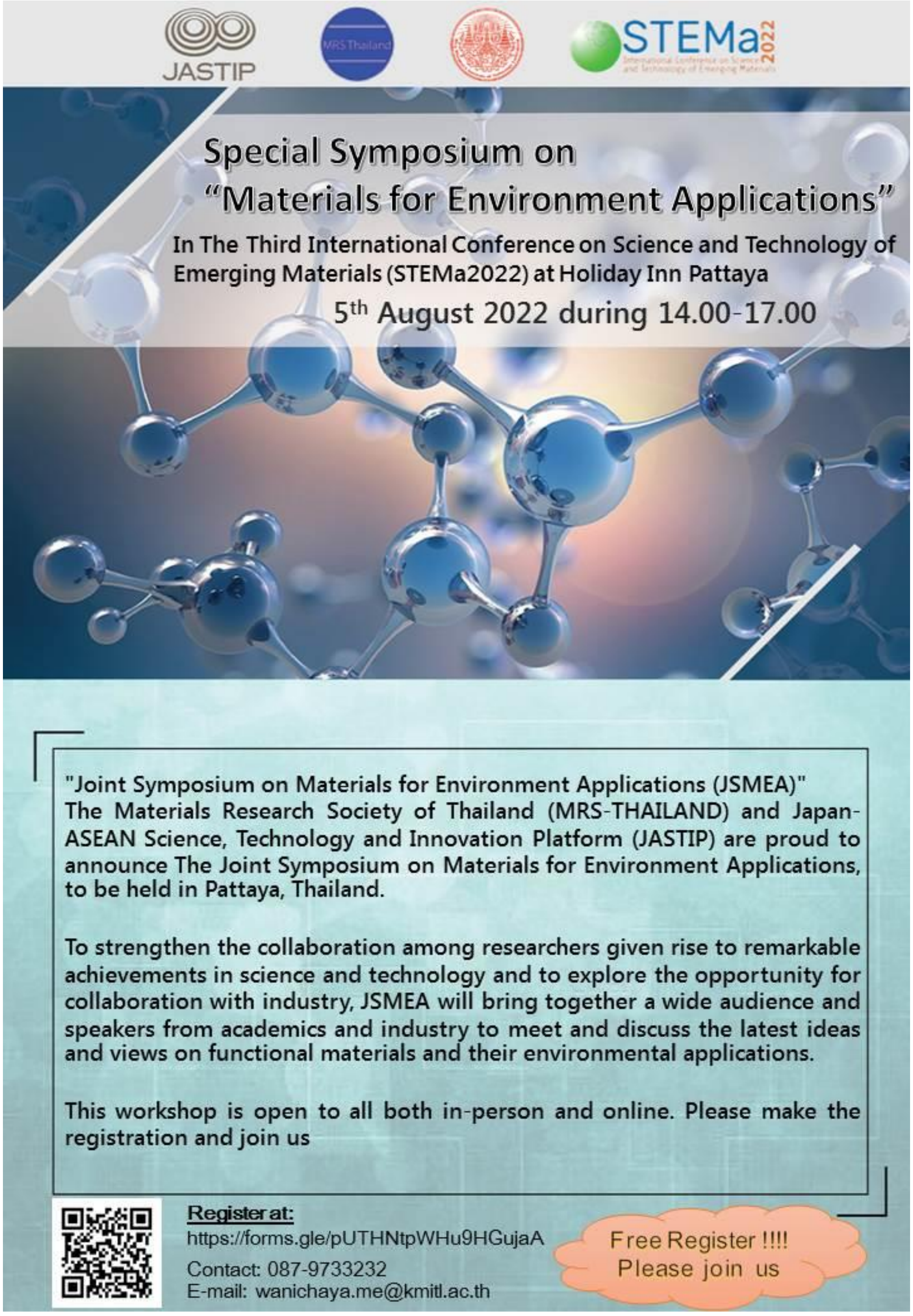

Special Symposium on
"Materials for Environment Applications"

In The Third International Conference on Science and Technology of Emerging Materials (STEMa2022) at Holiday Inn Pattaya

5th August 2022 during 14.00-17.00

"Joint Symposium on Materials for Environment Applications (JSMEA)"
The Materials Research Society of Thailand (MRS-THAILAND) and Japan-ASEAN Science, Technology and Innovation Platform (JASTIP) are proud to announce The Joint Symposium on Materials for Environment Applications, to be held in Pattaya, Thailand.

To strengthen the collaboration among researchers given rise to remarkable achievements in science and technology and to explore the opportunity for collaboration with industry, JSMEA will bring together a wide audience and speakers from academics and industry to meet and discuss the latest ideas and views on functional materials and their environmental applications.

This workshop is open to all both in-person and online. Please make the registration and join us

Register at:
https://forms.gle/pUTHNtpWHu9HGujaA
Contact: 087-9733232
E-mail: wanichaya.me@kmitl.ac.th

Free Register !!!!
Please join us

PROGRAM

Chairman: Prof. Dr. Keiichi N. Ishihara, Prof. Dr. Santi Maensiri and Assoc. Prof. Dr. Wisanu Pecharapa

Time	Activity
13.30-13.45	Registration for onsite and online participants
13.45-14.00	Welcome and Workshop Opening/ Group photo
14.00-14.20	Speaker 1 Prof. Dr. Keiichi N. Ishihara Graduate School of Energy Science, Kyoto University (Japan) *"The Mechanism of Z-scheme in Photocatalytic Degradation of Dyes"*
14.20-14.40	Speaker 2 Dr. Anis Natasha Shafawi (Online) School of Chemical Engineering, Universiti Sains Malaysia *"Bi_2O_3 Particles Decorated on Porous g-C_3N_4 Sheets: Enhanced Photocatalytic Activity through a Direct Z-scheme Mechanism for Degradation of Reactive Black 5 under UV–Vis Light"*
14.40-15.00	Speaker 3 Dr. Nonni Soraya Sambudi (Online) Chemical Engineering, Universiti Teknologi PETRONAS (Malaysia) *"Photoreduction of CO_2 by Using f-CQDs/TiO_2: Preliminary Study"*
15.00-15.20	Speaker 4 Assoc. Prof. Dr. Bridgid Chin Lai Fui (Online) Chemical and Energy Engineering, Curtin University (Malaysia) *"Catalytic Pyrolysis of Oil Palm Wastes for Bio-oil Production"*
15.20-15.40	*Coffee break*
15.40-16.00	Speaker 5 Assoc. Prof. Dr. Sorapong Pavasupree Faculty of Engineering, Rajamangala University of Technology Thanyaburi (RMUTT) *"Applications of Nano-materials from Thai Minerals"*
16.00-16.20	Speaker 6 Asst. Prof. Dr. Wanichaya Mekprasart College of Materials Innovation and Technology, King Mongkut's Institute of Technology Ladkrabang (KMITL) *"Photocatalytic performance of $BiVO_4$ Photocatalyst Incorporated with Different Metal Dopants"*
16.20-16.40	Speaker 7 Assoc. Prof. Dr. Pakorn Opaprakasit Sirindhorn International Institute of Technology, Thammasat University *"Towards A Circular Economy: Chemical Upcycling of Postconsumer Polymeric Products for Functional Materials"*
16.40-17.00	Speaker 8 Dr. Siwarutt Boonyarattanakalin SMS Corporation, SMS Group Thailand *"TAPIOPLAST®: The Functional Thermoplastic Starch Resin for Bioplastic Applications"*
17.00-17.10	*Q&A, Group discussion and Closing symposium*

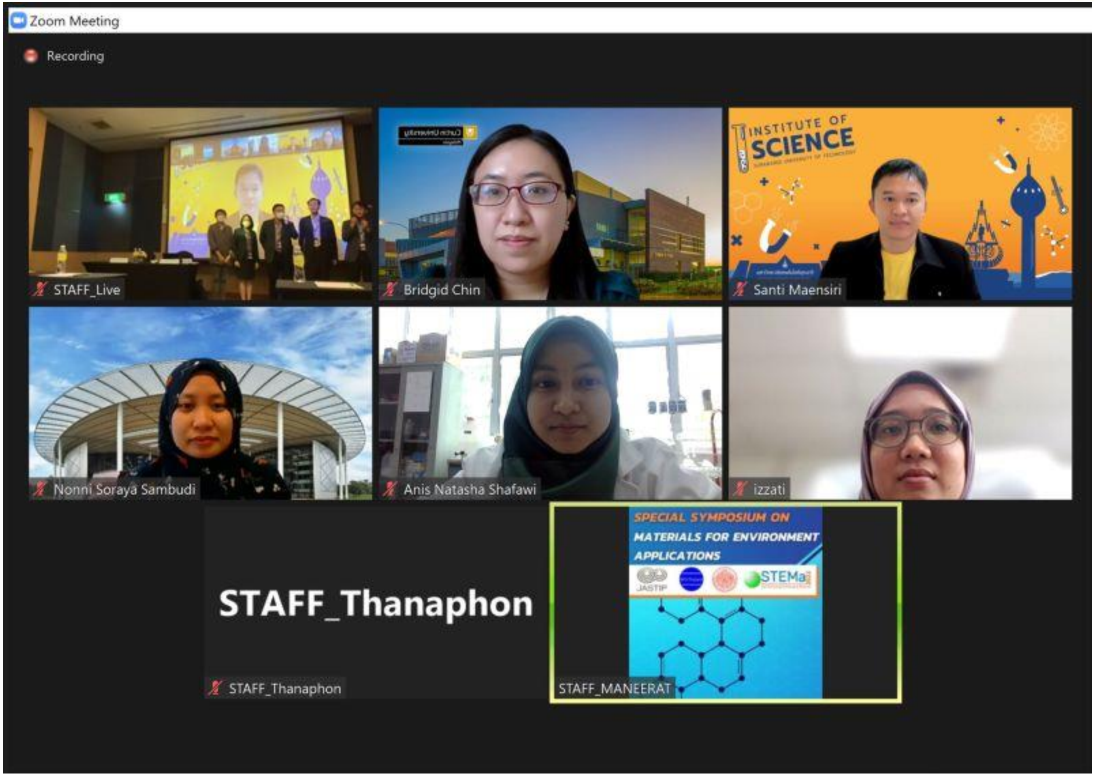

Figure 5: Group photo session on the STEMa2022 event. Dr Bridgid was invited to deliver a talk on 'Catalytic pyrolysis of palm oil wastes for bio-oil production' related to JASTIP-net 2022 project.

2. Group Discussion on the JASTIP-Net 2022 project on 17th August 2022 (Online session)

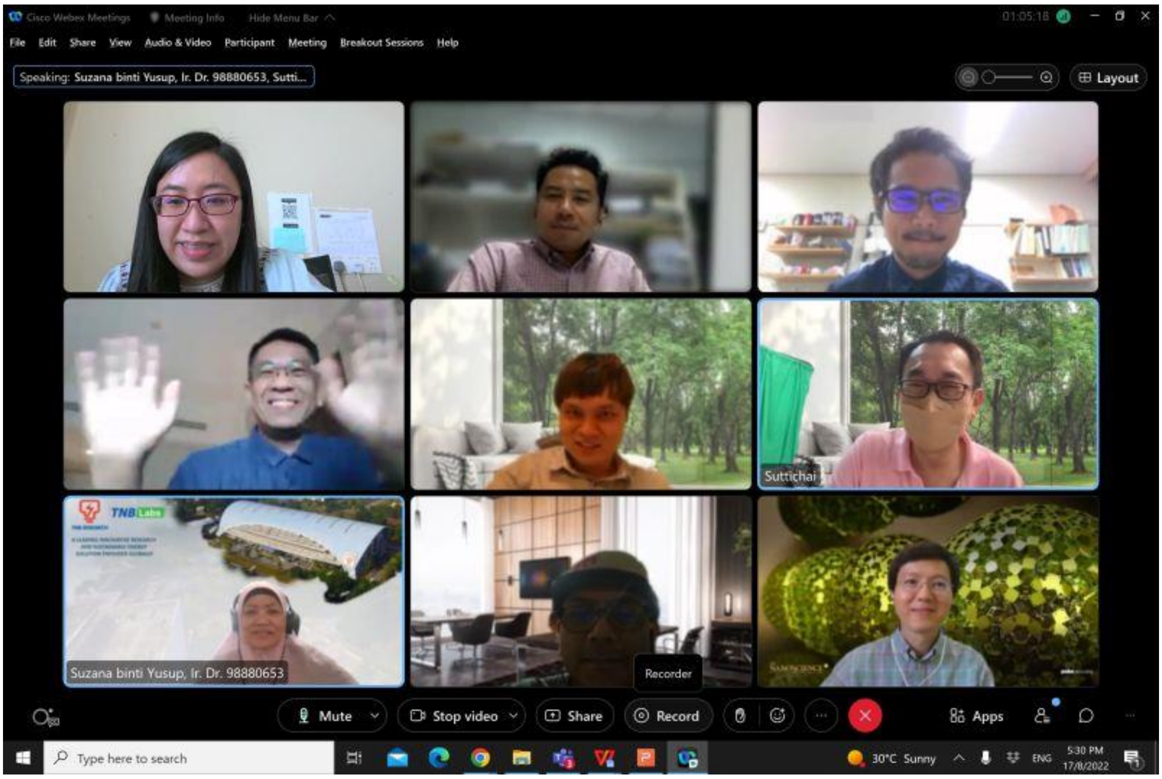

Figure 6: Screenshot on the group photo session after the group discussion on the JASTIP-Net 2022.

4. Courtesy Visit to Bio-Circular-Green Economy Technology & Engineering Center (BCGeTEC), Chulalongkorn University Thailand on 8th January 2023.

Figure 7: Group photo during the courtesy visit to Bio-Circular Green Economy Technology & Engineering Center (BCGeTEC) hosted by Prof Suttichai Assabumrungrat, Director of BCGeTEC.

Figure 8: Prof Suttichai Assabumrungrat hosted the visit introduces the initiatives of the BCGeTEC and the JASTIP-net 2022 team discussed on the research way forward.

3. The 8th JASTIP-WP2 Annual Workshop on 9th January 2023 at CO113, TSP, NSTDA.

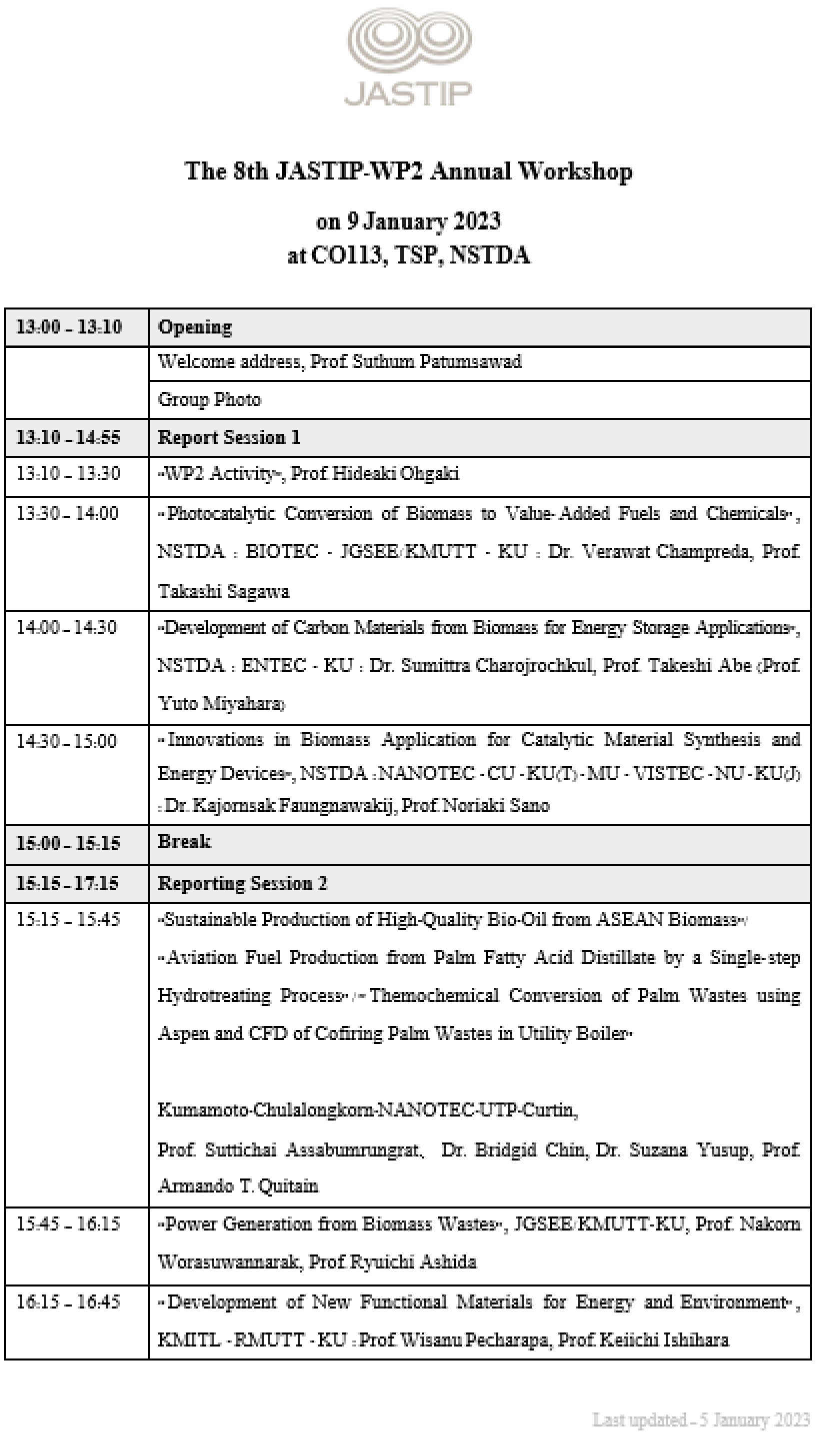

JASTIP

The 8th JASTIP-WP2 Annual Workshop

on 9 January 2023
at CO113, TSP, NSTDA

13:00 - 13:10	**Opening**
	Welcome address, Prof Suthum Patumsawad
	Group Photo
13:10 - 14:55	**Report Session 1**
13:10 - 13:30	«WP2 Activity», Prof Hideaki Ohgaki
13:30 - 14:00	«Photocatalytic Conversion of Biomass to Value-Added Fuels and Chemicals», NSTDA : BIOTEC - JGSEE/KMUTT - KU : Dr. Verawat Champreda, Prof Takashi Sagawa
14:00 - 14:30	«Development of Carbon Materials from Biomass for Energy Storage Applications», NSTDA : ENTEC - KU : Dr. Sumittra Charojrochkul, Prof. Takeshi Abe (Prof Yuto Miyahara)
14:30 - 15:00	«Innovations in Biomass Application for Catalytic Material Synthesis and Energy Devices», NSTDA : NANOTEC - CU - KU(T) - MU - VISTEC - NU - KU(J) : Dr. Kajornsak Faungnawakij, Prof. Noriaki Sano
15:00 - 15:15	**Break**
15:15 - 17:15	**Reporting Session 2**
15:15 - 15:45	«Sustainable Production of High-Quality Bio-Oil from ASEAN Biomass»/ «Aviation Fuel Production from Palm Fatty Acid Distillate by a Single-step Hydrotreating Process» / «Themochemical Conversion of Palm Wastes using Aspen and CFD of Cofiring Palm Wastes in Utility Boiler» Kumamoto-Chulalongkorn-NANOTEC-UTP-Curtin, Prof. Suttichai Assabumrungrat, Dr. Bridgid Chin, Dr. Suzana Yusup, Prof. Armando T. Quitain
15:45 - 16:15	«Power Generation from Biomass Wastes», JGSEE/KMUTT-KU, Prof. Nakorn Worasuwannarak, Prof Ryuichi Ashida
16:15 - 16:45	«Development of New Functional Materials for Energy and Environment», KMITL - RMUTT - KU : Prof. Wisanu Pecharapa, Prof. Keiichi Ishihara

Last updated - 5 January 2023

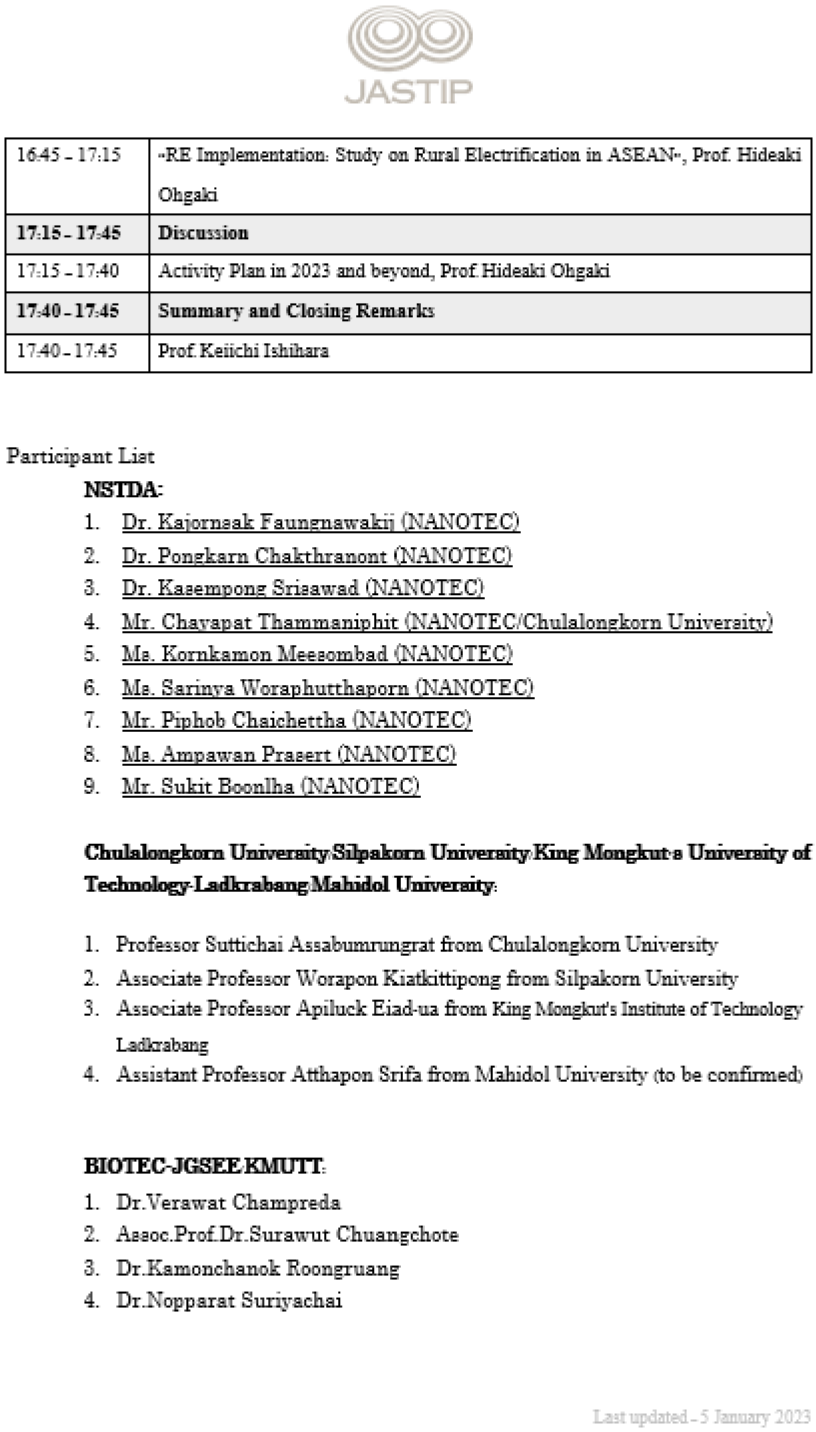

16:45 – 17:15	“RE Implementation: Study on Rural Electrification in ASEAN”, Prof. Hideaki Ohgaki
17:15 – 17:45	**Discussion**
17:15 – 17:40	Activity Plan in 2023 and beyond, Prof. Hideaki Ohgaki
17:40 – 17:45	**Summary and Closing Remarks**
17:40 – 17:45	Prof. Keiichi Ishihara

Participant List

NSTDA:

1. Dr. Kajornsak Faungnawakij (NANOTEC)
2. Dr. Pongkarn Chakthranont (NANOTEC)
3. Dr. Kasempong Srisawad (NANOTEC)
4. Mr. Chayapat Thammaniphit (NANOTEC/Chulalongkorn University)
5. Ms. Kornkamon Meesombad (NANOTEC)
6. Ms. Sarinya Woraphutthaporn (NANOTEC)
7. Mr. Piphob Chaichettha (NANOTEC)
8. Ms. Ampawan Prasert (NANOTEC)
9. Mr. Sukit Boonlha (NANOTEC)

Chulalongkorn University/Silpakorn University/King Mongkut's University of Technology-Ladkrabang/Mahidol University:

1. Professor Suttichai Assabumrungrat from Chulalongkorn University
2. Associate Professor Worapon Kiatkittipong from Silpakorn University
3. Associate Professor Apiluck Eiad-ua from King Mongkut's Institute of Technology Ladkrabang
4. Assistant Professor Atthapon Srifa from Mahidol University (to be confirmed)

BIOTEC-JGSEE-KMUTT:

1. Dr.Verawat Champreda
2. Assoc.Prof.Dr.Surawut Chuangchote
3. Dr.Kamonchanok Roongruang
4. Dr.Nopparat Suriyachai

Last updated – 5 January 2023

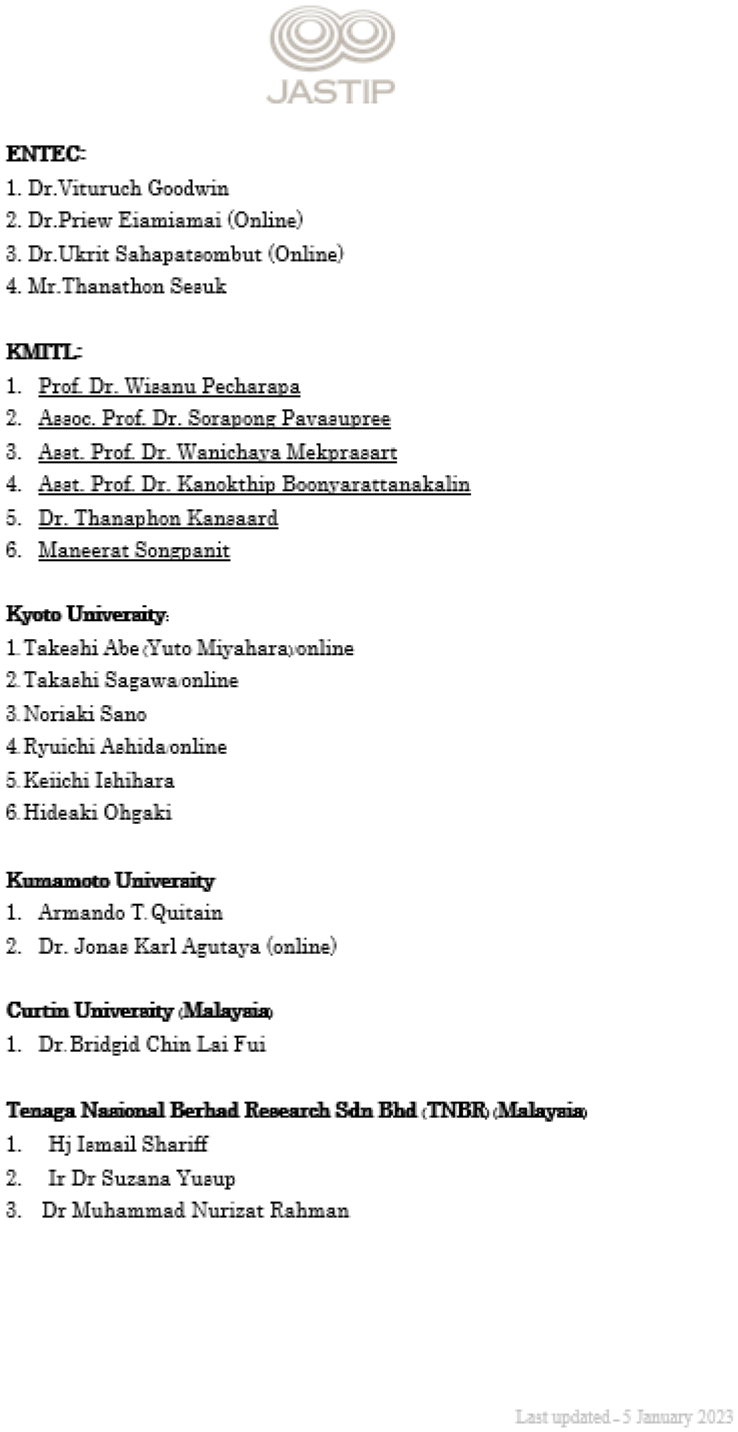

ENTEC:

1. Dr.Vituruch Goodwin
2. Dr.Priew Eiamiamai (Online)
3. Dr.Ukrit Sahapatsombut (Online)
4. Mr.Thanathon Sesuk

KMITL:

1. Prof. Dr. Wisanu Pecharapa
2. Assoc. Prof. Dr. Sorapong Pavasupree
3. Asst. Prof. Dr. Wanichaya Mekprasart
4. Asst. Prof. Dr. Kanokthip Boonyarattanakalin
5. Dr. Thanaphon Kansaard
6. Maneerat Songpanit

Kyoto University:

1. Takeshi Abe (Yuto Miyahara) online
2. Takashi Sagawa online
3. Noriaki Sano
4. Ryuichi Ashida online
5. Keiichi Ishihara
6. Hideaki Ohgaki

Kumamoto University

1. Armando T. Quitain
2. Dr. Jonas Karl Agutaya (online)

Curtin University (Malaysia)

1. Dr. Bridgid Chin Lai Fui

Tenaga Nasional Berhad Research Sdn Bhd (TNBR) (Malaysia)

1. Hj Ismail Shariff
2. Ir Dr Suzana Yusup
3. Dr Muhammad Nurizat Rahman

Last updated - 5 January 2023

Figure 9: Group photo of the team members from the JASTIP-Net 2022 research project, 'Techno-economics/Environmental/Societal/Governmental (TESG) evaluation of thermochemical conversion of oil palm residues to alternative energies for ASEAN region'.

Figure 10: Group photo after the 8th JASTIP-WP2 Annual Workshop in NSTDA, Thailand.

Development of New Functional Materials for Energy and Environment

Researchers

1. Prof. Keiichi N Ishihara, Kyoto University

2. Prof. Wisanu Pecharapa, King Mongkut's Institute of Technology Ladkrabang

3. Prof. Sorapong Pavasupree, Rajamangala University of Technology Thanyaburi

Abstract

Our group have studied the composite of Leucoxene /$BiVO_4$ composite material prepared by sonochemical-assisted process by using low-cost leucoxene derived material (LDM) as titanium dioxide source and BiVO4 with different composition ratios. Crystallinity of composite specimens shows the combining structure between monoclinic $BiVO_4$ and TiO_2 rutile phase with corresponding optical band gap of 2.4 eV and 2.85 eV, respectively. The 2:8-LDM:BV composite performs superior photocatalytic activity with complete decomposition of RhB dye under 20 min of light exposure due to heterojunction structure assisting the recombination retardment of photogenerated electron-hole pair. Superoxide radical ($\bullet O_{2-}$) is revealed to be major active specie induced by this composite. The composite catalyst exhibits excellent repeatability and reusability with 80% decomposition of organic compound after 10 times of usage.

Research Summary

In summary, LDM/$BiVO_4$ heterophotocatalyst material was prepared by single step sonochemical process with different composition ratios. The result reveals that the mixed crystalline structure of monoclinic $BiVO_4$ and rutile TiO_2. All specimens exhibited the visible light active with corresponding optical band gap around 2.5-2.8 eV, which result in the superior photocatalytic performance of 2:8-LDM:BV sample with decomposition rate constant $k = 0.2\ min^{-1}$. The enhancement of photocatalytic activity is promoted by the increase of electron-hole separation assisted by LDM acting as neighbor material to $BiVO_4$ host. The superoxide radical has a key role in the RhB photodecomposition process for LDM:BV heterophotocatalyst material. The work could contribute a novel process to prepare the new heterophotocatalyst material from $BiVO_4$ with low-cost Leucoxene mineral as an alternative for titanium-rich material.

Publications and Presentations

- T. Kansaard, K. N. Ishihara, W. Pecharapa, *Structural, optical, and photo-induced catalytic properties of derived-Leucoxene /$BiVO_4$ composite prepared by sonochemical process*. Optik, 267 (2022) 169665

- T. Kansaard, K. N. Ishihara, W. Pecharapa, Characterization and Visible Light-Driven Photocatalytic Activity of $BiVO_4$/BiOCl/Bi_2S_3 Nanocomposites Prepared by Sonochemical Process, Physica Status Solidi A, https://doi.org/10.1002/pssa.202200447 (article in press).

- K. Boonyarattanakalin, T. Noinonmueng, T. Kansaard, T. Wechprasit, W. Mekprasart, K. Phacheerak, W. Pecharapa, A. Jaruvanawat, *Structural, optical, and visible-light driven photocatalytic properties of yb-doped bivo4 nanoparticles prepared via rapid sonochemical process*, Suranaree Journal of Science and Technology, 30 (2023), 030095(1-6.

Group Workshops, meetings, and researcher exchange

- Special Workshop on Photocatalyst and Functional Optical materials (hybrid online-onsite meeting) 11 March 2022 at the 55th years Chalermprakiat Building, KMITL, Bangkok, Thailand

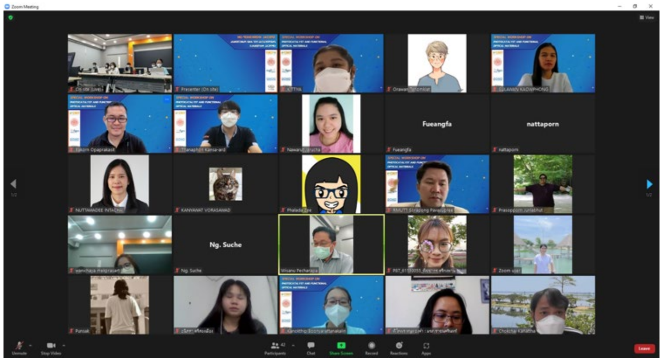

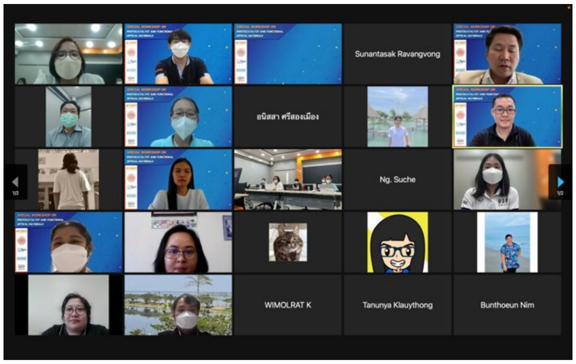

- Special Symposium on Materials for Environment Applications (hybrid online-onsite meeting) 6-8 April, 2022, Pullman Pattaya Hotel G, Pattaya, Thailand.

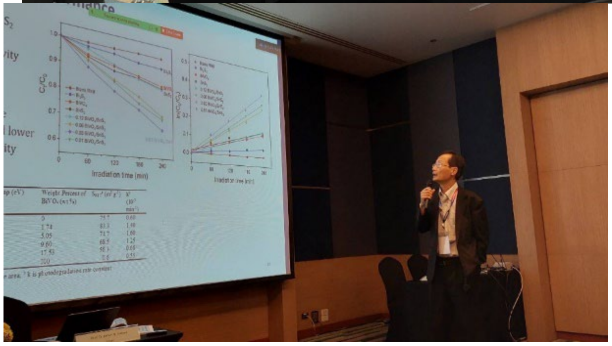

Transdisciplinary Studies on Sustainable and Equitable Energy Use in South East Asia

Researchers

1. Prof. Hideaki Ohgaki	Kyoto University
2. Assit Prof. Jordi Cravioto C.	Kyoto University
3. Prof. Nasrudin Abd Rahim	University of Malaya
4. Sen. Lect. Tan Chia Kwang	University of Malaya
5. Sen. Lect. Hang Seng Che	University of Malaya
6. Mr. Anugerah Yuka Asmara	BRIN
7. Dr. Bun Long	Institute of Technology of Cambodia
8. Dr. Vai Vannak	Institute of Technology of Cambodia

Abstract

The challenges for sustainable energy use in Southeast Asia are enormous. On the one hand, energy consumption in urban households in the region's large metropolises is increasing due to rising household incomes and the expansion of household appliances. In more rural settings, the lag in clean energy access remains a critical problem for energy sustainability and equity. However, research associated with such challenges have mostly lacked of approaches oriented on key human determinants that can improve both conditions. In such a context, our project investigates the human aspects related to energy access and efficient household consumption from rural and urban perspectives in Southeast Asia. In 2021-2022, we have developed two investigations. The first is an extension of our study of the effects of electrification on the quality of life of people living in remote areas. We have used qualitative methods to identify individual preferences, social barriers and other difficulties in the adoption of renewable energy technologies widely used for electrification in remote areas. The second, a study focused on equity inside the household and its effect on the adoption of energy-efficient appliances in metropolitan cities of the Philippines and Indonesia. Following the lifting of travel restrictions in 2022, we visited four villages in Rizal (Philippines) and two villages in Sarawak (Malaysia) to collect more than 50 interviews for our first study. So far, our analysis has revealed that, in general, the capacity of the system is a serious constraint to new economic activities and increased household incomes. Unreliability, difficulties with intermittent power production and the quality of the systems supplied are other major obstacles to electrification's sustainability. However, electrification even on a small scale has brought benefits on health, safety and certain productive activities. Some benefits are more unique to specific settings, such as those for children's education in the Philippines and

improved family and neighbourhood interaction in Malaysia. However, electrification is also associated with certain negative effects related to changing lifestyle and activity cycles in communities. In addition, it may have exacerbated existing inequalities testified by the ability to tap into the resource of the more privileged members of the community. For our second study, we studied how equity in household functions is related to sustainable behaviour as seen through the intention to purchase efficient household appliances. A sample of participants collected in metropolitan cities in Indonesia and the Philippines (n=864) was analysed using multinomial logistic regression and multiple correspondence analysis in 2022 - 2023. It was found that equity in decision-making had the most significant effect on the choice of efficient appliances over other roles of appliance management and use, and the role of breadwinner appeared to be the most unrelated. The results provide empirical evidence that equity inside household could be significant for sustainable behavior in energy use, having important implication on policy to consider for the future expansion of household appliances in cities from rapid economic growth.

Research Summary

Electrification and Quality of Life: Perspectives on the equitable and sustainable use of energy in rural contexts of South East Asia

Great strides have been made to achieve universal electrification by 2030 as set out by the UN in the Sustainable Development Goals. However, only seven years before the target date more than 30 million people still lack access in Southeast Asia. Myanmar and Cambodia have made great efforts to achieve the goal, but still rank the two lowest by population percentage in terms of electricity access, having 51% and 81% each [1]. Similarly, Myanmar, Indonesia and the Philippines have gradually reduced their total population without electric power, but still rank highest with roughly 16, 8 and 4 million people without access, respectively [1]. Other countries appear to have achieved universal access, but not in each of their hinterland regions. Malaysia is one such example as it has a high electrification rate nationally, but remains critically low in the eastern regions of Sarawak and Sabah on the island of Borneo [2]. Although efforts in recent years are evident, it is still necessary to understand the underlying reasons behind the lag of universal electrification in such contexts.

Under such context, our project started studying the effects of electrification on populations without access in South East Asia. The project has focused on studying changes in people's Quality of Life (QoL) during the electrification process. Few research had focused on the benefits and social disparities in renewable energy technology adoption from such a perspective to provide clues about individual preferences, social barriers and other difficulties related to the process of technology appropriation. We have been investigating QoL and electrification in villages of five countries: Myanmar, Cambodia, The Philippines, Indonesia and Malaysia. After the introduction of PV systems, we have observed both positive and negative changes in in people's quality of life based on primary surveyed data [3, 4]. However, the reasons behind these changes and possible disparities between groups had not been explored until 2022. Since then, the project has focused on the exploration of benefits and social disparities during electrification using qualitative methods.

After the lifting of travel restrictions in 2022, we have visited four villages in Rizal (Philippines) and two villages in Sarawak (Malaysia), collecting more 50 interviews from these visits. Our analysis of the data so far has found that overall the system's capacity is a serious limitation for new economic activities and household income increase. The unreliability, difficulties with intermittent energy production, and quality of the systems provided are other major obstacles to the sustainability of the projects in all the sites studied. Some benefits are also similar across contexts, e.g. health, safety and productivity effects from reduced reliance on more expensive kerosene lamps and car batteries, reduced fire risks, improved night-time manoeuvrability, reduced time spent collecting firewood or cooking, and the ability to store perishable goods for trade using a refrigerator. However, other benefits are more unique to specific environments, such as the marked benefits for children's education in the Philippines and improved family and neighbourhood interaction in Malaysia. Negative effects from electrification have also happened, such as an increased concern on the change of lifestyle and activity cycles in communities in both settings. Furthermore, electrification may have exacerbated previous inequalities, as some households appear to achieve greater benefits given a better off socio-economic status prior to electrification. Existing inequalities may have increased due to the developed ability to tap into the resource of more privileged members of the community. These results conform the preamble of the exploration using qualitative methods in conjunction with our colleagues in the Philippines, Malaysia and Indonesia.

As we progress the research, we have been presenting our results at various conferences. We have participated at the Grand Renewable Energy International Conference in December 2022 (online) [5], at the European Geosciences Union General Assembly (Austria) in February 2023 [6], and at the 6th International Conference on Clean Energy and Technology 2023 (Malaysia) in June 2023 [7].

Household roles and efficient appliance purchasing behavior: Perspectives on equitable and sustainable use of energy in urban contexts of South East Asia

Our second approach to the investigation of the social effects of energy consumption focuses on urban areas in Southeast Asia. During 2021 - 2022, we developed and tested a framework to analyse efficient appliance purchasing preference and household roles [8]. We designed a questionnaire based on the framework and collected a purposive sample from metropolitan cities in Indonesia and the Philippines (n=864). Following in 2022-2023, we found using Multinomial Logistic Regressions and Multiple Correspondence Analysis on the collected data that equity in the decision-making inside the household had the most important effect on choosing efficient appliances. Other roles related to household management or the appliance user were secondary, and the role of bread winner seemed unrelated. In general, the more inclusive households, i.e. having joint decisions, collaborative planning of payments and joint use, favoured purchasing efficient appliances. These results provided empirical evidence that more equitable household functions may be a significant configuration for sustainable transitions, complementing the common knowledge that gender differences (women compared to men) exhibit more sustainable behaviour. The results were presented in the 3rd Int. Conf. on Energy Research and Social Science in June 2022 [9]. Currently, we are undergoing a review to publish the findings in an international journal.

References

1. WB. World Bank Indicators, Data – Access to Electricity (% of population). https://data.worldbank.org/indicator/EG.ELC.ACCS.ZS (accessed on Jul 30, 2023).
2. Kearney, A roadmap to energy access for all in Sabah, Malaysia. Jan 26, 2021 https://www.kearney.com/why-us/sustainability-and-social-impact/article/-/insights/a-road-map-to-energy-access-for-all-in-sabah-malaysia (accessed on Jul 30, 2021)
3. Cravioto et al. (2020). The effects of rural electrification on quality of life: A southeast Asian perspective. Energies, 13(10), 2410
4. Cravioto et al. (2021). Household lighting and quality of life in rural Philippines: the effect of PV lamps use in non-electrified communities of Tanay. エネルギー・資源学会研究発表会講演論文集, 40, 487-492.
5. Cravioto et al. (2022) The effects of solar home systems on quality of life: Narratives from rural households in the Philippines. グランド再生可能エネルギー2022国際会議.
6. Cravioto and Ohgaki (2023) Can the circular economy be relevant for rural development? Insights from communities without electricity in Southeast Asia. European Geosciences Union General Assembly 2023, Energy Resources and the Environment. Viena, Austria.
7. Cravioto et al. (2023) Electrification effects on quality of life in Southeast Asia: A comparison of narratives in Malaysia and The Philippines. 6th International Conference on Clean Energy and Technology 2023. Penang, Malaysia.
8. Cravioto et al. (2022) Household roles and efficient appliances purchasing in urban contexts of Indonesia and The Philippines. 38th Conference on Energy Systems, Economics and Environment. Japanese Society of Energy and Resources.
9. Cravioto et al. (2022) Household roles and efficient appliances purchasing in urban Indonesia and The Philippines. Energy and Climate Transformations: 3rd International Conference on Energy Research and Social Science. Univ. of Manchester, UK.

Publications and Presentations

2021

1. Asmara, A.Y., Hidayat, A.R.T., Ohgaki, H., Mitsufuji, T., and Cravioto, J. Utilization of solar and wind energy to improve the quality of life for rural communities in Blora Regency–Indonesia: from triple helix to quadruple helix. In IOP Conference Series: Earth and Environmental Science (Vol. 916, No. 1, p. 012036). IOP Publishing. Nov, 2021. (oral presentation)

2022

1. Cravioto, J. The impact of rural electrification on QoL: PV lamps use in the Philippines. Shiga Prefectural ZeZe High School. Jan 15, 2022. (invited lecture)
2. Cravioto, J., Seniorita, L., Dumlao, S.M., Kumar, K., Qu, C., and Ohgaki, H. Household roles and efficient appliances purchasing in urban contexts of Indonesia and The Philippines. 38th Conference on Energy Systems, Economics and Environment. Japanese Society of Energy and Resources. Jan 25, 2022. (oral presentation)
3. Cravioto, J. Household roles and efficient appliances purchasing in urban Indonesia and The Philippines. Data-Oriented Approaches to the Social Sciences and Humanities Unit End-Year Workshop 2021. Center for Southeast Asian Studies, Kyoto University, Mar 02, 2022. (oral presentation)
4. Cravioto, J., Seniorita, L., Dumlao, S., Krishnamurthy, K., Qu, C., and Ohgaki, H. Household roles and efficient appliances purchasing in urban Indonesia and The Philippines. Energy and Climate Transformations: 3rd International Conference on Energy Research and Social Science. Univ. of Manchester, UK. June 20-23, 2022. (oral presentation)
5. Cravioto J. Household energy services and its relation with energy poverty measurements [Los servicios de energía y su relación con la medición de pobreza energética en hogares]. In Pobreza de Energía: Visiones desde América Latina (García-Ochoa R., coord.). Tijuana, Baja California: El Colegio de la Frontera Norte (COLEF); Zamora, Michoacán: El Colegio de Michoacán, pp. 61-84, Dec, 2022 [in Spanish]. (book chapter)
6. Cravioto, J., Ohgaki, H., Napao, J.M., Quinones, J. and Cabrera, J.A. The effects of solar home systems on quality of life: Narratives from rural households in the Philippines. グランド再生可能エネルギー2022 国際会議. Dec, 2022. (oral presentation)

2023

1. Cravioto, J. Solar electrification and Quality of Life in rural Philippines: Mixed-

research perspectives. Shiga Prefectural ZeZe High School. Jan 14, 2023. (invited lecture)

2. Asmara, A.Y., Hidayat, A.R.T., Kurniawan, B., Ohgaki, H., Mitsufuji, T. and Cravioto, J. Building a Sustainable Photovoltaic Innovation System in Indonesia Through Network Governance Perspective. In: Triyanti, A., Indrawan, M., Nurhidayah, L., Marfai, M.A. (eds) Environmental Governance in Indonesia. Environment & Policy, vol 61. Springer, Cham, 2023. (book chapter)
3. Cravioto, J., Seniorita, L., Dumlao G., S.M., Krishnamurthy, K., Qu, C. and Ohgaki, H. Does equity in household functions promote sustainable behaviour? Insights from Indonesia and the Philippines. Environment and Behaviour, submitted Jun 2023. (journal article, under review)
4. Cravioto, J. and Ohgaki, H. Can the circular economy be relevant for rural development? Insights from communities without electricity in Southeast Asia. European Geosciences Union General Assembly 2023, Energy Resources and the Environment. Viena, Austria. Apr, 2023. (oral presentation)
5. Cravioto, J. Vulnerability and the social dimensions associated with residential energy use [Vulnerabilidad y dimensiones sociales asociadas al uso de energía residencial]. Guanajuato Univ, Mexico. May 13, 2022. (invited lecture)
6. Cravioto, J. Household energy use and vulnerability [Uso de energía en hogares y vulnerabilidad]. Seminario Internacional de Investigación en Ciencias de la Sostenibilidad. UNAM ENES Leon, Mexico. May 24, 2022. (invited lecture)
7. Cravioto, J., Ohgaki, H., Tan, C.K., and Che, H.S. Electrification effects on quality of life in Southeast Asia: A comparison of narratives in Malaysia and The Philippines. 6th International Conference on Clean Energy and Technology 2023. Penang, Malaysia. Jun, 2023. (oral presentation)

Group Workshops, meetings, and researcher exchange

NA

Other outcomes

Best Presentation: Cravioto, J., Ohgaki, H., Tan, C.K., and Che, H.S. Electrification effects on quality of life in Southeast Asia: A comparison of narratives in Malaysia and The Philippines. 6th International Conference on Clean Energy and Technology 2023. Penang, Malaysia. Jun, 2023.